

Development of LMR-NMC Based Cathodes and Si-Based Anodes for High Energy Density Lithium-Ion Batteries

By
Krishna Kumar Sarode

A Dissertation Submitted to
Indian Institute of Technology Hyderabad
In Partial Fulfillment of the Requirements for
The Degree of Doctor of Philosophy



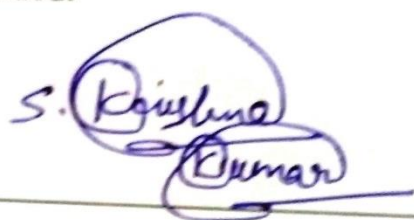
भारतीय प्रौद्योगिकी संस्थान हैदराबाद
Indian Institute of Technology Hyderabad

Department of Chemistry

February, 2018

Declaration

I declare that this written submission represents my ideas in my own words, and where others' ideas or words have been included, I have adequately cited and referenced the original sources. I also declare that I have adhered to all principles of academic honesty and integrity and have not misrepresented or fabricated or falsified any idea/data/fact/source in my submission. I understand that any violation of the above will be a cause for disciplinary action by the Institute and can also evoke penal action from the sources that have thus not been properly cited, or from whom proper permission has not been taken when needed.



(Signature)

(Krishna Kumar Sarode)

(Roll No. CY13P1010)

Approval Sheet

This thesis entitled '**Development of LMR-NMC Based Cathodes and Si-Based Anodes for High Energy Density Lithium-Ion Batteries**' by Krishna Kumar Sarode is approved for the degree of Doctor of Philosophy from IIT Hyderabad.



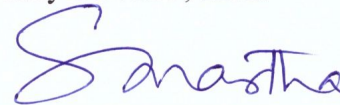
External Examiner
Professor M. V. Sangaranarayanan
Professor, Dept. of Chemistry
Indian Institute of Technology Madras
Chennai- 600 036, India



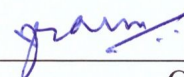
External Examiner
Professor Manoj Neergat
Dept. of Energy Science and Engineering
Indian Institute of Technology Bombay
Powai, Mumbai-400 076, India



Internal Examiner
Dr. M. Deepa
Associate Professor, Dept. of Chemistry
Indian Institute of Technology Hyderabad
Kandi, Sangareddy-502 285, India



Adviser
Dr. Surendra Kumar Martha
Assistant Professor, Dept. of Chemistry
Indian Institute of Technology Hyderabad
Kandi, Sangareddy-502 285, India



Chairman
Dr. Praveen Meduri
Assistant Professor, Dept. of Chemical Engineering
Indian Institute of Technology Hyderabad
Kandi, Sangareddy-502 285, India

Acknowledgements

I would like to express my deep and sincere gratitude to my mentor Dr. Surendra K. Martha, Assistant Professor, Department of Chemistry. He has always been a beacon of hope in times of hardship during my research work despite his busy schedule. I would like to thank him for his encouragement and support to grow as a researcher, and also for always having faith in me even when my own belief flickered. His suggestions in research field have always been priceless, which alone has made my research work fruitful.

I would like to show my greatest appreciation to my Doctoral Committee members, Prof. Ch. Subrahmanyam and Dr. M. Deepa, Department of Chemistry for their overwhelming support, and also for making my presentations more constructive with their thoughtful comments and suggestions. I also extend my gratitude to the Head, Department of Chemistry and all other faculties in the Department for their direct/indirect support throughout my research work.

I gratefully acknowledge CSIR-UGC for research fellowship and DST-SERB for the financial support for the project work. I also owe my gratitude to Prof. Rachid Yazami, Nanyang Technological University (NTU), Singapore for his valuable inputs during the time of my summer internship (2017) under his supervision.

I thank Dr. Sai Rama, Dr. Partha Ghosal for TEM facility. I would also like to express my sincere thanks to Dr. Atul Suresh Deshpande and Dr. Ranjith Ramadurai, Department of Materials Science and Metallurgical Engineering for their kind assistance in various characterization techniques. I also wish to extend my warmest thanks to the non-teaching staffs in the Department of Chemistry.

My special thanks are due to my colleagues Mr. V. Naresh, Mr. Sourav Ghosh, Mr. V. Kiran Kumar, Mr. Abhisek Padhy, Mr. Sadananda Muduli, Dr. K. Ajayakumar and Dr. Liju Elias for their encouragement and cooperation.

I take this opportunity to thank my all friends and batchmates from IITH, especially Ms. Mukkabla Radha, Mr. Damodar Devarakonda, Mr. Akkisetty Bhaskar, Ms.

Usha Rani, Mr. A. Soundar, Mr. Brince Paul K., Dr. Bhaskar Mukri, K. Srinivas and Mr. Bhairi Lakshminarayana for their help during the course of my research work. I must also remember all my teachers and every great soul who has perhaps anonymous for passing their knowledge to me in shaping my mind and developing confidence in me.

Special thanks to my family. Mere words cannot express how grateful I am to my Amma, Bapu, Anna, Akka and Bava for all sacrifices they made on my behalf. Their prayers gave me the endurance to sustain this far. Above all, I humbly thank God Almighty, who showered the choicest of his blessings to complete this endeavor.


S. KRISHNA KUMAR

Dedicated to
My Beloved Family

Preface

Li-ion Batteries (LIBs) have attracted much attention in recent times among all the rechargeable batteries available today due to highest energy density (150-200 Wh kg⁻¹), cell voltage (3.7 V), good cycle life (1000-1500) and low self-discharge (2% per month). Lithium being the third lightest element, has high potential (-3.07 V vs. SHE), high capacity (3861 mAh g⁻¹) is an excellent anode material for LIBs. However, pure Li is very reactive to moisture in air and also form dendrites in LIBs upon charging to high voltages. The Li dendrites can penetrate through the separator causing short circuit which leads to development of heat, fire or explosion. The origin of LIB lies in the discovery that Li⁺ ions can be reversibly intercalated within or de-intercalated from the van der Waals gap between graphene sheets of carbonaceous materials at a potential close to the Li/Li⁺. Thus, lithium metal is replaced by carbon based anode materials for LIBs and the problems associated with pure metallic lithium mitigated. LIBs were first introduced into market by Sony Corporation of Japan during 1991 by using LiCoO₂ cathode and graphite anode in standard electrolyte solution containing LiPF₆ salt in alkyl carbonates. Since then, the LIB market has grown from an R&D interest and the current market value close to US\$40 billion. The world demand for primary and secondary batteries is forecasted to be US\$120 billion in 2019 in which rechargeable LIBs has market share about 37%.

Initially, specific energy of commercial LIB was only about 120 Wh kg⁻¹. Extensive research has been carried out to develop high capacity, high durability, and efficient anodes and cathodes with high voltage for LIBs. Due to continuing improvements in various cell components including improved manufacturing technology, present day LIBs can provide a specific energy density close to 200 Wh kg⁻¹.

The pursuit for high capacity, high energy density LIBs has led to the emergence of the Lithium-air and Lithium-sulphur (Li-S) batteries as promising candidates, wherein a conversion process has replaced the conventional insertion processes. While reaction of Li with oxygen in the Li-air gives a capacity as high as

1200 mAh g⁻¹, the Li-S battery, assuming complete conversion, can yield energy density of upto 2500 Wh kg⁻¹. The research in these aspects are very new and may be the technology of the future.

It is believed that advanced materials research and development will play an important role in the area of LIBs and will contribute substantially the future need of the human society.

The thesis is an attempt to develop high energy density LMR-NMC based cathodes with minimized voltage decay, improved capacity retention and cycle life, coupled with high capacity silicon anodes for increasing energy density in LIBs.

Contents

Declaration	ii
Approval Sheet	iii
Acknowledgements	iv
Preface	vi
Nomenclature	xiv
Definitions	xvii
Chapter 1: Introduction to Lithium-Ion Battery	1
1.1 Abstract	1
1.2 Importance of Energy Storage	1
1.3 Lithium Ion Battery: Significance and Historic Outlook	2
1.4 Working principle of LIB	3
1.5 Electrochemical constituents of a Lithium-ion cell	5
1.5.1 Layered, spinel oxides and olivine cathodes	6
1.5.1.1 LiCoO ₂ and its derivatives	6
1.5.1.2 LiMnO ₂	8
1.5.1.3 LiNiO ₂	10
1.5.1.4 NMC	11
1.5.1.5 LiMn ₂ O ₄	12
1.5.1.6 LiMn _{1.5} Ni _{0.5} O ₄	14
1.5.1.7 Olivines	15
1.5.1.8 LMR-NMC	18
1.5.1.9 Future cathodes for LIB	22
1.5.2 Anodes	23
1.5.2.1 Lithium anode	23
1.5.2.2 Carbon based anodes	24
1.5.2.3 Tin (Sn) based anodes	26
1.5.2.4 Titanium oxide	27
1.5.2.5 Lithium Titanium oxide (LTO)	29

1.5.2.6 Silicon	31
1.5.3 Electrolytes	34
1.6 Drawbacks and Failure Modes of Lithium-Ion Batteries	36
1.7 Scope and Objectives of the Thesis	39
1.7.1 The present study	40
References	43
Chapter 2: Effect of Temperature and C rate on “Ragone Plots” of Lithium-Ion Batteries	71
2.1 Abstract	71
2.2 Background and Motivation	72
2.3 Experimental	74
2.3.1 Structural and physical characterizations of electrode materials	74
2.3.2 Electrochemical characterizations	74
2.4 Results and Discussion	76
2.4.1 Electrode materials characterization	76
2.4.2 Isothermal discharge profiles	77
2.4.3 Galvanostatic discharge profiles	80
2.4.4 Ragone plots and Power-Energy Index (PEI)	82
2.5 Conclusions	85
References	86
Chapter 3: Study of High Energy Density Li-Mn Rich (LMR) Ni-Mn- Co Oxide (NMC) Cathodes for Lithium-Ion Batteries through 3D Electrode Architecture and LiF Coating	91
3.1 Abstract	91
3.2 Background and Motivation	92
3.3 Experimental	94
3.3.1 Synthesis of LMR-NMC and F-LMR-NMC	94
3.3.2 Structural and physical characterization of LMR-NMC and F- LMR-NMC	95
3.3.3 Electrode preparation and cell assembly	96
3.3.4 Electrochemical characterizations of LMR-NMC and F-LMR- NMC	96

3.4 Results and Discussion	97
3.4.1 Structural characterization	97
3.4.2 Physical characterizations and compositional analyses	99
3.4.3 Electrochemical performance studies	105
3.4.3.1 Structural, physical, electrochemical assessment of carbon fibers	105
3.4.3.2 Electrochemical assessment of LMR and F-LMR-NMC	107
3.5 Conclusions	113
References	114
Chapter 4: Synergistic Effect of Magnesium and Fluorine Doping on the Electrochemical Performance of LMR-NMC Cathodes for Lithium-Ion Batteries	121
4.1 Abstract	121
4.2 Background and Motivation	122
4.3 Experimental	124
4.3.1 Synthesis of LMR-NMC and Mg-F doped -LMR-NMC	124
4.3.2 Structural, physical and electrochemical characterization of LMR- NMC and F-LMR-NMC	125
4.4 Results and Discussion	125
4.4.1 Structure and morphology	125
4.4.2 Electrochemical performance	129
4.5 Conclusions	134
References	135
Chapter 5: LMR-NMC-Carbon Coated-LiMnPO₄ Blended Electrodes for High Performance Lithium Ion Batteries	139
5.1 Abstract	139
5.2 Background and Motivation	139
5.3 Experimental	142
5.3.1 Synthesis of C-coated LiMnPO ₄ nanoparticles	142
5.3.2 Synthesis of LMR-NMC and blended cathode materials	143
5.3.3 Structural, physical and electrochemical characterization of LMR- NMC, LMP and blended materials	143
5.3.4 Ageing test LMR-NMC, LMP and blended materials	144
5.4 Results and Discussion	144

5.4.1	Structural, physical characterization of LMR-NMC, LMP and blended materials	144
5.4.2	Electrochemical performance studies of LMR-NMC, LMP and blended materials	147
5.4.3	Mn dissolution studies of LMR-NMC, LMP and blended materials	152
5.4.4	Discussions	152
5.5	Conclusions	152
	References	154
	Chapter 6: Binder and Conductive Additive Free Silicon Electrode Architectures for Advanced Lithium-Ion Batteries	159
6.1	Abstract	159
6.2	Background and Motivation	160
6.3	Experimental	162
6.3.1	Synthesis of Si-NPs by magnesiothermic reduction	162
6.3.2	Structural, physical and characterization of Si-NPs	162
6.3.3	Electrode preparation	162
6.3.4	Cell assembly and electrochemical characterization	163
6.3.5	Post-mortem TEM analyses	163
6.4	Results and Discussion	163
6.4.1	Structural, physical characterization of Si-NPs	163
6.4.2	Electrochemical performance studies of Si- electrodes	165
6.4.3	Post-mortem analysis of Si-electrodes	169
6.4.5	Discussions	170
6.5	Conclusions	171
	References	172
	Chapter 7: In-situ 3D Electrode Fabrication of High Capacity Silicon-Carbon Anodes for Lithium-Ion Batteries	175
7.1	Abstract	175
7.2	Background and Motivation	176
7.3	Experimental	178
7.3.1	Synthesis of Si-NPs and structural-physical characterizations	178
7.3.2	Structural-physical characterizations carbon fibers, carbonized pitch and electrodes	178
7.3.3	Electrode preparation and cell assembly	180
7.3.4	Electrochemical performance studies	181
7.4	Results and Discussion	181
7.4.1	Structural-physical properties of Si-NPs, Si-C composite electrodes	181

7.4.2 Electrochemical performance studies	186
7.4.3 Discussions	192
7.6 Conclusions	193
References	194
Appendix-1: Techniques Employed During the Study	195
A.1.1 Electrochemical impedance spectroscopy	199
A.1.2 Chronopotentiometry	209
A.1.3 Chronoamperometry	210
A.1.4 X-ray diffraction (XRD) analysis	212
A.1.5 Electron microscopy	215
A.1.6 X-ray photoelectron spectroscopy	218
A.1.7 Raman spectroscopy	221
References	223
List of Publications	226

Nomenclatures

AC	:	Alternating current
AEM	:	Analytical electron microscopy
BET	:	Brunauer–Emmett–Teller
CDF	:	Crystal Diffraction File
CF	:	Carbon Fiber
C-LMP	:	Carbon coated LiMnPO_4
CNFs	:	Carbon nano fibers
DEG	:	Diethylene glycol
DMC	:	Dimethyl carbonate
DOE	:	Department of Energy
E.D.	:	Energy Density
EC	:	Ethylene Carbonate
EDAX	:	Energy dispersive X-ray spectroscopy
EELS	:	Electron energy loss spectroscopy
EIS	:	Electrochemical Impedance Spectroscopy
EMC	:	Ethyl methyl carbonate
EPI	:	Energy-Power Index
EPMA	:	Electron probe microanalysis
ESCA	:	Electron spectroscopy for chemical analysis
EV	:	Electric vehicle
FRA	:	Frequency response analyzer
GITT	:	Galvanostatic Intermittent Titration Technique
HF	:	Hydrogen fluoride
HiFP	:	Tris (hexafluoroiso-propyl) phosphate
HTLCO	:	High temperature LiCoO_2
ILs	:	Ionic liquids
IR	:	Infrared
JCPDS	:	Joint Committee on Powder Diffraction Standards
LCO	:	Li_xCoO_2

LFMP	:	$\text{LiFe}_{0.2}\text{Mn}_{0.8}\text{PO}_4$
LFP	:	LiFePO_4
LIBs	:	Lithium-Ion Batteries
LiTf	:	Lithium trifluoromethanesulfonate
LiTFSI	:	Lithium bis(trifluoromethanesulfonyl)imide
LMO	:	LiMnO_2
LMR	:	Li-Mn Rich
LTLCO	:	Low temperature LiCoO_2
LTO	:	Lithium Titanium oxide
MCMB	:	Meso carbon microbeads
MSM	:	Molten salt method
NCA	:	$\text{LiNi}_{0.8}\text{Co}_{0.15}\text{Al}_{0.5}\text{O}_2$
NIR	:	Near infrared
NLLS	:	Non-linear-least-square
NMC	:	Ni-Mn-Co Oxide
NMS	:	$\text{LiNi}_{0.5}\text{Mn}_{1.5}\text{O}_4$
NVP	:	N-vinyl pyrrolidone
OCV	:	Open circuit voltage
O-LMO	:	Orthorhombic LiMnO_2
P.D.	:	Power Density
PC	:	Propylene carbonate
PEI	:	Power Energy Index
PEO	:	Poly(ethylene oxide)
PMP	:	Powder metallurgy pulverization
P-pitch	:	Petroleum pitch
PVdF	:	Polyvinylidene fluoride
SEI	:	Solid Electrolyte Interphase
SEM	:	Scanning electron microscopy
Si-C	:	Silicon-Carbon
Si-NPs	:	Silicon nanoparticles
SoC	:	State-of-charge

SOH	:	State-of-Health
TEM	:	Transmission electron microscopy
TM	:	Transition metal
UV	:	Ultraviolet
XPS	:	X-ray photoelectron spectroscopy
XRD	:	X-ray Diffraction
3DOM	:	Three-dimensionally ordered macroporous

Definitions

$$\text{Capacity} = \frac{26.8}{\text{Equivalent weight}} \text{ Ah g}^{-1}$$

Capacity fade: Gradual loss of capacity of a secondary battery with cycling.

Capacity retention: The fraction of the full capacity available from a battery under definite conditions of discharge after it has been stored for a period of time.

C rate: The rate at which a cell or battery is being charge-discharged. E.g., 1C refers to the capacity in 60 min, C/20 refers to the capacity in 20h and so on...

Coulombic efficiency: The ratio of output charge of a secondary cell or battery on discharge to the input required to restore it to the initial state-of-charge under specified conditions.

Constant-current (CC) charge: The method of charging a battery using a current having little variation.

Constant-voltage (CV) charge: The method of charging a battery by applying a fixed voltage, and allowing variations in the current.

Cutoff voltage: The battery voltage at which the discharge is terminated. This is also called end voltage.

Cycle life: The number of cycles under specified conditions that are available from a secondary battery before it fails to meet its performance.

Energy density: The ratio of the energy available from a battery to its weight (Wh kg⁻¹ or volume (Wh L⁻¹).

Irreversible capacity: The capacity loss due to irreversible consumption of lithium during first cycle.

Nominal voltage: The operating voltage of a cell or battery.

Open circuit voltage: The voltage of the battery under no load condition.

Operating voltage: The typical range of voltages of a battery during discharge

Power density: The ratio of the power available from a battery to its weight (W kg^{-1}) or volume (W L^{-1}).

Self-discharge: The loss of useful capacity of a cell or battery due to internal chemical action (side reactions).

Solid electrolyte interphase (SEI): The layer that is formed during 1st cycle at the anode (Graphite, Si, SnO_2 etc.) surface due to decomposition of solvents forming mixture of lithium carbonate, oxides, fluorides and semi carbonates. The SEI layer thickness in LIBs around 10's of nm.

State-of-charge: The ratio of capacity available at instant to the total available capacity.

State of health: It is a figure of merit of the condition of a battery compared to its ideal conditions.

Thermal runaway: A condition where a cell or battery on charge or discharge will overheat and destroy itself through internal heat generation caused by high overcharge or over discharge currents or other abusive condition.

Chapter 1

Introduction to Lithium-Ion Batteries

1.1. Abstract

Li-ion battery (LIB) technology continues to be the most successful electrochemical system developed in recent times. Because of its high energy density, LIB is the choice to power cellular phones, portable computers, camcorders, power tools and even in hybrid electric vehicles and electric vehicles. This Chapter describes a brief introduction to LIBs with a review of technical literature on the electrode materials, electrolytes and includes an account of studies presented in the thesis.

1.2. Importance of Energy Storage

Energy is the lifeblood of the modern society [1, 2]. The access to energy is very important for the prosperity, life style and growth of every country [3]. The effect of globalization, population increase and rising consumer demands across developed and developing countries have resulted in an exponential increase in energy consumption [4]. This has significantly increased the gap between energy production and demand over the last several decades. Fundamental breakthrough in clean energy research is needed to solve the problem of such magnitude. Innovations in materials and processing technology provide significant opportunities for the transition from fossil based sources to clean energy sources such as nuclear, wind and solar energy [5]. But renewable energy sources must be captured and stored until demanded. They are somewhat varying with time, and the amount of energy supply is unpredictable [6, 7]. The success of these technologies relies on development of efficient energy storage materials that can be utilized in smart batteries and capacitors. Fuel cells offer another

alternative clean energy but would probably require further research in bringing down the cost for mass market. Batteries are efficient energy storage devices than capacitors which supply pool of energy on demand [8].

Among the leading secondary battery systems: lead-acid batteries, Ni based batteries and LIBs, the LIBs are rising faster due to high energy density (150-200 Wh kg⁻¹ against 30 Wh kg⁻¹ for lead-acid and 50-80 Wh kg⁻¹ for the Ni-based batteries) and long cycle life [9, 10]. Because of high energy density, LIBs are the choice to power cellular phones, portable computers, camcorders, power tools and even in hybrid electric vehicles and electric vehicles [11-15]. Besides, LIBs are light weight, offer high voltage (~3.7 V) low memory effect and low self-discharge rate, high rate capability and good cycle life of about 1000 cycles [16-19].

1.3. Lithium-Ion Battery: Significance and Historic Outlook

Lithium batteries through intercalation chemistry were first proposed by M Stanley Whittingham at the Exxon Laboratories during 1970s [20] by using titanium (IV) sulfide cathode and lithium metal as anode. However, practical rechargeable lithium batteries have not realized during that time because of high moisture reactivity and cost of Titanium disulfide. Besides, LIBs with lithium metal anode have safety issues, as lithium reacts with moisture (H₂O and O₂) in normal atmospheric conditions [11]. So research intended to develop batteries with non-metallic lithium based anodes and only lithium compounds are present, being capable of accepting and releasing lithium ions.

Consequently, the reversible electrochemical intercalation of Li⁺ in graphite was demonstrated by Rachid Yazami in 1980, which paved the way to the discovery of an alternative anode for LIBs instead of pure lithium metal [21]. The reversible intercalation of Li⁺ along the van der Waals gap between graphene sheets of graphite, at a voltage (V) of 0.2 V vs. Li/Li⁺, was found to offer a theoretical capacity of 372 mAh g⁻¹ and with slow charge-discharge rates the electrodes perform well with no dendrite formation.

Li_xCoO₂ (LCO), as a feasible cathode material for LIBs was demonstrated by J. B. Goodenough and coworkers at Oxford University during 1980 [22]. The theoretical specific capacity of LCO is 274 mAh g⁻¹ (when one mole of lithium per

formula unit participates in electrochemical redox process), but shows the practical capacity about 140 mAh g⁻¹, when cycled in the voltage window between 2.5-4.2 V.

Practical LIBs came to market through SONY Company of Japan during 1990. The LIBs consists of graphite anode and LCO cathode revolutionized the energy storage market of mobile devices. After the commercialization of the LIB in 1990, several advances have helped to bring down the costs of the battery. Even today, LCO and graphite chemistries dominates the LIB market. But, the major drawback with LCO is that only half of the lithium can be extracted from the parent LCO compound due to structural stability limitation which restricts the broad spectrum of application. Besides, LCO is toxic, biohazardous and thermally unstable [23, 24, 25].

Later in 2005, SONY introduced Nexelion™, the first hybrid rechargeable LIB containing a tin-based amorphous anode and a mixed metal composite cathode having the mixture of cobalt, manganese, and nickel oxides such as LiNi_{0.33}Mn_{0.33}Co_{0.33}O₂ (NMC). The battery showed 30% more capacity per volume compared to conventional LIBs containing LCO as cathode and graphite as anode. These batteries are thermally more stable than LCO due to less Co content and practically deliver capacity in the range between 160-180 mAh g⁻¹.

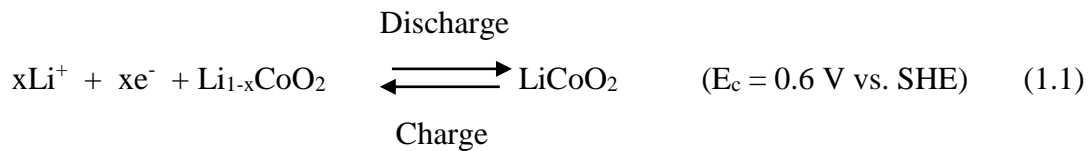
Subsequently in 2007, A123 Systems of USA developed LIB comprising LiFePO₄ (LFP) as cathode and graphite as anode which showed improved power capability, high thermal stability, stable cyclability, long battery life with minimized cost used for hybrid electric vehicles and grid. It delivers a calendar life of over 1500 cycles.

1.4. Working principle of LIB

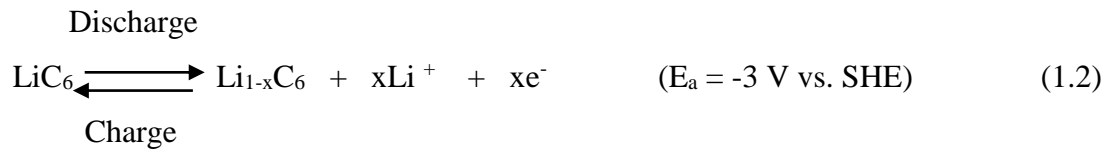
The important components of LIB comprises of anode (layered intercalation material (e.g., graphite) and cathodes based on intercalation materials like lithium transition metal oxide cathode (LiMO₂, e.g., LiCoO₂), a non-aqueous electrolyte consisting of a salt (1.0 M LiPF₆) [26] dissolved in an organic solvent (such as ethylene carbonate (EC) and dimethyl carbonate (DMC) etc.) [27] and separator (polyethylene polypropylene based or glass mat separators). In the lithium-ion cell, Li-ions from cathode are intercalated and de-intercalated without much structural modification.

While charging Li-ions are extracted from cathode and inserted into anode and while discharging vice versa takes place during which electrons moves through external circuit giving the energy. The fully-charged lithiated carbon anode has about the same electrochemical potential of metallic lithium. The half-cell reactions occurring at the cathode and anode during the charge-discharge cycles of a lithium-ion cell are presented as follows.

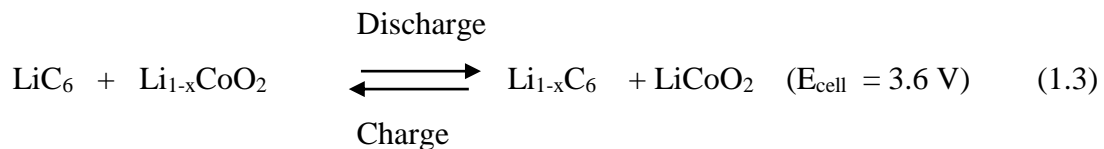
At the cathode:



At the Anode:



Accordingly, the net cell reactions during its charge-discharge process are:



The operating principle of a lithium-ion cell is shown schematically in Fig. 1.1.

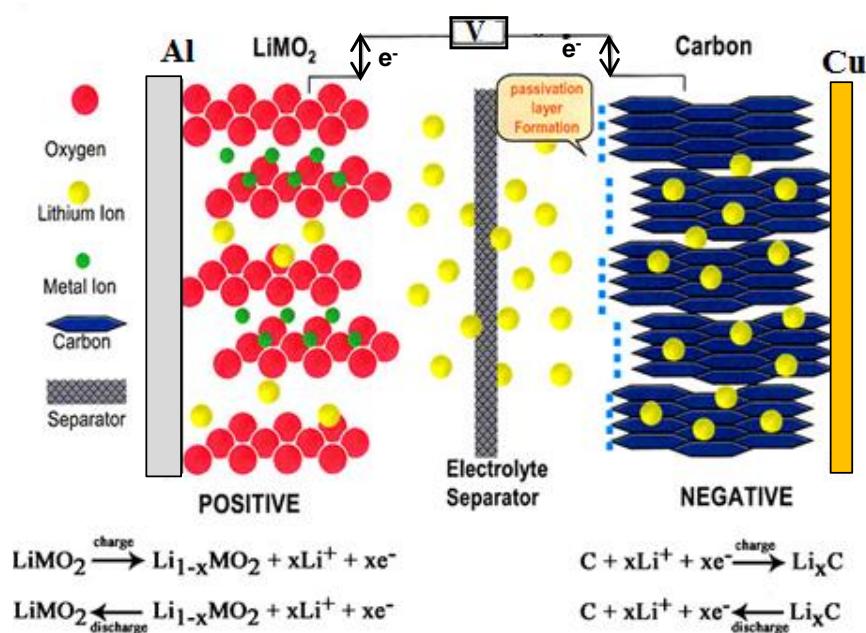


Fig. 1.1: Schematic representation of a Li-ion cell

1.5. Electrochemical Constituents of a Lithium-Ion Cell

Depending on the choice of cathode and anode material, the voltage, capacity consequently the energy density, life, and safety of a LIB changes drastically. Several reviews describing high performance of LIBs have been published in the literature. However, the present thesis comprises studies on cathode and anode material for LIBs and hence the discussion is limited to these aspects only.

During last 3 decades a large variety of materials have been synthesized and evaluated as cathode materials for LIBs. In general for the development of efficient cathodes, the cathode should have high voltage, high capacity consequently delivers high energy (Voltage × Capacity), high conductivity (helps to improve capacity retention, C rate performance and life), non-reactive in electrolyte solution (otherwise cause rapid dissolution), ease of synthesis (can be scaled up in large quantities), good cycle life, low self-discharge, safe and low cost.

In the light of the aforesaid factors, several-type of cathode materials have been studied for LIBs in the literature. These include layered transition metal oxides and spinels, olivines, halides [28-31], chalcogenides [32], organic compounds and conducting polymers [33, 34]. The first three categories of the compounds

commercially available today because of their superior performance and are briefly reviewed below.

1.5.1. Layered, spinel oxides and olivine cathodes

Subsequent to the discovery of LiCoO_2 by Goodenough and coworkers [30], several oxides with the layered- and spinel structures and olivine compounds have been investigated as cathodes.

1.5.1.1. LiCoO_2 and its derivatives

LiCoO_2 (LCO) is the first and the most commonly used cathode material in commercial LIBs even today [22]. LCO has many desirable properties like high discharge potential (>3.7 V), low molecular weight (97.87 g mol^{-1}), high capacity (274 mAh g^{-1}), high energy (530 Wh kg^{-1}), stable cycling performance (>500 charge-discharge cycles) and can be synthesized by simple methods. The de-lithiation potential of LCO is limited to 4.2 V (vs. Li/Li^+), which means, only half of the theoretical capacity of the cathode, around 140 mAh g^{-1} is delivered is mainly due to first-order phase transition between LiCoO_2 and $\text{Li}_{0.5}\text{CoO}_2$ [35]. LCO can be synthesized by solid state reaction [36-38], sol-gel technique [39,40], ultrasonic spray pyrolysis process [41], combustion synthesis [42,43], molten salt synthesis [44], co-precipitation method [45], complex formation method [46], freeze-drying method [47], mechano chemical, and microwave synthesis [48, 49], hydrothermal synthesis [50], and other methods. LCO exhibits two forms, a hexagonal layered structure and a cubic structure, are distinguished by the spatial arrangement of cations. Based on the synthesis methods, LCO may have either hexagonal layered structure for high temperature ($>800^\circ\text{C}$) LiCoO_2 (HTLCO) or cubic spinel-like structure for low-temperature ($500\text{-}600^\circ\text{C}$) LiCoO_2 (LTLCO) [51]. Gummow et al. [52,53] showed the structure of LTLCO is not preferably layered, and 6% of the cobalt ions reside in the octahedral (8a) sites of the lithium layers by using neutron diffraction data. According to Rossen et al. [54], LTLCO is supposed to form a spinel-relate structure (space group $\text{Fd}3\text{m}$) depending on a cubic closed packed oxygen network having alternating cation layers of 0.75 Co, 0.25 Li and 0.75 Li, 0.25 Co composition perpendicular to each of the four cubic direction. The structure of HTLCO relates to the trigonal system (space

group $R\bar{3}m$, O3 phase) having a perfect G-NaFeO₂ layered structure, in which Co and Li planes alternate in the ABCABC oxygen stacking [55]. The cell parameters reported in literature are in the range between 2.815 – 2.816 Å for the a-value (inter layer metal – metal distance), and in the range of 14.05 – 14.08 Å for the c-value (inter slab distance). HTLCO shows good electrochemical performance than LTLCO. LTLCO known to have structures intermediate to perfect-layered and perfect-lithiated spinels [52, 53].

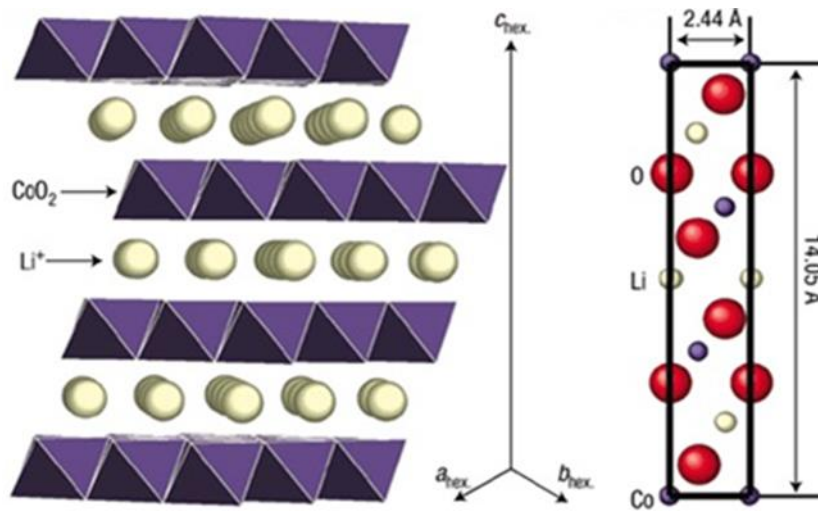


Fig. 1.2: Layered structure of LiMO₂ (M = Co, Ni, Mn, Fe) (Adopted from Ref. [52])

LCO practically delivers low discharge capacities, in the range of 135-150 mAh g⁻¹, which is about 50-55% of its theoretical capacity. Lithium de-insertion from LCO involves many two-phase and single phase regions with a monoclinic phase at Li_{0.5}CoO₂. In order to enhance the ionic conductivity and cycling performance of the LCO cathode, some approaches such as carbon coatings [56,57], coatings with oxide compounds such as Al₂O₃ [58, 59], ZnO [60], and Li₄Ti₅O₁₂ [61]. The coatings and dopings help LCO to improve interfacial stability. The coatings played an important role by enhancing the initial discharge capacity and also cycle life. Lu et al. [62] showed an 1st discharge capacity of 195 mAhg⁻¹ for the 1 wt. % Al₂O₃-coated LCO which is made by in-situ sol-gel method showing 85% capacity retention after 30 cycles [63]. Study by Li et al. [64], showed 11.3% capacity loss after 400 cycles for 3.0 wt. % FePO₄-coated LCO cathodes. Other coatings which have produced significant improvements on the electrochemical behavior of LCO include ZrO₂ [65]

and $\text{Li}_2\text{PO}_2\text{N}$ [66]. High voltage stability (4.4 V) of LCO cathodes can be achieved with a 10s of nm coating of LiPON onto LCO. LiPON improves interfacial stability at high voltages as coating reduces side reactions that increases cell impedance during cycling [67]. The major drawback of this coating is that when thicker films of LiPON coated on to LCO particles it increases impedance and hence reduces the power performance of the cells.

The major concern of LCO is limited cycling life due to structural instability during charge-discharge cycling. The lattice expansion rate along the c axis (Fig. 1.2) attains as much as 1.8% for 50% de-lithiation, while the contraction rate is up to 10 % for full de-lithiation, this non-uniform lattice variation exceeds the elastic strain tolerance of 0.1% for the LCO, leading to mechanical fracture and hence detrimental to battery performance during the cycle life. Substitution of Co sites with other metal ions has been exploited to enhance the structural stability of LCO during de-lithiation. Mg and La substitution of Co species has been demonstrated as an effective approach to retain the layered structure of LCO, suppress the phase transitions during Li interaction/deintercalation, and prominently improve the cycling performance of LIBs [68, 69]. Co-doped LCO using Cu and Al species has shown to high degree of crystallinity with improved phase purity [70]. Besides, cationic doping such as chromium [71] and silver [72] Zr and Mo [73, 74], B [75], Ti [76] have been employed. Al doping has received the greatest attention as it has been proven to produce significant improvement in capacity retention upon cycling, which is attributed to an increase of the diffusion coefficient of lithium ions in Al-doped cathodes and increased structural stability [77]. Compared to pristine LCO, doped LCO materials exhibit lower capacity fade, reduce irreversible capacity loss in the first cycle, and improve Coulombic efficiency and increased life.

1.5.1.2. LiMnO_2

LiMnO_2 (LMO) has been proposed as a cathode material in LIBs as early as the use of LCO came to reality in LIBs. Its use has not spread mainly due to performance limitations such as low capacity, difficulty of mass production, power performance and Mn dissolution. However, years of extensive research has led to significant improvement of its electrochemical performance. Compared to LCO, LMO has major

advantages safety and low cost which make it a promising substitute of LCO in LIBs. LMO material has two different crystal structures, i.e., orthorhombic and monoclinic phases. Compared with the orthorhombic LMO, the monoclinic LMO is always difficult to synthesize, even though it exhibits a theoretical capacity of only about 280 mAh g⁻¹, which is somewhat higher to that of orthorhombic LMO. Because of ease of synthesis of orthorhombic LMO, research efforts are focused on orthorhombic LMO. In general, high-temperature (>700 °C) synthesis methods of orthorhombic LMO (O-LMO). High-temperature synthesis generates structural defects which makes LMO electrochemically active [78]. O-LMO can be synthesized easily by solid-state reaction of manganese oxide (Mn₂O₃) and LiOH. H₂O at high temperatures between 700-1000 °C [78] or low temperatures (300-450 °C) under inert atmospheres [79].

The electrochemical performance of O-LMO cathode in LIBs is reported by several authors [80-82]. LMO known to have structural transformation to spinel phase during cycling between 2 - 4.3 V. It is difficult to analyze the structure of new LMO phase after cycling due cation arrangements in both cubic and hexagonal structures which cannot be distinguished by XRD [83]. The structural transformation takes place during early cycles depending on the synthesis conditions. Coating of O-LMO by various oxides has been used to prevent the structural transition during cycling and it is inferred that coating indeed helps to improve cycle performance of O-LMO [84]. The LMO synthesized through ion exchange exhibit high capacity of 220 mA h g⁻¹ in the voltage range between 2.4 to 4.8 V. This is because ion exchange process has great influence on the defect chemistry of the host structure which in turn influences the electrochemical performance of LMO. Orthorhombic LMO nanorods synthesized by Zhao et al. showed the enhanced discharge capacity of 183.2 mA h g⁻¹ with high capacity retention and coulombic efficiency at 0.1 C rate when operated in the voltage range between 2.0 and 4.3 V. Furthermore, the LMO nanorods presented excellent rate capability and small charge transfer resistance. Such high performance might be ascribed to the one-dimensional nanostructures with good crystallinity, which could effectively facilitate the charge and electron transport. Ni substitution in LMO (LiNi_{1/2}Mn_{1/2}O₂) exhibited superior electrochemical performance in terms of operating voltage, rechargeable capacity, cycleability, safety, and materials economy [85-88].

1.5.1.3. LiNiO₂

The Lithium Nickel Oxide (LiNiO₂), having similar layered structure of Lithium Cobalt Oxide (LiCoO₂), has been considered as a promising positive electrode material for LIBs due to its structural stability, environmental friendliness, low cost etc [89, 90]. The specific capacity obtained for LiNiO₂ is also higher than LCO. However, LiNiO₂ needs to be synthesized carefully due to the difficulties involved in oxidation of Ni²⁺ to Ni³⁺. The synthesis and treatment of LiNiO₂ often require harsh temperature conditions which further limit its current use in commercial LIBs despite its superior capacity. Nickel has higher energy density than cobalt; 50% of lithium ions can be transferred between anode and cathode for cobalt at the maximum voltage of a typical battery (4.7 V), while 70% of lithium ions can be mobilized for nickel at only 4.2 V. Moreover the thermal stability of LiNiO₂ is low compared to LCO which restricts its use in commercial batteries.

The problems associated with cation disordering and thermal instability have limited its wide application. But it is reported that the limitations of LiNiO₂ can be rectified to certain extent by the partial substitution of Ni, in LiNi_{1-y}M_yO₂, with other metals like Co (e.g., LiCo_yNi_{1-y}O₂ (0.2 ≤ y ≤ 1.0)) [91, 92], Fe (e.g., LiFe_yNi_{1-y}O₂ (0 ≤ y ≤ 0.23)) [93], Mn (e.g., Li_xMn_yNi_{1-y}O₂ (0.9 ≤ x ≤ 1.2, 0 ≤ y ≤ 0.5)) [94, 95], Al (e.g., LiAl_yNi_{1-y}O₂ (0 ≤ y ≤ 0.3)) [96], Ti (e.g., LiTi_yNi_{1-y}O₂ (y ≤ 0.3)) [97] etc which have improved electrochemical performance.

Further, bi-substitution is also reported as an excellent approach to improve the performance of LiNiO₂ derived materials for LIB applications. For example, Ti and Mg at Ni sites in LiNiO₂ results in LiNi_{1-y}Ti_{y/2}Mg_{y/2}O₂ with very high reversible capacity [98]. Furthermore, there is another approach of substituting Li in Ni sites with simultaneous partial-replacement of O with F to develop Li_{1.075}Ni_{0.755}Co_{0.17}O_{1.9}F_{0.1} with stable cycling performance [99]. Other than substitution for Ni, there are reports on the substitution for O by non-transition elements such as S (e.g., Li_{1.05}NiO_{1.98}S_{0.02}) [100] and F [101] to enhance the electrochemical performance of LiNiO₂ and its derivatives. Owing to the attractive properties of LiNiO₂ derivatives, many research and development work are under

progress to develop new electrode materials for LIBs based on LiNiO_2 and its substituted materials.

1.5.1.4. NMC

In order to overcome the issues related to individual layered metal oxides (LiCoO_2 , LiNiO_2 , LiMnO_2), a mixed metal oxide is developed which has more deliverable capacity, more stability than the individual metal oxides [102, 103]. Mixed ternary metal oxide $\text{LiNi}_{1-x-y}\text{Co}_x\text{Mn}_y\text{O}_2$ ($0 < x < 0.5$, $0 < y < 0.3$) was developed by Zhaolin Liu, which shows the reversible capacity of 140 mAh g^{-1} [104]. The symmetrical mixed metal oxide ($\text{LiNi}_{1/3}\text{Mn}_{1/3}\text{Co}_{1/3}\text{O}_2$ -NMC333) was studied by Ohzuku in the year of 2001 showed reversible capacity of 150 mAh g^{-1} when cycled in the voltage window of 2.5-4.3V and up to 200 mAh g^{-1} when charged up to 4.6 V [105]. But high voltage cycling up to 4.6 V could cause capacity fade. All these mixed metal oxides are layered structures of α - NaFeO_2 type having the space group $R\bar{3}m$. In situ X-Ray absorption spectroscopic studies on the electronic transitions and local structure of Mn, Ni and Co of NMC333 reveal as only Ni atom is electroactive. It shows $\text{Ni}^{2+}/\text{Ni}^{3+}$ and $\text{Ni}^{3+}/\text{Ni}^{4+}$ redox couple whereas Mn and Co exists in +4 and +3 oxidation states, and also confirms that oxygen acts as electron donor at the end of charge. Though it is considered as most promising cathode material for LIBs, its application is limited due to low rate capability and poor cycling stability. This is because of cation mixing of $\text{Li}^+/\text{Ni}^{2+}$ which retards the Li^+ mobility. Different strategies are employed to improve the rate capability and cycling stability. The high rate performance and enhanced discharge capacity of 188 mAh g^{-1} is attained by preparing NMC–grapheme composite (90:10 wt. %) by microemulsion followed by ball milling [106]. Hierarchical porous nano-/microsphere NMC (PNM-NMC) are developed which shows the discharge capacity of 207 mAh g^{-1} at C/10 rate and improved rate capability of 163 mAh g^{-1} at 1C and 149 mAh g^{-1} at 2C rates and stable cycling stability [107]. This improvement is attributed to the increase of contact area of unique hierarchical porous nano-/microsphere structure with electrolyte and with electrolyte, shorten Li^+ diffusion path and that improves the Li^+ ion mobility [107]. NMC333 prepared by coprecipitation method with 7 atom % excess lithium hydroxide in the precursor exhibits

discharge capacity of 180 mAh g⁻¹ at C/5 rate when charged up to at 4.6 V with 90% capacity retention in 50 cycles [108]. The higher reversible capacity is attributed to structural stability of de-lithiated NMC. Micro-spherical Ni–Mn–Co alloy particles synthesized by powder metallurgy pulverization (PMP) method with Ni, Mn, Co metal as raw materials shows initial discharge capacity of 164.4 mAh g⁻¹ at 0.1 C rate when charged till 4.3 V [109]. 1 wt. % amorphous carbon coated on to NMC333 shows improved thermal stability and electrochemical performance (87.4% capacity at 5C) compared with bare material. 0.02 mole % of Ce doping into NMC333 enhances capacity retention and reduces charge transfer resistance which is attributed to the addition of Ce⁴⁺ ion by stabilizing the layer structure. In a recent report of LiNi_{1/3}Mn_{1/3}Co_{1/3}O₂ (NMC333), LiNi_{0.6}Mn_{0.2}Co_{0.2}O₂ (NMC622), and LiNi_{0.8}Mn_{0.1}Co_{0.1}O₂ (NMC811) with respect to their cycling stability in NMC-graphite full-cells shows that NMC111 and NMC622 are stable up to 4.4 V cycling and 4.0 V for NMC811. At operating high voltages, significant capacity fade was observed, which is due to polarization of NMC cathode.

In this way lot of research has been reported to improve the electrochemical performance of NMC333 in terms of rate capability and capacity retention.

1.5.1.5. LiMn₂O₄

LiMn₂O₄ is extensively studied in the literature because of its lower cost, lower toxicity, high natural abundance and higher thermal stability in relation to LCO [110]. But, LiMn₂O₄ shows rapid capacity fade during cycling, which limits its application in commercial batteries [111]. LiMn₂O₄ crystallizes in Fd3m space-group with Li and Mn, occupying 8a tetrahedral and 16d octahedral sites of the cubic-close-packed oxygen array, respectively. In the structure MO₆ octahedra share edges to build a rigid 3-dimensional network with open interconnected channels in the <110> directions where Li⁺ ions are present (Fig. 1.3). Li⁺ ions are mobile within these channels along the 8a-16c-8a path.

A reversible extraction of Li from LiMn₂O₄ occurs at 4.05 V and 4.15 V resulting de-lithiated MnO₂. Operating voltage is larger for LiMn₂O₄ as compared to LiMO₂ (M = Co, Ni) layered compounds. However, LiMn₂O₄ delivers lower capacity (120-140 mAh g⁻¹) and have poor cycle life. Synthesis methods plays important role

for the good electrochemical performance of LiMn_2O_4 [112-116]. In order to get good electrochemical performance from LiMn_2O_4 , the average oxidation state of Mn should be higher than 3.5. Therefore, substituted cation-deficient spinels or Li-rich spinels have been focused, which show better electrochemical performance [117-123] and low capacity fade.

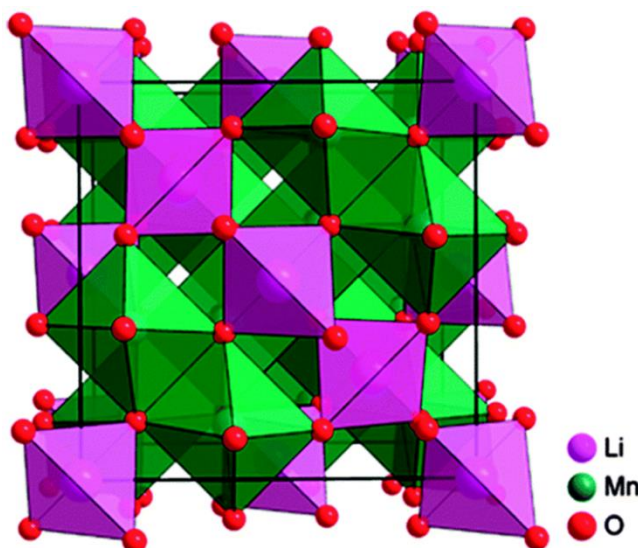


Fig. 1.3: Crystalline structure of LiMn_2O_4 spinel (Adopted from Ref. [124])

The capacity fade is attributed to the following factors: (1) Mn^{2+} dissolution in the electrolyte the carbonate electrolyte containing fluorinated salts (disproportionation of Mn^{3+}), (2) Jahn–Teller distortion of Mn^{3+} ions and (3) electrolyte decomposition products on the electrode surface [124-126]. Among all manganese dissolution into the electrolyte during cycling is the main issue for capacity fade. Mn dissolution causes the cations reach in the solution phase and migrate to the anode side, where they are reduced. The metallic clusters formed due to reduction destroy the passivation of Li and Li-graphite electrodes. Many strategies such doping of cations like Mg [127], Al [128], transition metal ions [129–132] etc., have been employed to improve the structural stability and hence capacity fade. Ohzuku et al.[133] investigated substituted spinels, such as $\text{Li}[\text{M}_{1/2}\text{Mn}_{2/3}]\text{O}_4$ ($\text{M} = \text{Cr}, \text{Ni}, \text{Cu}, \text{Co}, \text{Fe}$), and observed initial capacities of 120-125 mAh g^{-1} for the Fe- and Ni-substituted spinels [133]. Interestingly, Ni-substituted spinel provides most of its capacity at plateau voltage of about 4.5 V.

Careful investigation showed that manganese dissolution is due to the side reactions of carbonate electrolytes containing fluorinated salts, which generate HF. The Mn dissolution is initiated by the presence of hydrogen fluoride (HF), in the electrolyte with traces amount of moisture [134, 135]. Literature reports show that surface coatings is one of the effective way to avoid the electrode- electrolyte interface side reactions. There are many reports which shows the improvement in the electrochemical performance by various oxide coatings such as MgO [136, 137], CeO₂ [138], ZnO [139], Al₂O₃ [140, 141], ZrO₂ [142, 143], and Co–Al mixed metal oxide [144]. There are also some non-oxide coatings like AlPO₄ which enhanced the thermal stability and electrochemical performance.

1.5.1.6. LiMn_{1.5}Ni_{0.5}O₄ (NMS)

In order to address the issue of Jahn-Teller distortion due to Mn³⁺ ions in LiMn₂O₄, the average valence of Mn³⁺ should be raised by substituting some of Mn³⁺ with mono-, or di-, or trivalent cations. Among all newly developed spinels LiMn_{1.5}Ni_{0.5}O₄ has attained great importance due to its high voltage reversible capacity of 148 mAh g⁻¹ at an average voltage of about 4.7 V vs Li/Li⁺. It has two possible structures, one is face-centered structure (Fd3m) and other is Primitive simple cubic structure (P4₃32). The average oxidation state of Mn is nearly +4, thus reducing the Jahn-Teller distortion and shows improved electrochemical performance than LiMn₂O₄. But it has certain disadvantages like low C-rate capability and poor cyclic stability due to decomposition of electrolyte at higher voltages, formation of Li_xNi_{1-x}O impurity, and also due to formation of three cubic phases during electrochemical cycling.

Various strategies have been followed to alleviate the above mentioned drawbacks. Some of the strategies like surface coatings such as ZnO, TiO₂, LiPON, SiO₂ [145-147] etc. have been done to improve interfacial stability at high voltages and cationic dopings like Co, Cu, Cr etc. to stabilize the crystal structure and minimize the formation Li_xNi_{1-x}O phases. Different synthetic approaches such as co-precipitation method [148–153], sol-gel method [154], ultrasonic-assisted co-precipitation method, sucrose-aided combustion method, spray-drying method, emulsion-drying method, composite carbonate process, molten salt method (MSM), mechanochemical process, electrophoretic deposition, poly (methyl methacrylate)-

assisted method, ultrasonic spray pyrolysis, polymer-assisted synthesis, combinational annealing method, pulsed laser deposition are employed to obtain the pure phase spinel [155-165].

1.5.1.7. Olivines

Olivines, LiMPO_4 ($M = \text{Fe, Mn, Ni, Co}$) compounds are the promising cathode materials for LIBs with high structural and thermal stability, safe, low cost and environmentally benign materials. LiFePO_4 (LFP) is first demonstrated as cathode material for Li-ion battery by J. B. Goodenough and co-workers during 1997 [166]. It has orthorhombic structure with space group of Pnma with slightly distorted hexagonal close packed oxygen array of atoms. In the structure, oxygen is bound covalently to P^{5+} to form PO_4^{3-} tetrahedral polyanions which stabilizes the structure. The strong P-O covalent bond guarantees safe operation at high temperatures and abusive conditions. LiMPO_4 ($M = \text{Fe, Mn, Ni, Co}$) compounds have the theoretical capacities around 170 mAh g^{-1} . Among all the possible lithium phospho-olivines LiFePO_4 , LiMnPO_4 (LMP) and $\text{LiMn}_x\text{Fe}_{x-y}\text{PO}_4$ (LMFP) are the more feasible cathode materials because they deliver the capacity in the voltage range between 3.3-4.1 V vs Li/Li^+ within the electrolyte stability window [167-169]. But phospho olivines have poor internal electronic conductivity and lithium ion diffusion which limits its application in commercial batteries. Many approaches are opted to improve the electronic and ionic conductivity. Carbon coatings on to LFP improve the conductivity and hence electrochemical performance in LIBs.

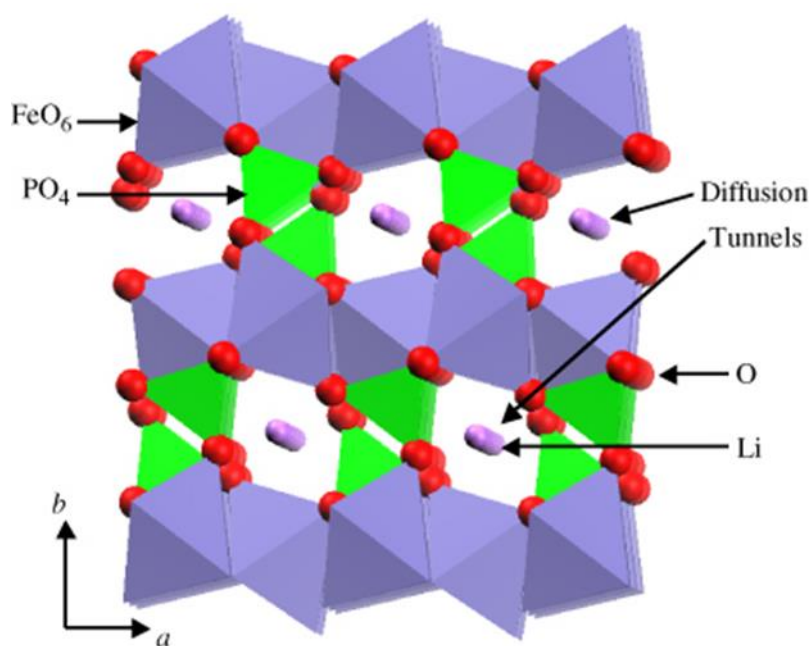


Fig. 1.4: Crystal structure of olivine LiFePO_4 (Adopted from Ref. [168])

Carbon coating activates the dynamics of the materials by inter particle conduction allowing the particles to be isolated [170]. But carbon coatings reduce the volumetric energy density. So 3-5% carbon coating in general is employed which satisfies the requirements of improving the conductivity and maintains the balance between gravimetric and volumetric energy density [171]. Reducing the particle size is the other strategy which decreases the diffusion length of lithium ion and therefore improves the conductivity [172]. But again minimizing the particle size (nano metre) would decrease the tap density and increases cost of production compared to micron sized particles and also reactivity in electrolyte solutions. Surface reactivity of LFP is sufficiently low which allow the use LFP in nanometric size. Nano metric size LFP with few % of carbon coating seems to deliver excellent capacity of 160 mAh g^{-1} , 100s of charge discharge cycles, good C rate performance and used currently in electric and hybrid electric vehicles. In addition to carbon coating, elemental dopings have been reported to have improved intrinsic electronic conductivity and lithium ion diffusion. Many dopants like Na, K, Nb, Al, Nd [173-176] with small ionic radii are used to dope in Li-sites and Mn, Mg, Ni, Bi, Co, Zn in Fe-sites.

LiMnPO_4 is another important olivine compound having the operating voltage of 4.1 V (0.6 V-0.7 V higher than LFP), energy density of 700 Wh kg^{-1} . Similar to

LFP, carbon coating found to be an effective way to improve the electronic conductivity. Li et al. successfully showed reversible capacity of 146 mAh g^{-1} in the first cycle and the stable capacity of 140 mAh g^{-1} for the 10 cycles. In a first report in 2009, Aurbach co-workers showed reversible capacity of 150 mAh g^{-1} for the carbon coated LMP for 100s of cycles. LMP nano particles were synthesized by polyol synthesis followed by carbon coating by ball milling process. Besides carbon coatings, various elemental dopings (Ti, Mg, Zr) were carried out in order to improve conductivity of LMP. Magnesium doped LMP samples showed the good improvement in rate capability and cycle life. Later 20-30 % Fe substitutions seems to improve electrochemical performance of LMP in terms power and safety. This is because Fe substitution in LMP may induce fewer defects owing to its effect on the synthesis of the material. Besides Fe will increase conductivity and hence kinetics of the material similar to LFP. As a result, both the capacity and the kinetics of the LMP cathode materials will be improved. Martha and co-workers successfully synthesized the $\text{LiMn}_{0.8}\text{Fe}_{0.2}\text{PO}_4$ with 10% carbon coating by ball milling method showed discharge capacity of $160\text{-}165 \text{ mAh g}^{-1}$ which is close to its theoretical capacity and excellent rate performance was also obtained. Later Zhou et al. also reported the carbon coated $\text{LiMn}_{0.8}\text{Fe}_{0.2}\text{PO}_4$ by using different carbon sources (Sucrose and carbon black). Different synthetic methods were used for synthesis of olivines like solid state method, co-precipitation, sol-gel, spray pyrolysis, hydrothermal, solvothermal methods etc. Still there is a lot of room for the research to develop olivines with excellent electrochemical properties like high energy density, stable cycle life etc. by simple and cost effective methods.

LFP and its charged counterpart FePO_4 have remarkable thermal stability where as LMP and its charged counterpart Li_xMnPO_4 (which contains a small amount of residual lithium), is relatively unstable in alkyl carbonate based electrolyte solution. There are reports when Li_xMnPO_4 is heated in inert atmosphere the Li_xMnPO_4 delithiated phase is decomposed to form Mn pyrophosphate ($\text{Mn}_2\text{P}_2\text{O}_7$) and release O_2 . There are limited reports on LiCoPO_4 and LiNiPO_4 compounds as these cathodes operate close to 5.5 V in order to get full capacity, beyond the stability window of carbonate based electrolytes.

1.5.1.8. LMR-NMC

In the recent times, research has been focused on developing high energy density (high voltage and high capacity), and safe cathodes to power electric vehicles. In the process of working for the development of high energy density cathode which can store and expel large number of lithium ions over a wide voltage range, M. M. Thackeray [110] and group developed $x\text{Li}_2\text{MnO}_3 \cdot (1-x)\text{LiMO}_2$ (Li-Mn- rich Ni-Mn-Co oxide, hereafter LMR-NMC) is the solid solution of Li_2MnO_3 and LiMO_2 ($M = \text{Ni}, \text{Mn}, \text{Co}$) which can show the reversible capacity of $>250 \text{ mAh g}^{-1}$ in the wide voltage window of 2.5 – 4.8 V with the possible energy density of 1000 Wh kg^{-1} .

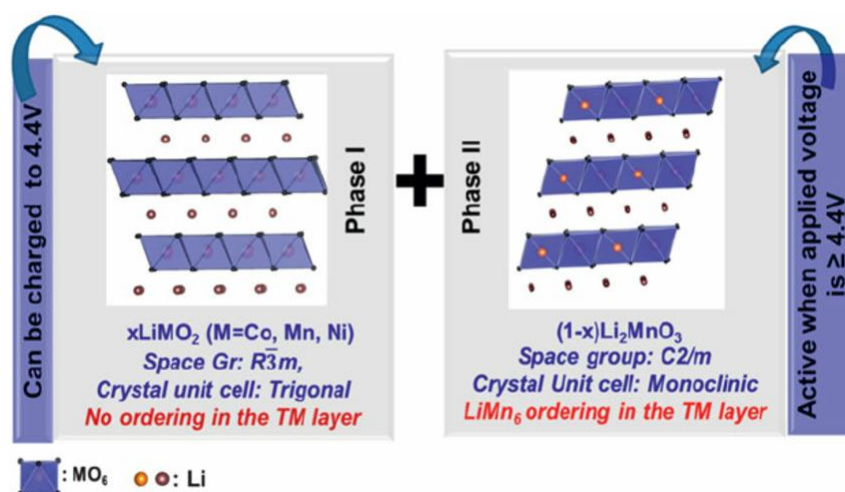


Fig. 1.5: Crystal structure LMR-NMC ($x\text{LiMO}_2 (1-x) \text{Li}_2\text{MnO}_3$) ($M = \text{Ni}, \text{Co}, \text{Mn}$) (Adopted from Ref. [178])

The structural characterization shows Li_2MnO_3 has monoclinic phase with $C2/m$ space group and LiMO_2 ($M = \text{Ni}, \text{Mn}, \text{Co}$) has rhombohedral phase with $R\bar{3}m$ space group. Both the materials have nearly close crystal system which allows to form the mixed solid solution [177]. In general, it is mentioned as lithium and manganese rich nickel manganese cobalt oxide and denoted by formula $x\text{Li}_2\text{MnO}_3 \cdot (1-x)\text{LiMO}_2$ ($M = \text{Ni}, \text{Mn}, \text{Co}$) or LMR-NMC or $\text{Li}_{1.2}\text{Ni}_{0.15}\text{Mn}_{0.55}\text{Co}_{0.1}\text{O}_2$. It is layered structure with alternating lithium and transition metal layers arranged in stacks [178]. LMR-NMC composite operate at high anodic potentials of 4.8 V vs. Li/Li^+ and provide high capacities $> 250 \text{ mAh g}^{-1}$ at an operating voltage of 3.8 V. Because of the high energy density, LMR-NMC is the choice of several high energy applications like EVs. But

LMR-NMC has several material issues which limits its application. It suffers from low conductivity, high interfacial instability due to high voltage cycling, high irreversible capacity during the first cycle and the major one is voltage fade which is associated with the structural change from layered to spinel phase.

In order to obtain maximum capacity from LMR-NMC, Li_2MnO_3 component need to be activated for which LMR-NMC has to be charged to high voltage (>4.4 V). Above 4.4 V, Li_2MnO_3 is activated which releases oxygen as Li_2O and forms MnO_2 . This could cause large irreversible capacity loss of about 50-100 mAh g^{-1} in the first cycle. The newly formed MnO_2 participate in the electrochemical process. Due to high voltage charging, electrolyte decomposes and deposits on the surface of electrode which causes interfacial instability leading to rise in impedance. Due to release of oxygen during the process of LiMn_2O_3 activation, vacancies are created in the crystal causing the instability in the structure due to non-stoichiometry [179]. So to get stability and stoichiometry in LMR-NMC the transition metal ion preferably Ni migrates from transition metal layer to lithium layer as depicted in Fig. 1.6. This migration leads to the structural changes from layered to spinel which causes the voltage decay from 3.8 V to below 3.0 V region leading to decay in energy density. Besides, because of less electronic and ionic conductivity of the material compared to NMC, LMR-NMC has poor cycle life.

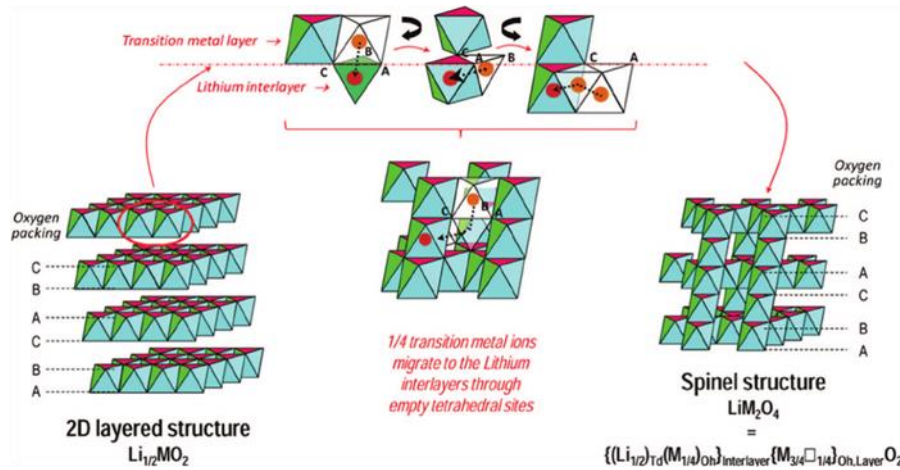


Fig. 1.6: Mechanism of layered to spinel transformation (Adopted from Ref. [179])

Conductivity is improved by adding the additives like carbon, graphene, carbon nanofiber (CNF) etc. 1.5 wt. % highly graphitic CNF additive to LMR-NMC

composite electrode increases cycle life, 2 fold increase in C rate performance and Coulombic efficiency. In contrast when CNFs are not used, the cells completely loss capacity in less than 200 cycles. CNFs makes a good electronic contact along the particles, improves interfacial stability even though salt decomposition products formed on the surface of the electrode during high voltage cycling. Reversible capacities close to 280 mAh g⁻¹ could be obtained for these CNF added composite LMR-NMC cathodes compared to 250 mAh g⁻¹ of the conventional electrodes.

Besides, interfacial stability is improved by coating with metal oxides, (such as ZrO₂, MgO, Al₂O₃, TiO₂), [179-182] solid electrolytes such as LiPON [183, 184], phosphates (AlPO₄) [185] and fluorides [186]. It was found that metal oxide coatings are transformed to metal fluorides during high voltage cycling which is proved by secondary ion mass spectroscopy. The coated material protects the surface from degradation due to electrolyte decomposition products on the surface of cathode and also from HF attack which is produced with reaction of salt LiPF₆ with trace amount of moisture present in the electrolyte. Coating of Al₂O₃ on Li[Li_{0.05}Ni_{0.4}Co_{0.15}Mn_{0.4}]O₂ shows the discharge capacity of 175 mAh g⁻¹ at 30 mA g⁻¹ with good cycling performance. AlF₃ coating on lithium transition metal oxides found to have improved the Coulombic efficiency than the pristine sample. Even phosphates like AlPO₄, Co₃(PO₄)₂[187], LiCoPO₄ [188], LiMnPO₄[189], LiNiPO₄ [190] are used as coatings which also acts as host structures for Li⁺ insertion and deinsertion. LMR-NMC attained the capacity of 215 mAh g⁻¹ at 2C rate and 295 mAh g⁻¹ at low rates by coating the surface with double layer (inner layer - 2 wt % AlPO₄ or CoPO₄ and outer layer of 2 wt % Al₂O₃. LMR-NMC coated with LiNiPO₄ attained the initial discharge capacity of 200 mAh g⁻¹ at 1C rate compared to uncoated material which has shown the capacity of 170 mAh g⁻¹.

LiPON coated LMR-NMC electrodes show improved cycle life performance at room temperature and 60 °C during high voltage cycling to 4.9 V. LiPON is a solid electrolyte has voltage stability up to 5.5 V, stabilizes the interface of LMR-NMC delivering high capacity >275 mAh g⁻¹, 3 fold enhanced C rate performance and Coulombic efficiency. The LiPON coatings were mostly non conformal, ~10s of nm which allows Li⁺ migration. However, thick (~100s nm) layers of LiPON found to be

less effective, compromises on the useable capacity because of the higher electronic resistance of LiPON.

Surface chemistry modification is another effective strategy to enhance the structural and thermal stability which improves the electrochemical performance. LMR-NMC treated with $(\text{NH}_4)_2\text{SO}_4$ [191] has delivered capacity of 230 mAh g^{-1} at 1.2 C discharge rate. The improvement is attributed to transformation of surface from layered to spinel structure with part of lithium ion de-insertion. Besides, there are numerous surface treating agents (HNO_3 , $\text{Na}_2\text{S}_2\text{O}_8$,) [192,193], which are used to enhance the electrochemical performance.

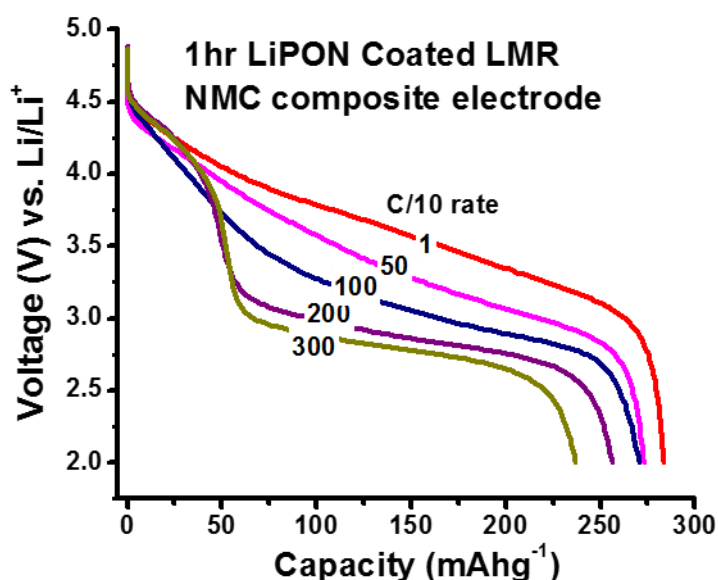


Fig. 1.7: Discharge voltage profiles of LiPON coated LMR-NMC during 300 cycles (Adopted from Ref. [193])

The surface coatings, conductive diluents increases capacity retention, improves cycle life, reduce irreversible capacity decay but not the voltage decay as shown in example for LIPON in Fig. 1.7 [193]. As discussed the voltage decay is due to structural transformation from layered to the spinel phase. In order to improve the conductivity and minimize the layered to spinel transformation, elemental dopings are considered as competent strategy to improve the efficiency of the material in terms of structural stability and capacity, C rate capability which in turn improve energy and power density. Doping includes cation dopings such as Mg [194], Cr [195], Al [196],

Ti [197], Fe[198] etc or anion doping such as Fluorine [199, 200] or even simultaneous doping. The electrochemical performance of LMR-NMC is enhanced significantly by doping with Ru [201]. It showed improvement in electrochemical performance at higher rates rather than lower C rates. The significant improvement is attributed to increase in lithium inter slab distance upon doping which allows the faster lithium diffusion and also more lithium insertion and de-insertion leading to increased energy density.

Still the issues voltage decay, capacity fade which are the main reason for the loss of energy density is not properly addressed. So there is lot of room for the effective research to prevent or minimize the voltage decay in LMR-NMC and boost performance and energy density.

1.5.1.9. Future cathodes for LIB

LIB is largely limited by the capacity of cathodes which is the most expensive and heaviest component of LIB. Besides LMR-NMC, lots of research are directed to achieve multi electron capacity from the polyanioninc multivalent Li_2Mn (or Co) SiO_4 systems, conversion compounds such as FeF_2 ($2 e^-$ system), FeF_3 ($3 e^-$), MnF_3 , CuF_2 , BiF_3 etc. are focused. List of materials with potential, specific capacity, energy density are given in Table 1.1 with the currently used LCO, LFP LiMn_2O_4 and cathodes.

Table. 1.1: List of materials with potential, specific capacity, energy density

Material	Potential	Specific capacity (Ah kg ⁻¹)	Energy (Wh kg ⁻¹)
LiCoO₂	3.9	140	546
LiFePO₄	3.3	160	528
LiMn₂O₄	3.9	148	585
FeF₂	2.66	571	1518
FeF₃	2.74	712	1951
BiF₃	3.13	302	945
MnF₂	2.65	719	1905
CuF₂	3.55	528	1874
Li₂FeSiO₄	3.3	328	1082
Li₂MnSiO₄	4.0	333	1332
Li₂CoSiO₄	4.3	325	1397
Li₂NiSiO₄	4.7	325	1530

The future energy storage systems should be cost-effective, safe, sustainable, eco-friendly, deliver high capacity/power density, rate capability, and can be manufactured in large-scale manufacturing. Accordingly, sodium, magnesium, metal–air, metal–sulfur, and metal–organic batteries are being considered for post-lithium ion batteries.

1.5.2. Anodes

Anode is the other main component of the battery. Similar to cathodes, an ideal anodes should have high capacity, high reduction potential, low first cycle irreversible capacity, fast kinetics, less volume or structure change during charge-discharge cycling, cost effective, safe, easy of synthesis, should be stable in electrolyte solution. In the light of the aforesaid discussion, several compounds such as carbon based compounds like graphite, hard carbon, graphene, carbon nanotubes etc., metal oxides such as TiO_2 , $\text{Li}_4\text{Ti}_5\text{O}_{12}$, SnO_2 , Mn_3O_4 , Co_3O_4 , V_2O_5 , metal and metal alloys such as lithium, Si, Sn, Sb, Al, Mg, Bi, In, Zn, Pb, Ag, Pt, Au, Cd, As, Ga and Ge have been well studied in the literature. Among them Li, carbon based anodes, TiO_2 , $\text{Li}_4\text{Ti}_5\text{O}_{12}$, Sn and SnO_2 and Si have been commercialized for variety of applications and these compounds are briefly reviewed below.

1.5.2.1. Lithium anode

Lithium is most attractive anode because of its high specific capacity (3861 mAh g^{-1}) [202] and lowest potential (-3.04 V). Because of these advantages it is not only used in lithium metal based primary batteries but also as anode in lithium-sulphur and lithium-air batteries which are anticipated as future high energy density batteries. Lithium anode has several limitations like safety and low rechargeability. Because of its low potential the electrolytes reduce at the electrode surface leading to formation solid electrolyte interphase (SEI). The tailored SEI will be ionic conductive and prevent further deposition of electrolyte. Moreover, due to heterogeneous deposition of lithium and dissolution during charge and discharge of lithium metal anode leads to the formation of high surface area lithium dendrites in organic electrolytes. Formation of lithium metal dendrite results in exposure of new lithium surface to the electrolyte and further decomposition of electrolyte takes place [202]. Besides, the

growth of dendrite may cause severe safety issue like, lithium grows across the separator and penetrate to the cathode side leading to short circuit. This limits the practical application of lithium as anode in rechargeable batteries. Many efforts have been made to tackle the issue of dendrite growth and lot of ground breaking research is going on throughout the world to prevent the dendrite formation, so it can be used efficiently as a high capacity anode in high energy density rechargeable batteries like lithium-sulphur and lithium-air batteries [204, 205].

1.5.2.2. Carbon based anodes

During early 1980s, Rachid Yazami reported the possible reversible intercalation of lithium in graphite at the potential of 0.2 V vs Li/Li⁺ deriving the capacity of 372 mAh g⁻¹ by considering one lithium per six carbons (LiC₆) [206, 207]. Based on this research, SONY Company of Japan launched a Li-ion battery by assembling graphite as anode, LCO as cathode in 1.0 M LiPF₆ in 1:1 ratio of ethylene carbonate and dimethyl carbonate electrolyte. Since then, lots of advances have been done on carbon based anodes such as graphite, hard carbons, graphenes, carbon nanotubes and fibers etc.

Graphite has layered structure. The individual layers of graphite are called graphene. Each graphene layer, carbon atoms are bonded covalently, arranged in a honeycomb lattice and the distance between planes is 0.335 nm. Graphite dominates the commercial LIB market because of its excellent electrochemical performance such as stable cycling performance with high coulombic efficiency and less volume change (~10%) during lithium insertion. But graphite has limited capacity of 372 mAh g⁻¹ which restricts the development of high energy density LIBs for powering the HEVs, EVs and for other high energy applications. In addition to limited capacity, the major failure of the graphite is due to solvated Li co-intercalation which exfoliates the graphite and degrades making it electrochemically inactive. In order to improve the reversible storage capacity of graphite, graphite anode should have good SEI (discussed later) which is formed due to reduction of alkyl carbonates at low potentials, and Li containing salts. A typical SEI should have thickness of 10s of nm which allow ions to pass but it is electronically insulator. A good SEI helps to improve further degradation of graphite which helps to improve capacity retention and cycle

life. Investigations have been carried out to introduce defects, functional groups, high volume voids (micro pores and macropores) etc. to further improve the electrochemical performance. Peled et al. was first to demonstrate the enhancement of the electrochemical performance by mild oxidation of artificial graphite. This improvement is attributed to two factors, one is formation of nanochannels or micropores which enhances the lithium intercalation or storage and other factor is formation of dense oxide layers which inhibits the electrolyte decomposition. Two types of oxidations like air oxidation and liquid oxidation can be used for producing defects, nanochannels. But the reproducibility and uniformity is not controlled in air oxidation whereas liquid oxidation has the advantage of controlling the above mentioned properties. The reversible capacity of 355 mAh g^{-1} is achieved by the graphite on mild oxidation with the aqueous solution of $(\text{NH}_4)_2\text{S}_2\text{O}_8$ which is the strongest oxidizing agent. HNO_3 , $\text{Ce}(\text{SO}_4)_2$, H_2O_2 are also used for the mild oxidation of the graphite to enhance its energy density.

Formation of composite by introducing metals and metal oxides on or into the graphite is the other strategy to enhance the storage capacity of the graphite, even metals and metal oxides also adds capacity since they de/intercalate or alloy with lithium. The increase in conductivity and additional lithium storage sites are resulted in the composite of graphite with silver, which improved the rate capability and storage capacity [208, 209]. Composite formation of graphite with nickel [210] inhibits the co-intercalation of solvated lithium in to graphite which improves Coulombic efficiency, cycling stability in propylene carbonate electrolyte. Nickel particles coated onto graphite blocks some of the edge surfaces from exposing to electrolyte which minimizes the intercalation of solvated lithium. Similarly composite formation of graphite with tin also improves the electrochemical performance where both graphite and tin acts as host to lithium [211-213]. Likewise there are many combinations of graphite with different metals and metal oxides like Al, Zn [214] and metal oxides like NiO [215], SnO [211], SnO₂ [216], Fe₂O₃ etc. are used for improving the performance as anode material. Coating of graphite with polymer or different type of carbon for modifying the surface improves the electrochemical performance. Polypyrrole [217], polythiophene [218], polyaniline [219] are

conductive polymers which are used to form composite with the graphite. The improved electrochemical performance is ascribed to enhanced conductivity due to conductive polymer and in addition polymer can also act as host for lithium, adding capacity to the graphite.

The performance of the graphite is still improved by deriving the graphene (one atom thick two dimensional carbon material) [220, 221]. Since then researchers started synthesizing graphene in many ways. One of the most accepted synthesis is conversion of graphite to graphene oxide followed by reduction to graphene chemically. Graphene shows enhanced capacity than graphite because of 1) insertion of lithium ions into the voids, 2) Li ion adsorption on the dual side of graphene, 3) binding of Li ion on the covalent sites of the graphene. So due to binding of lithium in multiple ways with graphene, the theoretical capacity of graphene is assumed to be 744 mAh g⁻¹. In addition to this, several carbon nanostructures are like multi-walled carbon nanotubes [222, 223], single-walled carbon nanotubes [224, 225], graphene nanosheets [226] etc., are developed to enhance the performance of the carbon anodes. Hard carbons [227, 228] have amorphous structure, and are considered as also attractive anodes due to its high capacity (> 300 mAh g⁻¹) and low cost. However, hard carbons shows high initial irreversible capacity loss, high capacity fade and low columbic efficiency which hinder practical application of hard carbon in LIBs.

1.5.2.3. Tin (Sn) based anodes

Tin (Sn) is one of the attractive anode material for LIBs because of its high capacity (Li_{4.4}Sn = 994 mAh g⁻¹) i.e., [229] 3 times more capacity than that of graphite whereas SnO₂ [230] has double the capacity (790 mAh g⁻¹) of graphite. The electrochemical redox processes of Sn and SnO₂ during charge-discharge are presented below.



The first reaction is irreversible where SnO₂ reduces to Sn and second reaction is reversible. During initial cycle, along with reduction of SnO₂ to Sn, SEI layer is formed on the electrode surface leading to high irreversible capacity. Moreover, due to alloying/de-alloying with large number of lithium ions Sn-anode undergoes volume change leading to pulverization resulting low electrochemical performance.

Numerous efforts have been made to enhance the electrochemical performance of Sn and SnO₂ anodes. Some of the strategies are: a) synthesizing the Sn/ SnO₂ nanoparticles [231] to prevent the stress due to volume change during cycling and avoid pulverization, b) fabricating the Sn-C composite [232, 233] where Sn is dispersed in carbon matrix which supports the volume change without losing the electrical contact of Sn with current collector. Paek and co-workers [234] showed the improved anode performance of SnO₂ by fabricating the SnO₂-graphene nano-porous electrodes. These electrodes exhibits the reversible capacity of 810 mAh g⁻¹ with the capacity retention of 70 % after 30 cycles. The enhanced electrochemical performance is attributed to buffering of volume change by the pores developed between graphene and SnO₂, besides confinement of SnO₂ between the graphene layers prevents the loss of electrical contact. Chen and co-workers [235] showed an improvement in the lithium storage properties and cycle life of SnO₂ by controlled carbon nano-coating using two-step hydrothermal method. 8 wt. % of carbon coating on SnO₂ showed improved capacity of 631 mAh g⁻¹ at the current density of 400 mA g⁻¹. Lou et al. [236] demonstrated an excellent electrochemical performance of spherical SnO₂ nanoparticles through conformal coating of carbon using glucose as carbon source by hydrothermal method. It showed the reversible capacity of 440 mAh g⁻¹ at a current density of 300 mA g⁻¹. Similarly, many nanostructures like nanorods [237], nanowires [238], nanoneedles [239], core-shell structures [240] are also employed to attain superior electrochemical performance.

1.5.2.4. Titanium oxide

Titanium dioxide (TiO₂) is extensively used as a multifunctional material because of its structural stability, sturdiness and physio-chemical properties with the advantage of reasonable cost. The appropriate electronic band structure of TiO₂ makes it a promising material for various applications such as photovoltaics, catalysis, and energy storage. TiO₂ is one of the most promising anode materials in LIBs with the theoretical capacity of 335 mAh g⁻¹, has significant advantages of low volume change during lithium insertion and extraction (<4%), has short path for lithium ion diffusion which enhances C rate performances, shows excellent structural stability which leads to excellent cycle stability. Besides it high charge-discharge plateau voltage of ≥ 1.7

V vs. Li/ Li⁺ which eliminates SEI formation at the surface. However, it has limitations of low practical capacity ~160 mAh g⁻¹ (0.5 Li transfer) due to poor electronic conductivity which leads to poor cycle life [241]. The reversible Li insertion and extraction in the TiO₂ anode material can be expressed as



Where, x can vary between 0 to 1 depending upon the different polymorphs of TiO₂.

However, due to relatively low practical capacity of ~160 mAh g⁻¹, low electrical conductivity and high operating voltage of TiO₂, it is not used significantly in practical application. Various strategies have been developed to solve the issues of conductivity and kinetics of Li-ion diffusion such as synthesis of nanostructured TiO₂ [40], coating with carbonaceous materials such as carbons, carbon fibers, graphenes and, incorporating metal oxides to enhance its capacity and cyclability [242-246].

In general, TiO₂, exhibits four different polymorphs such as anatase, rutile, brookite and TiO₂ (B) [247, 248]. In addition to these phases, different metastable phases of TiO₂ also exist. [249]. Among all, rutile is the thermodynamically stable phase of TiO₂; other metastable phases can be converted to rutile phase by high temperature treatment > 850 °C.

Macklin et al. first demonstrated successful Li⁺ intercalation/deintercalation at 120 °C into the bulk of rutile phase [250] and it was observed that rutile phase of TiO₂ is not electrochemically effective in room temperature. But later in 2006, Maier et. al. demonstrated a reversible Li⁺ insertion/extraction of ~0.5 mol of Li per mol of TiO₂ at room temperature into/from nanosized rutile [251]. Further, to improve the capacity retention and rate capability, the conductive phases such as carbon, polymers, and metals additives have been implemented [252, 253].

In general, anatase TiO₂ is found to be more electrochemically active in compare to the rutile phase. Based on the electrochemical reaction showed in equation (1), anatase TiO₂ can accumulate up to 0.5 Li when micro-sized bulk material is used. And the volume changed observed while insertion/ de-insertion process was found to be negligible (~ 4%) [254]. In order to improve the capacity of the anatase material, several strategies have been employed such as synthesis of nano size particles of

varying dimension [255] and carbon supported structures and coatings [256] which can improve the specific capacity as well as rate capability of the material.

Among all the phases of TiO₂, TiO₂ (B) is the better host for the lithium intercalation. TiO₂ It has a large unit cell with a more open crystal structure compared to other polymorphs. It has monoclinic crystal system with a particularly long a-axis (1.216 nm) [257]. The unique structure of TiO₂ (B) can accommodate a theoretical maximum of 1.25 Li per formula unit, [258] larger than the 1 Li per formula unit for anatase. The kinetics of Li-ion insertion is governed by the open channels along the b-axis, which improves the kinetics of Li ion diffusion, which leads to the better rate capability of this material. In order to obtain facile Li-ion diffusion pathways in TiO₂ (B) material, tailoring the morphology and structure play an important role.

Even though TiO₂ can be cycled 1000s of cycles with little loss in capacity and good C rate performance, but its use in LIBs is not significant in practical applications because of low capacity and high operating plateau voltage.

1.5.2.5. Lithium Titanium Oxide (LTO)

The lithium titanate, Li₄Ti₅O₁₂ (LTO) has attracted as an anode material in LIBs with flat plateau voltage of 1.55 V vs. Li/Li⁺, theoretical capacity ~175 mAhg⁻¹. LTO does not have SEI during lithiation) unlike graphite, and acts as a zero strain insertion material (volume change during charge-discharge is negligible) [259-261], which make LTO to be cycled hundreds of cycles with excellent structural stability. It has a cubic spinel structure and can be expressed as Li_{4/3}Ti_{5/3}O₄ or in the spinel form (Li[Li_{1/3}Ti_{5/3}]O₄). The lithium intercalation reaction into the LTO is based on the following equation.



Generally lithium titanate material doesn't have side reaction with electrolytes which can give rise to irreversible capacity. However, low electrical conductivity of this material affects its rate capability. Lot of efforts have been made to explore the electrochemical properties of LTO. It has been observed that morphology and particle size plays an important role in the electrochemical performance of LTO, such as nano sized LTO powders synthesised via sol-gel delivered the capacity 125 mAh g⁻¹ at end

of 50th cycle [262], three-dimensionally ordered macroporous (3DOM) showed the capacity of 145mAh g⁻¹ because of short diffusion length and porous morphology [263]. Wang et al. reported that rutile-TiO₂ as a carbon-free nanocoating to improve the kinetics of LTO toward fast lithium insertion/extraction [264].

Han et al. [265] reported the solid state synthesis of Li₄Ti₅O₁₂ from Li₂CO₃ and anatase TiO₂ precursors by solid state synthesis and obtained 0.3mm beads that showed improved electrochemical performance with capacity retention of 80% at 10 C rate. Wang et al. [266] also reported the Li₄Ti₅O₁₂ synthesized by solid state method attaining the improved performance like 98.25 % capacity retention at 10 C rate. It is also reported that obtaining smaller grains and crystallites by longer ball milling shows enhanced anode performance. Likewise many synthetic methods like sol gel, microwave method, molten-salt method, hydro-thermal method [267-270] are employed to improve the electrochemical performance in terms of rate capability, capacity retention, cycle life.

Surface modification is the other promising strategy applied to improve the electrochemical performance. Different surface coatings like metal oxides, carbons such as carbon nanotubes, graphenes are used. Luo et al. [271] synthesised Li₄Ti₅O₁₂ nanorods coated with carbon using glucose as carbon source by hydrothermal method. It showed 92.7 mAh g⁻¹ higher capacity than pristine Li₄Ti₅O₁₂ and stable cycling capacity. Jung et al. [272] improved the capacity retention to 95% after 1000 cycles by coating the carbon from pitch precursor on to Li₄Ti₅O₁₂. Pitch is taken as carbon source. Graphene coating on Li₄Ti₅O₁₂ enhanced the initial discharge capacity, showing 168.5 mAh g⁻¹. Whereas, pure Li₄Ti₅O₁₂ showing the capacity of 81.2 mAh g⁻¹.

Metal coating onto the Li₄Ti₅O₁₂ was found to be effective way of improving the conductivity. The nanocomposite Li₄Ti₅O₁₂ with Ag [273] as coating showed high capacity of 131 mAh g⁻¹ at 30 C rate. This improvement is may be due to activation of electrode. 3% of Ag was found to be optimum percentage for high performance of Li₄Ti₅O₁₂. Metal oxide coatings like Fe₂O₃ [274], CuO [275], ZrO₂ [276] coatings on Li₄Ti₅O₁₂ enhanced electrochemical performance in terms of capacity retention, rate capability, cycle life.

Though the surface coatings improve conductivity but may not enhance the electronic conductivity of the lattice. So to improve the as above mentioned conductivity substituting small percentage of Ti^{3+} , Li^+ with other ions improves the internal conductivity. Wang et al. [277] improved the electrical conductivity by doping with magnesium. Strontium (Sr) [278] doping is found to decrease the charge transfer resistance which is attributed to increase in lattice parameter and reduced particle size. Doping of Cu^{2+} [279] improved the diffusion coefficient of Li^+ and charge transfer resistance. Similarly many different cations and anions are used to improve the intrinsic electrical conductivity thus enhancing the electrochemical performance.

Co-doping of anion and cation was also followed for increasing the electrochemical performance in terms of electrochemical conductivity (rate capability), capacity retention and cycle life. Co-doping of Al^{3+} and F^- [280] showed better rate performance and La^{3+} and F^- [281] co-doping shows much better anode electrochemical performance.

1.5.2.6. Silicon

Silicon is an attractive anode material for LIBs due to high theoretical capacity of 4200 mAh g^{-1} which corresponds to fully lithiated state of $\text{Li}_{4.4}\text{Si}$ [282]. Silicon is the second most abundant, non-toxic, low cost anode material [283]. But its application is limited in commercial LIBs due to its high volume change ($\sim 400\%$) [284] during charge/discharge cycling, which creates huge stress on the particles leading to pulverization of the silicon [285]. Another failure mode for silicon particles is to lose electrical contact during volume change. This results in rapid capacity fade leading to the failure of the cell. In addition, it has poor electronic conductivity which limits its power (rate) performance. Unlike graphite, SEI layer is formed on the surface of Si anodes due to salt decomposition and electrolyte reduction, due to the swelling of the silicon during cycling, the SEI layer form fissures and become porous. As a result a thick SEI layer is formed which increases cell resistance, reduces cell performance.

Many efforts have been made for alleviating the above mentioned problems. Nanostructured silicon anodes circumvent the issues of pulverization as they can

provide enough free space to accommodate volume expansion during Li insertion, thus minimizing the strain. In addition, nanoscale dimensions provide good electronic contact and have fast lithium ion diffusion, thereby enhancing the rate performance and specific capacity.

Various nanostructured morphologies of silicon have been reported during last decade addressing the issues of volume expansion. Nanowires [286, 287] and nanotubes [288], interconnected hollow nanospheres [289], thin films [290, 291], vesical [292] and nanoparticles [293] are found to be very attractive as nanoscale designs, incorporate pores or voids to accommodate the volume modification, circumvent the problems of pulverization and thereby enhance the electrochemical performance.

Some of the researchers made the silicon-carbon (Si-C) composites as an effective strategy to prevent the stress on silicon due to volume change. Carbon based materials enhances the electronic conductivity of Si and also addresses the issues of pulverization. Kumta and Kim [294] made the composite of polystyrene and silicon by mechanical milling followed by pyrolysis in inert atmosphere. This composite showed the reversible capacity of 850 mAh g⁻¹ with capacity retention of 98.9% was achieved over 30 cycles. Liu and coworkers [295] made Si-C composite by using polyvinyl alcohol (90%) and silicon (10%) which attained the capacity of 754 mAh g⁻¹ with Coulombic efficiency of 80.3%. In this way many carbon sources like polyvinyl chloride, resorcinol-formaldehyde resin, graphite etc. [296-298] were used as carbon matrix to support volume change of silicon. Si and meso-carbon micro-beads (MCMB) [299] made by mechanical milling, showed early capacity fade. Composites of graphite (80%) and silicon (20%) [300] showed an initial capacity of 1350 mAh g⁻¹, about 1000 mAh g⁻¹ for 100 cycles, respectively. Besides blending, other approaches such carbon coating is used to mitigate the pulverization. Coating of silicon particles with carbon layer is reported as containing the 27% of carbon and showed stable capacity of 1000 mAh g⁻¹ at the current density of 300 mA g⁻¹.

Metals like silver (Ag) [301] and copper (Cu) [302] were used to make Si-M (M = Ag, Cu) composite to improve the conductivity. But the capacity retention and

cycle life is not impressive because of poor contact of silicon particles from metal due huge volume change of silicon during cycling.

Silicon dense thin films were used as potential anodes for lithium ion batteries. However, dense films showed the inferior performance due to stress followed by pulverization. The mass loading and adherence of silicon to substrate are the critical factors that decide the performance of the silicon anode. Amorphous silicon thin film of 200 nm [303] was fabricated by magnetron sputtering and exhibited excellent electrochemical performance with the capacity of 3000 mAh g⁻¹ which is ascribed to optimization of loading density and strong adhesion of silicon to copper. The thin film alloy of silicon-aluminum on copper foil [304] displayed the enhanced anode performance than silicon thin film. The capacity retention for silicon-aluminum on copper foil was 80% after 350 cycles whereas silicon thin film showed 61%. Liu and co-workers demonstrated the influence of different types of copper current collectors on the electrochemical performance of Si-Al thin film anodes. Si-Al alloy on copper foam showed enhanced performance than on flat mesh grid and expanded copper. Improved performance is accredited to unique 3D macro-porous structure of copper foam which facilitated the silicon electrolyte contact, improved conductivity, free space for volume change. In addition to 2D silicon thin films 2D silicon nano sheets are also fabricated as anodes for lithium ion batteries. These 2D nano sheets have the advantages like small volume expansion, easy accessibility to lithium ions.

Core-shell of Silicon and carbon is the most effective strategy in improving the electrochemical performance in terms of capacity retention and rate capability than Si-C composites. The superior performance of core-shell of silicon carbon is due to complete covering of silicon with limited carbon layer and shell of carbon provides the enough mechanical strength for the volume change of the silicon. Solid core-shell of silicon-carbon fabricated by surface induced coagulation process attained capacity of 1800 mAh g⁻¹ at the current density of 100 mA g⁻¹ with good capacity retention and C rate performance [305]. Core-shell of silicon-carbon nano fibers fabricated by dual nozzle electrospinning method displayed the capacity of 721 mAh g⁻¹ with capacity retention of 99% after 300 cycles [306]. This 1D core-shell supported the volume change, improved the conductivity and stabilized the SEI formation. Likewise many

strategies are followed like synthesizing the silicon wires, tubes, and different nano structures, different silicon-carbon composites to mitigate the volume change and improve the electrochemical performance in terms of capacity retention, stable cycle life and enhanced conductivity.

Moreover, binder less electrode architectures are becoming popular as these facilitate charge transport efficiently, eliminate the need for binders, which would otherwise contribute extra weight and add resistivity to the cell and also solve the issues of pulverization. Thereby it drastically improves electrochemical performance. More on these electrode architectures are discussed in Chapter 6 and 7.

If the issues of pulverization of Silicon, and Sn based anodes can be mitigated, these anodes could find a room for the next generation anodes for high energy density LIBs.

1.5.3. Electrolytes

Electrolyte plays an important role in determining the current (power density), life, and safety of the battery. The performance of the electrode materials depend largely on their chemical stability and compatibility with electrolytes. A good electrolyte acts as an inert part of the battery without undergoing any net chemical change, ensuring stability against both the electrode surfaces and facilitates all the redox processes at the electrodes [307].

An ideal electrolyte should be a) a good ionic conductor and electronic insulator, b) have wide operating potential window, c) inert to all the cell components including electrodes, separators and packing materials, d) have thermal stability under operating temperatures, e) environmentally benign and less toxic, and f) be cost-effective and g) easily available [308]. The different type electrolytes of interest for room temperature Li based batteries are: a) non-aqueous electrolytes (lithium salt solubilized in organic solvent or solvent mixtures), b) aqueous electrolytes ((lithium salt solubilized in water), c) ionic liquids (ILs) (organic salt doped with a fraction of the lithium salt equivalent), d) polymer electrolytes, and e) hybrid electrolytes [307-309].

Non-aqueous electrolytes are used in most of the commercial LIBs, like non-coordinating anion salts such as lithium hexafluorophosphate (LiPF_6), lithium hexafluoroarsenate monohydrate (LiAsF_6), lithium perchlorate (LiClO_4), lithium tetrafluoroborate (LiBF_4) and lithium triflate (LiCF_3SO_3), dissolved in organic carbonates, in particular, mixtures of ethylene carbonate (EC) with dimethyl carbonate (DMC), propylene carbonate (PC), diethyl carbonate (DEC), and/or ethyl methyl carbonate (EMC) [309]. Among the salts LiPF_6 found to have voltage stability close to 4.5 V and even can be stable up to 5 V with additives. The recent reports reveal that the commercial electrolytes are unstable above certain operating voltage limit [310-312]. Hence, to meet the present market demand for LIBs with higher energy, power density and safety, it is very much important to search for an alternate electrolyte with high voltage stability. Organic fluoro alkyl carbonate in 1.2 M LiPF_6 has been emerged as 5 V electrolytes due to the higher oxidation potential of the fluorinated molecules [313]. Since the battery performance is significantly influenced by a porous and ionic conductive solid electrolyte interphase (SEI) layer, the property of the LIBs can be further enhanced through intentionally controlling thick SEI by adding small amount of additives, like tris (hexafluoroiso-propyl) phosphate (HiFP) etc. [314, 315].

Though LIBs with non-aqueous electrolytes are widely used in most of the electronic applications, its large scale applications is limited due to the flammability of the organic electrolytes. This leads the attention of researchers to test the feasibility of utilizing non-flammable, internally environmental and low cost aqueous solutions with high ionic conductivity as electrolytes for LIBs [316, 317]. In this way, many salt solutions like LiNO_3 [318, 319], Li_2SO_4 [320] etc. have been reported.

The non-volatility and non-flammability of room temperature ionic liquids (ILs) made them as a promising alternative to organic electrolytes for next generation LIBs. ILs can also offer high ionic conductivity, thermal stability, high voltage window and larger solubility of organic and inorganic compounds [307, 321]. But their high viscosity which result in reduced mobility and high cost limits its wide applications. The recent reports show a progress in mitigating this limitations through searching new cations and anions, mixtures with traditional organic carbonates. The

commonly used cations in ILs are imidazolium, quaternary ammonium, pyrrolidinium and piperidinium, while anions are PF_6^- , BF_4^- etc. [321, 322].

The polymer electrolytes (solid polymer electrolytes and gel polymer electrolytes) have been emerged as new attractive class of electrolytes that can overcome the limitations of low mechanical strength and safety issues of liquid electrolytes. Poly(ethylene oxide) (PEO) is the most commonly used polymer electrolytes [323]. However, over all benefits of polymer electrolytes, their low ionic conductivity makes adverse effect on its application. The research is progressing worldwide in this direction to improve the ionic conductivity of polymer electrolytes through different methods like adding lithium salts (like Lithium trifluoromethanesulfonate (LiTf), lithium bis(trifluoromethanesulfonyl)imide (LiTFSI) etc.) [324] and ceramic nanoparticles (like SiO_2 , Al_2O_3 , Fe_3O_4 , TiO_2) to the solid electrolytes [323, 325]. The poly(vinylidene fluoride) (PVdF) base polymer gel electrolytes has also been emerged as an attractive electrolyte for LIBs [326].

The goal of mitigating the limitations of ILs and polymer based electrolytes lead the researchers to development of hybrid electrolytes (ionic liquid base and polymer based hybrid electrolytes) for LIB. There are different ionic liquid-nanoparticle hybrid electrolytes like IL- SiO_2 [327, 328], TiO_2 etc. have been reported. The polymer based hybrid electrolytes having organic and inorganic materials (nanoparticles like SiO_2 , TiO_2 etc as inorganic part and polymer as the organic part) synthesized through sol-gel method is also reported as a promising electrolytes for battery applications [329].

1.6. Drawbacks and Failure Modes of Lithium-Ion Batteries

The energy density of the current LIBs is limited by the capacity and potential of the of cathode. So the key to improve energy density of LIBs lies in the choice of appropriate cathode materials, that have higher redox potentials (~ 5 V) and can reversibly intercalate more than one lithium ion per atom. But, the low electrochemical stability window (~ 0.8 V – 4.5 V) of the organic carbonate-based electrolyte avoids the usage of high-voltage cathodes. In addition, these organic electrolytes are highly flammable posing serious threats to safety. On battery getting

overheated, there is uncontrolled rise in temperature generating flammable gases during which separator tends to burn, trigger short circuiting, resulting explosion of cell. So, there is an utmost need of safe cathode materials having high thermal stability with high operational voltages and capacity that can guarantee an improvement in the energy density, as well as a suitable electrolyte with high thermal stability and broad electrochemical voltage window that may be well-matched with the high voltage cathodes [329]. The thermal runaway in LIB is schematically shown in Fig. 1.8.

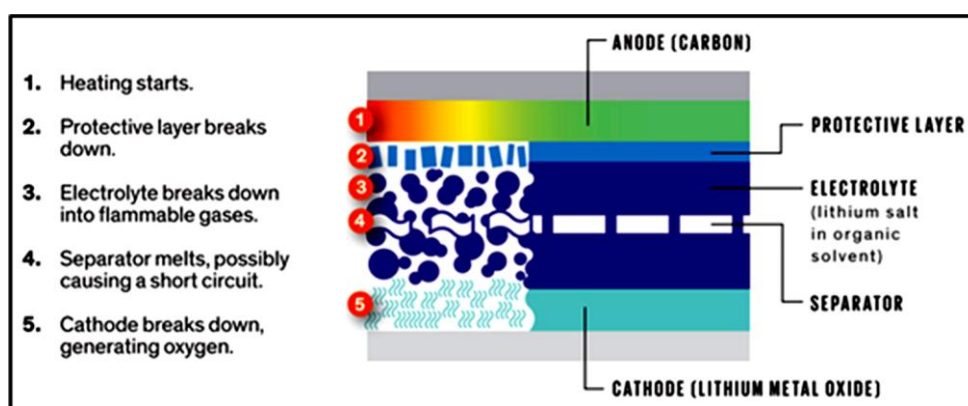


Fig. 1.8: Thermal runaway in a lithium-ion battery (Adopted from Ref. [329])

Another major factor that is critical to the battery performance is solid electrolyte interphase (SEI) formation (below 1V) during lithiation of graphite and silicon anodes. The electrolyte reduces on the electrode surface during initial charge (lithiation) which form a passive layer that is electronically insulating but is ionic conductive. Typically a good SEI thickness is about 10s of nms. SEI acts as an interphase between the metal and the electrolyte solution and stops further degradation of the electrolyte and anode after the second charge. The SEI is composed of inorganic components such as LiF, Li_2CO_3 as well as organic components like $(\text{CH}_2\text{OCO}_2\text{Li})_2$, ROCO_2Li which are partial or complete reduction products of the electrolyte solvents and salts (Fig 1.9). Formation of polymeric compounds on the surface causes formation of bad SEI.

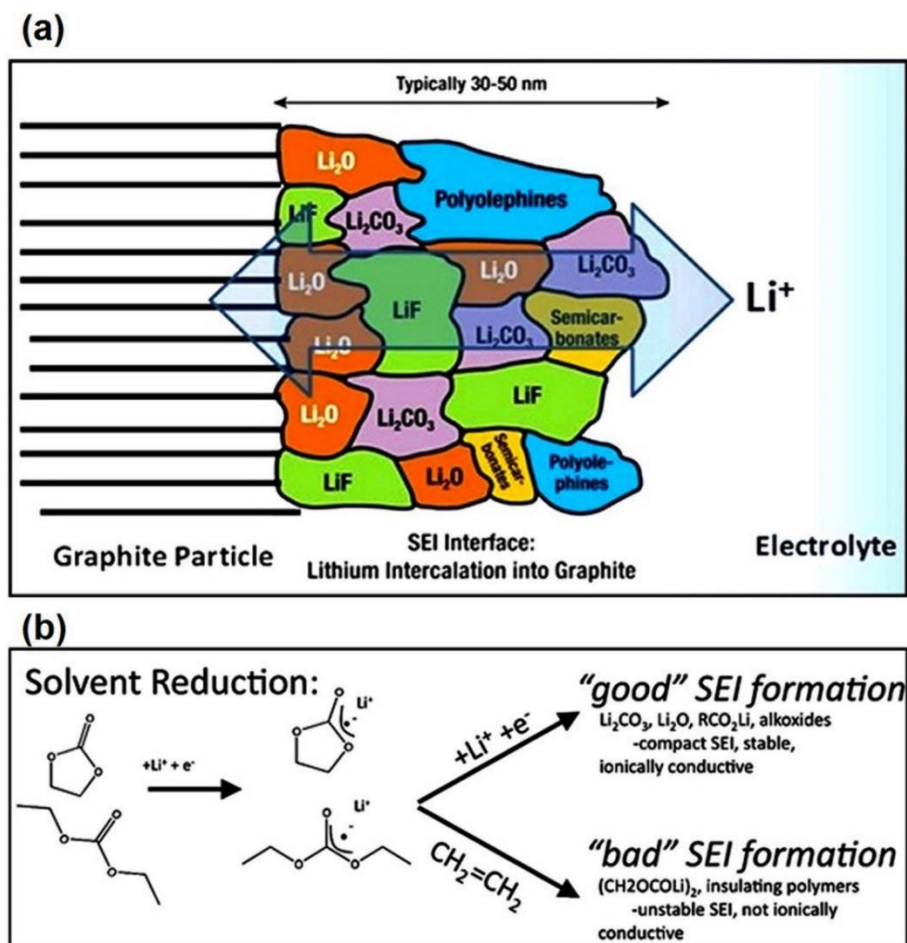


Fig. 1.9: (a) Diagrammatic representation of SEI formation, and (b) the reaction mechanism of SEI formation (Adopted from Ref. [330])

In graphite and Si anodes, SEI formation causes loss in capacity of about 25-50%, called as irreversible capacity. An efficient, stable SEI stabilizes the electrode surface and helps in good cycle life of the battery, avoiding additional decomposition of electrolyte in succeeding cycles although allowing migration of Li^+ through the electrode/electrolyte interface. The development of a surface layer (SEI) is also observed in cathodes, but in contrast to anodes, the decomposition of the electrolyte takes place not only in first charge-discharge cycle but electrolyte decomposition happens even in successive cycles at high operating voltages >4 V, resulting in a thicker SEI which stops the electronic and ionic conduction, resulting in cell failure.

1.7. Scope and Objectives of the Thesis

US Department of Energy (DOE) year 2022 goals to develop next generation lithium ion batteries (LIBs) that have high energy density (300-400 Wh kg⁻¹) which enable a large market penetration of hybrid and electric vehicles (HEVs and EVs) [330]. Besides, the LIBs should have reduced cost, improved safety and cycle life. State-of-art LIBs use transition metal (TM, such as Ni, Mn, Co) oxide (LCO, NMC-333₂ or LiNi_{0.8}Co_{0.15}Al_{0.15}O₂) or olivines (LFP, LMP), spinels (LiMn₂O₄, LiNi_{0.5}Mn_{1.5}O₄ (NMS) based cathodes and graphitic carbon as anode [326]. The nominal capacity of most of these cathodes are in the range of 120-180 mAh g⁻¹ when cycled up to 4.2 V, is only half the specific capacity of graphite anode (theoretical capacity = 372 mAh g⁻¹) [321]. Thus, there has been an intense research activity during the last decade to develop high capacity-high voltage or high energy cathodes for LIBs. LMR-NMC cathodes which has almost double the capacity (372 mAh g⁻¹ for 1.2 Li transfer) of currently available cathodes have been investigated as a promising cathode material for LIBs [312-318]. To get high capacity from LMR-NMC, the material need to be electrochemically cycled above 4.4 V. During high voltage cycling (> 4.4 V), oxygen release takes place from Li₂MnO₃ component in the form of Li₂O and MnO₂ which causes interfacial instability of LMR-NMC electrode. The major issue of LMR-NMC is voltage decay mostly due to structural transformation of layered to the spinel structure. An improved interfacial stability, capacity retention and rate performance of LMR-NMC can be achieved by surface coatings such as metal oxides like Al₂O₃, ZrO₂, TiO₂ etc., metal phosphate coatings (AlPO₄, LiFePO₄ etc.), and solid electrolyte coating like lithium phosphorous oxynitrides or blending with another cathode material [325]. But voltage fade is not properly addressed by these surface coatings or blendings.

To enhance the performance of anodes which meet the requirement of the automotive industry, researchers have been investigating materials which form alloys with lithium to generate anodes that have specific capacities in an order of magnitude higher than graphite. Silicon is an attractive anode material for Li-ion batteries mainly because of its very high theoretical charge capacity of 4200 mAh g⁻¹ (Li_{4.4}Si) [311, 316]. But silicon has various issues of low electronic and ionic conductivity and most

important one is high volume change of ~400% during lithiation and delithiation leading to structural degradation (pulverization) followed by capacity fade and reduced cycle life.

Thus, there has been an intense research to mitigate volume change during cycling, such as producing Si-NPs, aligned Si-nanowires/nanotubes, dispersing silicon into an active (such as carbon) /inactive (Eg. SiO₂) matrix, silicon based thin films, free standing Si-C electrodes and different morphologies of silicon. Taking benefit of high conductivity of carbon and high capacity silicon, recent reports demonstrated carbon-silicon nanocomposites can circumvent the issues associated with silicon and improve the overall electrochemical performance of Si-anode for Li-ion batteries.

So current research emphasis is given to develop high energy density Li-ion batteries through high capacity-high voltage cathodes, high voltage electrolytes and high capacity anodes.

The studies reported in the present thesis are confined to develop high energy density LMR-NMC based cathodes with minimized voltage decay, coupled with high capacity silicon anodes for increasing energy density in LIBs.

1.7.1. The present study

From the above review of literature on the cathode, anode materials for lithium-ion batteries (Chapter 1), it is clear that next generation LIBs can have double the energy and power density of the currently available LIBs with reduced cost and improved safety. With this background, Chapters 2 of the thesis is an attempt to evaluate energy and power density of currently available LIBs with respect to C rate and temperature. Chapter 3-5 comprise studies on development of LMR-NMC cathode materials with improved energy density. Chapter 6-7 deals with development of Si anode material for the next generation LIBs.

LIBs operating at high-low temperatures and high C rates pose a technical barrier for operating hybrid and electric vehicles is due to substantial reduction in energy and power. **Chapter 2** explains simultaneous effect of temperature and C rate on state-of-health, power and energy density of LIBs. Ragone charts are developed on

LIBs based on LiCoO₂ cathode and graphite anode chemistry at various temperatures between -20 and 55 °C and C rates (C/5-10C). The “Energy-Power Index” (EPI) (%) vs. T profile shows a linear increase from -10 °C to 25 °C and then it makes a semi-plateau between 25 °C and 55 °C. Besides, for the optimum performance of LIBs operating at low temperatures, low C-rate application is most preferable.

Chapter 3 describes an effort to improve capacity retention, C rate performance and energy density of LMR-NMC by 3D electrode architecture and LiF coating (F⁻ anion doping). LMR-NMC is synthesized by solution combustion method followed by LiF coating onto LMR-NMC by solid state synthesis. The fluorine doped cathodes deliver high capacity of ~300 mAh g⁻¹ at C/10 rate (10-20% greater than the pristine LMR-NMC cathodes), have high discharge voltage plateau (> 0.25 V) and low charge voltage plateau (0.2 to 0.4 V) compared to pristine LMR-NMC cathodes. Besides, irreversible capacity, voltage fade and capacity loss are significantly reduced in-relation to the pristine LMR-NMC electrodes. LiF coating onto LMR-NMC, partially replaces M-O bonds of the material by M-F bonds, thus increasing the interfacial and structural stability. The Chapter also describes possible replacement of aluminium current collector with 3D carbon fiber current collector which delivers high capacity of >200 mAh g⁻¹ at 1C rate, with good capacity retentions for over 200 cycles.

In order to improve the voltage fade in LMR-NMC an attempt is made with both cation (Mg²⁺) and anion dopings (F⁻) is described in **Chapter 4**. Mg-doped LMR-NMC (Li_{1.2}Ni_{0.15-x}Mg_xMn_{0.55}Co_{0.1}O₂) is synthesized by combustion method followed by fluorine doping by solid state synthesis is investigated as a promising cathode material for LIBs. In this approach, we substituted the Ni²⁺ by Mg²⁺ in varying mole percentages (x = 0.02, 0.05, 0.08) and partly oxygen by fluorine (LiF: LMR-NMC= 1:50 wt. %). The synergistic effect of both magnesium and fluorine substitution on electrochemical performance of LMR-NMC is studied by electrochemical impedance spectroscopy and galvanostatic-charge-discharge cycling. Mg-F doped LMR-NMC (Mg-0.02 mole) composite cathodes shows excellent discharge capacity of ~300 mAh g⁻¹ at C/20 rate whereas pristine LMR-NMC shows the initial capacity around 250 mAh g⁻¹ in the voltage range between 2.5 and 4.7 V. Mg-F doped LMR-NMC shows

lesser Ohmic and charge transfer resistance, cycles well and delivers a stable high capacity of $\sim 280 \text{ mAh g}^{-1}$ at C/10 rate. The voltage decay which is the major issue of LMR-NMC is minimized in Mg-F doped LMR-NMC compared to pristine LMR-NMC.

Chapter 5 describes another approach of improving energy density, C rate performance of LMR-NMC material by blending with carbon coated LiMnPO_4 (CLMP) using mechanical milling. The presence of the CLMP provides interfacial stability under high current (rate) and voltage cycling conditions and thereby improves the energy loss over cycle life in relation to the pristine LMR-NMC. Blended composite electrodes show stable reversible capacities of $>225 \text{ mAh g}^{-1}$ in the voltage window of 2.5 to 4.7 V for more than 200 cycles, and shows improvements in the rate performance, reduction in irreversible capacity loss and Mn dissolution than the pristine LMR-NMC composite electrode. We characterize the details of electrochemical performance studies to understand the role of CLMP in improving the interfacial stability at the interface.

The studies based on LMR-NMC cathodes opens a possibility for cathode material which has almost double the capacity of currently used cathodes, can be a possible substitute cathode for LIBs used in electric vehicles.

To enhance the electrochemical performance of Silicon anodes we demonstrate two electrode architectures for LIBs which are described in **Chapter 6** and **7**. **Chapter 6** presents binder and conducting additive free Silicon nanoparticles (Si-NPs) as anodes for LIBs. The Si-NPs are pressure embedded onto copper (Cu) foil current collector without using any organic binder or conductive carbon additive. Binder-free Si-NP electrodes exhibit an initial reversible capacity of 950 mAh g^{-1} at C/10 rate and more than 650 mAh g^{-1} during 500 cycles at 1C rate. The electrodes show excellent rate capability (800 mAh g^{-1} at 5C rate) and cycling stability, because of available free space for volume change during cycling of silicon NPs without pulverization. The binder-free anode fabrication enables Si-NPs to obtain the real capacity of silicon without any interference of capacity contribution from composite materials.

Organic binder and conducting diluent free Silicon- Carbon 3D free standing electrodes as anodes for LIBs are described in **Chapter 7**. Si-NPs are synthesized by magnesiothermic reduction in Chapter VI are used as active mass along with carbons derived from petroleum pitch (P-Pitch) onto 3D carbon fiber (CF) current collector. Highly conductive CFs of 5-10 μm in diameter have been used to replace a conventional Cu foil current collector. We demonstrate here P-Pitch which adequately coat between the CFs and Si-NPs above 700 $^{\circ}\text{C}$ under Argon atmosphere. P-Pitch makes uniform continuous layer of 10-15 nm thick coating along the exterior surfaces of Si-NPs. Capacities in excess of 2200-2050 mAh g^{-1} (at C/10) for 100s cycles at 900 and 1000 $^{\circ}\text{C}$, respectively have been achieved in half cell configuration. Synergistic effect of carbon coating and 3D carbon fiber electrode architecture improves the efficiency of the Si-C composite during long cycling at 1000 $^{\circ}\text{C}$. This is because silicon-carbon nanocomposites can accommodate huge strain with reduced pulverization, provide good electronic contact, and exhibit short diffusion path for lithium ion insertion. The usual organic binder and current collector can be replaced by a high temperature binder of carbonized P-pitch and CFs, respectively. Together these replacements increase the specific energy density and energy per unit area of the electrode. Full cells based on LMR-NMC cathodes and Si-C composite free standing electrodes deliver an energy density of 530 Wh kg^{-1} , which is almost double the energy density of currently available LIBs.

References

- [1] H. Chen, T.N. Cong, W. Yang, C. Tan, Y. Li, Y. Ding, Progress in electrical energy storage system: A critical review, *Prog. Nat. Sci.* 19 (2009) 291–312.
- [2] H. Ibrahim, A. Ilinca, J. Perron, Energy storage systems—characteristics and comparisons, *Renewable Sustainable Energy Rev.* 12 (2008) 1221–1250.
- [3] J.O.G. Posada, A.J. Rennie, S.P. Villar, V.L. Martins, J. Marinaccio, A. Barnes, C.F. Glover, D.A. Worsley, P.J. Hall, Aqueous batteries as grid scale energy storage solutions, *Renewable Sustainable Energy Rev.* 68 (2017) 1174–1182.
- [4] S. Chu, A. Majumdar, Opportunities and challenges for a sustainable energy future, *Nat.* 488 (2012) 294–303.

- [5] V. Etacheri, R. Marom, R. Elazari, G. Salitra, D. Aurbach, Challenges in the development of advanced Li-ion batteries: a review, *Energy Environ. Sci.* 4 (2011) 3243–3262.
- [6] M.S. Whittingham, Lithium batteries and cathode materials, *Chemical Rev.* 104 (2004) 4271–4302.
- [7] C.M. Shepherd, Design of primary and secondary cells II. An equation describing battery discharge, *J. Electrochem. Soc.* 112 (1965) 657–664.
- [8] B. Dunn, H. Kamath, J.-M. Tarascon, Electrical energy storage for the grid: a battery of choices, *Sci.* 334 (2011) 928–935.
- [9] A. Taniguchi, N. Fujioka, M. Ikoma, A. Ohta, Development of nickel/metal-hydride batteries for EVs and HEVs, *J. Power Sources.* 100 (2001) 117–124.
- [10] P. Van den Bossche, F. Vergels, J. Van Mierlo, J. Matheys, W. Van Autenboer, SUBAT: An assessment of sustainable battery technology, *J. Power Sources.* 162 (2006) 913–919.
- [11] J.-M. Tarascon, M. Armand, Issues and challenges facing rechargeable lithium batteries, in: *Materials For Sustainable Energy: A Collection of Peer-Reviewed Research and Review Articles from Nature Publishing Group*, World Scientific, 2011: pp. 171–179.
- [12] A.S. Aricò, P. Bruce, B. Scrosati, J.-M. Tarascon, W. Van Schalkwijk, Nanostructured materials for advanced energy conversion and storage devices, *Nat. Mater.* 4 (2005) 366–377.
- [13] A. Du Pasquier, I. Plitz, S. Menocal, G. Amatucci, A comparative study of Li-ion battery, supercapacitor and nonaqueous asymmetric hybrid devices for automotive applications, *J. Power Sources.* 115 (2003) 171–178.
- [14] P.J. Hall, E.J. Bain, Energy-storage technologies and electricity generation, *Energy Policy.* 36 (2008) 4352–4355.
- [15] J. Hassoun, S. Panero, P. Reale, B. Scrosati, A New, Safe, High-Rate and High-Energy Polymer Lithium-Ion Battery, *Adv. Mater.* 21 (2009) 4807–4810.
- [16] J. Gao, S.-Q. Shi, H. Li, Brief overview of electrochemical potential in lithium ion batteries, *Chin. Phys. B.* 25 (2015) 018210.
- [17] L. Lu, X. Han, J. Li, J. Hua, M. Ouyang, A review on the key issues for lithium-ion battery management in electric vehicles, *J. Power Sources.* 226 (2013) 272–288.
- [18] F. Sun, X. Hu, Y. Zou, S. Li, Adaptive unscented Kalman filtering for state of charge estimation of a lithium-ion battery for electric vehicles, *Energy.* 36 (2011) 3531–3540.
- [19] M.S. Whittingham, Electrical energy storage and intercalation chemistry, *Sci.* 192 (1976) 1126–1127.

- [20] M.S. Whittingham, The role of ternary phases in cathode reactions, *J. Electrochem. Soc.* 123 (1976) 315–320.
- [21] R. Yazami, P. Touzain, A reversible graphite-lithium negative electrode for electrochemical generators, *J. Power Sources.* 9 (1983) 365–371.
- [22] K. Mizushima, P.C. Jones, P.J. Wiseman, J.B. Goodenough, Li_xCoO_2 ($0 < x < 1$): A new cathode material for batteries of high energy density, *Mater. Res. Bull.* 15 (1980) 783–789.
- [23] Y. Gan, L. Zhang, Y. Wen, F. Wang, H. Su, Carbon combustion synthesis of lithium cobalt oxide as cathode material for lithium ion battery, *Particuology.* 6 (2008) 81–84.
- [24] X. Wei, G.R. Han, Progress in research of positive materials of lithium ion secondary batteries and hydrothermal synthesis of LiCoO_2 . *J. Mater. Sci. Eng.* 24 (1) (2006), 118–123.
- [25] J. Ying, C. Jiang, C. Wan, Preparation and characterization of high-density spherical LiCoO_2 cathode material for lithium ion batteries, *J. Power Sources.* 129 (2004) 264–269.
- [26] S.E. Sloop, J.K. Pugh, S. Wang, J.B. Kerr, K. Kinoshita, Chemical Reactivity of PF₅ and LiPF_6 in Ethylene Carbonate/Dimethyl Carbonate Solutions, *Electrochem. Solid-State Lett.* 4 (2001) A42–A44.
- [27] D. Aurbach, Y. Ein-Eli, B. Markovsky, A. Zaban, S. Luski, Y. Carmeli, H. Yamin, The study of electrolyte solutions based on ethylene and diethyl carbonates for rechargeable Li batteries II. Graphite electrodes, *J. Electrochem. Soc.* 142 (1995) 2882–2890.
- [28] P. He, H. Yu, H. Zhou, Layered lithium transition metal oxide cathodes towards high energy lithium-ion batteries, *J. Mater. Chem.* 22 (2012) 3680–3695.
- [29] L. Guohua, H. Ikuta, T. Uchida, M. Wakihara, The Spinel Phases $\text{LiM}_y\text{Mn}_{2-y}\text{O}_4$ (M= Co, Cr, Ni) as the Cathode for Rechargeable Lithium Batteries, *J. Electrochem. Soc.* 143 (1996) 178–182.
- [30] A.K. Padhi, K.S. Nanjundaswamy, J.B. Goodenough, Phospho-olivines as positive-electrode materials for rechargeable lithium batteries, *J. Electroch. Soc.* 144 (1997) 1188–1194.
- [31] F. Wang, S.-W. Kim, D.-H. Seo, K. Kang, L. Wang, D. Su, J.J. Vajo, J. Wang, J. Graetz, Ternary metal fluorides as high-energy cathodes with low cycling hysteresis, *Nat. Commun.* 6 (2015) 6668.
- [32] P. Lavela, J. Morales, L. Sánchez, J.L. Tirado, Novel layered chalcogenides as electrode materials for lithium-ion batteries, *J. Power Sources.* 68 (1997) 704–707.

- [33] R. Zeng, L. Xing, Y. Qiu, Y. Wang, W. Huang, W. Li, S. Yang, Polycarbonyl (quinonyl) organic compounds as cathode materials for sustainable lithium ion batteries, *Electrochim. Acta.* 146 (2014) 447–454.
- [34] L. Zhao, W. Wang, A. Wang, K. Yuan, S. Chen, Y. Yang, A novel polyquinone cathode material for rechargeable lithium batteries, *J. Power Sources.* 233 (2013) 23–27.
- [35] Y. Shao-Horn, S. Levasseur, F. Weill, C. Delmas, Probing Lithium and Vacancy Ordering in O₃ Layered Li_xCoO₂ (x≈0.5) An Electron Diffraction Study, *J. Electrochem. Soc.* 150 (2003) A366–A373.
- [36] A. Lundblad, B. Bergman, Synthesis of LiCoO₂ starting from carbonate precursors I. The reaction mechanisms, *Solid State Ionics.* 96 (1997) 173–181.
- [37] Y. Lee, A. Woo, K.S. Ryu, Y.J. Park, B.Y. Jung, J.H. Lee, K. Han, 7 Li MAS NMR studies of layered Li_xCoO₂ prepared using eutectic self-mixing technique for a cathode material, *Solid State Ionics.* 175 (2004) 311–314.
- [38] A. Lundblad, S. Schwartz, B. Bergman, Effect of sintering procedures in development of LiCoO₂-cathodes for the molten carbonate fuel cell, *J. Power Sources.* 90 (2000) 224–230.
- [39] C.-Z. Lu, J.-M. Chen, Y.-D. Cho, W.-H. Hsu, P. Muralidharan, G.T.-K. Fey, Electrochemical performance of LiCoO₂ cathodes by surface modification using lanthanum aluminum garnet, *J. Power Sources.* 184 (2008) 392–401.
- [40] M.-S. Park, S.-H. Hyun, S.-C. Nam, S.B. Cho, Performance evaluation of printed LiCoO₂ cathodes with PVDF-HFP gel electrolyte for lithium ion microbatteries, *Electrochim. Acta.* 53 (2008) 5523–5527.
- [41] K.Y. Choi, K. Do Kim, J.W. Yang, Optimization of the synthesis conditions of LiCoO₂ for lithium secondary battery by ultrasonic spray pyrolysis process, *J. Mater. Proces. Technol.* 171 (2006) 118–124.
- [42] E.I. Santiago, A.V.C. Andrade, C.O. P.-Santos, L.O.S. Bulhões Structure and electrochemical properties of LiCoO₂ prepared by combustion synthesis *Solid State Ionics*, 158 (2003) 91-102.
- [43] P. Kalyani, N. Kalaiselvi, N. Muniyandi, A new solution combustion route to synthesize LiCoO₂ and LiMn₂O₄, *J. Power Sources.* 111 (2002) 232–238.
- [44] J. Fu, Y. Bai, C. Liu, H. Yu, Y. Mo, Physical characteristic study of LiCoO₂ prepared by molten salt synthesis method in 550–800° C, *Mater. Chem. Phys.* 115 (2009) 105–109.
- [45] G. Li, Z. Yang, W. Yang, Effect of FePO₄ coating on electrochemical and safety performance of LiCoO₂ as cathode material for Li-ion batteries, *J. Power Sources.* 183 (2008) 741–748.

- [46] M. Yoshio, H. Tanaka, K. Tominaga, H. Noguchi, Synthesis of LiCoO_2 from cobalt—organic acid complexes and its electrode behaviour in a lithium secondary battery, *J. Power Sources*. 40 (1992) 347–353.
- [47] O.A. Shlyakhtin, S.H. Choi, Y.S. Yoon, Y.-J. Oh, Characterization of nanocrystalline HT- LiCoO_2 cathode materials for secondary lithium batteries, *Electrochim. Acta*. 50 (2004) 511–516.
- [48] P. Kalyani, N. Kalaiselvi, N.G. Renganathan, Microwave-assisted synthesis of LiNiO_2 —a preliminary investigation, *J. Power Sources*. 123 (2003) 53–60.
- [49] H. Yan, X. Huang, L. Zhonghua, H. Huang, R. Xue, L. Chen, Microwave synthesis of LiCoO_2 cathode materials, *J. Power Sources*. 68 (1997) 530–532.
- [50] P.N. Kumta, D. Gallet, A. Waghray, G.E. Blomgren, M.P. Setter, Synthesis of LiCoO_2 powders for lithium-ion batteries from precursors derived by rotary evaporation, *J. Power Sources*. 72 (1998) 91–98.
- [51] E. Antolini, LiCoO_2 : formation, structure, lithium and oxygen nonstoichiometry, electrochemical behaviour and transport properties, *Solid State Ionics*. 170 (2004) 159–171.
- [52] Y. Shao-Horn, L. Croguennec, C. Delmas, E.C. Nelson, M.A. O’Keefe, Atomic resolution of lithium ions in LiCoO_2 , *Nat. Mater.* 2 (2003) 464.
- [53] R.J. Gummow, M.M. Thackeray, Lithium-cobalt-nickel-oxide cathode materials prepared at 400 C for rechargeable lithium batteries, *Solid State Ionics*. 53 (1992) 681–687.
- [54] E. Rossen, J.N. Reimers, J.R. Dahn, Synthesis and electrochemistry of spinel LT LiCoO_2 , *Solid State Ionics*. 62 (1993) 53–60.
- [55] H.J. Orman, P.J. Wiseman, Cobalt (III) lithium oxide, CoLiO_2 : structure refinement by powder neutron diffraction, *Acta Crystallograph. Section C: Crystal Structure Commun.* 40 (1984) 12–14.
- [56] J.R. Ying, C.Y. Jiang, C.R. Wan, Preparation and characterization of high-density spherical LiCoO_2 cathode material for lithium ion batteries *J. Power Sources*, 129 (2004) 264-269.
- [57] Q. Cao, H.P. Zhang, G.J. Wang, Q. Xia, Y.P. Wu, H.Q. Wu, A novel carbon-coated LiCoO_2 as cathode material for lithium ion battery, *Electrochem. Commun.* 9 (2007) 1228–1232.
- [58] J.-T. Lee, F.-M. Wang, C.-S. Cheng, C.-C. Li, C.-H. Lin, Low-temperature atomic layer deposited Al_2O_3 thin film on layer structure cathode for enhanced cycleability in lithium-ion batteries, *Electrochim. Acta*. 55 (2010) 4002–4006.

- [59] J. Xiang, C. Chang, L. Yuan, J. Sun, A simple and effective strategy to synthesize Al_2O_3 -coated $\text{LiNi}_{0.8}\text{Co}_{0.2}\text{O}_2$ cathode materials for lithium ion battery, *Electrochem. Commun.* 10 (2008) 1360–1363.
- [60] W. Chang, J.-W. Choi, J.-C. Im, J.K. Lee, Effects of ZnO coating on electrochemical performance and thermal stability of LiCoO_2 as cathode material for lithium-ion batteries, *J. Power Sources.* 195 (2010) 320–326.
- [61] T.-F. Yi, J. Shu, C.-B. Yue, X.-D. Zhu, A.-N. Zhou, Y.-R. Zhu, R.-S. Zhu, Enhanced cycling stability of micro-sized LiCoO_2 cathode by $\text{Li}_4\text{Ti}_5\text{O}_{12}$ coating for lithium ion battery, *Mater. Res. Bull.* 45 (2010) 456–459.
- [62] H.Y. Liang, X.P. Qiu, S.C. Zhang, Z.Q. He, W.T. Zhu, L.Q. Chen, High performance lithium cobalt oxides prepared in molten KCl for rechargeable lithium-ion batteries, *Electrochemistry Communications*, 6 (2004) 505-509.
- [63] K. Zaghib, A. Mauger, J.B. Goodenough, F. Gendron, C.M. Julien, Positive electrode: Lithium iron phosphate. In *Encyclopedia of Electrochemical Power Sources*; Garcke, J., Ed.; Elsevier Science Ed.: Amsterdam, the Netherlands, 5 (2009) 264–296.
- [64] G.T.-K. Fey, C.-Z. Lu, J.-D. Huang, T.P. Kumar, Y.-C. Chang, Nanoparticulate coatings for enhanced cyclability of LiCoO_2 cathodes, *J. Power Sources.* 146 (2005) 65–70.
- [65] K.-H. Choi, J.-H. Jeon, H.-K. Park, S.-M. Lee, Electrochemical performance and thermal stability of LiCoO_2 cathodes surface-modified with a sputtered thin film of lithium phosphorus oxynitride, *J. Power Sources.* 195 (2010) 8317–8321.
- [66] S.P. Sheu, C.Y. Yao, J.M. Chen, Y.C. Chiou, Influence of the LiCoO_2 particle size on the performance of lithium-ion batteries, *J. Power Sources*, 68 (1997) 533-535.
- [67] S. Shi, C. Ouyang, M. Lei, W. Tang, Effect of Mg-doping on the structural and electronic properties of LiCoO_2 : A first-principles investigation, *Journal of Power Sources.* 171 (2007) 908–912.
- [68] P. Ghosh, S. Mahanty, R.N. Basu, Lanthanum-doped LiCoO_2 cathode with high rate capability, *Electrochim. Acta.* 54 (2009) 1654–1661.
- [69] P. Prahasini, M. Sivakumar, R. Subadevi, F.M. Wang, Synthesis and characterization of Cu doped LiCoO_2 cathode material for lithium batteries using microwave assisted sol-gel synthesis, in: *Adv. Mater. Res., Trans. Tech. Publ.* (2012) 345–349.
- [70] S. Madhavi, G.S. Rao, B.V.R. Chowdari, S.F.Y. Li, Effect of Cr dopant on the cathodic behavior of LiCoO_2 , *Electrochim. Acta.* 48 (2002) 219–226.
- [71] S. Huang, Z. Wen, X. Yang, Z. Gu, X. Xu, Improvement of the high-rate discharge properties of LiCoO_2 with the Ag additives, *J. Power Sources.* 148 (2005) 72–77.

- [72] S.H. Kim, C.-S. Kim, Improving the rate performance of LiCoO₂ by Zr doping, *J. Electroceramics*. 23 (2009) 254.
- [73] A. Büyükburç, M.K. Aydinol, Effect of Cr and Mo doping on the electrochemical properties of freeze-dried LiCoO₂, *Int. J. Mater. Res.* 105 (2014) 983–991.
- [74] R. Alcantara, P. Lavela, J.L. Tirado, R. Stoyanova, E. Zhecheva, Structure and electrochemical properties of boron-doped LiCoO₂, *J. Solid State Chem.* 134 (1997) 265–273.
- [75] M.C. Rao, O.M. Hussain, Synthesis and electrochemical properties of Ti doped LiCoO₂ thin film cathodes, *J. Alloys Compd.* 491 (2010) 503–506.
- [76] S.-T. Myung, N. Kumagai, S. Komaba, H.-T. Chung, Effects of Al doping on the microstructure of LiCoO₂ cathode materials, *Solid State Ionics*. 139 (2001) 47–56.
- [77] L. Croguennec, P. Deniard, R. Brec, A. Lecerf, Preparation, physical and structural characterization of LiMnO₂ samples with variable cationic disorder, *J. Mater. Chem.* 5 (1995) 1919–1925.
- [78] T. Ohzuku, Y. Iwakoshi, K. Sawai, Formation of Lithium-Graphite Intercalation Compounds in Nonaqueous Electrolytes and Their Application as a Negative Electrode for a Lithium Ion (Shuttlecock) Cell, *J. Electrochem. Soc.* 140 (1993) 2490–2498.
- [79] R.J. Gummow, D.C. Liles, M.M. Thackeray, Lithium extraction from orthorhombic lithium manganese oxide and the phase transformation to spinel, *Mater. Res. Bull.* 28 (1993) 1249–1256.
- [80] I.J. Davidson, R.S. McMillan, J.J. Murray, J.E. Greedan, Lithium-ion cell based on orthorhombic LiMnO₂, *J. Power Sources*. 54 (1995) 232–235.
- [81] L. Croguennec, P. Deniard, R. Brec, P. Biensan, M. Broussely, Electrochemical behavior of orthorhombic LiMnO₂: influence of the grain size and cationic disorder, *Solid State Ionics*. 89 (1996) 127–137.
- [82] J.N. Reimers, W. Li, E. Rossen, J.R. Dahn, Structure, Diffraction and Energetic Stability of the Spinel Form of LiCoO₂, *MRS Online Proceedings Library Archive*. 293 (1992).
- [83] J. Cho, Y.J. Kim, T.-J. Kim, B. Park, Effect of Al₂O₃-Coated o LiMnO₂ Cathodes Prepared at Various Temperatures on the 55° C Cycling Behavior, *J. Electrochem. Soc.* 149 (2002) A127–A132.
- [84] A.D. Robertson, A.R. Armstrong, A.J. Fowkes, P.G. Bruce, Li_x(Mn_{1-y}Co_y)O₂ intercalation compounds as electrodes for lithium batteries: influence of ion exchange on structure and performance Basis of a presentation given at Materials Discussion No. 3, 26–29 September, 2000, University of Cambridge, UK., *J. Mater. Chem.* 11 (2001) 113–118.

- [85] T.E. Quine, M.J. Duncan, A.R. Armstrong, A.D. Robertson, P.G. Bruce, Layered $\text{Li}_x\text{Mn}_{1-y}\text{Ni}_y\text{O}_2$ intercalation electrodes, *J. Mater. Chem.* 10 (2000) 2838–2841.
- [86] J.M. Paulsen, C.L. Thomas, J.R. Dahn, Layered Li-Mn-Oxide with the O_2 Structure: A Cathode Material for Li-Ion Cells Which Does Not Convert to Spinel, *J. Electrochem. Soc.* 146 (1999) 3560–3565.
- [87] J.M. Paulsen, C.L. Thomas, J.R. Dahn, O_2 Structure $\text{Li}_{2/3}[\text{Ni}_{1/3}\text{Mn}_{2/3}]\text{O}_2$: A New Layered Cathode Material for Rechargeable Lithium Batteries. I. Electrochemical Properties, *J. Electrochem. Soc.* 147 (2000) 861–868.
- [88] S. Megahed, B. Scrosati, Lithium-ion rechargeable batteries, *J. Power Sources.* 51 (1994) 79–104.
- [89] R. Koksang, J. Barker, H. Shi, M.Y. Saidi, Cathode materials for lithium rocking chair batteries, *Solid State Ionics.* 84 (1996) 1–21.
- [90] R.V. Chebiam, F. Prado, A. Manthiram, Soft Chemistry Synthesis and Characterization of Layered $\text{Li}_{1-x}\text{Ni}_{1-y}\text{Co}_y\text{O}_{2-\delta}$ ($0 \leq x \leq 1$ and $0 \leq y \leq 1$), *Chem. Mater.* 13 (2001) 2951–2957.
- [91] C. Delmas, M. Menetrier, L. Croguennec, I. Saadoun, A. Rougier, C. Pouillier, G. Prado, M. Grüne, L. Fournes, An overview of the $\text{Li}(\text{Ni},\text{M})\text{O}_2$ systems: syntheses, structures and properties, *Electrochim. Acta.* 45 (1999) 243–253.
- [92] J.N. Reimers, E. Rossen, C.D. Jones, J.R. Dahn, Structure and electrochemistry of $\text{Li}_x\text{Fe}_y\text{Ni}_{1-y}\text{O}_2$, *Solid State Ionics.* 61 (1993) 335–344.
- [93] S. Venkatraman, A. Manthiram, Structural and Chemical Characterization of Layered $\text{Li}_{1-x}\text{Ni}_{1-y}\text{Mn}_y\text{O}_{2-\delta}$ ($y = 0.25$ and 0.5 , and $0 \leq (1-x) \leq 1$) Oxides, *Chem. Mater.* 15 (2003) 5003–5009.
- [94] Y. Nitta, K. Okamura, K. Haraguchi, S. Kobayashi, A. Ohata, Crystal structure study of $\text{LiNi}_{1-x}\text{Mn}_x\text{O}_2$, *J. Power Sources.* 54 (1995) 511–515.
- [95] T. Ohzuku, A. Ueda, M. Kouguchi, Synthesis and Characterization of $\text{LiAl}_{1/4}\text{Ni}_{3/4}\text{O}_2$ ($R\bar{3}m$) for Lithium-Ion (Shuttlecock) Batteries, *J. Electrochem. Soc.* 142 (1995) 4033–4039.
- [96] H. Arai, S. Okada, Y. Sakurai, J. Yamaki, Electrochemical and Thermal Behavior of $\text{LiNi}_{1-z}\text{M}_z\text{O}_2$ ($M = \text{Co}, \text{Mn}, \text{Ti}$), *J. Electrochem. Soc.* 144 (1997) 3117–3125.
- [97] Y. Gao, M.V. Yakovleva, W.B. Ebner, Novel $\text{LiNi}_{1-x}\text{Ti}_{x/2}\text{Mg}_{x/2}\text{O}_2$ Compounds as Cathode Materials for Safer Lithium-Ion Batteries, *Electrochem. Solid-State Lett.* 1 (1998) 117–119.
- [98] K. Kubo, S. Arai, S. Yamada, M. Kanda, Synthesis and charge–discharge properties of $\text{Li}_{1+x}\text{Ni}_{1-x-y}\text{Co}_y\text{O}_{2-z}\text{F}_z$, *J. Power Sources.* 81 (1999) 599–603.

- [99] S.H. Park, K.S. Park, Y.K. Sun, K.S. Nahm, Y.S. Lee, M. Yoshio, Y.K. Lee, K.W. Han, Electrochemical Society Proceedings Volume 2000–21, M. Doyle, E. Takeuchi and KM Abraham, Eds. (2001) 45.
- [100] A.R. Naghash, J.Y. Lee, Lithium nickel oxyfluoride ($\text{Li}_{1-z}\text{Ni}_{1+z}\text{FyO}_{2-y}$) and lithium magnesium nickel oxide ($\text{Li}_{1-z}(\text{Mg}_x\text{Ni}_{1-x})_{1+z}\text{O}_2$) cathodes for lithium rechargeable batteries: II. Electrochemical investigations, *Electrochim. Acta.* 46 (2001) 2293–2304.
- [101] K.M. Shaju, G.S. Rao, B.V.R. Chowdari, Performance of layered $\text{Li}(\text{Ni}_{1/3}\text{Co}_{1/3}\text{Mn}_{1/3})\text{O}_2$ as cathode for Li-ion batteries, *Electrochim. Acta.* 48 (2002) 145–151.
- [102] J.-M. Kim, H.-T. Chung, Role of transition metals in layered $\text{Li}[\text{Ni}, \text{Co}, \text{Mn}]\text{O}_2$ under electrochemical operation, *Electrochim. Acta.* 49 (2004) 3573–3580.
- [103] Z. Liu, A. Yu, J.Y. Lee, Synthesis and characterization of $\text{LiNi}_{1-x-y}\text{Co}_x\text{Mn}_y\text{O}_2$ as the cathode materials of secondary lithium batteries, *J. Power Sources.* 81 (1999) 416–419.
- [104] T. Ohzuku, Y. Makimura, Layered lithium insertion material of $\text{LiNi}_{1/2}\text{Mn}_{1/2}\text{O}_2$: A possible alternative to LiCoO_2 for advanced lithium-ion batteries, *Chem. Lett.* 30 (2001) 744–745.
- [105] C. Venkateswara Rao, A. Leela Mohana Reddy, Y. Ishikawa, P.M. Ajayan, $\text{LiNi}_{1/3}\text{Co}_{1/3}\text{Mn}_{1/3}\text{O}_2$ –graphene composite as a promising cathode for Lithium-ion batteries, *ACS Appl. Mater. Interface.* 3 (2011) 2966–2972.
- [106] Z. Chen, J. Wang, D. Chao, T. Baikie, L. Bai, S. Chen, Y. Zhao, T.C. Sum, J. Lin, Z. Shen, Hierarchical porous $\text{LiNi}_{1/3}\text{Co}_{1/3}\text{Mn}_{1/3}\text{O}_2$ nano-/micro spherical cathode material: minimized cation mixing and improved Li^+ mobility for enhanced electrochemical performance, *Sci. Reports.* 6 (2016) 25771.
- [107] X. Zhang, W.J. Jiang, A. Mauger, F. Gendron, C.M. Julien, Minimization of the cation mixing in $\text{Li}_{1+x}(\text{NMC})_{1-x}\text{O}_2$ as cathode material, *J. Power Sources.* 195 (2010) 1292–1301.
- [108] Q. Jiang, K. Du, Y. He, A novel method for preparation of $\text{LiNi}_{1/3}\text{Mn}_{1/3}\text{Co}_{1/3}\text{O}_2$ cathode material for Li-ion batteries, *Electrochim. Acta.* 107 (2013) 133–138.
- [109] R. Pitchai, V. Thavasi, S.G. Mhaisalkar, S. Ramakrishna, Nanostructured cathode materials: a key for better performance in Li-ion batteries, *J. Mater. Chem.* 21 (2011) 11040–11051.
- [110] M.M. Thackeray, Manganese oxides for lithium batteries, *Progress in Solid State Chem.* 25 (1997) 1–71.
- [111] Y. Tong, M. Shao, Y. Ni, G. Qian, Y. Ye, P. Zhang, Low temperature route to nanocrystalline LiMn_2O_4 spinel, *Mater. Lett.* 60 (2006) 2578–2581.

- [112] S. Vivekanandhan, M. Venkateswarlu, N. Satyanarayana, P. Suresh, D.H. Nagaraju, N. Munichandraiah, Effect of calcining temperature on the electrochemical performance of nanocrystalline LiMn_2O_4 powders prepared by polyethylene glycol (PEG-400) assisted Pechini process, *Mater. Lett.* 60 (2006) 3212–3216.
- [113] X. Wang, X. Chen, L. Gao, H. Zheng, M. Ji, T. Shen, Z. Zhang, Citric acid-assisted sol–gel synthesis of nanocrystalline LiMn_2O_4 spinel as cathode material, *Journal of Crystal Growth.* 256 (2003) 123–127.
- [114] C.-Z. Lu, G.T.-K. Fey, Nanocrystalline and long cycling LiMn_2O_4 cathode material derived by a solution combustion method for lithium ion batteries, *J. Phys. Chem. Solids.* 67 (2006) 756–761.
- [115] S.-H. Park, S.-T. Myung, S.-W. Oh, C.S. Yoon, Y.-K. Sun, Ultrasonic spray pyrolysis of nano crystalline spinel LiMn_2O_4 showing good cycling performance in the 3V range, *Electrochim. Acta.* 51 (2006) 4089–4095.
- [116] D. Capsoni, M. Bini, G. Chiodelli, V. Massarotti, C.B. Azzoni, M.C. Mozzati, A. Comin, Inhibition of Jahn–Teller cooperative distortion in LiMn_2O_4 spinel by transition metal ion doping, *Phys. Chem. Chem. Phys.* 3 (2001) 2162–2166.
- [117] L. Sanchez, J.L. Tirado, Synthesis and Electrochemical Characterization of a New Li-Co-Mn-O Spinel Phase for Rechargeable Lithium Batteries, *J. Electrochem. Soc.* 144 (1997) 1939–1943.
- [118] L. Lu, Development of Nanostructure Materials and Architecture for High Performance Li-rechargeable Batteries with Ultrafast Charge Rate, National University of Singapore Dept. of Mechanical Engineering, 2011, 22.
- [119] J.M. Tarascon, W.R. McKinnon, F. Coowar, T.N. Bowmer, G. Amatucci, D. Guyomard, Synthesis Conditions and Oxygen Stoichiometry Effects on Li Insertion into the Spinel LiMn_2O_4 , *J. Electrochem. Soc.* 141 (1994) 1421–1431.
- [120] A. Yamada, Lattice instability in $\text{Li}(\text{Li}_x\text{Mn}_{2-x})\text{O}_4$, *Journal of Solid State Chemistry.* 122 (1996) 160–165.
- [121] A.D. Robertson, S.H. Lu, W.F. Averill, W.F. Howard, M^{3+} -Modified LiMn_2O_4 Spinel Intercalation Cathodes I. Admetal Effects on Morphology and Electrochemical Performance, *J. Electrochem. Soc.* 144 (1997) 3500–3505.
- [122] R.J. Gummow, A. De Kock, M.M. Thackeray, Improved capacity retention in rechargeable 4 V lithium/lithium-manganese oxide (spinel) cells, *Solid State Ionics.* 69 (1994) 59–67.

- [123] G.G. Amatucci, C.N. Schmutz, A. Blyr, C. Sigala, A.S. Gozdz, D. Larcher, J.M. Tarascon, Materials' effects on the elevated and room temperature performance of CLiMn_2O_4 Li-ion batteries, *J. Power Sources*. 69 (1997) 11–25.
- [124] L.-X. Yuan, Z.-H. Wang, W.-X. Zhang, X.-L. Hu, J.-T. Chen, Y.-H. Huang, J.B. Goodenough, Development and challenges of LiFePO_4 cathode material for lithium-ion batteries, *Energy Environ. Sci.* 4 (2011) 269–284.
- [125] Y. Xia, Y. Zhou, M. Yoshio, Capacity Fading on Cycling of 4 V Li/LiMn₂O₄ Cells, *J. Electrochem. Soc.* 144 (1997) 2593–2600.
- [126] Y. Xia, Q. Zhang, H. Wang, H. Nakamura, H. Noguchi, M. Yoshio, Improved cycling performance of oxygen-stoichiometric spinel $\text{Li}_{1+x}\text{Al}_y\text{Mn}_{2-x-y}\text{O}_{4+\delta}$ at elevated temperature, *Electrochim. Acta.* 52 (2007) 4708–4714.
- [127] I.-S. Jeong, J.-U. Kim, H.-B. Gu, Electrochemical properties of $\text{LiMg}_y\text{Mn}_{2-y}\text{O}_4$ spinel phases for rechargeable lithium batteries, *J. Power Sources*. 102 (2001) 55–59.
- [128] Y.-K. Sun, K.-J. Hong, J. Prakash, K. Amine, Electrochemical performance of nano-sized ZnO-coated $\text{LiNi}_{0.5}\text{Mn}_{1.5}\text{O}_4$ spinel as 5 V materials at elevated temperatures, *Electrochem. Commun.* 4 (2002) 344–348.
- [129] Y. Ein-Eli, J.T. Vaughey, M.M. Thackeray, S. Mukerjee, X.Q. Yang, J. McBreen, $\text{LiNi}_x\text{Cu}_{0.5-x}\text{Mn}_{1.5}\text{O}_4$ Spinel Electrodes, Superior High-Potential Cathode Materials for Li Batteries: I. Electrochemical and Structural Studies, *J. Electrochem. Soc.* 146 (1999) 908–913.
- [130] J. Molenda, J. Marzec, K. Świerczek, D. Pałubiak, W. Ojczyk, M. Ziernicki, The effect of 3d substitutions in the manganese sublattice on the electrical and electrochemical properties of manganese spinel, *Solid State Ionics*. 175 (2004) 297–304.
- [131] T.-F. Yi, Y.-R. Zhu, X.-D. Zhu, J. Shu, C.-B. Yue, A.-N. Zhou, A review of recent developments in the surface modification of LiMn_2O_4 as cathode material of power lithium-ion battery, *Ionics*. 15 (2009) 779.
- [132] T. Ohzuku, S. Takeda, M. Iwanaga, Solid-state redox potentials for $\text{Li}[\text{Me}_{1/2}\text{Mn}_{3/2}]\text{O}_4$ (Me: 3d-transition metal) having spinel-framework structures: a series of 5 volt materials for advanced lithium-ion batteries, *J. Power Sources*. 81 (1999) 90–94.
- [133] J. Choa, M.M. Thackeray, Structural Changes of LiMn_2O_4 Spinel Electrodes during Electrochemical Cycling, *J. Electrochem. Soc.* 146 (1999) 3577–3581.
- [134] S. Lim, J. Cho, PVP-functionalized nanometre scale metal oxide coatings for cathode materials: successful application to LiMn_2O_4 spinel nanoparticles, *Chem. Commun.* (2008) 4472–4474.

- [135] J.S. Gnanaraj, V.G. Pol, A. Gedanken, D. Aurbach, Improving the high-temperature performance of LiMn_2O_4 spinel electrodes by coating the active mass with MgO via a sonochemical method, *Electrochem. Commun.* 5 (2003) 940–945.
- [136] H.-W. Ha, N.J. Yun, K. Kim, Improvement of electrochemical stability of LiMn_2O_4 by CeO_2 coating for lithium-ion batteries, *Electrochim. Acta.* 52 (2007) 3236–3241.
- [137] D. Liu, X. Liu, Z. He, Surface modification by ZnO coating for improving the elevated temperature performance of LiMn_2O_4 , *J. Alloy Compd.* 436 (2007) 387–391.
- [138] J.-S. Kim, C.S. Johnson, J.T. Vaughey, S.A. Hackney, K.A. Walz, W.A. Zeltner, M.A. Anderson, M.M. Thackeray, The Electrochemical Stability of Spinel Electrodes Coated with ZrO_2 , Al_2O_3 , and SiO_2 from Colloidal Suspensions, *J. Electrochem. Soc.* 151 (2004) A1755–A1761.
- [139] S.-W. Lee, K.-S. Kim, H.-S. Moon, H.-J. Kim, B.-W. Cho, W.-I. Cho, J.-B. Ju, J.-W. Park, Electrochemical characteristics of Al_2O_3 -coated lithium manganese spinel as a cathode material for a lithium secondary battery, *J. Power Sources.* 126 (2004) 150–155.
- [140] Y.-M. Lin, H.-C. Wu, Y.-C. Yen, Z.-Z. Guo, M.-H. Yang, H.-M. Chen, H.-S. Sheu, N.-L. Wu, Enhanced high-rate cycling stability of LiMn_2O_4 cathode by ZrO_2 coating for Li-ion battery, *J. Electrochem. Soc.* 152 (2005) A1526–A1532.
- [141] Z. Yang, W. Yang, D.G. Evans, Y. Zhao, X. Wei, The effect of a Co–Al mixed metal oxide coating on the elevated temperature performance of a LiMn_2O_4 cathode material, *J. Power Sources.* 189 (2009) 1147–1153.
- [142] Y.-K. Sun, C.S. Yoon, I.-H. Oh, Surface structural change of ZnO -coated $\text{LiNi}_{0.5}\text{Mn}_{1.5}\text{O}_4$ spinel as 5 V cathode materials at elevated temperatures, *Electrochim. Acta.* 48 (2003) 503–506.
- [143] Y. Fan, J. Wang, Z. Tang, W. He, J. Zhang, Effects of the nanostructured SiO_2 coating on the performance of $\text{LiNi}_{0.5}\text{Mn}_{1.5}\text{O}_4$ cathode materials for high-voltage Li-ion batteries, *Electrochim. Acta.* 52 (2007) 3870–3875.
- [144] J. Liu, A. Manthiram, Improved electrochemical performance of the 5 V spinel cathode $\text{LiMn}_{1.5}\text{Ni}_{0.42}\text{Zn}_{0.08}\text{O}_4$ by surface modification, *J. Electrochem. Soc.* 156 (2009) A66–A72.
- [145] T.-F. Yi, C.-Y. Li, Y.-R. Zhu, J. Shu, R.-S. Zhu, Comparison of structure and electrochemical properties for 5 V $\text{LiNi}_{0.5}\text{Mn}_{1.5}\text{O}_4$ and $\text{LiNi}_{0.4}\text{Cr}_{0.2}\text{Mn}_{1.4}\text{O}_4$ cathode materials, *J Solid State Electrochem.* 13 (2009) 913.
- [146] M. Akhlouch, J.M. Amarilla, R.M. Rojas, I. Saadoune, J.M. Rojo, Sub-micrometric $\text{LiCr}_{0.2}\text{Ni}_{0.4}\text{Mn}_{1.4}\text{O}_4$ spinel as 5V-cathode material exhibiting huge rate capability at 25 and 55° C, *Electrochem Commun.* 12 (2010) 548–552.

- [147] J. Liu, A. Manthiram, Understanding the improved electrochemical performances of Fe-substituted 5 V spinel cathode $\text{LiMn}_{1.5}\text{Ni}_{0.5}\text{O}_4$, *J Phys Chem C*. 113 (2009) 15073–15079.
- [148] G.Q. Liu, L. Wen, G.Y. Liu, Y.W. Tian, Rate capability of spinel $\text{LiCr}_{0.1}\text{Ni}_{0.4}\text{Mn}_{1.5}\text{O}_4$, *J. Alloy Compd.* 501 (2010) 233–235.
- [149] L.J. Fu, H. Liu, C. Li, Y.P. Wu, E. Rahm, R. Holze, H.Q. Wu, Electrode materials for lithium secondary batteries prepared by sol–gel methods, *Progress Mater Sci.* 50 (2005) 881–928.
- [150] H.Y. Xu, S. Xie, N. Ding, B.L. Liu, Y. Shang, C.H. Chen, Improvement of electrochemical properties of $\text{LiNi}_{0.5}\text{Mn}_{1.5}\text{O}_4$ spinel prepared by radiated polymer gel method, *Electrochim. Acta.* 51 (2006) 4352–4357.
- [151] M.G. Lazarraga, L. Pascual, H. Gadjov, D. Kovacheva, K. Petrov, J.M. Amarilla, R.M. Rojas, M.A. Martin-Luengo, J.M. Rojo, Nanosize $\text{LiNi}_y\text{Mn}_{2-y}\text{O}_4$ ($0 < y \leq 0.5$) spinels synthesized by a sucrose-aided combustion method. Characterization and electrochemical performance, *J. Mater. Chem.* 14 (2004) 1640–1647.
- [152] H.M. Wu, J.P. Tu, X.T. Chen, D.Q. Shi, X.B. Zhao, G.S. Cao, Synthesis and characterization of abundant Ni-doped $\text{LiNi}_x\text{Mn}_{2-x}\text{O}_4$ ($x = 0.1–0.5$) powders by spray-drying method, *Electrochim. Acta.* 51 (2006) 4148–4152.
- [153] D. Kovacheva, B. Markovsky, G. Salitra, Y. Talyosef, M. Gorova, E. Levi, M. Riboch, H.-J. Kim, D. Aurbach, Electrochemical behavior of electrodes comprising micro- and nano-sized particles of $\text{LiNi}_{0.5}\text{Mn}_{1.5}\text{O}_4$: a comparative study, *Electrochim. Acta.* 50 (2005) 5553–5560.
- [154] J.C. Arrebola, A. Caballero, L. Hernan, J. Morales, Expanding the rate capabilities of the $\text{LiNi}_{0.5}\text{Mn}_{1.5}\text{O}_4$ spinel by exploiting the synergistic effect between nano and microparticles, *Electrochem. Solid-State Lett.* 8 (2005) A641–A645.
- [155] L. Wen, Q. Lu, G. Xu, Molten salt synthesis of spherical $\text{LiNi}_{0.5}\text{Mn}_{1.5}\text{O}_4$ cathode materials, *Electrochim. Acta.* 51 (2006) 4388–4392.
- [156] J.-H. Kim, S.-T. Myung, Y.-K. Sun, Molten salt synthesis of $\text{LiNi}_{0.5}\text{Mn}_{1.5}\text{O}_4$ spinel for 5 V class cathode material of Li-ion secondary battery, *Electrochim. Acta.* 49 (2004) 219–227.
- [157] J.M. Amarilla, R.M. Rojas, F. Pico, L. Pascual, K. Petrov, D. Kovacheva, M.G. Lazarraga, I. Lejona, J.M. Rojo, Nanosized $\text{LiM}_y\text{Mn}_{2-y}\text{O}_4$ ($M = \text{Cr, Co and Ni}$) spinels synthesized by a sucrose-aided combustion method: Structural characterization and electrochemical properties, *J. Power Sources.* 174 (2007) 1212–1217.

- [158] A. Caballero, M. Cruz, L. Hernan, M. Melero, J. Morales, E.R. Castellón, Oxygen Deficiency as the Origin of the Disparate Behavior of $\text{LiM}_{0.5}\text{Mn}_{1.5}\text{O}_4$ (M= Ni, Cu) Nanospinels in Lithium Cells, *J. Electrochem. Soc.* 152 (2005) A552–A559.
- [159] J.C. Arrebola, A. Caballero, L. Hernán, J. Morales, Polymer-Mediated Growth of Highly Crystalline Nano- and Micro-Sized $\text{LiNi}_{0.5}\text{Mn}_{1.5}\text{O}_4$ Spinel, *Europ. J. Inorg. Chem.* 2008 (2008) 3295–3302.
- [160] M. Kunduraci, G.G. Amatucci, The effect of particle size and morphology on the rate capability of 4.7 V $\text{LiMn}_{1.5+\delta}\text{Ni}_{0.5-\delta}\text{O}_4$ spinel lithium-ion battery cathodes, *Electrochim. Acta.* 53 (2008) 4193–4199.
- [161] A. Yamada, S.-C. Chung, Crystal Chemistry of the Olivine-Type $\text{Li}(\text{Mn}_y\text{Fe}_{1-y})\text{PO}_4$ and $(\text{Mn}_y\text{Fe}_{1-y})\text{PO}_4$ as Possible 4 V Cathode Materials for Lithium Batteries, *J. Electrochem. Soc.* 148 (2001) A960–A967.
- [162] A. Yamada, Y. Kudo, K.-Y. Liu, Reaction Mechanism of the Olivine-Type $\text{Li}_x(\text{Mn}_{0.6}\text{Fe}_{0.4})\text{PO}_4$ ($0 \leq x \leq 1$), *J. Electrochem. Soc.* 148 (2001) A747–A754.
- [163] A.S. Andersson, J.O. Thomas, The source of first-cycle capacity loss in LiFePO_4 , *J. Power Sources.* 97 (2001) 498–502.
- [164] A.S. Andersson, B. Kalska, L. Häggström, J.O. Thomas, Lithium extraction/insertion in LiFePO_4 : an X-ray diffraction and Mössbauer spectroscopy study, *Solid State Ionics.* 130 (2000) 41–52.
- [165] N. Ravet, Y. Chouinard, J.F. Magnan, S. Besner, M. Gauthier, M. Armand, Electroactivity of natural and synthetic triphylite, *J. Power Sources.* 97 (2001) 503–507.
- [166] N.-H. Kwon, T. Drezen, I. Exnar, I. Teerlinck, M. Isono, M. Graetzel, Enhanced electrochemical performance of mesoparticulate LiMnPO_4 for lithium ion batteries, *Electrochem. and Solid-State Lett.* 9 (2006) A277–A280.
- [167] Z.-H. Wang, L.-X. Yuan, J. Ma, L. Qie, L.-L. Zhang, Y.-H. Huang, Electrochemical performance in Na-incorporated nonstoichiometric LiFePO_4/C composites with controllable impurity phases, *Electrochim. Acta.* 62 (2012) 416–423.
- [168] A. Kulka, A. Braun, T.-W. Huang, A. Wolska, M.T. Klepka, A. Szewczyk, D. Baster, W. Zając, K. Świerczek, J. Molenda, Evidence for Al doping in lithium sublattice of LiFePO_4 , *Solid State Ionics.* 270 (2015) 33–38.
- [169] H. Capacity, S.-M.L. Li, $3\text{Mn}(2-x)/3\text{Ni}x/3\text{Co}x/3$ O₂ Cathodes with Low Irreversible Capacity Loss Wu, Y.; Manthiram, A, *Electrochem. and Solid-State Lett.* 9 (2006) A221–A224.

- [170] X. Fang, J. Li, K. Huang, S. Liu, C. Huang, S. Zhuang, J. Zhang, Synthesis and electrochemical properties of K-doped LiFePO_4/C composite as cathode material for lithium-ion batteries, *Journal of Solid State Electrochemistry*. 16 (2012) 767–773.
- [171] Q. Zhang, S. Wang, Z. Zhou, G. Ma, W. Jiang, X. Guo, S. Zhao, Structural and electrochemical properties of Nd-doped LiFePO_4/C prepared without using inert gas, *Solid State Ionics*. 191 (2011) 40–44.
- [172] M.M. Thackeray, C.S. Johnson, J.T. Vaughey, N. Li, S.A. Hackney, Advances in manganese-oxide ‘composite’ electrodes for lithium-ion batteries, *J. Mater. Chem.* 15 (2005) 2257–2267.
- [173] S.-T. Myung, K. Izumi, S. Komaba, H. Yashiro, H.J. Bang, Y.-K. Sun, N. Kumagai, Functionality of oxide coating for $\text{Li}[\text{Li}_{0.05}\text{Ni}_{0.4}\text{Co}_{0.15}\text{Mn}_{0.4}]\text{O}_2$ as positive electrode materials for lithium-ion secondary batteries, *J. Phys. Chem. C*. 111 (2007) 4061–4067.
- [174] J.M. Zheng, J. Li, Z.R. Zhang, X.J. Guo, Y. Yang, The effects of TiO_2 coating on the electrochemical performance of $\text{Li}[\text{Li}_{0.2}\text{Mn}_{0.54}\text{Ni}_{0.13}\text{Co}_{0.13}]\text{O}_2$ cathode material for lithium-ion battery, *Solid State Ionics*. 179 (2008) 1794–1799.
- [175] Y. Wu, A. Manthiram, High Capacity, Surface-Modified Layered $\text{Li}[\text{Li}_{(1-x)/3}\text{Mn}_{(2-x)/3}\text{Ni}_{x/3}\text{Co}_{x/3}]\text{O}_2$ Cathodes with Low Irreversible Capacity Loss, *Electrochem. Solid-State Lett.* 9 (2006) A221–A224.
- [176] S.J. Shi, J.P. Tu, Y.Y. Tang, X.Y. Liu, Y.Q. Zhang, X.L. Wang, C.D. Gu, Enhanced cycling stability of $\text{Li}[\text{Li}_{0.2}\text{Mn}_{0.54}\text{Ni}_{0.13}\text{Co}_{0.13}]\text{O}_2$ by surface modification of MgO with melting impregnation method, *Electrochim. Acta*. 88 (2013) 671–679.
- [177] Y. Zhao, C. Zhao, H. Feng, Z. Sun, D. Xia, Enhanced electrochemical performance of $\text{Li}[\text{Li}_{0.2}\text{Ni}_{0.2}\text{Mn}_{0.6}]\text{O}_2$ modified by manganese oxide coating for lithium-ion batteries, *Electrochem. Solid-State Letters*. 14 (2011) A1–A5.
- [178] D. Mohanty, J. Li, S.C. Nagpure, D.L. Wood, C. Daniel, Understanding the structure and structural degradation mechanisms in high-voltage, lithium-manganese-rich lithium-ion battery cathode oxides: A review of materials diagnostics, *MRS Energy Sustainability*. 2 (2015).
- [179] M. Guilmard, L. Croguennec, D. Denux, C. Delmas, Thermal Stability of Lithium Nickel Oxide Derivatives. Part I: $\text{Li}_x\text{Ni}_{1.02}\text{O}_2$ and $\text{Li}_x\text{Ni}_{0.89}\text{Al}_{0.16}\text{O}_2$ ($x = 0.50$ and 0.30), *Chemistry of Materials*. 15 (2003) 4476–4483
- [180] S.K. Martha, J. Nanda, Y. Kim, R.R. Unocic, S. Pannala, N.J. Dudney, Solid electrolyte coated high voltage layered-layered lithium-rich composite cathode: $\text{Li}_{1.2}\text{Mn}_{0.525}\text{Ni}_{0.175}\text{Co}_{0.1}\text{O}_2$, *J. Mater. Chem. A*. 1 (2013) 5587–5595.

- [181] Q.Y. Wang, J. Liu, A.V. Murugan, A. Manthiram, High capacity double-layer surface modified $\text{Li}[\text{Li}_{0.2}\text{Mn}_{0.54}\text{Ni}_{0.13}\text{Co}_{0.13}]\text{O}_2$ cathode with improved rate capability, *J. Mater. Chem.* 19 (2009) 4965–4972.
- [182] S.H. Lee, B.K. Koo, J.-C. Kim, K.M. Kim, Effect of $\text{Co}_3(\text{PO}_4)_2$ coating on $\text{Li}[\text{Co}_{0.1}\text{Ni}_{0.15}\text{Li}_{0.2}\text{Mn}_{0.55}]\text{O}_2$ cathode material for lithium rechargeable batteries, *J. Power Sources.* 184 (2008) 276–283.
- [183] B. Liu, Q. Zhang, S. He, Y. Sato, J. Zheng, D. Li, Improved electrochemical properties of $\text{Li}_{1.2}\text{Ni}_{0.18}\text{Mn}_{0.59}\text{Co}_{0.03}\text{O}_2$ by surface modification with LiCoPO_4 , *Electrochim. Acta.* 56 (2011) 6748–6751.
- [184] Q.Q. Qiao, H.Z. Zhang, G.R. Li, S.H. Ye, C.W. Wang, X.P. Gao, Surface modification of Li-rich layered Li ($\text{Li}_{0.17}\text{Ni}_{0.25}\text{Mn}_{0.58}$) O_2 oxide with Li–Mn– PO_4 as the cathode for lithium-ion batteries, *J. Mater. Chem. A.* 1 (2013) 5262–5268.
- [185] S.-H. Kang, M.M. Thackeray, Enhancing the rate capability of high capacity $x\text{Li}_2\text{MnO}_3(1-x)\text{LiMO}_2$ (M= Mn, Ni, Co) electrodes by Li–Ni– PO_4 treatment, *Electrochem. Commun.* 11 (2009) 748–751.
- [186] Y.W. Denis, K. Yanagida, H. Nakamura, Surface modification of Li-excess Mn-based cathode materials, *J. Electrochem. Soc.* 157 (2010) A1177–A1182.
- [187] J.-S. Kim, C.S. Johnson, J.T. Vaughey, M.M. Thackeray, Pre-conditioned layered electrodes for lithium batteries, *J. Power Sources.* 153 (2006) 258–264.
- [188] J. Zheng, S. Deng, Z. Shi, H. Xu, H. Xu, Y. Deng, Z. Zhang, G. Chen, The effects of persulfate treatment on the electrochemical properties of Li [$\text{Li}_{0.2}\text{Mn}_{0.54}\text{Ni}_{0.13}\text{Co}_{0.13}$] O_2 cathode material, *J. Power Sources.* 221 (2013) 108–113.
- [189] Q. Liu, K. Du, G. Hu, Z. Peng, Y. Cao, W. Liu, Characterization of $\text{LiNi}_{0.9}\text{Co}_{0.05}[\text{Mn}_{1/2}\text{Mg}_{1/2}]_{0.05}\text{O}_2$ solid solution for secondary lithium ion batteries, *Solid State Ionics.* 227 (2012) 23–29.
- [190] L.F. Jiao, M. Zhang, H.T. Yuan, M. Zhao, J. Guo, W. Wang, X. Di Zhou, Y.M. Wang, Effect of Cr doping on the structural, electrochemical properties of $\text{Li}[\text{Li}_{0.2}\text{Ni}_{0.2-x/2}\text{Mn}_{0.6-x/2}\text{Cr}_x]\text{O}_2$ ($x= 0, 0.02, 0.04, 0.06, 0.08$) as cathode materials for lithium secondary batteries, *J. Power Sources.* 167 (2007) 178–184.
- [191] S.H. Park, Y.-K. Sun, Synthesis and electrochemical properties of layered $\text{Li}[\text{Li}_{0.15}\text{Ni}_{(0.275-x/2)}\text{Al}_x\text{Mn}_{(0.575-x/2)}]\text{O}_2$ materials prepared by sol–gel method, *J. Power Sources.* 119 (2003) 161–165.
- [192] M. Tabuchi, Y. Nabeshima, T. Takeuchi, H. Kageyama, J. Imaizumi, H. Shibuya, J. Akimoto, Synthesis of high-capacity Ti-and/or Fe-substituted Li_2MnO_3 positive

- electrode materials with high initial cycle efficiency by application of the carbothermal reduction method, *J. Power Sources*. 221 (2013) 427–434.
- [193] K. Shah, N. Balsara, S. Banerjee, M. Chintapalli, A.P. Cocco, W.K.S. Chiu, I. Lahiri, S. Martha, A. Mistry, P.P. Mukherjee, State of the Art and Future Research Needs for Multiscale Analysis of Li-Ion Cells, *J. Electrochem. Energy Convers. Storage*. 14 (2017) 020801.
- [194] S.-H. Kang, K. Amine, Layered $\text{Li}(\text{Li}_{0.2}\text{Ni}_{0.15+0.5z}\text{Co}_{0.10}\text{Mn}_{0.55-0.5z})\text{O}_{2-z}\text{F}_z$ cathode materials for Li-ion secondary batteries, *J. Power Sources*. 146 (2005) 654–657.
- [195] B. Song, M.O. Lai, L. Lu, Influence of Ru substitution on Li-rich 0.55 $\text{Li}_2\text{MnO}_{30.45}\text{LiNi}_{1/3}\text{Co}_{1/3}\text{Mn}_{1/3}\text{O}_2$ cathode for Li-ion batteries, *Electrochim. Acta*. 80 (2012) 187–195.
- [196] O. Sha, Z. Tang, S. Wang, W. Yuan, Z. Qiao, Q. Xu, L. Ma, The multi-substituted $\text{LiNi}_{0.475}\text{Al}_{0.01}\text{Cr}_{0.04}\text{Mn}_{1.475}\text{O}_{3.95}\text{F}_{0.05}$ cathode material with excellent rate capability and cycle life, *Electrochim. Acta*. 77 (2012) 250–255.
- [197] J.P. Zheng, R.Y. Liang, M. Hendrickson, E.J. Plichta, Theoretical energy density of Li–air batteries, *J. Electrochem. Soc.* 155 (2008) A432–A437.
- [198] B. Kumar, J. Kumar, R. Leese, J.P. Fellner, S.J. Rodrigues, K.M. Abraham, A solid-state, rechargeable, long cycle life lithium–air battery, *J. Electrochem. Soc.* 157 (2010) A50–A54.
- [199] X. Xu, Z. Wen, J. Wu, X. Yang, Preparation and electrical properties of NASICON-type structured $\text{Li}_{1.4}\text{Al}_{0.4}\text{Ti}_{1.6}(\text{PO}_4)_3$ glass-ceramics by the citric acid-assisted sol–gel method, *Solid State Ionics*. 178 (2007) 29–34.
- [200] J.B. Bates, N.J. Dudney, B. Neudecker, A. Ueda, C.D. Evans, Thin-film lithium and lithium-ion batteries, *Solid State Ionics*. 135 (2000) 33–45.
- [201] J.R. Dahn, T. Zheng, Y. Liu, J.S. Xue, Mechanisms for lithium insertion in carbonaceous materials, *SCIENCE-NEW YORK THEN WASHINGTON*-. (1995) 590–590.
- [202] K. Sato, M. Noguchi, A. Demachi, N. Oki, M. Endo, A mechanism of lithium storage in disordered carbons, *Sci*. 264 (1994) 556–559.
- [203] H. Momose, H. Honbo, S. Takeuchi, K. Nishimura, T. Horiba, Y. Muranaka, Y. Kozono, H. Miyadera, X-ray photoelectron spectroscopy analyses of lithium intercalation and alloying reactions on graphite electrodes, *J. Power Sources*. 68 (1997) 208–211.

- [204] K. Nishimura, H. Honbo, S. Takeuchi, T. Horiba, M. Oda, M. Koseki, Y. Muranaka, Y. Kozono, H. Miyadera, Design and performance of 10 Wh rechargeable lithium batteries, *J. Power Sources*. 68 (1997) 436–439.
- [205] T. Takamura, K. Sumiya, J. Suzuki, C. Yamada, K. Sekine, Enhancement of Li doping/undoping reaction rate of carbonaceous materials by coating with an evaporated metal film, *J. Power Sources*. 81 (1999) 368–372.
- [206] Y. Wang, J.Y. Lee, Microwave-assisted synthesis of SnO₂–graphite nanocomposites for Li-ion battery applications, *J. Power Sources*. 144 (2005) 220–225.
- [207] B. Veeraraghavan, A. Durairajan, B. Haran, B. Popov, R. Guidotti, Study of Sn-coated graphite as anode material for secondary lithium-ion batteries, *J. Electrochem. Society*. 149 (2002) A675–A681.
- [208] Kim, Sung-Soo, Yoshihiro Kadoma, Hiromasa Ikuta, Yoshiharu Uchimoto, and Masataka Wakihara. Electrochemical performance of natural graphite by surface modification using aluminium, *Electrochem. Solid-State Lett.* 8 (2001): A109-A112.
- [209] H. Huang, E.M. Kelder, J. Schoonman, Graphite–metal oxide composites as anode for Li-ion batteries, *J. Power Sources*. 97 (2001) 114–117.
- [210] J.K. Lee, D.H. Ryu, J.B. Ju, Y.G. Shul, B.W. Cho, D. Park, Electrochemical characteristics of graphite coated with tin-oxide and copper by fluidised-bed chemical vapour deposition, *J. Power Sources*. 107 (2002) 90–97.
- [211] S. Kuwabata, N. Tsumura, S. Goda, C.R. Martin, H. Yoneyama, Charge-Discharge Properties of Composite of Synthetic Graphite and Poly (3-n-hexylthiophene) as an Anode Active Material in Rechargeable Lithium-Ion Batteries, *J. Electrochem. Soc.* 145 (1998) 1415–1420.
- [212] B. Veeraraghavan, J. Paul, B. Haran, B. Popov, Study of polypyrrole graphite composite as anode material for secondary lithium-ion batteries, *J. Power Sources*. 109 (2002) 377–387.
- [213] M. Gaberšček, M. Bele, J. Drofenik, R. Dominko, S. Pejovnik, Improved carbon anode properties: pretreatment of particles in polyelectrolyte solution, *J. Power Sources*. 97 (2001) 67–69.
- [214] Fan, Zhuangjun, J. Yan, G. Ning, T. Wei, L. Zhi, F. Wei, Porous graphene networks as high performance anode materials for lithium ion batteries, *Carbon* 60 (2013) 558-561.
- [215] Li, N, Zongping Chen, Wencai Ren, Feng Li, and Hui-Ming Cheng, Flexible graphene-based lithium ion batteries with ultrafast charge and discharge rates. *Proceedings of the National Academy of Sciences* 109, 43 (2012) 17360-17365.

- [216] Oktaviano, H.S., Yamada, K. and Waki, K., Nano-drilled multiwalled carbon nanotubes: characterizations and application for LIB anode materials. *J. Mater. Chem.*, 22 (2012) 25167-25173.
- [217] Zhang, Yanping, T. Chen, J. Wang, G. Min, L. Pan, Z. Song, Z. Sun, W. Zhou, and Jing Zhang, The study of multi-walled carbon nanotubes with different diameter as anodes for lithium-ion batteries, *Appl. Surf. Sci.* 10 (2012) 4729-4732.
- [218] Claye, Agnès S., John E. Fischer, Chad B. Huffman, Andrew G. Rinzler, and Richard E. Smalley, Solid-State Electrochemistry of the Li Single Wall Carbon Nanotube System, *J. Electrochem. Soc.* 8 (2000) 2845-2852.
- [219] B. Gao, C. Bower, J.D. Lorentzen, L. Fleming, A. Kleinhammes, X.P.Tang, L.E. McNeil, Y. Wu, and O. Zhou, Enhanced saturation lithium composition in ball-milled single-walled carbon nanotubes. *Chem. Phys. Lett.* 327 (2000) 69-75.
- [220] G. Wang, X. Shen, J. Yao, J. Park, Graphene nanosheets for enhanced lithium storage in lithium ion batteries, *Carbon.* 47 (2009) 2049–2053.
- [221] E. Buiel, J.R. Dahn, Li-insertion in hard carbon anode materials for Li-ion batteries, *Electrochim. Acta.* 45 (1999) 121–130.
- [222] E. Buiel, J.R. Dahn, Reduction of the Irreversible Capacity in Hard-Carbon Anode Materials Prepared from Sucrose for Li-Ion Batteries, *J. Electrochem. Society.* 145 (1998) 1977–1981.
- [223] Courtney, A. Ian, J. R. Dahn, Electrochemical and in situ X-ray diffraction studies of the reaction of lithium with tin oxide composites, *J. Electrochem. Soc.* 6 (1997) 2045-2052.
- [224] Idota, Yoshio, T. Kubota, A. Matsufuji, Y. Maekawa, T. Miyasaka, Tin-based amorphous oxide: a high-capacity lithium-ion-storage material, *Sci.* 5317 (1997) 1395-1397.
- [225] K. Kravchyk, L. Protesescu, M.I. Bodnarchuk, F. Krumeich, M. Yarema, M. Walter, C. Guntlin, M.V. Kovalenko, Monodisperse and inorganically capped Sn and Sn/SnO₂ nanocrystals for high-performance Li-ion battery anodes, *J. Am. Chem. Soc.* 135 (2013) 4199–4202.
- [226] Zhu, Zhiqiang, S. Wang, J. Du, Q. Jin, T. Zhang, F. Cheng, J. Chen, Ultrasmall Sn nanoparticles embedded in nitrogen-doped porous carbon as high-performance anode for lithium-ion batteries, *Nano Lett.* 1 (2013) 153-157.
- [227] Xu, Yunhua, Q. Liu, Y. Zhu, Y. Liu, A. Langrock, M. R. Zachariah, C. Wang, Uniform nano-Sn/C composite anodes for lithium ion batteries, *Nano Lett.* 2 (2013) 470-474.

- [228] Paek, S.-Min, E. Yoo, I. Honma, Enhanced cyclic performance and lithium storage capacity of SnO₂/graphene nanoporous electrodes with three-dimensionally delaminated flexible structure, *Nano Lett.* 1 (2008) 72-75.
- [229] J.S. Chen, Y.L. Cheah, Y.T. Chen, N. Jayaprakash, S. Madhavi, Y.H. Yang, X.W. Lou, SnO₂ nanoparticles with controlled carbon nanocoating as high-capacity anode materials for lithium-ion batteries, *J. Phys. Chem. C*, 113(47) 20504-20508.
- [230] X.W. Lou, J.S. Chen, P. Chen, L.A. Archer, One-pot synthesis of carbon-coated SnO₂ nanocolloids with improved reversible lithium storage properties, *Chem. Mater.*, 21(2009) 2868-2874.
- [231] C. Xu, J. Sun, L. Gao, Direct growth of monodisperse SnO₂ nanorods on graphene as high capacity anode materials for lithium ion batteries, *Journal of Materials Chemistry*. 22 (2012) 975–979.
- [232] M.-S. Park, G.-X. Wang, Y.-M. Kang, D. Wexler, S.-X. Dou, H.-K. Liu, Preparation and Electrochemical Properties of SnO₂ Nanowires for Application in Lithium-Ion Batteries, *Angew. Chem.* 119 (2007) 764–767.
- [233] L.-L. Xing, Y.-Y. Zhao, J. Zhao, Y.-X. Nie, P. Deng, Q. Wang, X.-Y. Xue, Facile synthesis and lithium storage performance of SnO₂-Co₃O₄ core-shell nanoneedle arrays on copper foil, *J. Alloy. Compd.* 586 (2014) 28–33.
- [234] X.-Y. Xue, B. He, S. Yuan, L.-L. Xing, Z.-H. Chen, C. Ma, SnO₂/WO₃ core-shell nanorods and their high reversible capacity as lithium-ion battery anodes, *Nanotech.* 22 (2011) 395702.
- [235] R. Yu, Z. Liu, F. Pourpoint, A. R. Armstrong, C. P. Grey, P. G. Bruce. Nanoparticulate TiO₂ (B): an anode for lithium-ion batteries, *Angew. Chem.* 9 (2012) 2206-2209.
- [236] F.-F. Cao, X.-L. Wu, S. Xin, Y.-G. Guo, L.-J. Wan, Facile synthesis of mesoporous TiO₂-C nanosphere as an improved anode material for superior high rate 1.5 V rechargeable Li ion batteries containing LiFePO₄-C cathode, *J. Phys. Chem. C*. 114 (2010) 10308–10313.
- [237] R. Sahay, P. Suresh Kumar, V. Aravindan, J. Sundaramurthy, W. Chui Ling, S.G. Mhaisalkar, S. Ramakrishna, S. Madhavi, High aspect ratio electrospun CuO nanofibers as anode material for lithium-ion batteries with superior cycleability, *J Phys. Chem C*. 116 (2012) 18087–18092.
- [238] X. Zhou, J. Zhang, Q. Su, J. Shi, Y. Liu, G. Du, Nanoleaf-on-sheet CuO/graphene composites: microwave-assisted assemble and excellent electrochemical performances for lithium ion batteries, *Electrochim. Acta*, 125 (2014) 615-621.

- [239] J.-H. Jeun, K.-Y. Park, D.-H. Kim, W.-S. Kim, H.-C. Kim, B.-S. Lee, H. Kim, W.-R. Yu, K. Kang, S.-H. Hong, SnO₂@ TiO₂ double-shell nanotubes for a lithium ion battery anode with excellent high rate cyclability, *Nanoscale*. 5 (2013) 8480–8483.
- [240] N. Wang, J. Yue, L. Chen, Y. Qian, J. Yang, Hydrogenated TiO₂ branches coated Mn₃O₄ nanorods as an advanced anode material for lithium ion batteries, *ACS Appl. Mater. Interfaces*. 7 (2015) 10348–10355.
- [241] D.K. McCarty, J.N. Moore, W.A. Marcus, Mineralogy and trace element association in an acid mine drainage iron oxide precipitate; comparison of selective extractions, *Appl. Geochem*. 13 (1998) 165–176.
- [242] J.F. Banfield, D.R. Veblen, Conversion of perovskite to anatase and TiO₂ (B): A TEM study and the use of fundamental building blocks for understanding relationships among the TiO₂ minerals, *Am. Mineralogist*. 77 (1992) 545–557.
- [243] V. Aravindan, Y.-S. Lee, R. Yazami, S. Madhavi, TiO₂ polymorphs in ‘rocking-chair’ Li-ion batteries, *Mater. Today*. 18 (2015) 345–351.
- [244] W.J. Macklin, R.J. Neat, Performance of titanium dioxide-based cathodes in a lithium polymer electrolyte cell, *Solid State Ionics*. 53 (1992) 694–700.
- [245] Y.-S. Hu, L. Kienle, Y.-G. Guo, J. Maier, High lithium electroactivity of nanometer-sized rutile TiO₂, *Adv. Mater*. 18 (2006) 1421–1426.
- [246] D. Wang, D. Choi, Z. Yang, V.V. Viswanathan, Z. Nie, C. Wang, Y. Song, J.-G. Zhang, J. Liu, Synthesis and Li-ion insertion properties of highly crystalline mesoporous rutile TiO₂, *Chem. Mater*. 20 (2008) 3435–3442.
- [247] M. Zhen, X. Guo, G. Gao, Z. Zhou, L. Liu, Rutile TiO₂ nanobundles on reduced graphene oxides as anode materials for Li ion batteries, *Chem. Commun*. 50 (2014) 11915–11918.
- [248] D. Deng, M.G. Kim, J.Y. Lee, J. Cho, Green energy storage materials: nanostructured TiO₂ and Sn-based anodes for lithium-ion batteries, *Energy Envir Sci*. 2 (2009) 818–837.
- [249] P. Tammawat, N. Meethong, Synthesis and characterization of stable and binder-free electrodes of TiO₂ nanofibers for li-ion batteries, *J. Nanomater*. 2013 (2013) 1.
- [250] J.S. Chen, H. Liu, S.Z. Qiao, X.W.D. Lou, Carbon-supported ultra-thin anatase TiO₂ nanosheets for fast reversible lithium storage, *J. Mater. Chem*. 21 (2011) 5687–5692.
- [251] R. Marchand, L. Brohan, M. Tournoux, TiO₂ (B) a new form of titanium dioxide and the potassium octatitanate K₂Ti₈O₁₇, *Mater. Res. Bull*. 15 (1980) 1129–1133.
- [252] A.S. Dalton, A.A. Belak, A. Van der Ven, Thermodynamics of lithium in TiO₂ (B) from first principles, *Chem. Mater*. 24 (2012) 1568–1574.

- [253] J.-Y. Shin, D. Samuelis, J. Maier, Sustained Lithium-Storage Performance of Hierarchical, Nanoporous Anatase TiO₂ at High Rates: Emphasis on Interfacial Storage Phenomena, *Adv. Functional Mater.* 21 (2011) 3464–3472.
- [254] E. Ferg, R.J. Gummow, A. De Kock, M.M. Thackeray, Spinel anodes for lithium-ion batteries, *J. Electrochem. Soc.* 141 (1994) L147–L150.
- [255] T. Ohzuku, A. Ueda, N. Yamamoto, Zero-Strain Insertion Material of Li [Li_{1/3}Ti_{5/3}]O₄ for Rechargeable Lithium Cells, *J. Electrochem. Soc.* 142 (1995) 1431–1435.
- [256] M. Venkateswarlu, C.H. Chen, J.S. Do, C.W. Lin, T.-C. Chou, B.J. Hwang, Electrochemical properties of nano-sized Li₄Ti₅O₁₂ powders synthesized by a sol–gel process and characterized by X-ray absorption spectroscopy, *J. Power Sources.* 146 (2005) 204–208.
- [257] E.M. Sorensen, S.J. Barry, H.-K. Jung, J.M. Rondinelli, J.T. Vaughey, K.R. Poeppelmeier, Three-dimensionally ordered macroporous Li₄Ti₅O₁₂: effect of wall structure on electrochemical properties, *Chem. Mater.* 18 (2006) 482–489.
- [258] Y.-Q. Wang, L. Gu, Y.-G. Guo, H. Li, X.-Q. He, S. Tsukimoto, Y. Ikuhara, L.-J. Wan, Rutile-TiO₂ nanocoating for a high-rate Li₄Ti₅O₁₂ anode of a lithium-ion battery, *J. Am. Chem. Soc.* 134 (2012) 7874–7879.
- [259] S.-W. Han, J.H. Ryu, J. Jeong, D.-H. Yoon, Solid-state synthesis of Li₄Ti₅O₁₂ for high power lithium ion battery applications, *J. Alloy. Compd.* 570 (2013) 144–149.
- [260] S.-L. Chou, J.-Z. Wang, H.-K. Liu, S.-X. Dou, Rapid synthesis of Li₄Ti₅O₁₂ microspheres as anode materials and its binder effect for lithium-ion battery, *J. Phys. Chem. C.* 115 (2011) 16220–16227.
- [261] Y. Hao, Q. Lai, Z. Xu, X. Liu, X. Ji, Synthesis by TEA sol–gel method and electrochemical properties of Li₄Ti₅O₁₂ anode material for lithium-ion battery, *Solid State Ionics.* 176 (2005) 1201–1206.
- [262] J. Li, Y.-L. Jin, X.-G. Zhang, H. Yang, Microwave solid-state synthesis of spinel Li₄Ti₅O₁₂ nanocrystallites as anode material for lithium-ion batteries, *Solid State Ionics.* 178 (2007) 1590–1594.
- [263] Y. Bai, F. Wang, F. Wu, C. Wu, L. Bao, Influence of composite LiCl–KCl molten salt on microstructure and electrochemical performance of spinel Li₄Ti₅O₁₂, *Electrochim. Acta.* 54 (2008) 322–327.
- [264] H. Hayashi, T. Nakamura, T. Ebina, Hydrothermal synthesis of Li₄Ti₅O₁₂ nanoparticles using a supercritical flow reaction system, *J. Ceramic Soc. Japan.* 122 (2014) 78–82.
- [265] H. Luo, L. Shen, K. Rui, H. Li, X. Zhang, Carbon coated Li₄Ti₅O₁₂ nanorods as superior anode material for high rate lithium ion batteries, *J. Alloy. Compd.* 572 (2013) 37–42.

- [266] H.-G. Jung, S.-T. Myung, C.S. Yoon, S.-B. Son, K.H. Oh, K. Amine, B. Scrosati, Y.-K. Sun, Microscale spherical carbon-coated $\text{Li}_4\text{Ti}_5\text{O}_{12}$ as ultra-high power anode material for lithium batteries, *Energy Environ. Sci.* 4 (2011) 1345–1351.
- [267] S. Huang, Z. Wen, X. Zhu, Z. Gu, Preparation and electrochemical performance of Ag doped $\text{Li}_4\text{Ti}_5\text{O}_{12}$, *Electrochem. Commun.* 6 (2004) 1093–1097.
- [268] M. Chen, W. Li, X. Shen, G. Diao, Fabrication of core–shell $\alpha\text{-Fe}_2\text{O}_3@ \text{Li}_4\text{Ti}_5\text{O}_{12}$ composite and its application in the lithium ion batteries, *ACS Appl. Mater. Interfaces.* 6 (2014) 4514–4523.
- [269] J.P. Zhu, G. Yang, J.J. Zhao, Q.S. Wang, H.W. Yang, Synthesis and electrochemical properties of $\text{Li}_4\text{Ti}_5\text{O}_{12}/\text{CuO}$ anode material for Li-ion batteries, In: *Adv. Mater. Res.* 279 (2011) 77–82.
- [270] J. Liu, X. Li, M. Cai, R. Li, X. Sun, Ultrathin atomic layer deposited ZrO_2 coating to enhance the electrochemical performance of $\text{Li}_4\text{Ti}_5\text{O}_{12}$ as an anode material, *Electrochim. Acta.* 93 (2013) 195–201.
- [271] W. Wang, B. Jiang, W. Xiong, Z. Wang, S. Jiao, A nanoparticle Mg-doped $\text{Li}_4\text{Ti}_5\text{O}_{12}$ for high rate lithium-ion batteries, *Electrochim. Acta.* 114 (2013) 198–204.
- [272] H. Wu, S. Chang, X. Liu, L. Yu, G. Wang, D. Cao, Y. Zhang, B. Yang, P. She, Sr-doped $\text{Li}_4\text{Ti}_5\text{O}_{12}$ as the anode material for lithium-ion batteries, *Solid State Ionics.* 232 (2013) 13–18.
- [273] C. Lin, B. Ding, Y. Xin, F. Cheng, M.O. Lai, L. Lu, H. Zhou, Advanced electrochemical performance of $\text{Li}_4\text{Ti}_5\text{O}_{12}$ -based materials for lithium-ion battery: Synergistic effect of doping and compositing, *J. Power Sources.* 248 (2014) 1034–1041.
- [274] W. Xu, X. Chen, W. Wang, D. Choi, F. Ding, J. Zheng, Z. Nie, Y.J. Choi, J.-G. Zhang, Z.G. Yang, Simply AlF₃-treated $\text{Li}_4\text{Ti}_5\text{O}_{12}$ composite anode materials for stable and ultrahigh power lithium-ion batteries, *J. Power Sources.* 236 (2013) 169–174.
- [275] M. Ji, Y. Xu, Z. Zhao, H. Zhang, D. Liu, C. Zhao, X. Qian, C. Zhao, Preparation and electrochemical performance of La³⁺ and F⁻ co-doped $\text{Li}_4\text{Ti}_5\text{O}_{12}$ anode material for lithium-ion batteries, *J. Power Sources.* 263 (2014) 296–303.
- [276] B.A. Boukamp, G.C. Lesh, R.A. Huggins, All-solid lithium electrodes with mixed-conductor matrix, *J. Electrochem. Soc.* 128 (1981) 725–729.
- [277] H. Wu, Y. Cui, Designing nanostructured Si anodes for high energy lithium ion batteries, *Nano Today.* 7 (2012) 414–429.
- [278] L.Y. Beaulieu, K.W. Eberman, R.L. Turner, L.J. Krause, J.R. Dahn, Colossal reversible volume changes in lithium alloys, *Electrochem. Solid-State Lett.* 4 (2001) A137–A140.

- [279] M. Rahman, G. Song, A.I. Bhatt, Y.C. Wong, C. Wen, Nanostructured Silicon Anodes for High-Performance Lithium-Ion Batteries, *Adv. Functional Mater.* 26 (2016) 647–678.
- [280] X.H. Liu, H. Zheng, L. Zhong, S. Huang, K. Karki, L.Q. Zhang, Y. Liu, A. Kushima, W.T. Liang, J.W. Wang, Anisotropic swelling and fracture of silicon nanowires during lithiation, *Nano Lett.* 11 (2011) 3312–3318.
- [281] X.H. Liu, L.Q. Zhang, L. Zhong, Y. Liu, H. Zheng, J.W. Wang, J.-H. Cho, S.A. Dayeh, S.T. Picraux, J.P. Sullivan, Ultrafast electrochemical lithiation of individual Si nanowire anodes, *Nano Lett.* 11 (2011) 2251–2258.
- [282] Z. Wen, G. Lu, S. Mao, H. Kim, S. Cui, K. Yu, X. Huang, P.T. Hurley, O. Mao, J. Chen, Silicon nanotube anode for lithium-ion batteries, *Electrochem. Commun.* 29 (2013) 67–70.
- [283] W. Li, Z. Li, W. Kang, Y. Tang, Z. Zhang, X. Yang, H. Xue, C.-S. Lee, Hollow nanospheres of loosely packed Si/SiO_x nanoparticles encapsulated in carbon shells with enhanced performance as lithium ion battery anodes, *J. Mater. Chem. A.* 2 (2014) 12289–12295.
- [284] B. Peng, F. Cheng, Z. Tao, J. Chen, Lithium transport at silicon thin film: Barrier for high-rate capability anode, *J Chem Phys.* 133 (2010) 034701.
- [285] S. Pal, S.S. Damle, S.H. Patel, M.K. Datta, P.N. Kumta, S. Maiti, Modeling the delamination of amorphous-silicon thin film anode for lithium-ion battery, *J. Power Sources.* 246 (2014) 149–159.
- [286] J. Liang, X. Li, Q. Cheng, Z. Hou, L. Fan, Y. Zhu, Y. Qian, High yield fabrication of hollow vesica-like silicon based on the Kirkendall effect and its application to energy storage, *Nanoscale.* 7 (2015) 3440–3444.
- [287] X.H. Liu, L. Zhong, S. Huang, S.X. Mao, T. Zhu, J.Y. Huang, Size-dependent fracture of silicon nanoparticles during lithiation, *ACS Nano.* 6 (2012) 1522–1531.
- [288] I.-S. Kim, P.N. Kumta, High capacity Si/C nanocomposite anodes for Li-ion batteries, *J. Power Sources.* 136 (2004) 145–149.
- [289] Z.P. Guo, E. Milin, J.Z. Wang, J. Chen, H.-K. Liu, Silicon/disordered carbon nanocomposites for lithium-ion battery anodes, *J. Electrochem. Soc.* 152 (2005) A2211–A2216.
- [290] Y. Liu, K. Hanai, J. Yang, N. Imanishi, A. Hirano, Y. Takeda, Silicon/carbon composites as anode materials for Li-ion batteries, *Electrochem. Solid-State Lett.* 7 (2004) A369–A372.

- [291] K. Hanai, Y. Liu, N. Imanishi, A. Hirano, M. Matsumura, T. Ichikawa, Y. Takeda, Electrochemical studies of the Si-based composites with large capacity and good cycling stability as anode materials for rechargeable lithium ion batteries, *J. Power Sources*. 146 (2005) 156–160.
- [292] G.X. Wang, J.H. Ahn, J. Yao, S. Bewlay, H.K. Liu, Nanostructured Si–C composite anodes for lithium-ion batteries, *Electrochem. Commun.* 6 (2004) 689–692.
- [293] G.X. Wang, J. Yao, H.-K. Liu, Characterization of nanocrystalline Si-MCMB composite anode materials, *Electrochem. Solid-State Lett.* 7 (2004) A250–A253.
- [294] L. Chai, Q. Qu, L. Zhang, M. Shen, L. Zhang, H. Zheng, Chitosan, a new and environmental benign electrode binder for use with graphite anode in lithium-ion batteries, *Electrochim. Acta.* 105 (2013) 378–383.
- [295] X. Wu, Z. Wang, L. Chen, X. Huang, Ag-enhanced SEI formation on Si particles for lithium batteries, *Electrochem. Commun.* 5 (2003) 935–939.
- [296] J.W. Kim, J.H. Ryu, K.T. Lee, S.M. Oh, Improvement of silicon powder negative electrodes by copper electroless deposition for lithium secondary batteries, *J. Power Sources*. 147 (2005) 227–233.
- [297] T. Moon, C. Kim, B. Park, Electrochemical performance of amorphous-silicon thin films for lithium rechargeable batteries, *J. Power Sources*. 155 (2006) 391–394.
- [298] L.B. Chen, J.Y. Xie, H.C. Yu, T.H. Wang, Si–Al thin film anode material with superior cycle performance and rate capability for lithium ion batteries, *Electrochim. Acta.* 53 (2008) 8149–8153.
- [299] Y. Hwa, W.-S. Kim, S.-H. Hong, H.-J. Sohn, High capacity and rate capability of core–shell structured nano-Si/C anode for Li-ion batteries, *Electrochim. Acta.* 71 (2012) 201–205.
- [300] T.H. Hwang, Y.M. Lee, B.-S. Kong, J.-S. Seo, J.W. Choi, Electrospun core–shell fibers for robust silicon nanoparticle-based lithium ion battery anodes, *Nano Lett.* 12 (2012) 802–807.
- [301] Q. Li, J. Chen, L. Fan, X. Kong, Y. Lu, Progress in electrolytes for rechargeable Li-based batteries and beyond, *Green Energy Environ.* 1 (2016) 18–42.
- [302] K. Xu, Nonaqueous liquid electrolytes for lithium-based rechargeable batteries, *Chem. Rev.* 104 (2004) 4303–4418.
- [303] J.R. Croy, A. Abouimrane, Z. Zhang, Next-generation lithium-ion batteries: The promise of near-term advancements, *MRS Bull.* 39 (2014) 407–415.
- [304] P. Roy, S.K. Srivastava, Nanostructured anode materials for lithium ion batteries, *J. Mater. Chem. A.* 3 (2015) 2454–2484.

- [305] L. Yang, B. Ravdel, B.L. Lucht, Electrolyte reactions with the surface of high voltage $\text{LiNi}_{0.5}\text{Mn}_{1.5}\text{O}_4$ cathodes for lithium-ion batteries, *Electrochem. Solid-State Lett.* 13 (2010) A95–A97.
- [306] L. Hu, Z. Zhang, K. Amine, Electrochemical investigation of carbonate-based electrolytes for high voltage lithium-ion cells, *J. Power Sources.* 236 (2013) 175–180.
- [307] Z. Zhang, L. Hu, H. Wu, W. Weng, M. Koh, P.C. Redfern, L.A. Curtiss, K. Amine, Fluorinated electrolytes for 5 V lithium-ion battery chemistry, *Energy Environ. Sci.* 6 (2013) 1806–1810.
- [308] P. Verma, P. Maire, P. Novák, A review of the features and analyses of the solid electrolyte interphase in Li-ion batteries, *Electrochim. Acta.* 55 (2010) 6332–6341.
- [309] A. von Cresce, K. Xu, Electrolyte additive in support of 5 V Li ion chemistry, *J. Electrochem. Soc.* 158 (2011) A337–A342.
- [310] N. Alias, A.A. Mohamad, Advances of aqueous rechargeable lithium-ion battery: A review, *J. Power Sources.* 274 (2015) 237–251.
- [311] C. Wessells, R.A. Huggins, Y. Cui, Recent results on aqueous electrolyte cells, *J. Power Sources.* 196 (2011) 2884–2888.
- [312] W. Li, J.R. Dahn, D.S. Wainwright, Rechargeable lithium batteries with aqueous electrolytes, *Sci.* 264 (1994) 1115–1117.
- [313] W. Li, W.R. McKinnon, J.R. Dahn, Lithium intercalation from aqueous solutions, *J. Electrochem. Soc.* 141 (1994) 2310–2316.
- [314] M. Zhao, B. Zhang, G. Huang, H. Zhang, X. Song, Excellent rate capabilities of $(\text{LiFePO}_4/\text{C})/\text{LiV}_3\text{O}_8$ in an optimized aqueous solution electrolyte, *J. Power Sources.* 232 (2013) 181–186.
- [315] H. Ohno, *Electrochemical aspects of ionic liquids*, John Wiley & Sons, 2005.
- [316] M. Armand, F. Endres, D.R. MacFarlane, H. Ohno, B. Scrosati, Ionic-liquid materials for the electrochemical challenges of the future, *Nat. Mater.* 8 (2009) 621–629.
- [317] J.L. Schaefer, Y. Lu, S.S. Moganty, P. Agarwal, N. Jayaprakash, L.A. Archer, Electrolytes for high-energy lithium batteries, *Appl. Nanosci.* 2 (2012) 91–109.
- [318] J.W. Fergus, Ceramic and polymeric solid electrolytes for lithium-ion batteries, *J. Power Sources.* 195 (2010) 4554–4569.
- [319] Z. Zhu, M. Hong, D. Guo, J. Shi, Z. Tao, J. Chen, All-solid-state lithium organic battery with composite polymer electrolyte and pillar [5] quinone cathode, *J. Am. Chem. Soc.* 136 (2014) 16461–16464.
- [320] J.Y. Song, Y.Y. Wang, C.C. Wan, Review of gel-type polymer electrolytes for lithium-ion batteries, *J. Power Sources.* 77 (1999) 183–197.

- [321] S. Delacroix, F. Sauvage, M. Reynaud, M. Deschamps, S. Bruyère, M. Becuwe, D. Postel, J.-M. Tarascon, A.N. Van Nhien, SiO₂/ionic liquid hybrid nanoparticles for solid-state Lithium ion conduction, *Chem. Mater.* 27 (2015) 7926–7933.
- [322] J.-K. Kim, J. Scheers, T.J. Park, Y. Kim, Superior Ion-Conducting Hybrid Solid Electrolyte for All-Solid-State Batteries, *Chem. Sus. Chem.* 8 (2015) 636–641.
- [323] H.-M. Kao, C.-L. Chen, An Organic–Inorganic Hybrid Electrolyte Derived from Self-Assembly of a Poly (Ethylene Oxide)–Poly (Propylene Oxide)–Poly (Ethylene Oxide) Triblock Copolymer, *Angew. Chem. Int. Ed.* 43 (2004) 980–984.
- [324] Year 2022 Major Goals for Batteries, Office of EERE, Department of Energy, (USA) <https://energy.gov/eere/vehicles/batteries>.
- [325] J.W. Choi, D. Aurbach, Promise and reality of post-lithium-ion batteries with high energy densities, *Nat. Rev. Mater.* 1 (2016) 16013.
- [326] M.M. Thackeray, S.-H. Kang, C.S. Johnson, J.T. Vaughey, R. Benedek, S.A. Hackney, Li₂MnO₃-stabilized LiMO₂ (M= Mn, Ni, Co) electrodes for lithium-ion batteries, *J. Mater. Chem.* 17 (2007) 3112–3125.
- [327] Y. Li, M. Bettge, B. Polzin, Y. Zhu, M. Balasubramanian, D.P. Abraham, Understanding long-term cycling performance of Li_{1.2}Ni_{0.15}Mn_{0.55}Co_{0.1}O₂–Graphite lithium-ion cells, *J. Electrochem. Soc.* 160 (2013) A3006–A3019.
- [328] P. Rozier, J.M. Tarascon, Li-rich layered oxide cathodes for next-generation Li-ion batteries: chances and challenges, *J. Electrochem. Soc.* 162 (2015) A2490–A2499.
- [329] Q. Wang, P. Ping, X. Zhao, G. Chu, J. Sun, C. Chen, Thermal runaway caused fire and explosion of lithium ion battery, *J. Power Sources.* 208 (2012) 210–224.
- [330] P. Verma, P. Maire, P. Novák, A review of the features and analyses of the solid electrolyte interphase in Li-ion batteries, *Electrochim. Acta.* 55 (2010) 6332–6341.

Chapter 2

Effect of Temperature and C rate on “Ragone Plots” of Lithium-Ion Batteries

2.1. Abstract

Lithium-ion batteries operating at high-low temperatures and high C rates pose a technical barrier for operating hybrid and electric vehicles due to substantial reduction in energy and power. This Chapter explains simultaneous effect of temperature and C rate on state-of-health, power and energy density of LIBs. Ragone charts are developed on LIBs based on LiCoO_2 cathode and graphite anode chemistry at various temperatures between -20 and 55 °C, and C rates (C/5-10C). To account for varying power and temperature Ragone isotherms are integrated over the power range yielding a functional Integrated Energy-Power ($\sqrt{\int_P E(P)dP |_{T}}$). The ratio of integrated areas at various temperatures to 25 °C gives the “Energy-Power Index” (EPI) (%). The EPI vs. T profile shows a linear increase between -10 °C and 25 °C then it makes a semi-plateau between 25 °C and 55 °C. Besides, for the optimum performance of LIBs operating at low temperatures, low C-rate application is most preferable.

2.2. Background and Motivation

The LIBs should have high energy density (E.D.) and power density (P.D.) to be used in hybrid and electric vehicles [1-7]. The E.D. is influenced by capacity and voltage of the battery. The E.D. and P.D. are inversely related. An ideal battery should have high E.D. and P.D. and should not be influenced by climatic conditions and the rate at which battery is cycled. The application of LIBs are limited because the electrochemical performance of the batteries are temperature dependent [8-19]. There are different climatic conditions in different parts of world where the temperature is lower or higher than ambient temperature (25 °C) [8-19]. There are many reports which states that operating LIBs at ambient temperature show excellent electrochemical performance compared to lower or higher temperatures [8-19]. Viscosity of carbonate based electrolytes (particularly ethylene carbonate (EC)), changes at low temperatures, leading to sluggish ion transport, promote high concentration polarization, yielding depleted electrolyte areas that could cause higher cell impedances and can lead to formation of EC-rich solid phases [12,15, 19, 20]. Besides, at low temperature polymeric components within the cell tend to become brittle [21]. The active electrodes materials tend to fall apart due to binder. All these factors lead to reduction in cell capacity and lifetime of the battery at low temperatures. At high temperatures, side reactions occur much faster, so battery degrades much earlier. Heating could cause thermal runaway of the cell and lead to flame or explosion [11, 17-18]. The life, energy and power density of LIBs decreases when operated at low or high ambient temperatures. Besides, under high C rate operations, the cell capacity decrease is due to fast local depletion of Li-ions in the electrolyte at the interface of electrode active materials and electrolyte by the EC reaction [19, 20, 22].

In overall, the major factors controlling the nominal energy of a battery are: i) state of health (SOH), ii) temperature, and iii) the drain power. SOH accounts for the ageing of the cell components including electrochemically active materials (anode, cathode, and electrolyte) [23] and inactive materials (separator, metal sheet substrates, electrode binder, additives, gasket, seals etc.) [24]. Ageing adversely affects the lithium storage capability of electrode materials owing to crystal structure degradation

[25] and to inter-particles electrical disconnection [24]. Ageing also decreases the electrolyte conductivity leading to increased overall cell Ohmic resistance [26-29]. SOH is usually determined from the cell' discharge profile at a well-defined temperature and discharge rate. The integration of the discharge curve (voltage vs. time or vs. capacity) gives the energy provided by the cell. The energy of an aged cell is related to that of a fresh under the same discharge rate to yield the SOH (usually given in %).

Besides, temperature plays a major role in the cell energy density and power density. LIB discharge reaction is exothermic in nature (enthalpy variation $\Delta H < 0$) [30]. Therefore, the amount of energy should decrease as temperature increases. On the other hand, the lithium ions diffusion in anode and cathode materials and their mobility in the electrolyte are thermally activated processes. This implies that within the range of the cell' thermal stability the rate of charge and discharge should increase with temperature [31-32]. In general, the temperature dependence of energy has a bell shape starting with an increase up to a maximum and then decreases with temperature [33].

The charge and discharge rates also play a major role in the cell's performance [34-35]. In fact, by increasing the rate, increases the anode and cathode polarization together with the Ohmic effect. Accordingly, with higher current rates the charge and discharge voltage limits are reached faster resulting in cell not being fully charged and fully discharged. This reduces the energy density and the charge-discharge cycle coulombic and energy efficiency. There is also a Joule effect which increases with the charge and discharge rate and at low temperatures leading to cell' heating [36].

Hence, there is an intense need to understand the change in electrochemical performance of the LIBs with change in temperature and rate so that we can find the minimum threshold temperature and rate for optimized performance of the battery. Moreover, we can find the temperature where the performance is poor which helps in taking proper precautions for normal running of battery.

The energy vs. power "Ragone plots" [37-38] are convenient charts for comparing the energy and power densities of various energy storage devices and predicting the energy output under a well-defined power drain [39]. Ragone plots are

usually achieved by discharging a fully charged cell (or battery pack) under a constant power and by integrating the voltage over the discharge capacity (Ah) to get energy. The power (P) and energy (E) are related to the total mass or volume of the battery (W/kg or W/L and Wh/kg or Wh/L, respectively), which makes it possible to compare different battery systems as E vs. P or P vs. E charts.

In this chapter, we explain the change of energy and power densities of real lithium ion cells with change in temperature and C-rate by using Ragone plots [37-38]. In this study, lithium ion cells based on LiCoO₂ cathode and graphite anode initially fully charged at the ambient temperature (~25 °C) are discharged isothermally between -20 °C and 55 °C at different C-rates (C/5 to 10C). This enables Ragone plots to be achieved at different temperatures. To account for temperatures and rates variables we introduce a new metrics; the Power Energy Index (PEI). PEI (in %) is defined as the ratio of the root squared integrated area under the Ragone profile achieved at temperature T vs. the same at 25 °C. The PEI vs. T profile shows a linear increase and semi-plateau. This feature is discussed in terms of trade-off between temperature effects on the thermodynamics and the kinetics of LIB.

2.3. Experimental

2.3.1. Structural and physical characterizations of electrode materials

The Powder XRD measurements were performed by using an X'Pert Pro diffractometer (The Netherlands) (reflection θ - θ geometry, Cu K α radiation, receiving slit of 0.2 mm, scintillation counter, 30 mA, 40 kV). The diffraction data were collected at 0.02 step widths over a 2θ range from 10 to 70°. The surface morphologies of the composite powders were further measured by scanning electron microscope (Carle Zeiss Supra 40VP field emission scanning electron microscope) and compositions of cathodes by energy dispersive analysis of X-rays (EDAX) systems from Oxford instruments (UK).

2.3.2. Electrochemical characterizations

Two batches of six identical 700 mAh commercial lithium-ion cylindrical cells, comprised of graphite anode and LiCoO₂ cathode are used for testing (as shown in Fig. 2.1) in the present study. The dimensions of cylindrical lithium ion cells are 4.4

cm (length) x 1.25 cm (diameter), having average weight of 12.125 g. The nominal voltage and capacity of cylindrical cells are 3.7 V and 700 mAh, respectively. The lithium ion cells are cycled between 2.5 V to 4.2 V at different temperatures (-20 °C, -10 °C, 0 °C, 10 °C, 25 °C, 35 °C, 45 °C and 55 °C) by using an environment chamber (Weiss Technik, UK). Each lithium ion cells were cycled at a particular C rate (C/5, C/2, 1C, 2C, 5C and 10C) at varying temperatures (mentioned above) using Arbin battery cycler (Arbin BT2000 – Battery Test Equipment, USA). Charging was carried out using CC-CV protocols till the current decreases to C/25 followed by discharging at CC. The obtained data are plotted by using Origin software. The energy density and power density are derived from voltage vs. capacity curves which are shown pictorially. The schematic of experimental part is shown in Fig. 2.1 for better understanding.



Fig. 2.1: Photograph of 700 mAh lithium ion cells used for electrochemical testing at different C rates and different temperatures

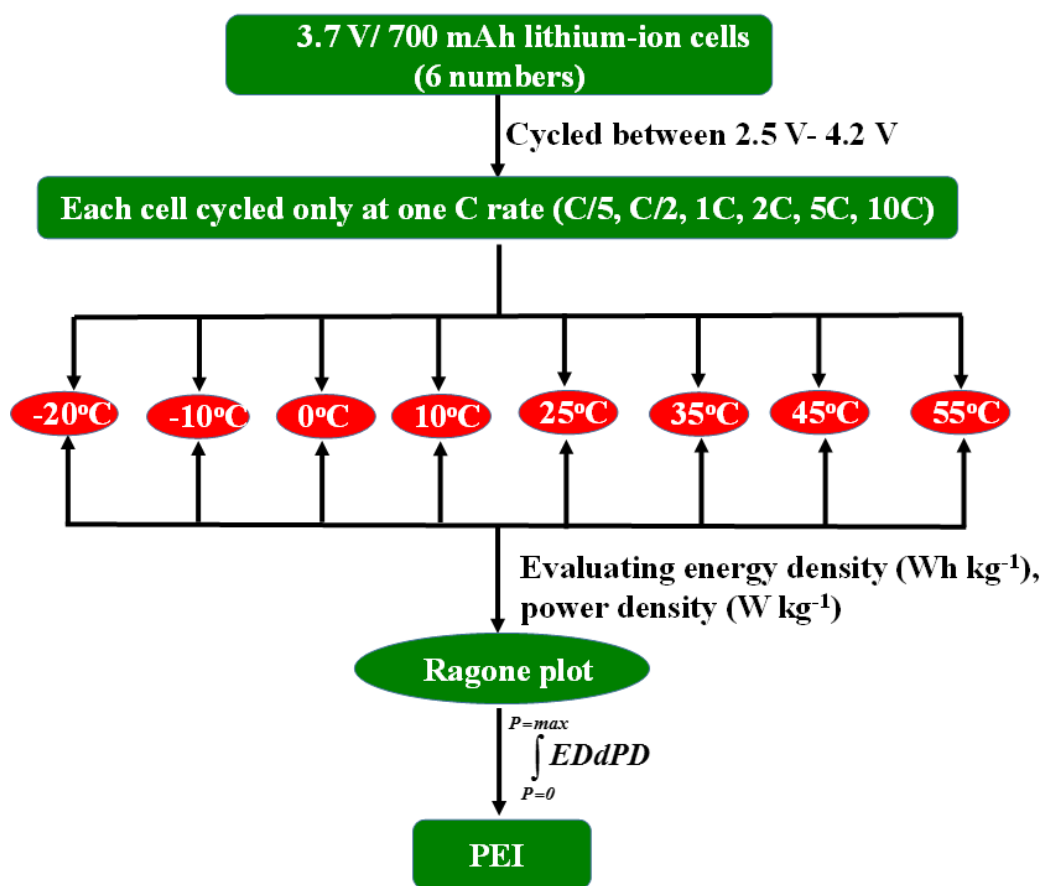


Fig. 2.2: Schematic of the experimental of 3.7V/ 700 mAh lithium-ion cells cycled at different C rates and different temperatures for calculating integrated energy density and power density

2.4. Results and Discussion

2.4.1. Electrode materials characterization

In order to know the exact chemistry of the electrodes used in lithium ion cells, the cells were disassembled, materials are collected by washing several times with dimethyl carbonate solution, dried and structural, physical properties of the electrodes are determined by XRD, SEM and EDAX. Fig. 2.3(a) shows XRD patterns of the LiCoO_2 layered materials, indexed by a hexagonal lattice structure of $\alpha\text{-NaFeO}_2$, space group 166, $R\bar{3}m$. XRD results confirms no impurities in the cathode material. The SEM image presented in Fig. 2.3(b-c) indicates LiCoO_2 have multifaceted morphologies having particle sizes in the range of 1 μm . Small particles are belonging to the additives such as carbon black and polyvinylidene fluoride binder. Elemental analysis of cathode by EDAX (Fig. 2.3(c)) shows that it has consistent atomic % of

cobalt and oxygen corresponding to LiCoO_2 . The XRD pattern shown in Fig. 2.3(d) shows a characteristic (002) peak at $2\theta = 26.7^\circ$ corresponds to graphite.

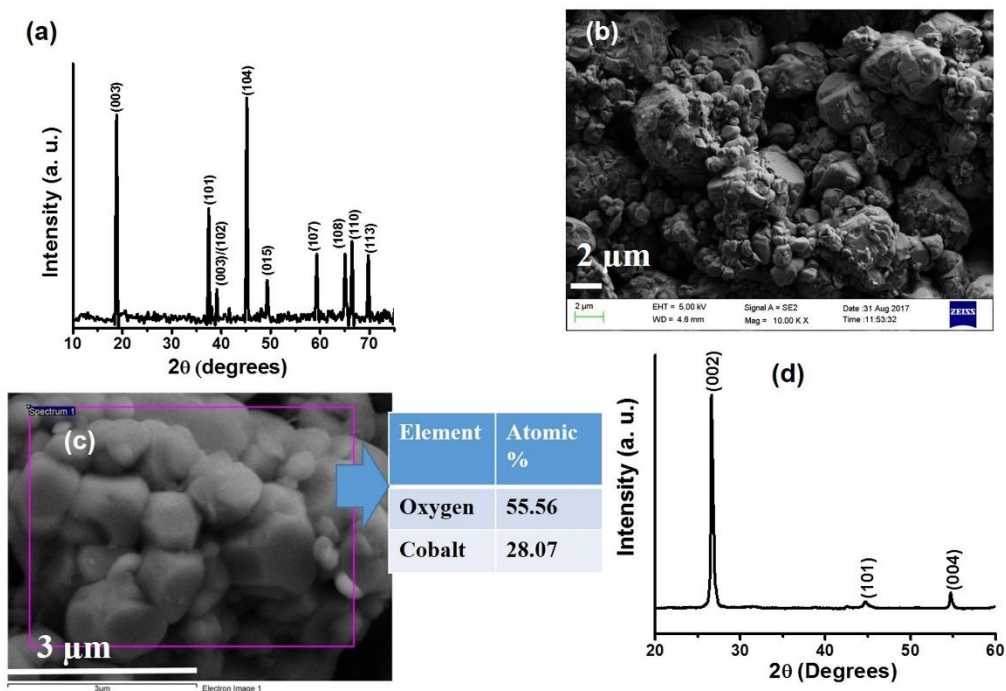


Fig. 2. 3: (a) XRD patterns, (b) SEM image, (c) EDAX analysis of composite LiCoO_2 cathode; and (d) XRD patterns of graphite anode

2.4.2. Isothermal discharge profiles

The voltage vs. discharge capacity profiles at different C rates and at same temperatures between -20 and $+55^\circ\text{C}$ are shown in Fig. 2.4(a-h) and discharge capacity values are presented in Table 2.1. From Fig. 2.4(a-h) and discharge capacity values presented in Table 1 clearly indicates that similar capacities close to 700 mAh are obtained at low ($C/5$) to high C rates of $2C$ between 55 and -10°C (highlighted in Table 2.1). However, the energy density and power densities are not same at all rates and temperatures. This clearly indicates the electrochemical performance of lithium

ion cells are rate and temperature limited. There is voltage decay or voltage dip similar to coup-de-fouet that observed in lead-acid batteries at high C rates and/or all low temperatures result in decrease in energy and power density. A voltage delay is observed at the beginning of discharge as temperature decreases and rate increases such as at 0 °C, 10C-rate, -10 °C, 5C and 10C and at -20 °C almost all C-rates. A voltage delay at early discharge may be due to cell' polarization due to sluggish electrode kinetics and lithium ion mobility in the electrolyte. Due to higher Ohmic and ionic resistances temperature increases locally which affects the kinetics therefore, reducing the cell's overpotential, which in turn converts to enhance discharge voltage. At low temperature of -20 °C, the cells perform poorly at C/5, C/2 and high rates of 5C and 10C. At low temperature of -20 °C, cells have slow Li ion diffusion in anode [40-41] and cathode [42-43] and to lower electrolyte conductivity which lead to initial voltage dip. The increase in capacities at moderates C rates of 1C and 2C at -20 °C, after coup-de-fouet, could be due to the Joule heating. At high C rates of 5C and 10 C at -20 °C, the coup-de-fouet phenomena is not observed as the voltage drops below cut-off voltage of 2.5 V in fraction of seconds. Consequently the cells do not deliver any capacity at high C rates of 5C and 10 C at -20 °C.

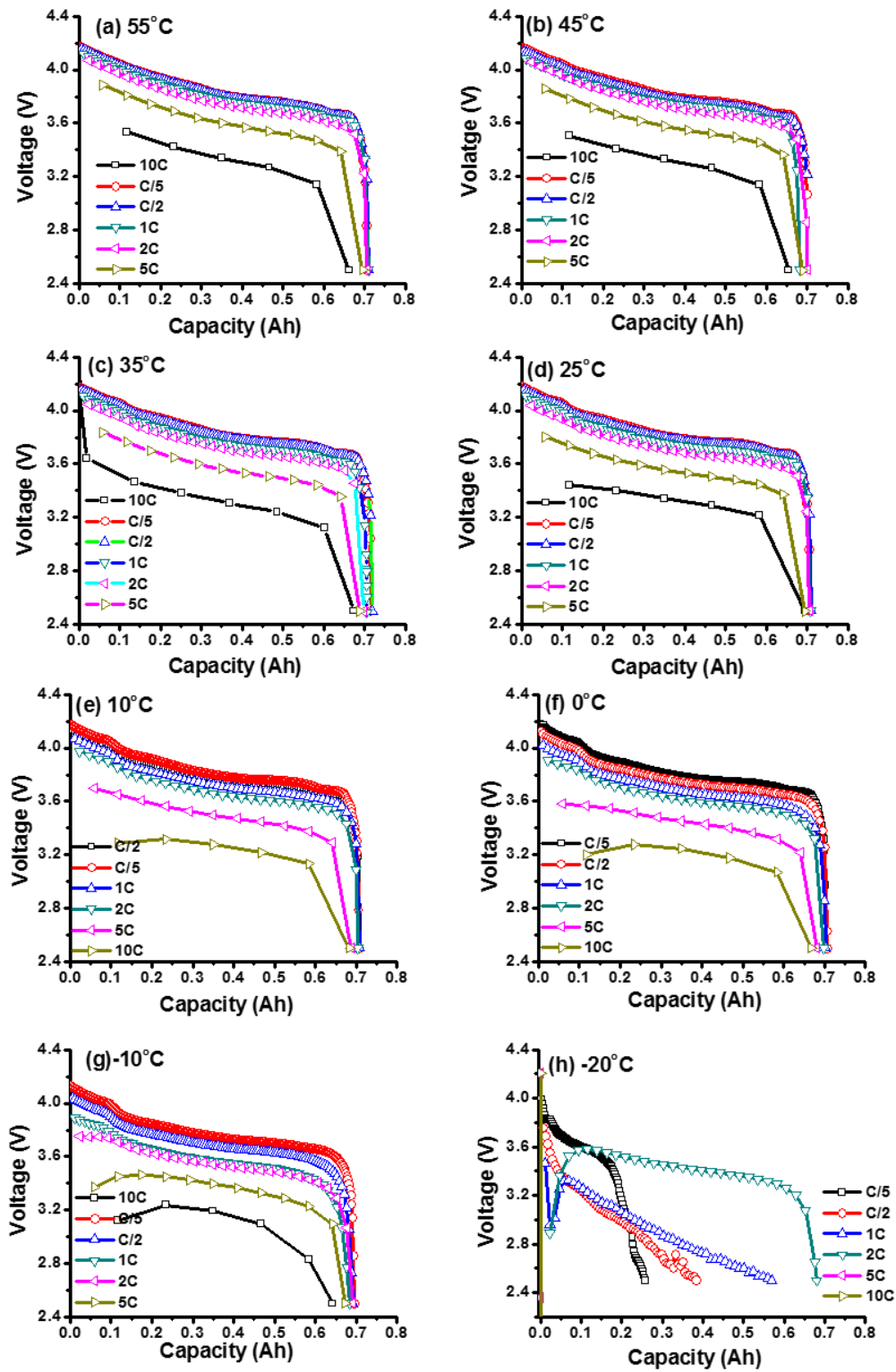


Fig. 2.4: The voltage vs. discharge capacity profiles for lithium ion cells cycled at different C rates (as indicated), at same temperatures (a) 55 °C, (b) 45 °C, (c) 35 °C, (d) 25 °C, (e) 10 °C, (f) 0 °C, (g) -10 °C, and (h) -20 °C

Table 2.1: Summary of discharge capacities for lithium ion cells cycled at different C rates (as indicated), at same temperatures (55 °C, 45 °C, 35 °C, 25 °C, 10 °C, 0 °C, -10 °C and -20 °C

Temperature (°C) →	55	45	35	25	10	0	-10	-20
Rate ↓	Capacity (Ah)							
C/5	0.704	0.705	0.706	0.714	0.706	0.705	0.704	0.257
C/2	0.709	0.709	0.7	0.6911	0.718	0.708	0.706	0.382
1C	0.684	0.709	0.709	0.708	0.709	0.682	0.706	0.570
2C	0.691	0.706	0.7	0.697	0.706	0.703	0.698	0.680
5C	0.673	0.695	0.689	0.688	0.695	0.687	0.681	-
10C	0.642	0.662	0.655	0.672	0.694	0.682	0.666	-

2.4.3. Galvanostatic discharge profiles

Voltage vs. discharge capacity profiles for the 3.7 V/700 mAh lithium ion cells, each cycled at same rate (a) C/5, (b) C/2, (c) 1C, (d) 2C, (e) 5C, (f) 10C, and different temperatures between 55 and -10 °C are shown in the Fig. 2.5 and corresponding discharge capacities in Table 2.2. From Fig. 2.5 and Table 2.2 it is again very clear that the cell capacities are almost identical at same rate and different temperatures between 55 and -10 °C, except for -20 °C. Further, at C/5 rate, the energy density of all the cells cycled at different temperatures is almost similar (voltage profiles are similar) and performance starts declining slowly at C/2 rate depending on temperature and the decay in energy density is significant at higher rates (1C and higher) and is maximum at lower temperatures. The performance limitations at high-rates of >1C during discharge is essentially due to the cell overpotential of anode and cathode polarization and Ohmic drops [12, 15, 19, 20]. Accordingly, the cut-off voltage of 2.5 V is reached before the cell is fully discharged, which translates to lower energy density. From the Figs. 2.4-5 and Table 1-2, it can be concluded that the rate and temperature at which lithium ion cells are discharged show cumulative effects on the

electrochemical performance. The discharge voltage of cells decreases with the decreasing of temperature and increasing discharge rate.

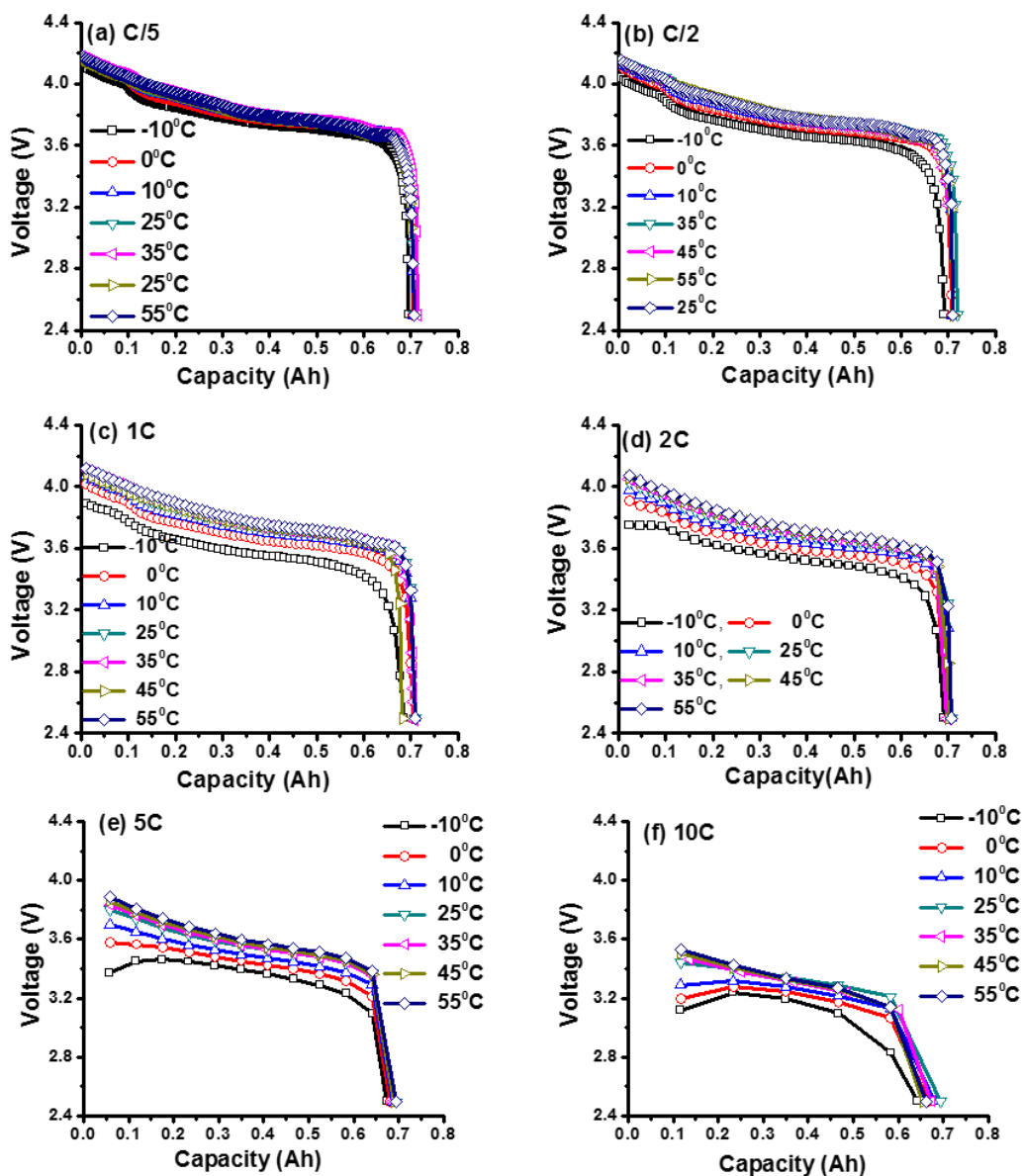


Fig. 2.5: Voltage vs. discharge capacity profiles for the 700 mAh cells, each cycled at same rate (a) C/5, (b) C/2, (c) 1C, (d) 2C, (e) 5C, (f) 10C, and different temperature as shown in the figure

Table 2. 2: The parameters obtained from the voltage vs. discharge capacity profiles for the 700 mAh, each cycled at same rate: a) C/5, (b) C/2, (c) 1C, (d) 2C, (e) 5C, and (f) 10C at different temperatures

Rate →	C/5	C/2	1C	2C	5C	10C
Temperature (°C) ↓	Capacity (Ah)	Capacity (Ah)	Capacity (Ah)	Capacity (Ah)	Capacity (Ah)	Capacity (Ah)
55	0.706	0.709	0.709	0.706	0.695	0.662
45	0.7	0.7	0.682	0.7	0.69	0.655
35	0.714	0.711	0.706	0.697	0.688	0.672
25	0.706	0.709	0.709	0.706	0.695	0.694
10	0.705	0.708	0.708	0.703	0.687	0.682
0	0.704	0.706	0.703	0.698	0.681	0.664
-10	0.694	0.691	0.685	0.691	0.673	0.642
-20	0.257	0.382	0.57	0.68	-	-

2.4.4. Ragone plots and Power-Energy Index (PEI)

In order to analyze the change in energy and power densities of lithium ion cells, with respect to temperature and C-rate, it is essential to have all the parameters in single Ragone plot. Ragone chart of lithium ion cells discharged at different C rates and temperatures are shown in Fig. 2.6. It is evident from Ragone chart that the cells cycled at high C rates have low energy density and cells discharged at lower temperatures show less efficiency in terms of energy compared to lithium ion cells cycled at high temperatures. As the temperature increases, there is an increase in efficiency of lithium ion cells. Moreover, there is no change in power density (Fig. 2.6.) with change in temperature which illustrates that power density of lithium ion

cells is independent of its operating temperature. Power fade in general is not because of operating temperature but mostly results from cycling because of surface passivation films of electrolyte decomposition products [8].

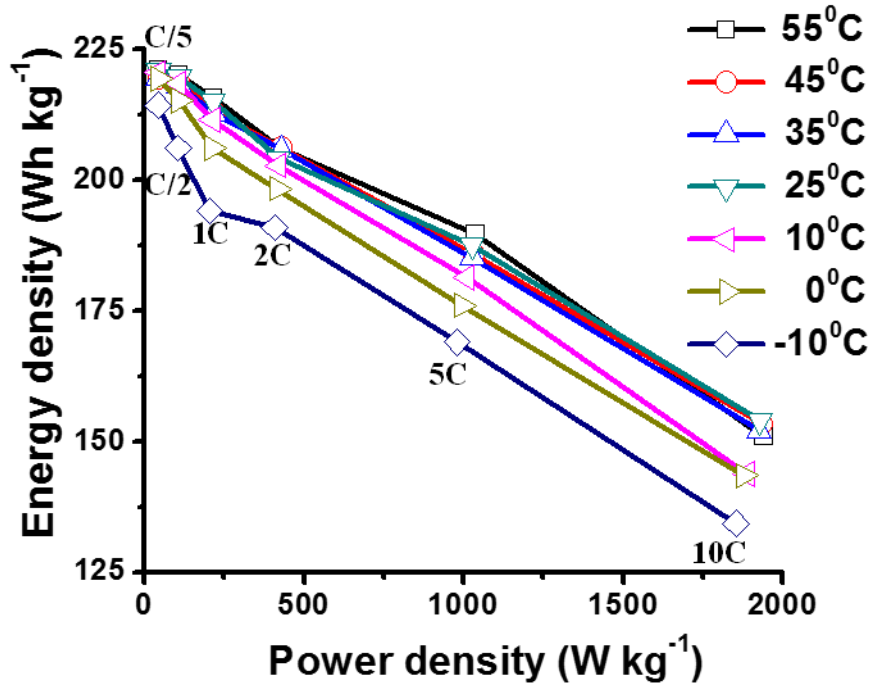


Fig. 2. 6: Ragone chart of lithium ion cells cycled at C rates and temperatures (as indicated)

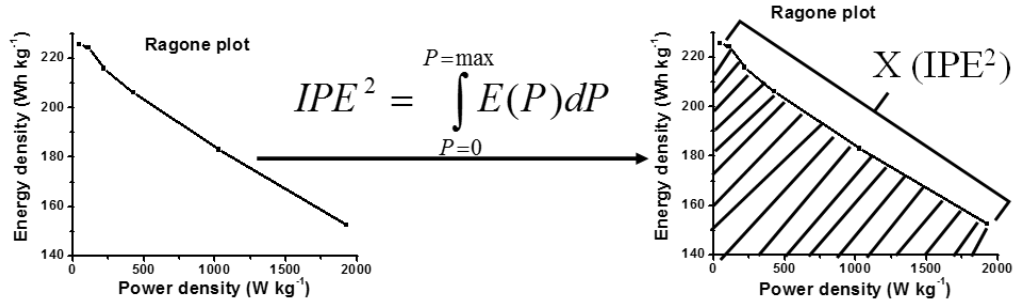
The Ragone charts obtained at 25 °C, 35 °C, 45 °C and 55 °C are very close which is making it difficult to differentiate their efficiencies. In these temperatures, the cells energy output is almost stable. This should be assigned to opposite effects as temperature increases; an increase in electrode kinetics and electrolyte conductivity on one hand and a decrease in electrode utilization rate due to the overall exothermic character of discharge reaction.

In order to account for the cell energy performance over the whole power range we introduce the integrated power energy (IPE) function. IPE is achieved by integrating the Ragone charts. And individual integrated energy or integrated power are obtained by taking the square root of the obtained integrated values in Eq. 2.1

followed by multiplying or dividing by time 1 hour to convert to energy density and to power density as IPE is expressed in $Wh^{\frac{1}{2}}kg^{-1}$.

$$IPE(T) = \sqrt{\int_P E(P)dP} |_T \quad (\text{Eq. 2.1})$$

The values are converted to percentages by considering the value obtained at 25 °C as standard or 100%. The detailed calculation structure is presented in scheme 2.1.



Scheme 2.1: Details of IPE calculation from Ragone plot

To normalize IPE data, we use the power energy index (PEI) where the obtained square root integrated values are converted to percentages by considering the value obtained at 25 °C as standard or 100% as shown in Eq. 2.2.

$$PEI(T) = 100 \sqrt{\frac{\int_P E(P)dP|_T}{\int_P E(P)dP|_{25\text{ }^\circ\text{C}}} \quad (\text{Eq. 2.2})$$

PEI or normalized electrochemical performance of lithium ion cells presented in Fig. 2.7 increases linearly from -10 °C to 25 °C then PEI stabilizes between 25 °C and 55 °C. Table 2.3 summarize the PEI and EPI data.

The low efficiency of the lithium ion cells at low temperatures is due to reduced electrolyte conductivity and lithium ion diffusivity. As temperature increases up to 25 °C the PEI increases linearly mostly due to improved lithium ion transport kinetics. Then the PEI increase and becomes almost negligible above 25 °C. The specific cell chemistry based on graphite anode and LiCoO₂ cathode operating cells ambient temperature should yield the best in terms of power and energy together with cycle life. In fact it is established that as operating temperature increases the cycle life decreases due to enhanced electrode and electrolyte degradation. Noteworthy is the good performance of these cells over wide ranges of temperatures and discharge rates

provided charging is performed at the ambient temperature and under relatively low rates.

In overall, on operating lithium ion cells at higher temperatures there is little improvement in efficiency but life time reduces significantly which limits its applications under different climatic conditions. So there is an intense need of development of lithium ion cells which sustain at higher and lower temperatures and shows enhanced efficiency through new electrode materials, electrolytes or electrolyte additives or novel separators.

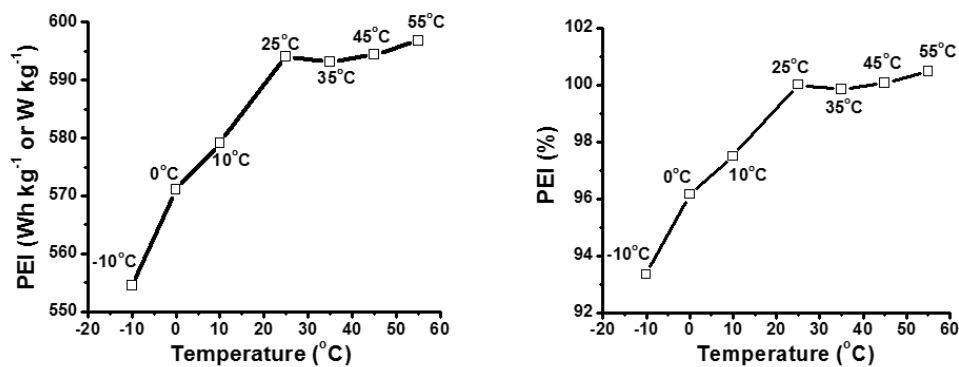


Fig. 2. 7: Conversion of energy and power density into (a) integrated power -energy, (b) % of power –energy index w.r.t. temperature

Table 2. 3: IPE values of lithium-ion cells w.r.t. temperatures and corresponding PEI values in percentages

Temperature (°C)	IPE (Wh kg ⁻¹) or W kg ⁻¹	PEI (%)
-10	554.4	93.34
0	571.09	96.15
10	579.3	97.49
25	594.2	100
35	591.7	99.85
45	594.3	100.06
55	597.1	100.47

2.5. Conclusions

The discharge temperature and C-rate have great influence on the performance of graphite/LCO lithium ion battery. Using integrated energy vs. power function and normalizing data to a new Power-Energy Index 'PEI' we show that PEI increases

linearly with temperature up to 25 °C and remain almost constant between 25 °C and 55 °C. This suggests that operating these cells close to 25 °C should provide the best trade-off between energy storage performances and cycle life. An increase in PEI with temperature is expected as at low temperatures the performance is controlled by the cell reaction kinetics and by the electrolyte conductivity. The fact that PEI stabilizes above 25 °C is less expected and denotes a tradeoff between the cell reaction kinetics and thermodynamics, which are respectively favorable and unfavorable to the overall energy output.

A decrease in energy density at low temperatures and high rates is mainly due to a decay in discharge voltage rather than discharge capacity. At low temperatures and high rates cells show a voltage delay perhaps due to local heat due to Joule effect.

It is also observed that for the optimum performance of the LIBs at low temperatures, low C-rate applications are most preferable. Either the temperature is too high or too low will result in low electrochemical performance, which means that the life of LIBs will not reach as expected. Consequently, in order to improve the battery performance for practical applications, the LIBs should be heated at low temperature and cooled at high temperature. More work is needed to understand the effect of the cell chemistry and the state of health on the PEI.

The Ragone chart presented in this chapter of same LIB chemistry but different temperatures and rates act as guide for the usage of batteries for different temperature and C rate applications. Moreover, the chart guide us in improving the electrochemical performance of the LIBs at the temperatures where the battery performance is very poor.

References

- [1] K. Kang, Y. S. Meng, J. Bre´ger, C. P. Grey, G. Ceder, Electrodes with high power and high capacity for rechargeable Lithium batteries, *Science* 311 (2006) 977-979.
- [2] B. Scrosati, J. Garche, Lithium batteries: Status, prospects and future, *J. Power Sources* 195 (2010) 2419–2430.

- [3] R. Marom, S. F. Amalraj, N. Leifer, D. Jacob, D. Aurbach, A review of advanced and practical lithium battery materials, *J. Mater. Chem.* 21 (2011) 9938.
- [4] M. M. Thackeray, C. Wolverton, E. D. Isaacs, Electrical energy storage for transportation—approaching the limits of and going beyond lithium-ion batteries, *Energy Environ. Sci.* 5 (2012) 7854-7863.
- [5] J. B. Goodenough, K.-S. Park, The Li-Ion rechargeable battery: A perspective, *J. Am. Chem. Soc.* 135 (2013) 1167–1176.
- [6] D. Larcher, J.-M. Tarascon, Towards greener and more sustainable batteries for electrical energy storage, *Nat. Chem.* 7 (2015) 19–29.
- [7] N. Nitta, F. Wu, J. T. Lee and G. Yushin, Li-ion battery materials: present and future, *Mater. Today*, 18 (2015) 252-262.
- [8] J. R. Belta, C. D. Ho, T. J. Miller, M. A. Habib, T. Q. Duong, The effect of temperature on capacity and power in cycled lithium ion batteries, *J. Power Sources* 142 (2005) 354–360.
- [9] M. Zang J. Xie, J. Ouyang, S. Wang, X. Wu, Investigation of temperature performance of Lithium-ion batteries for electric vehicles, 2014 IEEE conference and Expo Transportation Electrification Asia-Pacific (ITEC-Asia-Pacific), Beijing, 2014, pp 1-8.
- [10] M. Ecker, J. B. Gerschler, J. Vogel, S. Käbitz, F. Hust, P. Dechent, D. U. Sauer, Development of a lifetime prediction model for lithium-ion batteries based on extended accelerated aging test data, *J. Power Sources* 215 (2012) 248-257.
- [11] F. Leng, C. M. Tan, M. Pecht, Effect of Temperature on the Aging rate of Li Ion Battery Operating above Room Temperature, *Nat. Sci. Rep.*, 5 (2015) 12967.
- [12] G.G. Amatucci, C.N. Schmutz, A. Blyr, C. Sigala, A.S. Gozdz, D. Larcher, J.M. Tarascon, Materials effects on the elevated and room temperature performance of C/LiMn₂O₄ Li-ion batteries, *J. Power Sources* 69 (1997) 11-25.
- [13] K. L. Gering, Low-temperature performance limitations of lithium-ion batteries, *ECS Transactions*, 1 (26) (2006) 119-149.
- [14] J. Fan, On the discharge capability and its limiting factors of commercial 18650 Li-ion cell at low temperatures, *J. Power Sources* 117 (2003) 170–178.
- [15] M. C. Smart, B. V. Ratnakumar, S. Surampudi, Electrolytes for low-temperature lithium batteries based on ternary mixtures of aliphatic carbonates, *J. Electrochem. Soc.*, 146 (2) (1999) 486-492.
- [16] S.S. Zhang, K. Xu, T.R. Jow, Electrochemical impedance study on the low temperature of Li-ion batteries, *Electrochim. Acta* 49 (2004) 1057–1061.

- [17] Q. Wang, P. Ping, X. Zhao, G. Chu, J. Sun, C. Chen, Thermal runaway caused fire and explosion of lithium ion battery, *J. Power Sources* 208 (2012) 210–224.
- [18] R. M. Spotnitz, J. Weaver, G. Yeduvaka, D.H. Doughty, E.P. Roth, Simulation of abuse tolerance of lithium-ion battery packs, *J. Power Sources* 163 (2007) 1080–1086.
- [19] F. Jiang, P. Peng, Elucidating the performance limitations of lithium-ion batteries due to species and charge transport through five characteristic parameters, *Sci. Rep.* 6 (2016) 32639.
- [20] D. Aurbach, Y. Talyosef, B. Markovsky, E. Markevich, E. Zinigrad, L. Asraf, J. S. Gnanaraj, H.-J. Kim, Design of electrolyte solutions for Li and Li-ion batteries: a review, *Electrochim. Acta.* 50 (2004) 247–254.
- [21] A. S. Argon, A theory for the low-temperature plastic deformation of glassy polymers, *Philosophical Magazine* 28 (1973) 839-865.
- [22] S. K. Martha, H. Sclar, Z. S. Framowitz, D. Kovacheva, N. Saliyski, Y. Gofer, P. Sharon, E. Golik, B. Markovsky, D. Aurbach A comparative study of electrodes comprising nanometric and submicron particles of $\text{LiNi}_{0.50}\text{Mn}_{0.50}\text{O}_2$, $\text{LiNi}_{0.33}\text{Mn}_{0.33}\text{Co}_{0.33}\text{O}_2$ and $\text{LiNi}_{0.40}\text{Mn}_{0.40}\text{Co}_{0.20}\text{O}_2$ layered compounds, *J. Power Sources* 189 (2009) 248–255.
- [23] C. Zhang, F. W. Yan, C. Q. Du, J. Q. Kang, R. F. Turkson, Evaluating the degradation mechanism and state-of-health of LiFePO_4 lithium-ion batteries in real world plug-in Hybrid electric vehicles application for different aging paths, *Energies* 10 (2017)110.
- [24] F. Leng, Z. B. Wei, C. M. Tan, R. Yazami, Hierarchical degradation processes in lithium-ion batteries during ageing, *Electrochim. Acta* 256 (2017) 52-62.
- [25] K. Maher, R. Yazami, A thermodynamic and crystal structure study of thermally aged lithium ion cells, *J. Power Sources* 261 (2014)389-400.
- [26] R. Imhof, P. Novak, Oxidative electrolyte solvent degradation in lithium-ion batteries: An in situ differential electrochemical mass spectrometry investigation, *J. Electrochem. Soc.* 146 (1999)1702-1706.
- [27] S. Nowak, M. Winter, Review—chemical analysis for a better understanding of aging and degradation mechanisms of non-aqueous electrolytes for lithium ion batteries: method development, application and lessons learned, *J. Electrochem. Soc.* 162 (2015) A2500-A2508.
- [28] P. Lu, C. Li, E. W. Schneider, and S. J. Harris, Chemistry, impedance, and morphology evolution in solid electrolyte interphase films during formation in lithium ion Batteries, *J. Phys. Chem. C*, 118 (2014) 896–903.

- [29] S. H. Ahmed, X. Kang, S. O. Bade Shrestha, Effects of temperature on internal resistances of lithium-ion batteries, *J. Ener. Res. Tech.-Trans. ASME* 137(2015) 031901.
- [30] Y. Saito, K. Kanari, K. Takano, Thermal studies of a lithium-ion battery, *J. Power Sources* 68 (1997) 451-454.
- [31] J. R. Belt, C. D. Ho, T. J. Miller, M. A. Habib, T. Q. Duong, The effect of temperature on capacity and power in cycled lithium ion batteries, *J. Power Sources* 42(2005)354-360.
- [32] H. Chaoui, H. Gualous, Online parameter and state estimation of lithium-ion batteries under temperature effects, *Elec. Power Sys. Res.*, 145 (2017) 73-82.
- [33] G. M. Ehrlich, Ch. 35 in *Handbook of Batteries*, 3rd Ed. David Linden and Thomas B. Reddy Eds, McGraw-Hill, (2002).
- [34] G. Ning, B. Haran, B. N. Popov, Capacity fade study of lithium-ion batteries cycled at high discharge rates, *J. Power Sources* 117 (2003) 160-169.
- [35] D. N. Wong, D. A. Wetz, A. M. Mansour, J. M. Heinzl, The influence of high C rate pulsed discharge on lithium-ion battery cell degradation, *Proc. 2015 IEEE Pulsed Power Conf. (PPC)*, Austin, TX, May 31-Jun 04, 2015.
- [36] C-Y. Wang, T. Xu, S. Ge, G. Zhang, X-G. Yang, Y. Ji, A fast rechargeable lithium-ion battery at subfreezing temperatures, *J. Electrochem. Soc.* 163 (2016) A1944-A1950.
- [37] P. Flynn, *Meeting the energy needs of future warriors*, The National Acad. Press, 2004. <https://doi.org/10.17226/11065>.
- [38] T. Christen, M. W. Carlen, Theory of Ragone plots, *J. Power Sources* 91 (2000) 210–216.
- [39] B. D. McCloskey, Expanding the ragone plot: Pushing the limits of energy storage, *J. Phys. Chem. Lett.* 6 (2015)3592-3593.
- [40] Y. Ji, Y. Zhang, C.-Y. Wang, Li-ion cell operation at low temperature, *J. Electrochem Soc.* 160(2013) A636-A649.
- [41] H. Y. Wang, M. Yoshio, Electrochemical performance of raw natural graphite flakes as an anode material for lithium-ion batteries at the elevated temperature, *Mater. Chem. Phys.* 79(2003)76-80.
- [42] M. Kise, S. Yoshioka, K. Hamano, H. Kuriki, T. Nishimura, H. Urushibata and H. Yoshiyasu, Effect of the addition of conductive material to positive temperature coefficient cathodes of lithium-ion batteries, *J. Electrochem. Soc.* 152(2005) A1516-A1520.

- [43] Y-C. Jin, J-G. Duh, Kinetic study of high voltage spinel cathode material in a wide temperature range for lithium ion battery, *J. Electrochem. Soc.*, 164(2017) A735-A740.

Chapter 3

Study of High Energy Density Li-Mn Rich (LMR) Ni-Mn-Co Oxide (NMC) Cathodes for Lithium-Ion Batteries through 3D Electrode Architecture and LiF Coating

3.1. Abstract

This Chapter describes synthesis of Li-Mn Rich (LMR) Ni-Mn-Co Oxide (NMC) cathodes such as $\text{Li}_{1.2}\text{Ni}_{0.15}\text{Mn}_{0.55}\text{Co}_{0.1}\text{O}_2$ (here after LMR-NMC) by solution combustion method followed by LiF coating onto LMR-NMC by solid state synthesis. The electrochemical performance of the pristine LMR-NMC and corresponding F-doped (LiF coated) samples as cathodes for LIBs are investigated by galvanostatic charge-discharge cycling and impedance spectroscopy. The fluorine doped cathodes deliver high capacity of $\sim 300 \text{ mAh g}^{-1}$ at C/10 rate (10-20% greater than the pristine LMR-NMC cathodes), have high discharge voltage plateau ($> 0.25 \text{ V}$) and low charge voltage plateau (0.2 to 0.4 V) compared to pristine LMR-NMC cathodes. Beside, irreversible capacity, voltage fade, capacity loss are significantly reduced in-relation to the pristine LMR-NMC electrodes. LiF coating onto LMR-NMC, partially replaces M-O bonds of the material by M-F bonds, thus increasing the interfacial and structural stability. Besides, in order to improve the electronic conductivity and complete utilization of the active materials, this Chapter also describes a possible replacement of aluminium current collector with 3D carbon fiber current collector. The 3D

electrode architecture of LMR-NMC delivers high capacity of $>200 \text{ mAh g}^{-1}$ at 1C rate, good capacity retentions for over 200 cycles. The study opens a possibility for LMR-NMC cathode material which has almost double the capacity of currently used cathodes, and can be a possible substitute cathode for LIBs used in electric vehicles.

3.2. Background and Motivation

The current research in lithium based batteries are focused to achieve high energy density batteries with reduced cost and improved safety [1-4]. State-of-art LIBs use transition metal (TM, such as Ni, Mn and Co) oxide (LiCoO_2 , $\text{LiNi}_{1/3}\text{Mn}_{1/3}\text{Co}_{1/3}\text{O}_2$ or $\text{LiNi}_{0.8}\text{Co}_{0.15}\text{Al}_{0.05}\text{O}_2$) or olivines (LiFePO_4 , LiMnPO_4 , $\text{LiMn}_{0.8}\text{Fe}_{0.2}\text{PO}_4$, LiCoPO_4), spinels (LiMn_2O_4 , $\text{LiNi}_{0.5}\text{Mn}_{1.5}\text{O}_4$ (NMS) based cathodes and graphitic carbon as anode [1-20]. The nominal capacity of most of these cathodes are in the range of $120\text{-}180 \text{ mAh g}^{-1}$ when cycled up to 4.2 V, is only half the specific capacity of graphite anode (Theoretical capacity = 372 mAh g^{-1}) [1-4, 18-20]. The issues of low energy density cathode materials and high energy density but highly unstable batteries (Li-S, Li-Air systems), limits the application of LIBs in electric vehicles [22-23]. Thus, there has been an intense research activity during the last decade to develop high capacity-high voltage or high energy cathodes for LIBs. Lithium and manganese rich transition metal oxides such as $\text{Li}_{1.2}\text{Ni}_{0.15}\text{Mn}_{0.55}\text{Co}_{0.1}\text{O}_2$ (LMR-NMC) has almost double the capacity of layered TM oxides, and is one of the stable, sustainable high energy cathode material which have suitable properties to use in the electric vehicles (Specific capacity – 372 mAh g^{-1} corresponding to 1.2 Li insertion/de-insertion and energy density $\sim 1000 \text{ Wh kg}^{-1}$) [23-36]. To get high capacity from LMR-NMC, the material need to be electrochemically cycled above 4.4 V. During high voltage cycling ($>4.4 \text{ V}$), oxygen release takes place from Li_2MnO_3 component in the form of Li_2O and MnO_2 which causes interfacial instability of LMR-NMC electrode [30]. Besides, oxygen release causes large irreversible capacity loss of about $50\text{-}100 \text{ mAh g}^{-1}$ in the first cycle. The major issue of LMR-NMC is voltage decay mostly due to structural transformation of layered to the spinel structure [10-13]. The structural change is associated with migration of transition metal ions to lithium layer during high

voltage cycling (>4.4 V). The migration takes place because of vacancies created by oxygen release as Li_2O from Li_2MnO_3 component during high voltage cycling [23-30]. Because of migration, the layered structure slowly transforms to spinel during the course of cycling due to which there is decay in the voltage plateau from 3.7 V region to 2.8 V region which decreases the energy density [24-28, 31-33]. The interfacial instability can be minimized by surface coatings such as metal oxides like Al_2O_3 , ZrO_2 , TiO_2 etc., metal phosphate coatings like AlPO_4 , LiFePO_4 etc. blending with another cathode material [33-45]. And solid electrolyte coating like LiPON improved the capacity retention and rate performance of LMR-NMC [33]. But voltage fade is not properly addressed by these surface coatings or blending. LMR-NMC suffers from poor cyclability (capacity retention), rate capability due to low electronic conductivity of LMR-NMC and deposition of thick SEI layer formed by a reaction of the cathode surface with the organic electrolytes at high voltage cyclings (>4.4 V) [46].

Besides, F-substitution or coating helps in the improvement of electrochemical performance at high cut-off voltages, improves thermal stability and reduces charge transfer resistance [47-48]. Many researchers have postulated that substituting oxygen by fluorine is highly advantageous method to improve electrochemical performance [49-50]. In the literature it has been demonstrated that both F-substituted layered cathode materials such as $\text{LiNi}_{0.8}\text{Co}_{0.1}\text{Mn}_{0.1}\text{O}_2$ and $\text{LiNi}_{1/3}\text{Mn}_{1/3}\text{Co}_{1/3}\text{O}_2$ delivered stable cycling performance and improved high rate capacity [50-51]. F-doping in $\text{LiNi}_{0.5}\text{Mn}_{1.5}\text{O}_4$ (NMS) resulted in improvement of electrochemical performance like increase in initial capacity and high rate capability $\sim 10\%$ and also shows better thermal stability [52]. Manganese dissolution is also reduced ($\sim 30\%$), as electrode surface is less prone to HF attack. Generally 2-5 % of fluorine is recommended for best electrochemical performance. In overall, the effect of fluorine on enhanced electrochemical performance of Lithium TM oxide compounds was proposed to originate from a combination of following features [53]. These include (1) the physical properties like high tap density

(high volumetric energy density) [44], (2) enhanced cation ordering, (3) improved structural stability associated to the smaller c-axis variation during charge, and (4) in fluorine doped spinels, the presence of fluorine near the surface provides protection from HF attack at high voltages (~5 V) [52].

To overcome the issues of interfacial instability (to improve cycle life, C rate performance, irreversible capacity and voltage decay or energy loss) in this Chapter, we present a method of LiF coating which stabilizes the interface and decreases the voltage fade. LiF coating prevents the electrode surface from direct contact of electrolyte thus reducing the electrolyte decomposed deposits on the surface, hence stabilizing the interface. Moreover, on coating and doping with LiF some of the M-O bonds are replaced by M-F bonds on the surface [47-48, 53]. The M-F bond is stronger and thus stabilizes the structure during cycling. Partially O^{2-} is replaced by F^- on the surface of LMR-NMC and due to which the average oxidation state of the surface metal ions is slightly decreased which lead to decrease in charge potential thus minimizing the electrolyte decomposition and delivering better electrochemical performance. There are similar reports that LaF_3 and AlF_3 coatings also enhances electrochemical performance of $LiMn_2O_4$, NMC respectively [54-55]. Besides, it is also reported that Al foil coated with porous layered cathodes of $LiNi_{0.8}Co_{0.15}Al_{0.5}O_2$ (NCA) is susceptible to undergo corrosion in 3:7 ratio of ethylene carbonate (EC) and ethyl methyl carbonate (EMC) with 1.2 M $LiPF_6$ which is significantly contributing to the capacity fade of the battery [56]. So to avoid capacity and power fade due to corrosion of Al-foil, we made an attempt to replace Al-foil by highly conductive, corrosion resistant non-graphitic carbon fibers (CFs) of ~10 micro meter in diameter. The cathode material disperses throughout the CF and thus making a good electronic contact with CF current collector and have high active material utilization which improves the energy density.

3.3. Experimental

3.3.1. Synthesis of LMR-NMC and F-LMR-NMC

The LMR-NMC materials were synthesized by solution combustion method by taking stoichiometric amount of Li (NO_3), $Ni(NO_3)_2 \cdot 6H_2O$, $Mn(NO_3)_2 \cdot 4H_2O$,

$\text{Co}(\text{NO}_3)_2 \cdot 6\text{H}_2\text{O}$ (all chemicals are from Alfa Aesar, Chennai, India) as oxidants and glycine as fuel. The metal nitrates and glycine were dissolved in appropriate amount of water in a beaker, subsequently heated at 100 °C till viscous slurry was formed and placed it in a preheated furnace at 400 °C. Few minutes after keeping the material in the furnace at 400 °C auto ignition takes place forming amorphous LMR-NMC. The as prepared sample was kept at 400 °C for about 30 min for complete removal of organics. Various weight ratios (100:1, 75:1, 50:1, 25:1) of LMR-NMC and LiF were made by grinding in an agate mortar for about 30 min followed by annealing at 800 °C in an alumina crucible for 20 hrs in air (Hereafter this product is termed as F-LMR-NMC). Similarly for comparison, pristine LMR-NMC (No LiF coatings) was prepared from amorphous LMR-NMC by annealing at 800 °C in an alumina crucible for 20 hrs in air.

3.3.2. Structural and physical characterization of LMR-NMC and F-LMR-NMC

The Powder XRD measurements on LMR-NMC and doped LMR-NMC were performed by using an X'Pert Pro diffractometer (Netherlands) (reflection θ - θ geometry, Cu $\text{K}\alpha$ radiation, receiving slit of 0.2 mm, scintillation counter, 30 mA, 40 kV). The diffraction data were collected at 0.02 step widths over a 2θ range from 10 to 70°. The structural parameters were refined by Rietveld refinement analysis that was performed using Full Prof Suite program. The surface morphology of the composite powders were further measured by scanning electron microscope (Carle Zeiss Supra 40vp field emission scanning electron microscope) and transmission electron microscopy (JEOL-JSM-700F) and compositions by energy dispersive X-ray microanalysis (EDAX) systems from Oxford instruments. It was further characterized by Raman spectroscopy using a micro Raman spectrometer HR800 (Jobin Yovn Horiba, France), with He-Ne laser (excitation line 632.8nm) and a microscope objective (50X, Olympus Mplan, 0.4 mm working, numerical aperture 0.75 in back scattering configuration). X-ray photoelectron spectroscopy (XPS) measurements were

carried out ESCA+, (Omicron nanotechnology, Oxford Instruments plc, Germany) equipped with monochromic AlK α (1486.6 eV) X-ray beam radiation operated at 15 kV and 20mA, binding energy was calibrated vs. carbon (C1s = 284.6 eV). For these measurements, the powder samples were transferred to the XPS device using a hermetically sealed unit, which contains a sample holder attached to a magnetic manipulator, and a gate valve. The spectra were deconvoluted using Gaussian functions based on Origin 8.0 software.

3.3.3. Electrode preparation and cell assembly

The composite electrode comprised slurry of 82% active material, 10% carbon black (Timcal) and 8% PVdF (Kynar, Japan) in N methyl pyrrolidone (Aldrich), were coated on to Aluminum (>99.9%, Strem chemicals, Inc., US) and carbon fiber (Hollingsworth & Vose, USA) current collectors using doctor blade technique. The composite electrodes were dried under vacuum at 90 °C and punched into 1 cm diameter electrodes. The active masses of the electrodes are about 5 mg cm⁻². Li foils (Alfa Aesar) were used as counter electrodes. Swagelok cells are assembled in an ultrahigh pure Argon (99.999%) filled glove box (M-braun, Germany). The moisture and oxygen content in the glove box were less than 0.1 ppm. The cells are assembled using composite electrodes comprising LMR-NMC, F-LMR-NMC (1:100, 1:50, 1:25) powder as active masses, Li-foils as counter and reference electrode, and polyethylene-polypropylene trilayer separator (Celgard, Inc., Canada). The electrolyte was EC: DMC (1:2) / LiPF₆ (1.2 M). The HF and H₂O content in the electrolyte was less than 20 ppm.

3.3.4. Electrochemical characterizations of LMR-NMC and F-LMR-NMC

The electrochemical performance of the LMR-NMC and F-LMR-NMC composite electrodes were measured by using Solartron cell test system consists of 1470E multi-channel potentiostats and multiple 1455A series frequency

response analyzers (FRAs) (driven by Corrware and Z-Plot software from Scribner Associates) and Arbin battery cycler (Arbin BT2000 - Battery Test Equipment, USA). The impedance measurements were carried out in a frequency range between 1 MHz and 10 mHz in fully discharged condition (SoC 0) after 50 cycles at 3.1 V (2 hrs rest after discharging to 2.5 V). The charge-discharge cycling were carried out in the potential range between 2.5 V and 4.7 V using CC-CV protocol. All the experiments were carried out at 25 °C \pm 2 °C.

3.4. Results and Discussion

3.4.1. Structural characterization

The diffraction pattern of the samples shown in the Fig. 3.1, are indexed based on α -NaFeO₂ structure. Li_{1.2}Ni_{0.15}Mn_{0.55}Co_{0.1}O₂ is a mixed composite of rhombohedral LiMO₂ (Space group R $\bar{3}$ m) and monoclinic Li₂MnO₃ (space group C2/m) structure. The extra less intense peak between 20 – 23° belongs to monoclinic Li₂MnO₃ which formed due to ordering of Li and Mn in transition metal layer. In Fig. 1(a) - (d), it is observed that the relative integral intensity ratio of I(003) to I(104) peaks, are decreased from 1.28 for pristine to 0.98 for 1:100, to 0.95 for 1:75, to 0.70 for 1:50, to 0.63325 for 1:25 wt. % LiF: LMR-NMC. The decrease in the I(003) to I(104) peaks shows increase in cation mixing and the crystal structure becomes closer to cubic with increasing the fluorine content. The proper splitting of (006)/(102) and (018)/(110) doublets of all samples indicates that there is a formation of well-ordered layered structure [23-36].

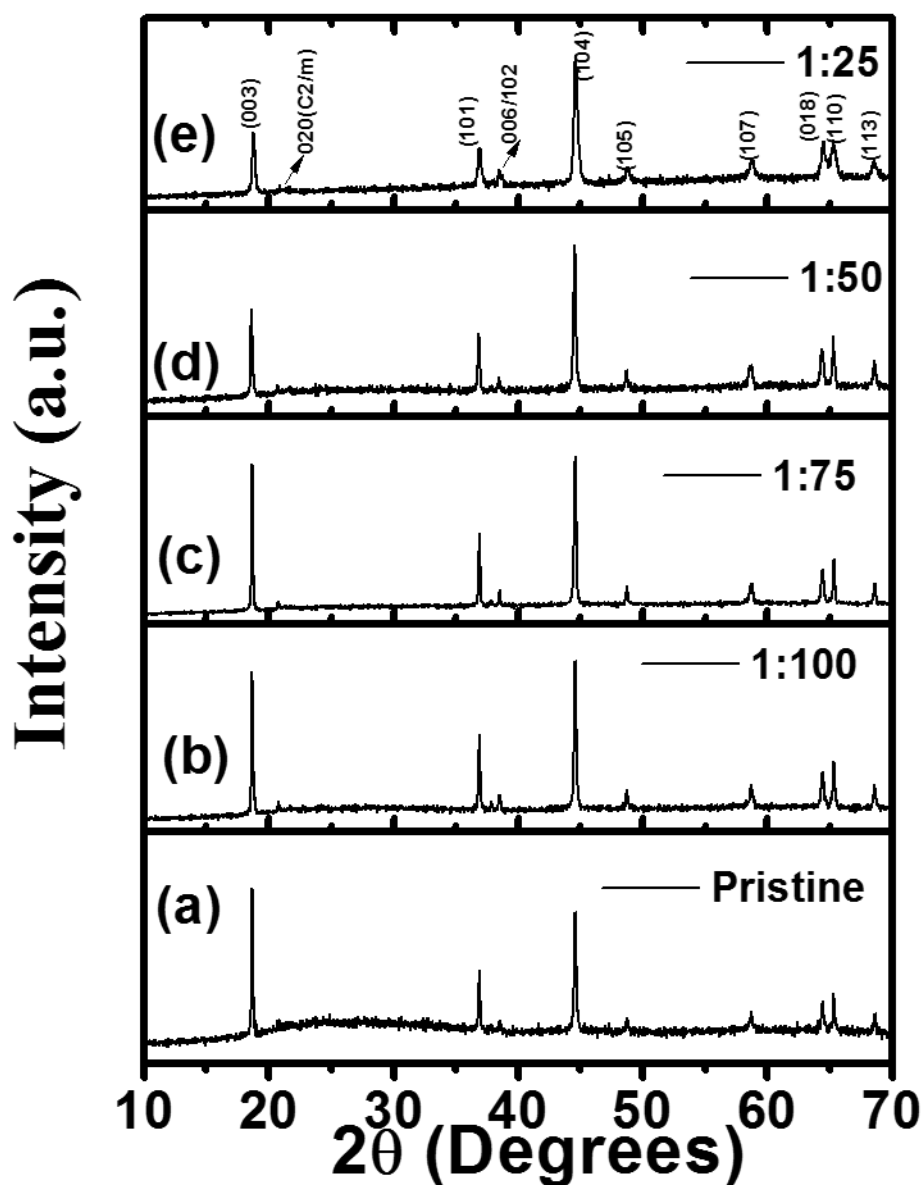


Fig. 3.1: XRD patterns of: (a) pristine LMR-NMC, (b) F-LMR-NMC (1:100 wt. %), (c) F-LMR-NMC(1:75 wt. %), (d) F-LMR-NMC(1:50 wt. %), and (e) F-LMR-NMC (1:25 wt. %) synthesized by solution combustion method followed by LiF coating onto LMR-NMC by solid state synthesis at 800 °C for 20 hrs

The XRD pattern of LMR-NMC and F-LMR-NMC are refined by Rietveld refinement. The lattice parameter of F-LMR-NMC shows $a=2.8612 \text{ \AA}$ and $c=14.2496 \text{ \AA}$ (1:50 wt. %) while LMR-NMC shows $a=2.8539 \text{ \AA}$ and $c=14.2519 \text{ \AA}$. Full chart of lattice parameters of varying compositions of LiF and LMR-NMC are presented in Table.3.1. The increase of a-axis is due to partial reduction of metal ions for charge compensation of fluoride (F^-) ion. The

increase in a-lattice parameter suggest that there is replacement of some of O^{2-} with F^- [51-53] thus decreasing the average oxidation state of metals partially, since the a-parameter is the measure of M-M bond length in the basal plane of hexagonal structure. Hence, on coating with LiF there is no change in the crystal system of the LMR-NMC and it retains its layered structure in all ratios.

Table.3.1: The comparison of lattice parameter values of pristine material and different ratios of LiF and LMR-NMC material

Ratio (LiF : LMR-NMC) wt. %	a (Å)	c (Å)
Pristine	2.8539	14.2510
1 : 100	2.8542	14.2520
1 : 75	2.8564	14.2481
1 : 50	2.8612	14.2496
1 : 25	2.8631	14.2366

3.4.2. Physical characterizations and compositional analyses

The morphologies of both pristine LMR-NMC and F-LMR-NMC are investigated by HR-SEM and HR-TEM as shown in Fig. 3.2 and Fig. 3.3. The HR-SEM and HR-TEM images in both pristine LMR-NMC and F-LMR-NMC materials converge. They have multifaceted, mostly platelet like morphology (Fig. 3.2(a-c), Fig. 3.2(a-b)). The pristine LMR-NMC (Fig. 3.2(a), Fig. 3.3(a)) has particle sizes are in the range of 25-125 nm uniformly distributed whereas F-LMR-NMC (Fig. 3.2(b-c), Fig. 3.3(b)) have agglomeration of primary particles in the ranges between 100-300 nm leading to secondary particles in the range of 1.5-2 μm (Fig.3.2(b)). This clearly indicates F doping increases the tap density of the F-LMR-NMC material.

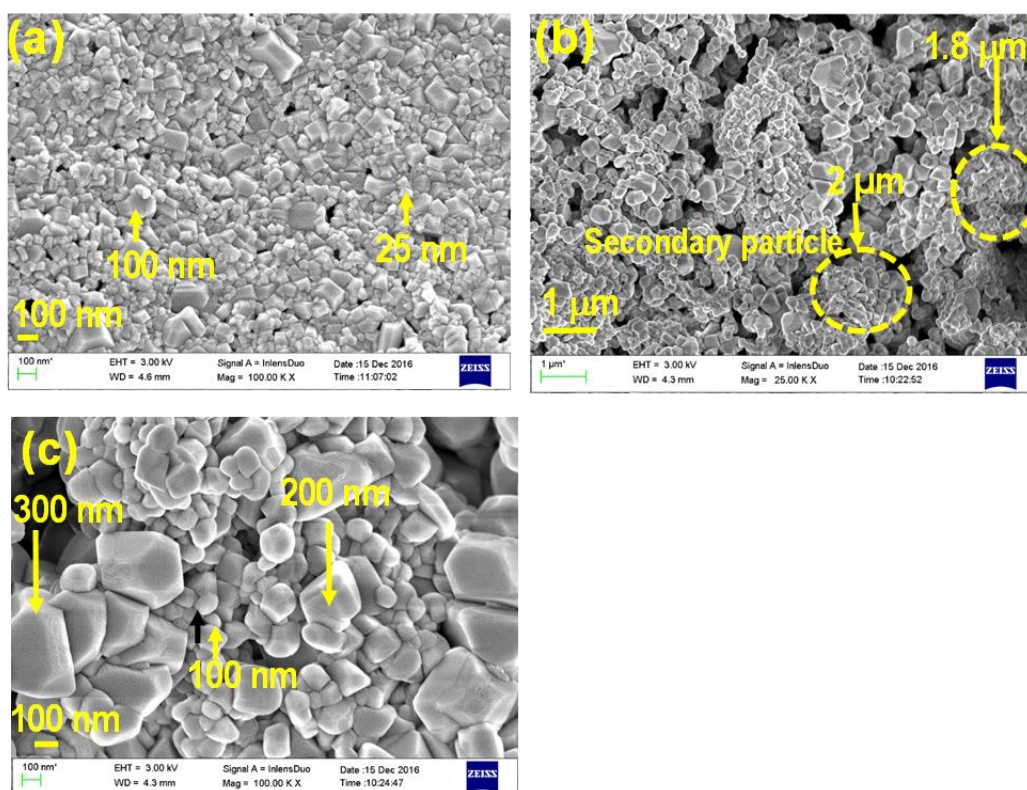


Fig. 3.2: HR-SEM image of: (a) pristine LMR-NMC at 100 KX magnification, and (b-c) F-LMR-NMC (1:50) at 25 KX and 100 KX magnifications, respectively

F-LMR-NMC materials are coated with thin layer (~10 nm) of LiF as shown in Fig. 3.3(a). HRTEM image in Fig. 3.3(b) confirms formation of secondary particles in F-LMR-NMC. The lattice fringes and atomic layers of LiF coatings are shown in Fig. 3.3(c-d). The LiF crystallites have a typical, well-defined cubic symmetry, and the atomic layers are also clearly observed in the HR-TEM images in Fig. 3.3(c and d). The d-spacing values of 0.204 nm correspond to (200) reflection in the LiF XRD pattern.

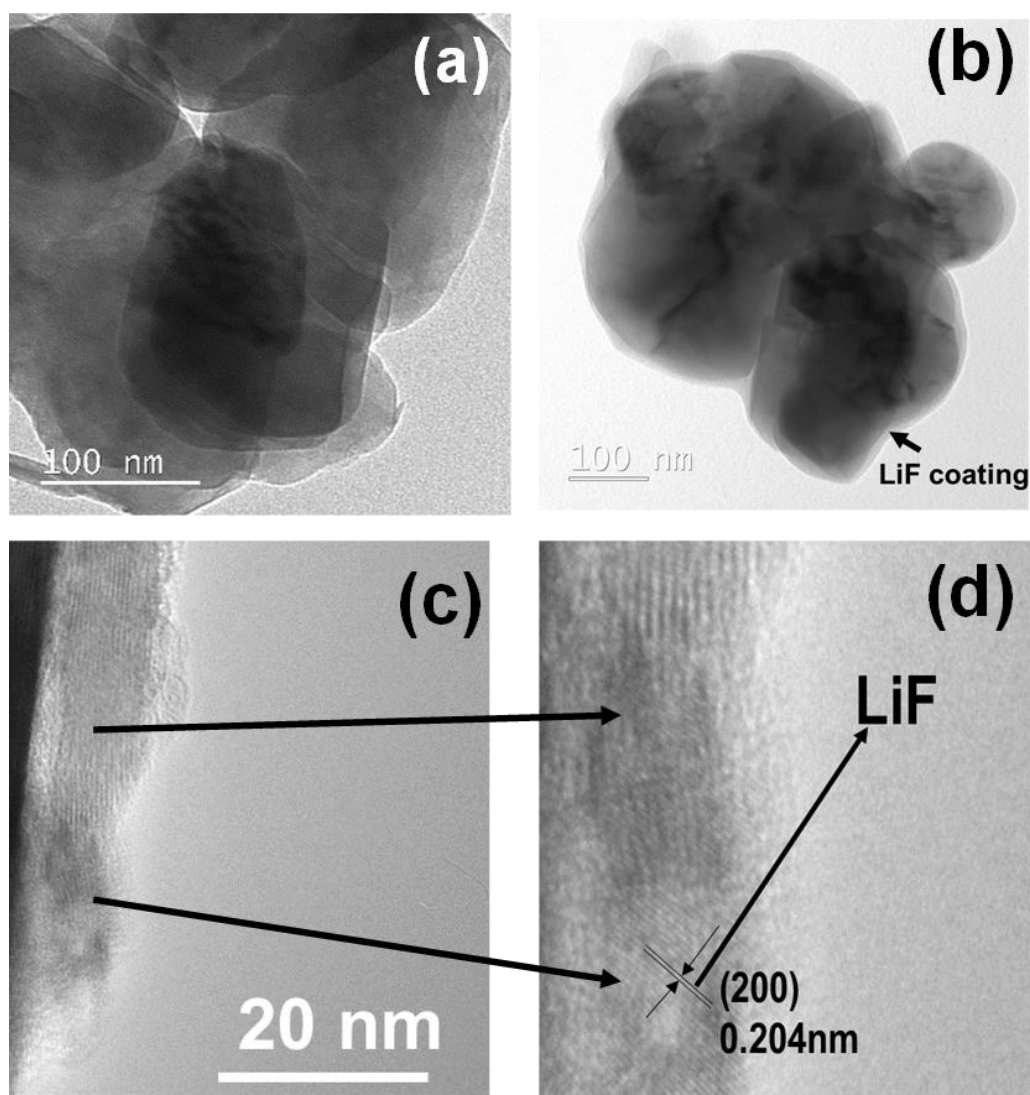


Fig. 3.3: HR-TEM image of: (a) pristine LMR-NMC, (b) F-LMR-NMC (1:50), (c) high resolution image of the surface of F-LMR-NMC, and (d) Lattice fringes and atomic layers of the F- LMR-NMC

Elemental mapping of F-LMR-NMC (1:50 wt. %) and corresponding SEM image is shown in Fig. 3.4. The elemental mapping in Fig. 3.4 shows the uniform distribution of elements O, Mn, Ni, Co and F in the material. EDAX analysis shown in Fig. 3.5(a) and weight percentages of elements of 1:50 wt. % F-LMR-NMC in Fig. 3.5(b). The EDAX confirms F substitution in LMR-NMC.

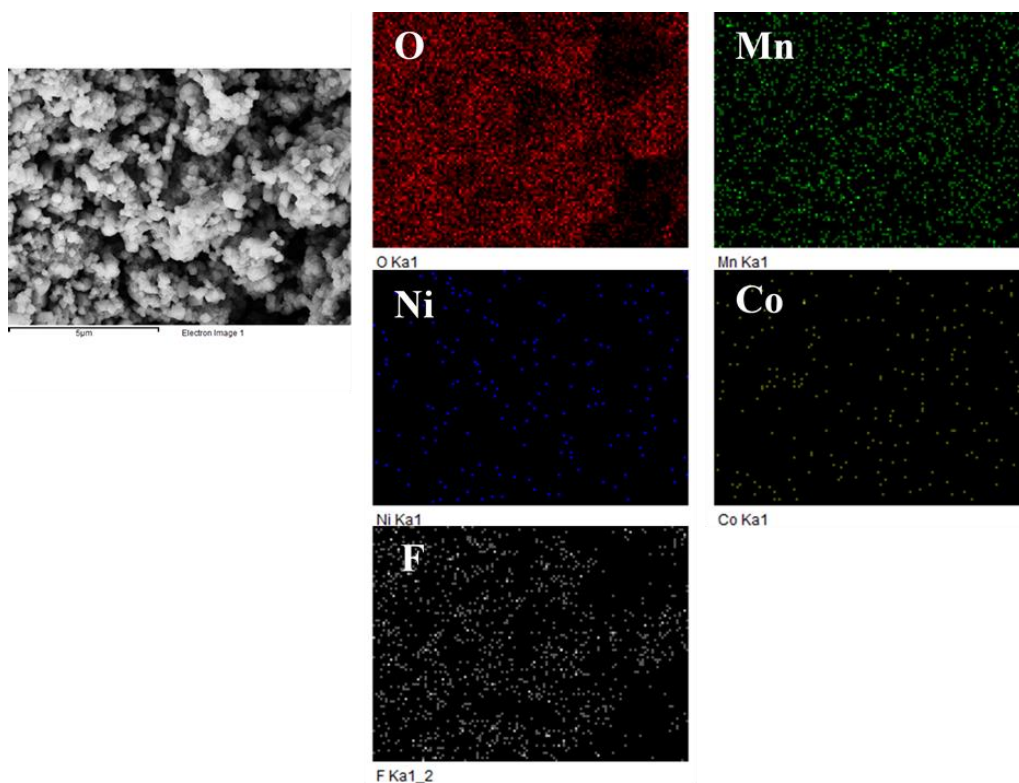


Fig. 3.4: The elemental mapping (O, Mn, Ni, Co and F) of F-LMR-NMC (1:50 wt. %) and corresponding SEM image

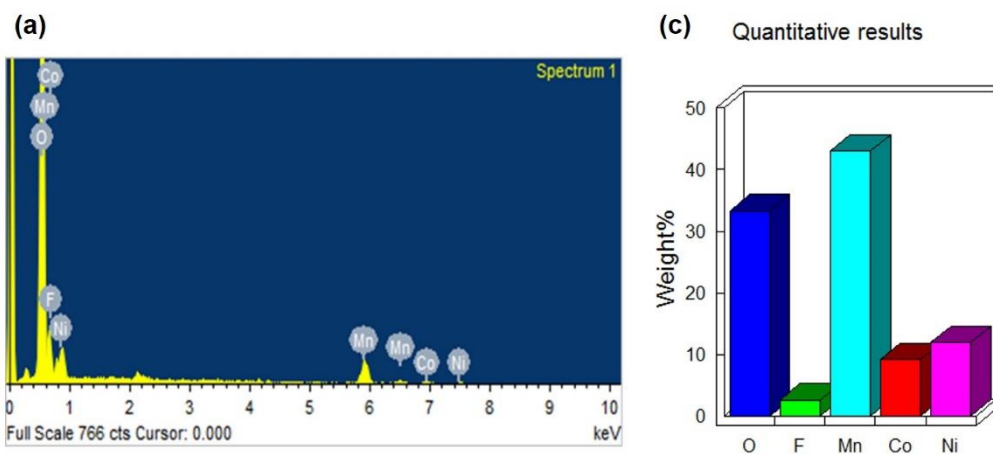


Fig. 3.5: (a) EDAX analysis result, and (b) weight percentages of elements of 1:50 wt. % F-LMR-NMC

Raman spectroscopy is a powerful technique for probing crystal Chemistry of layered transition metal oxides [46, 57]. Figure 3.6 show three major Raman bands at 596 cm^{-1} , 474 cm^{-1} and 425 cm^{-1} for pristine LMR-NMC and F-LMR-NMC (1:50 wt. %). Raman active vibrational modes for an ideal

layered lithium transitional metal oxide (LMR-NMC) with $R\bar{3}m$ symmetry have A_{1g} symmetry stretching and E_g symmetric deformation of M-O which corresponds to two sharp Raman peaks near 596 cm^{-1} and 474 cm^{-1} respectively. There is a weak peak at 419 cm^{-1} corresponding to the monoclinic Li_2MnO_3 due to reduced local symmetry of $C2/m$ rather than $R\bar{3}m$. The obtained Raman band values matches with literature values given for a hexagonal ($R\bar{3}m$) and a monoclinic ($C2/m$) crystals respectively. The Raman spectra clearly supports XRD indicating no change in crystal structure of LMR-NMC due to F-doping (or coating).

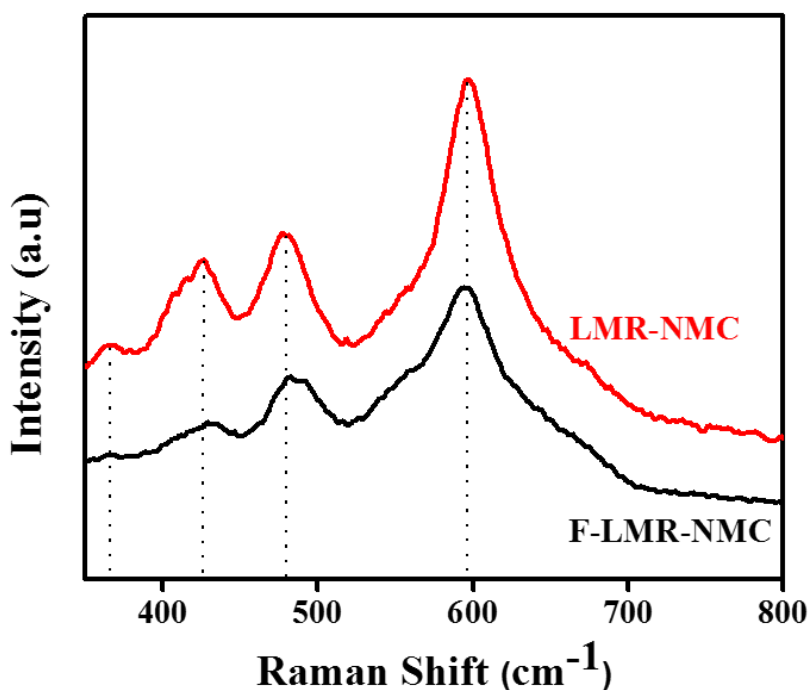


Fig. 3.6: Raman spectrum of F-LMR-NMC (1:50 wt. %) and pristine LMR-NMC

Figure 3.7 presents XPS spectra of (a) survey analysis of pristine F-LMR-NMC (1:50 wt. %) between 0-900 eV, (b) O1s, (c) F1s, (d) C1s, (e) Li1s, (f) Mn2p, (g) Ni 2p and (h) Co2p.

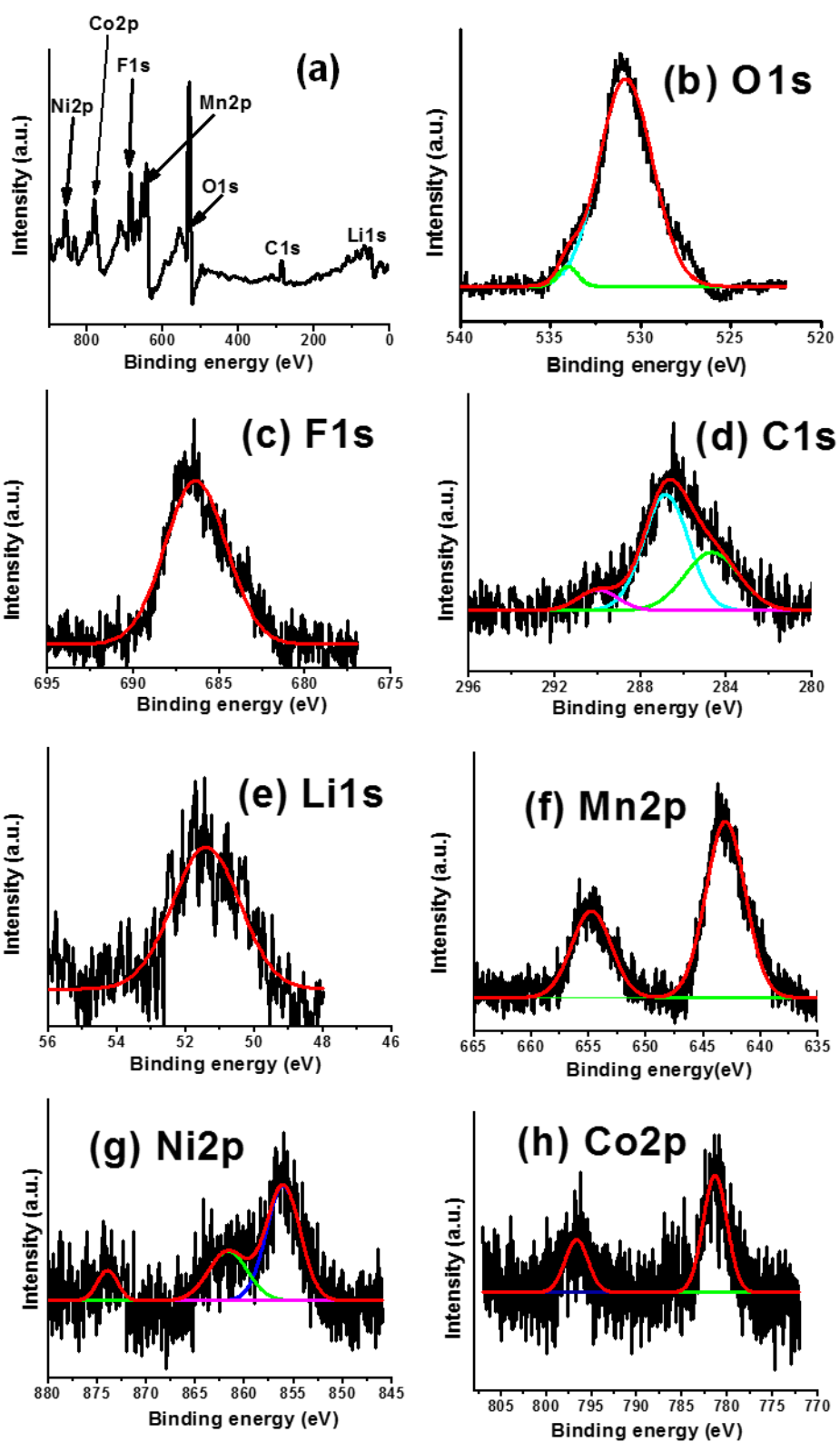


Fig. 3.7: (a). XPS survey analysis of F-LMR-NMC (1:50 wt. %) between 0-900 eV, XPS spectrum of (b) O1s, (c) F1s, (d) C1s, (e) Li1s, (f) Mn2P , (g) Ni2P and (h) Co2p

The survey scan in Fig. 3.7(a) clearly indicates the presence of all the elements of F-LMR-NMC including Fluorine and Carbon (from synthesis). The O1s spectra in Fig. 3.7(b) show a strong O1s peak at 530 eV, which corresponds to lattice oxygen of LMR-NMC, and a small peak due to OH or metal carbonates at 533 eV [46, 58]. The F1s spectrum in Fig. 3.7(c) of pristine F-LMR-NMC shows strong XPS signal close to 685 eV clearly indicates the presence of F due to LiF compounds [46, 58]. The C1s spectra in Fig. 3.7(d) show two significant peaks around 284.5 and ~286 eV. The 284.5 eV peak could be attributed to residual carbon from the synthesis and contaminants present in the analysis chamber. The higher B.E. peak ~286 and 289 eV corresponds to C-O and C=O linkages could be ascribed to the formation of Li₂CO₃ surface impurity, or a product of reactions between CO₂ in the atmosphere and F-LMR-NMC. Fig. 3.7(e-h) clearly indicates the signature peaks of Li1s, Mn2p, Ni2p and Co2p peaks for the F-LMR-NMC [46].

3.4.3. Electrochemical performance studies

3.4.3.1 Structural, physical, electrochemical assessment of carbon fibers

In general Aluminium current collectors are used as cathode current collectors for Li-ion batteries. However, aluminium is not completely corrosion free and its contact and corrosion resistance increases with increase in cycling [59-60]. Almost all the potentials above 4.0 V, the current decreases quickly to a steady state value (Fig. 3.8(a)) similar to the data reported in the literature [61]. Fig. 3.8(b) shows current-time plots for the aluminium electrode at potentials between 3.0 V and 4.8 V at 25 °C. The low current densities (0-1 $\mu\text{A cm}^{-2}$) are obtained for voltages except for the potentials between 3.0-4.0 V during the 1st cycle. The aluminium current collector is stable in contact with electrolyte up to 4.8 V. The steady-state currents after 2-3 hrs have been taken out from current-time plot and are compared for different voltages (Fig. 3.8(b)). There is a clear peak for 3.0-4.0 V with the maximum current reaching about 20 $\mu\text{A cm}^{-2}$ at 3.4 V is due to anodic oxidation of Al to Al³⁺ (such as Al₂O₃ or Al₂(CO₃)₃ etc.) on the surface [60-61]. This occurs during 1st chronoamperometry cycle and does not recur during the 2nd cycle (Fig. 3.8(b)) indicating a stable passive layer (such as Al₂O₃ or Al₂(CO₃)₃ formed on the surface. The high currents observed at 3.3-4.0 V could be due to cleaning of Al in NMP which may remove the preformed

surface passivation layer. The total charge associated with this passivation reaction is significant being $>250 \mu\text{Ah}/\text{cm}^2$ (obtained from integration of currents between 3.4-4.0 V).

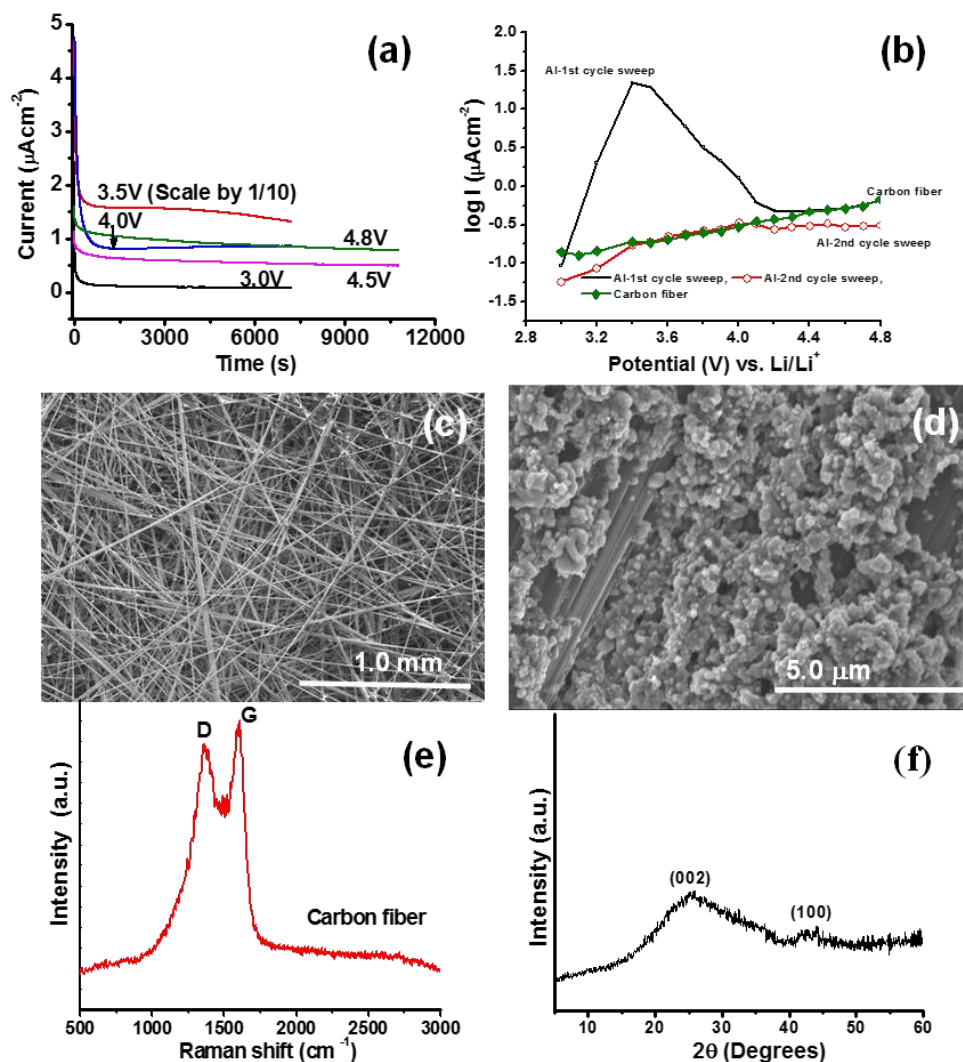


Fig. 3.8: (a) The current density-time plots obtained at various potentials (as indicated) at Al electrodes in EC-DMC 1:1/ LiPF_6 1.1M solutions at 25°C . Current at 3.5V is scaled by 1/10, (b) Comparison of the steady-state currents at various voltages for aluminum (during 1st and 2nd sweep) and carbon fiber current collector (1st sweep), (c) SEM image of carbon fiber mat, (d) cathode fabricated on carbon fiber mat, (e) Raman spectra of carbon fibers used as current collectors, and (f) XRD of carbon fibers used as current collectors

This may contribute to irreversible capacity. In contrast, the stability CF as current collector is also presented along with aluminium in Fig. 3.8(b). It is seen from Fig. 3.8(b) that at all potentials the current quickly decreases to a steady state value

(0-3 $\mu\text{A cm}^{-2}$), similar to Al current collector, indicating good stability of the CFs. Unlike aluminium, the corrosion of these fibers do not occur between the potentials 3.0 V and 4.0 V. The SEM image of CF mat and electrode structure are presented in Fig. 3.8(b) and c respectively. The thickness of CF are in the range of 5-10 μm (Fig. 3.8(c)). Electrode structure presented in Fig. 3.8(d) clearly indicates that the active materials are densely packed and still some empty spaces are available for active material loading. The Raman spectra presented in Fig. 3.8(e) shows strong D band at 1350 cm^{-1} confirms non-graphitic nature of the CFs. This is further supported by the XRD pattern of CFs presented in Fig. 3.8(f) clearly indicating the non-graphitic nature of CFs. Graphitic CFs are not used here for this study as possibility of PF_6 anion intercalation to the CF may occur while charging the cells above 4.5 V, which may contribute to the capacity and also may destroy the fiber structure during long cycling [62].

We present here a 3D electrode architecture of LMR-NMC onto CF current collector which provides good electronic conductivity, good structural, mechanical stability and corrosion resistant.

3.4.3.2 Electrochemical assessment of LMR and F-LMR-NMC

Figure 3.9 shows the galvanostatic charge-discharge cycling plots of F-LMR-NMC ($\text{Li}_{1.2}\text{Ni}_{0.15}\text{Mn}_{0.55}\text{Co}_{0.1}\text{O}_{2-z}\text{F}_z$) and pristine LMR-NMC ($\text{Li}_{1.2}\text{Ni}_{0.15}\text{Mn}_{0.55}\text{Co}_{0.1}\text{O}_2$) at various C rates between voltages of 2.5 to 4.7 V on CF current collector. As shown in Fig. 3.9(a), on charging above 4.4 V, Li_2MnO_3 component is getting activated and converted to Li_2O and MnO_2 . The voltage profiles presented in Fig. 3.9(a) clearly indicates that F-LMR-NMC shows low charge voltage and hence more charge capacity at low voltages (less than 4.4 V) than pristine LMR-NMC. This is due to partial decrease of average oxidation state of metal ions and suggests that there is partial substitution of O^{2-} by F^- which is evident from increase in a-lattice parameter as it is the measure of M-M bond length [63]. This helps in getting the charge capacity at low voltages ($>200\text{ mAh g}^{-1}$ capacity below 4.4 V for F-LMR-NMC) which minimizes the decomposition of electrolyte on electrode surface thus increasing the interfacial stability. Besides, high stable capacity of LMR-NMC could be obtained in the F-doped sample without adding any high voltage electrolytes. Higher discharge

voltage plateau is also obtained for F-doped LMR-NMC compared to pristine LMR-NMC on CF as presented in Fig. 3.9(b). F-LMR-NMC shows high initial discharge capacity of $\sim 300 \text{ mAh g}^{-1}$ (Fig. 3.9(b)) as compared to pristine material of $\sim 250 \text{ mAh g}^{-1}$ at low discharge rates of C/10 (Fig. 3.9(b)). The irreversible capacity is significantly low, about 5% for the F-doped LMR-NMC compared to pristine LMR-NMC $\sim 25\%$ on CF as presented in charge-discharge voltage profiles in Fig. 3.9(a-b). The high capacity of F-doped LMR-NMC is attributed to high stability of structure.

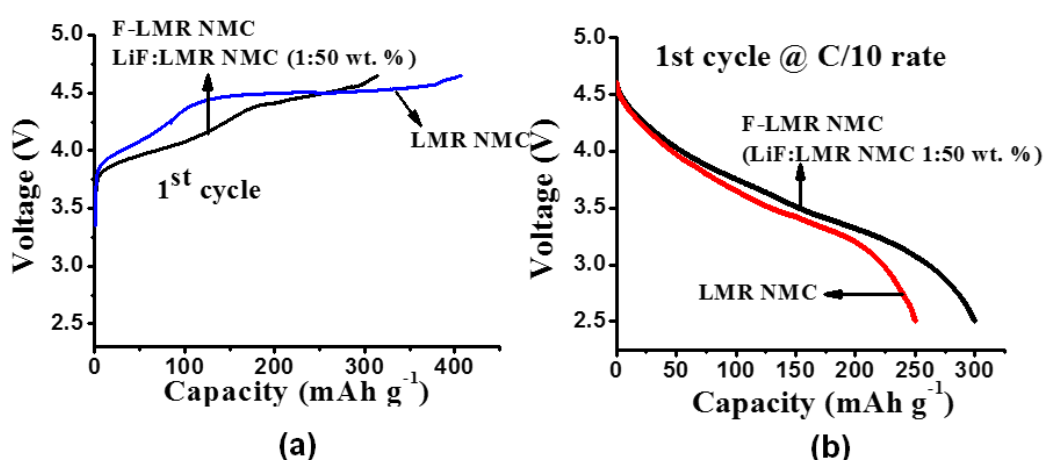


Fig. 3.9: (a) Voltage vs. charge capacity during charge of pristine LMR-NMC and F-LMR-NMC (1:50 wt.%) on CF at C/10 rate. (b) Voltage vs. discharge capacity of pristine LMR-NMC and F-LMR-NMC on CF at C/10 rate

Both pristine LMR-NMC and F-LMR-NMC on CF shows good cycling stability as shown in Fig. 3.10(a) compared electrodes prepared on Al current collector. The electrodes prepared on Al current collector shows gradual decrease in capacity where as both pristine and F-LMR-NMC on CF retain their capacity for long cycles. This is because CF provides good electrical contact to the material in a 3D electrode architecture compared to Aluminum in a 2D structure. Hence, in this work we focus the electrochemical studies of pristine and F-LMR-NMC on CF current collector only. The fluorination of Mn, Ni and Co based layered oxide cathode material has led to significant improvement in cycle life and power capability of the lithium cells. Besides, the specific energy calculated from the discharge voltage profiles presented in Fig. 3. 9(a) are 875 and 1050 Wh kg^{-1} for LMR-NMC and F-LMR-NMC of CF current collector respectively.

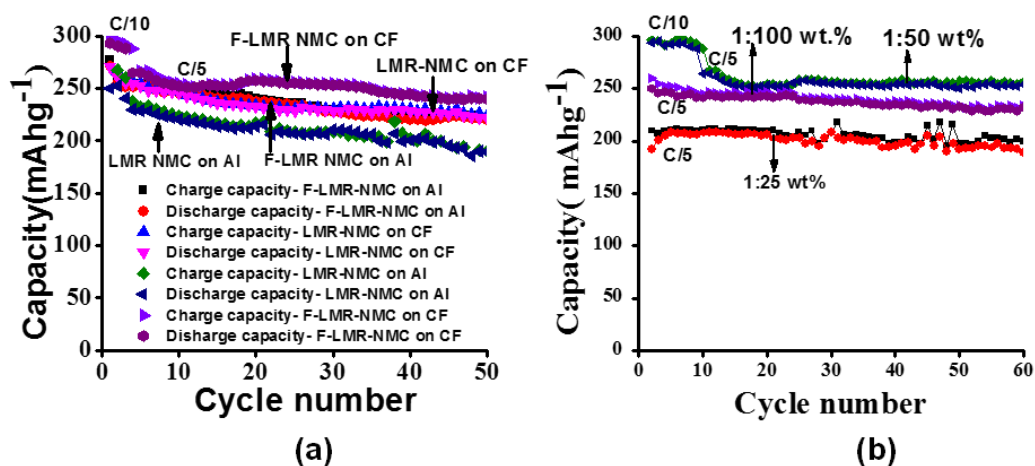


Fig. 3.10: (a) Capacity vs. cycle number of pristine LMR-NMC, F-LMR-NMC (1:50 wt.%), on carbon fiber and Al-foil current collector at C/10 and C/5 rate (as indicated). 1st cycle data is not shown here, (b) Capacity vs. cycle number of different weight ratios of LiF and LMR-NMC (F-LMR-NMC) composite electrode at C/5 rate (as indicated) and 25 °C

The 1:50 weight ratio of LiF: LMR-NMC shows good electrochemical performance in terms of high capacity, good cycling stability compared all other weight ratios as shown in Fig. 3.10(b). So 1:50 wt. % is the optimized ratio for the better electrochemical performance of the LMR-NMC. Whereas, other ratios are showing good cycling stability but less capacity compared to 1:50 wt. % ratio (LiF: LMR-NMC). The 1:25 wt. % is showing less capacity because of high LiF content induces formation strong M-F bonds which will hinder the lithium ion migration. Besides, high amount of LiF will form a thick layer on the surface which also hinders the migration of Lithium ion. Cycle life data of 1:75 wt. % ratio (LiF: LMR-NMC) is not shown here as this composition has very similar capacity of 1:100 wt. % ratio. C rate performance of pristine LMR-NMC, F-LMR-NMC (1:50 wt. %) on CF are shown in Fig. 3.11(a) indicate a high reversible capacity of 15-20 % more can be achieved at low discharge rates and 10-15 % for high C rates (1C and 3C) for F-LMR-NMC compared to pristine LMR-NMC. The coulombic efficiency of both composite cathodes are over 99%. The cycling performance presented in Fig. 3. 11(a-b) indicates a very good capacity retention of F-LMR-NMC during 200 cycles. F-LMR-NMC electrodes delivers high 1C rate capacity of >200 mAh g⁻¹. Besides, cycling performance of various composition F: LMR-NMC carried out at C/5 rate (Fig.

3.10(b) indicates 1:50 wt. % of F: LMR-NMC (2% F in LMR-NMC) electrodes delivers high capacity compared to the 1:100, 1:75 and 1:25 wt. % compositions.

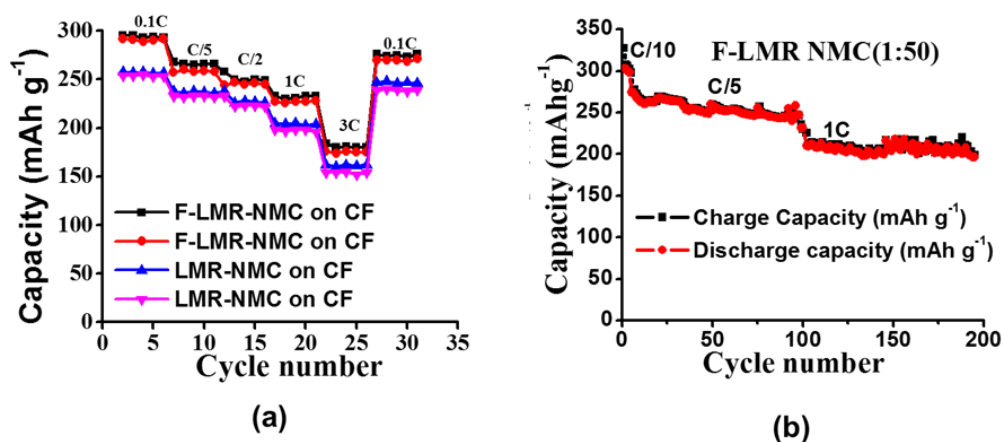


Fig. 3.11: (a) C rate performance of pristine LMR-NMC, F-LMR-NMC (1:50 wt. %), on carbon fiber, (b) Capacity vs. Cycle number of F-LMR-NMC (1:50 wt. %) on carbon fiber during 200 cycles (1-5 at C/10; 6-100 at C/5 and 101-200 at 1 C rate)

There is significant improvement in electrochemical performance of F-LMR-NMC (1:50 wt. %) compared to pristine LMR-NMC in terms of cycling stability, capacity retention and minimized voltage fade as shown in the 5th-50th discharge cycle in Fig. 3.12(a-b). Most of the capacity are obtained at 3 V region in LMR-NMC whereas average operating voltage for F-LMR-NMC has been increased close to 3.5 V. The capacity vs. voltage profiles during 110th and 200th cycles of F-LMR-NMC (1:50 wt. %) at 1C rate is presented in Fig. 3.12(c). The figure shows that there is good capacity retention and very less voltage fade even at high rate of 1C which is due to stability of the crystal structure, minimized surface degradation of electrode surface by LiF coating and high conductivity and corrosion resistance by CF. From the Fig. 3.12(c), it is very clear that there is almost no voltage fade during long term cycling (110th and 200th cycle). Besides, there is very less capacity fade during long cycling.

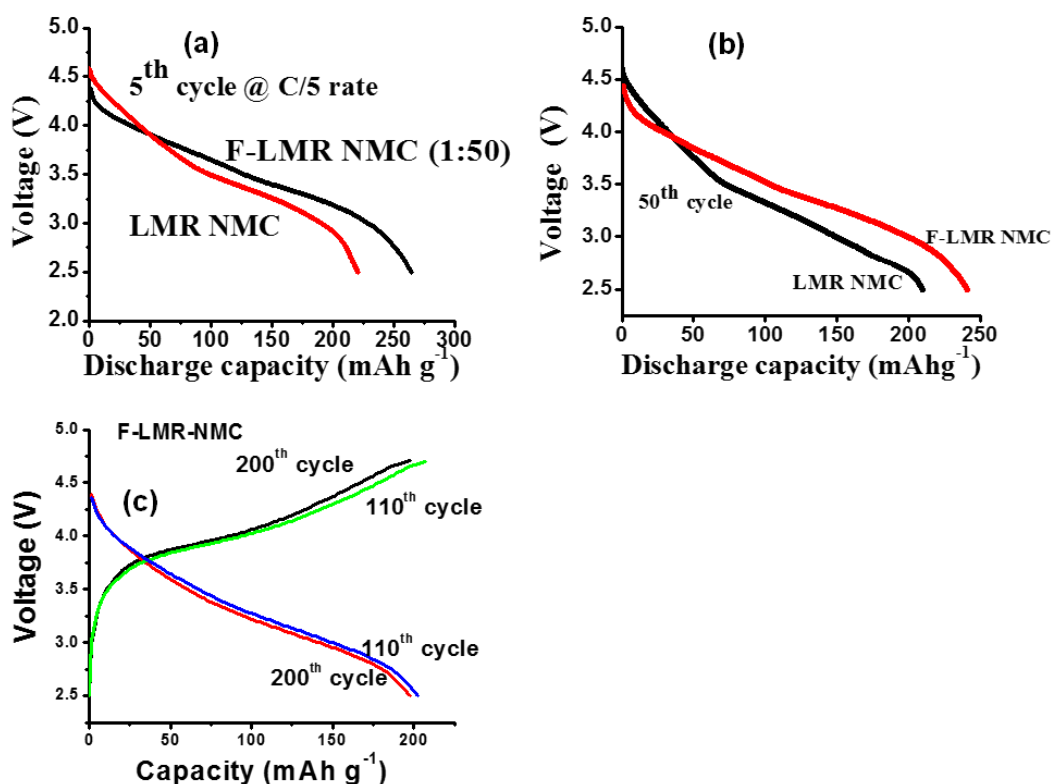


Fig.3.12: Voltage vs. capacity of pristine LMR-NMC and F-LMR-NMC (1:50 wt. %) on carbon fiber during: (a) 5th cycle, (b) 50th cycle, at C/5 rate (the energy loss is calculated from these voltage profiles), and (c) Voltage profile of 110th and 200th cycle of F-LMR-NMC (1:50 wt. %) at 1C rate

The minimized voltage fade in F-LMR-NMC is further supported by the dQ/dV vs. V plots of LMR-NMC and F-LMR-NMC (1:50 wt. %) during 10th, 20th, 30th, and 50th cycles as shown in Fig. 3.13(a-b), respectively. Significant change in voltage dQ/dV vs. V plots of LMR-NMC is observed whereas voltage fade in F-LMR-NMC is minimized. The minimized voltage fade in F-LMR-NMC is attributed to structure stability and decreased inter layer transition metal ion migration which can be explained in the following way, the partial substitution of O²⁻ by F⁻ leads to M-F bond formation which is more stronger than M-O bond and hence stabilizes the structure during cycling. Moreover, the ionic radii of transitional metal ions increases as evident from the increase in ‘a’ lattice parameter. So, the movement (migration) of transition metal ions from transition metal layer to lithium layer decrease is due to high ionic size of transition metal ions which minimizes the cation mixing and in return it minimizes the layered to spinel transformation and finally it minimizes the

voltage fade. The decrease in the average oxidation state of metals on the surface helps in minimizing the voltage fade of the material during long term cycling thus maintaining stable energy density. The specific energy loss for pristine and F-LMR-NMC were $\sim 12.5\%$ and 2% at C/5 rate, respectively.

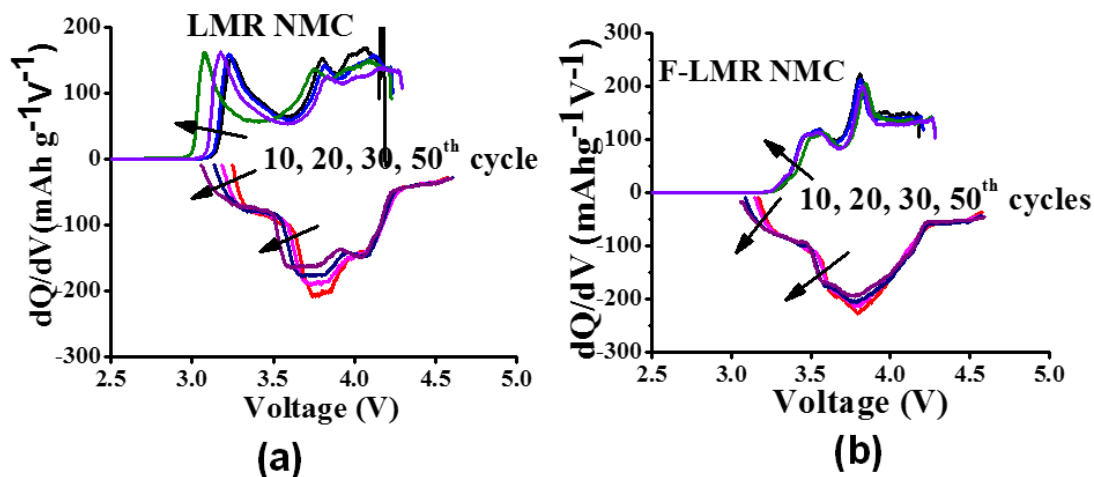


Fig. 3.13: Comparison of dQ/dV vs. V plots of: (a) LMR-NMC, and (b) F-LMR-NMC (1:50 wt. %) during 10th, 20th, 30th, and 50th charge-discharge cycles

The EIS data provides very useful information about Ohmic resistance and charge transfer resistance associated with the cell. In order to get understanding of enhanced capacity and good capacity retention, we present the Nyquist plots of LMR-NMC and F-LMR-NMC on CF current collector and F-LMR-NMC on Al foil current collector during 50th cycles in Fig. 3.14(a-b). The impedance spectra in Fig. 3.14(a-b) shows a comparison of impedances of LMR-NMC and F-LMR-NMC on CF current collector and F-LMR-NMC on Al foil current collector under similar conditions. The data shows both LMR-NMC and F-LMR-NMC on CF have identical Ohmic resistances of about 10 Ohm cm^2 whereas F-LMR-NMC on Al foil current collector shows 18 Ohm cm^2 in 50th cycle. The charge transfer resistance for F-LMR-NMC on CF is much lower (482 Ohm cm^2) in relation to LMR-NMC (902 Ohm cm^2) on CF. However, the charge transfer resistance for F-LMR-NMC (2068 Ohm cm^2) on Al foil current collector is significantly higher in relation to F-LMR-NMC and LMR-NMC on CF. The increase in Ohmic resistances and charge transfer resistance reduces the capacity (Fig. 3.10(a)) during long cycling for F-LMR-NMC on Al foil current collector. From this, it can be explained that both LiF coating and CF current collector

are synergistically helping in decreasing the impedance and thereby improving the rate capability, cycling performance and storage capacity of the electrode thus decreasing the polarization.

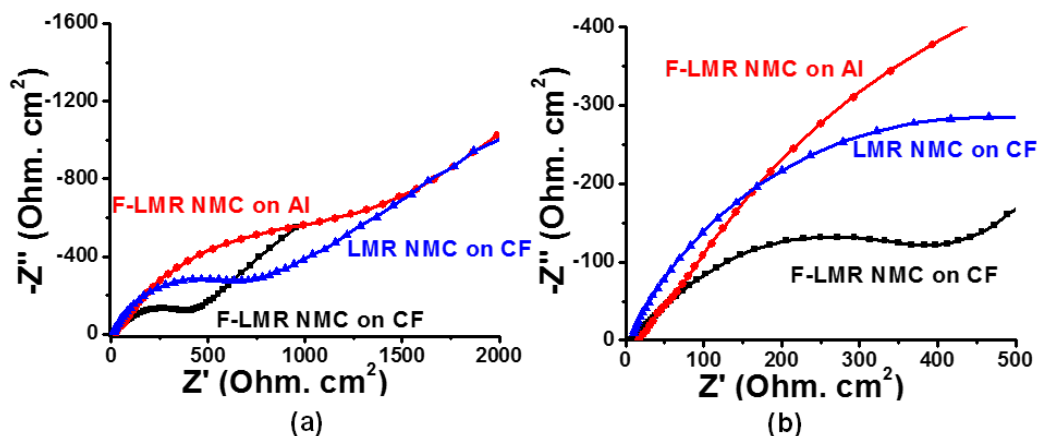


Fig. 3.14: (a) Comparison of impedance spectra of LMR-NMC and F-LMR-NMC on CF current collector and F-LMR-NMC on Aluminum foil current collector after 50 cycles in discharged condition (SoC 0) at equilibrium potential of 3.1 V, (b) Is the zoomed image in the high frequency region of (a)

3.5. Conclusions

LMR-NMC is synthesized by solution combustion followed by fluorine doping by solid state synthesis. XRD of all the F-LMR-NMC samples do not show any impure peaks suggesting crystal structure does not change upon substitution of oxygen with fluorine. F-substitution is confirmed by the change in lattice parameter. LMR-NMC and F-LMR-NMC have multifaceted, mostly platelet like morphologies. Particle sizes between 25-125 nm are observed for LMR-NMC whereas F-LMR-NMC (Fig. 3.2(b-c)) have agglomeration of primary particles in the ranges between 100-300 nm leading to secondary particles in the range of 1.5-2 μm . The fluorine doped cathodes deliver high capacity of $\sim 300 \text{ mAh g}^{-1}$ at C/10 rate (10-20% greater than the conventional LMR-NMC electrodes) and have high discharge voltage plateau (0.25 V) and low charge voltage plateau (0.2 to 0.4 V) compared to pristine LMR-NMC electrodes. Besides, voltage fade, capacity and energy loss are significantly reduced in-relation to the pristine LMR-NMC electrodes. The LiF coating onto LMR-NMC, partially replaces M-O bonds of the material by M-F bonds, thus increasing the interfacial and structural stability. Also, 3D electrode architecture of LMR-NMC onto CF current

collector provides better electronic conductivity, good structural and mechanical stability, thereby delivers high capacity at high C rates, compared to Al foil current collector. It is believed that the study opens a possibility for LMR-NMC cathode material which has almost double the capacity of currently used lithium transition metal oxide or olivine cathodes, can be a substitute cathode for LIBs used in EVs.

References

- [1] J. B. Goodenough, K.-S. Park, The Li-Ion Rechargeable Battery: A Perspective, *J. Am. Chem. Soc.* 135 (2013) 1167–1176.
- [2] B. Scrosati, J. Garche, Lithium batteries: Status, prospects and future, *J. Power Sources* 195 (2010) 2419–2430.
- [3] T. Ohzuku, R. J. Brodd, An overview of positive-electrode materials for advanced lithium-ion batteries, *J. Power Sources* 174 (2007) 449-456.
- [4] V. Etacheri, R. Marom, R. Elazari, G. Salitra, & D. Aurbach, Challenges in the development of advanced Li-ion batteries: a review. *Energy & Environmental Science*, 4 (2011) 3243-3262.
- [5] J. Cho, Y. J. Kim and B. Park, Novel LiCoO₂ Cathode Material with Al₂O₃ Coating for a Li Ion Cell, *Chem. Mater.* 2000 12 (12), 3788-3791.
- [6] T. H. Cho, S. M. Park, M. Yoshio, Preparation of Layered Li [Ni_{1/3}Mn_{1/3}Co_{1/3}] O₂ as a Cathode for Lithium Secondary Battery by Carbonate Coprecipitation Method. *Chem. Lett.*, 33(6) (2004) 704-705.
- [7] S. K. Martha, D. Aurbach et al. A comparative study of electrodes comprising nanometric and submicron particles of LiNi_{0.5}Mn_{0.5}O₂, LiNi_{0.33}Mn_{0.33}Co_{0.33}O₂, and LiNi_{0.4}Mn_{0.4}Co_{0.2}O₂ layered compounds, *J. Power Sources* 189 (2009) 248–255.
- [8] A.K. Padhi, K. S. Naujundaswamy, J. B. Goodenough, LiFePO₄: a novel cathode material for rechargeable batteries, *Electrochim. Soc. Meeting Abstracts*, 96-1 (1996) 73 and Phospho-olivines as positive-electrode materials for rechargeable lithium batteries. *J. Electrochem.Soc.*, 144 (4), 1188-1194.
- [9] S. Y. Chung, J. T Bloking, Y. M. Chiang, Electronically conductive phospho-olivines as lithium storage electrodes". *Nat. Mater.* 1 (2) (2002) 123–128.
- [10] G. Li, H. Azuma, M. Tohda, LiMnPO₄ as the cathode for lithium batteries, *Electrochemical and Solid-State Letters*, 5(6) (2002) A135-A137.

- [11] S. K. Martha, B. Markovsky, J. Grinblat, Y. Gofer, O. Haik, E. Zinigrad, D. Aurbach et al. LiMnPO_4 as an advanced cathode material for rechargeable lithium batteries." *J. Electrochem. Soc.* 156 (2009) A541-A552.
- [12] S. K. Martha, J. Grinblat, O. Haik, E. Zinigrad, T. Drezen, J. H. Miners & Aurbach, $\text{LiMn}_{0.8}\text{Fe}_{0.2}\text{PO}_4$: an advanced cathode material for rechargeable lithium batteries. *Angew. Chem. Int. Edn.* 48 (2009) 8559-8563.
- [13] K. Amine, H. Yasuda, M. Yamachi, Olivine LiCoPO_4 as 4.8 V electrode material for lithium batteries. *Electrochemical and Solid-State Letters*, 3(4) (2000) 178-179.
- [14] H. H. Li, J. Jin, J. P. Wei, Z. Zhou, J. Yan, Fast synthesis of core-shell LiCoPO_4/C nanocomposite via microwave heating and its electrochemical Li intercalation performances. *Electrochem. Commun.*, 11(1) (2009) 95-98.
- [15] M. M. Thackeray, P. J. Johnson, L. A. De Picciotto, P. G. Bruce, J. B. Goodenough, Electrochemical extraction of lithium from LiMn_2O_4 , *Mater. Res. Bull.*, 19(2) (1984) 179-187.
- [16] D. K. Kim, P. Muralidharan, H.-W. Lee, R. Ruffo, Y. Yang, C. K. Chan, H. Peng, R. A. Huggins, and Y. Cui, Spinel LiMn_2O_4 nanorods as lithium ion battery cathodes." *Nano Letters* 8, (2008) 3948-3952.
- [17] Y. Talyosef, B. Markovsky, R. Lavi, G. Salitra, D. Aurbach, D. Kovacheva, R. Stoyanova, Comparing the behavior of nano- and micro-sized particles of $\text{LiMn}_{1.5}\text{Ni}_{0.5}\text{O}_4$ spinel as cathode materials for Li-ion batteries. *J. Electrochem. Soc.*, 154 (2007) A682-A691.
- [18] M. Zanini, S. Basu, J. E. Fischer, Alternate synthesis and reflectivity spectrum of stage 1 lithium-graphite intercalation compound, *Carbon*. 16 (3) ((1978) 211-212.
- [19] S. Basu, C. Zeller, P. J. Flanders, C. D. Fuerst, W. D. Johnson, J. E. Fischer, Synthesis and properties of lithium-graphite intercalation compounds, *Materials Science and Engineering*. 38 (3) (1979) 275-283.
- [20] R. Yazami, P. Touzain, Reversible graphite-lithium negative electrode for electrochemical generators, *J. Power Sources*. 9 (3) (1983) 365-371.
- [21] M. M. Thackeray, C. Wolverton, E. D. Isaacs, Electrical energy storage for transportation—approaching the limits of and going beyond lithium-ion batteries, *Energy Environ. Sci.* 5 (2012) 7854-7863.
- [22] P. G. Bruce, L. J. Hardwick, K. M. Abraham, Lithium-air and lithium-sulfur batteries, *Mater. Res. Soc. Bull.* 36 (2011) 506-512.

- [23] M. M. Thackeray, S.-H. Kang, C. S. Johnson, J. T. Vaughey, R. Benedek, S. A. Hackney, Li_2MnO_3 -stabilized LiMO_2 (M= Mn, Ni, Co) electrodes for lithium-ion batteries, *Mater. Chem.* 17 (2007) 3112-3125.
- [24] S. K. Martha, J. Nanda, G. M. Veith, N. J. Dudney, Electro-chemical and rate performance study of high-voltage lithium-rich composition: $\text{Li}_{1.2}\text{Mn}_{0.525}\text{Ni}_{0.175}\text{Co}_{0.1}\text{O}_2$, *J. Power Sources* 199 (2012) 220-226.
- [25] P. Rozier, J.M. Tarascon, Li-rich layered oxide cathodes for next-generation Li-ion batteries: chances and challenges, *J. Electrochem. Soc.* 162 (2015) A2490–A2499.
- [26] J. Yan, X. Liu, B. Li, Recent progress in Li-rich layered oxides as cathode materials for Li-ion batteries. *RSC Advances*, 4 (2014) 63268-63284.
- [27] J. Zheng, S. Myeong, W. Cho, P. Yan, J. Xiao, C. Wang, C., J. Cho, J. G. Zhang, Li- and Mn-Rich Cathode Materials: Challenges to Commercialization. *Advanced Energy Materials* 7 (2017) 1601284.
- [28] M. Ko, P. Oh, S. Chae, W. Cho, J. Cho, Considering Critical Factors of Li-rich Cathode and Si Anode Materials for Practical Li-ion Cell Applications. *Small*, 11(33), (2015) 4058-4073.
- [29] P. K. Nayak, J. Grinblat, E. Levi, T.R. Penki, M. Levi, Y.-K. Sun, B. Markovsky, D. Aurbach, Remarkably Improved Electrochemical Performance of Li- and Mn-Rich Cathodes upon Substitution of Mn with Ni, *ACS Appl. Mater. Interfaces.* 9 (2016) 4309–4319.
- [30] R. A. Armstrong, M. Holzapfe, P. Novák, C. S. Johnson, S.-H. Kang, M. M. Thackeray, P. G. Bruce, Demonstrating Oxygen Loss and Associated Structural Reorganization in the Lithium Battery Cathode $\text{Li}[\text{Ni}_{0.2}\text{Li}_{0.2}\text{Mn}_{0.6}]\text{O}_2$, *J. Am. Chem. Soc.* 128 (2006) 8694–8698.
- [31] A. Vu, Y. Qin, C.-K. Lin, A. Abouimrane, A. K. Burrell, S. Bloom, D. Bass, J. Barenó, I. Bloom, Effect of composition on the voltage fade phenomenon in lithium-manganese-rich $x\text{Li}_2\text{MnO}_3-(1-x)\text{LiNi}_a\text{Mn}_b\text{Co}_c\text{O}_2$: A combinatorial synthesis approach, *J. Power Sources* 294 (2015) 711-718.
- [32] D. Mohanty, A. S. Sefat, S. Kalnaus, J. Li, R. A. Meisner, E. A. Payzant, D. P. Abraham, L. Wood, C. Daniel, Investigating phase Transformation in the $\text{Li}_{1.2}\text{Co}_{0.1}\text{Mn}_{0.55}\text{Ni}_{0.15}\text{O}_2$ Lithium-ion Battery Cathode during high-voltage hold (4.5 V) via magnetic, X-ray diffraction and electron microscopy studies, *J. Mater. Chem. A*, 1 (2013) 6249–6261.

- [33] S. K. Martha, J. Nanda, Y. Kim, R. Raymond, Uno-cic, S. Pannala, N. J. Dudney, Solid electrolyte coated high voltage layered-layered lithium-rich composite cathode: $\text{Li}_{1.2}\text{Mn}_{0.525}\text{Ni}_{0.175}\text{Co}_{0.1}\text{O}_2$, *J. Mater. Chem. A*, 1 (2013) 5587–5595
- [34] M. Bettge, Y. Li, B. Sankaran, N. D. Rago, T. Spila, R. T. Haasch, I. Petrov, D. P. Abraham, Improving high-capacity $\text{Li}_{1.2}\text{Ni}_{0.15}\text{Mn}_{0.55}\text{Co}_{0.1}\text{O}_2$ -based lithium-ion cells by modifying the positive electrode with alumina, *J. Power Sources* 233 (2013) 346-357.
- [35] J. Zheng, M. Gu, J. Xiao, B. J. Polzin, P. Yan, X. Chen, C. Wang, Ji-G. Zhang, Functioning Mechanism of AlF_3 Coating on the Li- and Mn-Rich Cathode Materials. *Chem. Mater.* 26 (22) (2014) 6320–6327.
- [36] J. Liu, A. Manthiram, Functional surface modifications of a high capacity layered $\text{Li}[\text{Li}_{0.2}\text{Mn}_{0.54}\text{Ni}_{0.13}\text{Co}_{0.13}]\text{O}_2$ cathode, *J. Mater. Chem.* 20 (2010) 3961–3967.
- [37] L. Fu, H. Liu, C. Li, Y.P. Wu, E. Rahm, R. Holze, H. Wu, Surface modifications of electrode materials for lithium ion batteries, *Solid State Sci.* 8 (2006) 113–128.
- [38] K.G. Gallagher, S.-H. Kang, S.U. Park, S.Y. Han, $x\text{Li}_2\text{MnO}_3 \cdot (1-x)\text{LiMO}_2$ blended with LiFePO_4 to achieve high energy density and pulse power capability, *J. Power Sources*. 196 (2011) 9702–9707.
- [39] Y. Zuo, B. Huang, C. Jiao, R. Lv, G. Liang, Enhanced electrochemical properties of $\text{Li}[\text{Li}_{0.2}\text{Mn}_{0.54}\text{Ni}_{0.13}\text{Co}_{0.13}]\text{O}_2$ with ZrF_4 surface modification as cathode for Li-ion batteries, *J. Mater. Sci. - Mater. Electron.* (2017) 1–11.
- [40] Q. Wang, J. Liu, A.V. Murugan, A. Manthiram, High capacity double-layer surface modified $\text{Li}[\text{Li}_{0.2}\text{Mn}_{0.54}\text{Ni}_{0.13}\text{Co}_{0.13}]\text{O}_2$ cathode with improved rate capability, *J. Mater. Chem.* 19 (2009) 4965–4972.
- [41] Y.-K. Sun, M.-J. Lee, C.S. Yoon, J. Hassoun, K. Amine, B. Scrosati, The Role of AlF_3 Coatings in Improving Electrochemical Cycling of Li-Enriched Nickel-Manganese Oxide Electrodes for Li-Ion Batteries, *Adv. Mater.* 24 (2012) 1192–1196.
- [42] S. Shi, J. Tu, Y. Tang, X. Liu, Y. Zhang, X. Wang, C. Gu, Enhanced cycling stability of $\text{Li}[\text{Li}_{0.2}\text{Mn}_{0.54}\text{Ni}_{0.13}\text{Co}_{0.13}]\text{O}_2$ by surface modification of MgO with melting impregnation method, *Electrochim. Acta.* 88 (2013) 671–679.
- [43] J. Zheng, J. Li, Z. Zhang, X. Guo, Y. Yang, The effects of TiO_2 coating on the electrochemical performance of $\text{Li}[\text{Li}_{0.2}\text{Mn}_{0.54}\text{Ni}_{0.13}\text{Co}_{0.13}]\text{O}_2$ cathode material for lithium-ion battery, *Solid State Ionics.* 179 (2008) 1794–1799.
- [44] S. B. Chikkannanavar, D. M. Bernardi, L. Liu, A review of blended cathode materials for use in Li-ion batteries, *J. Power Sources* 248 (2014) 91-100.

- [45] P. Oh, M. Ko, S. Myeong, Y. Kim, J. Cho, A Novel Surface Treatment Method and New Insight into Discharge Voltage Deterioration for High-Performance 0.4 Li₂MnO₃–0.6 LiNi_{1/3}Co_{1/3}Mn_{1/3}O₂ Cathode Materials. *Advanced Energy Materials*, 4 (2014) 1400631.
- [46] S. K. Martha, J. Nanda, G. M. Veith, N. J. Dudney, Surface studies of high voltage lithium rich composition: Li_{1.2}Mn_{0.525}Ni_{0.175}Co_{0.1}O₂, *J. Power Sources* 216 (2012) 179–186.
- [47] G. H. Kim, J. H. Kim, S. T. Myung, C. S. Yoon, Y. K. Suna, Improvement of High-Voltage Cycling Behavior Surface-Modified Li[Ni_{1/3}Co_{1/3}Mn_{1/3}]O₂ Cathodes by Fluorine Substitution for Li-Ion Batteries, *J. Electrochem. Soc.* 152 (9) (2005) A1707–A1713.
- [48] O. Sha, Z. Tang, S. Wang, W. Yuan, Z. Qiao, Q. Xu, L. Ma, The multi-substituted LiNi_{0.475}Al_{0.01}Cr_{0.04}Mn_{1.475}O_{3.95}F_{0.05} cathode material with excellent rate capability and cycle life, *Electrochimica. Acta.* 77 (2012) 250.
- [49] K. Kubo, M. Fujiwara, S. Yamada, S. Arai, M. Kanda, Synthesis and electrochemical properties for LiNiO₂ substituted by other elements, *J. Power Sources* 68 (1997) 553.
- [50] G. H. Kim, M. H. Kim, S. T. Myung, Y. K. Sun, Effect of fluorine on LiNi_{1/3}Co_{1/3}Mn_{1/3}O_{2-z}F_z as lithium intercalation material, *J. Power Sources* 146 (2005) 602.
- [51] S. U. Woo, B. C. Park, C. S. Yoon, S. T. Myung, J. Prakash, Y. K. Sun, Improvement of electrochemical performances of LiNi_{0.8}Co_{0.1}Mn_{0.1}O₂ cathode materials by fluorine substitution, *J. Electrochem. Soc.* 154 (2007) A649.
- [52] S.-W. Oh, S.-H. Park, J.-H. Kim, Y. C. Bae, Y.-K. Sun, Improvement of electrochemical properties of LiNi_{0.5}Mn_{1.5}O₄ spinel material by fluorine substitution, *J. Power Sources* 157 (2006) 464–470.
- [53] G. G. Amatucci, N. Pereira, Fluoride based electrode materials for advanced energy storage devices, *J. Fluorine Chemistry* 128 (2007) 243–262.
- [54] Q. Zhu, S. Zheng, X. Lu, Y. Wan, Q. Chen, J. Yang, L. Zhang, Z. Lu, Improved cycle performance of LiMn₂O₄ cathode material for aqueous rechargeable lithium battery by LaF₃ coating, *J. Alloys Compounds*, 654 (2016) 384–391.
- [55] Y.-K. Sun, M.-J. Lee, C.S. Yoon, J. Hassoun, K. Amine, B. Scrosati, The Role of AlF₃ Coatings in Improving Electrochemical Cycling of Li-Enriched Nickel-Manganese Oxide Electrodes for Li-Ion Batteries, *Adv. Mater.* 24 (2012) 1192–1196.

- [56] T. C. Hyams, J. Go, T. M. Devine, Corrosion of Aluminum Current Collectors in High-Power Lithium-Ion Batteries for Use in Hybrid Electric Vehicles, *J. Electrochem. Soc.* 154(8) (2007) C390-C396.
- [57] R. E. Ruther, A. F. Callender, H. Zhou, S. K. Martha, J. Nanda, Raman microscopy of lithium-manganese-rich transition metal oxide cathodes, *J. Electrochem. Soc.* 162 (2015) A98-A102.
- [58] S. K. Martha, H. Sclar, Z. Framowitz, D Kovacheva, N. Saliyski, Y. Gofer, P. Sharon, E. Golik, B. Markovsky, Doron Aurbach, A comparative study of electrodes comprising nanometric and submicron particles of $\text{LiNi}_{0.5}\text{Mn}_{0.5}\text{O}_2$, $\text{LiNi}_{0.33}\text{Mn}_{0.33}\text{Co}_{0.33}\text{O}_2$, and $\text{LiNi}_{0.4}\text{Mn}_{0.4}\text{Co}_{0.2}\text{O}_2$ layered compounds, *J. Power Sources* 189 (2009) 248–255.
- [59] A. H. Whitehead, M. Schreiber, Current Collectors for Positive Electrodes of Lithium-Based Batteries, *J. Electrochem. Soc.* 152 (2005) A2105-A2113.
- [60] B. Markovsky, F. Amalraj, H. E. Gottlieb, Y. Gofer, S. K. Martha, D. Aurbach, On the Electrochemical Behavior of Aluminum Electrodes in Nonaqueous Electrolyte Solutions of Lithium Salts, *J. Electrochem. Soc.* 157 (2010) A423-A429.
- [61] S. K. Martha, N. J. Dudney, J. O. Kiggans, J. Nanda, Electrochemical Stability of Carbon Fibers Compared to Aluminum as Current Collectors for Lithium-Ion Batteries, *J. Electrochem. Soc.* 159(10) (2012) A1652-A1658.
- [62] J. A. Seel, J. R. Dahn, Electrochemical Intercalation of PF_6 into Graphite. *J. Electrochem. Soc.* 147 (2000) 892-898.
- [63] H.-S. Shin, S.-H. Park, C. S. Yoon, Y.-K. Sun, Effect of Fluorine on the Electrochemical Properties of Layered $\text{Li}[\text{Ni}_{0.43}\text{Co}_{0.22}\text{Mn}_{0.35}]\text{O}_2$ Cathode Materials via a Carbonate Process. *Electrochem. Solid-State Lett.* 8 (2005) A559-A563.

Chapter 4

Synergistic Effect of Magnesium and Fluorine Doping on the Electrochemical Performance of LMR-NMC Cathodes for Lithium-Ion Batteries

4.1. Abstract

This Chapter describes Mg-doped LMR-NMC ($\text{Li}_{1.2}\text{Ni}_{0.15-x}\text{Mg}_x\text{Mn}_{0.55}\text{Co}_{0.1}\text{O}_2$), synthesized by combustion method followed by LiF coating through solid state synthesis. In this approach, we substituted the Ni^{2+} by Mg^{2+} in varying mole percentages ($x = 0.02, 0.05, 0.08$) and partly oxygen by fluorine (LiF: LMR-NMC= 1:50 wt. %). The synergistic effect of both magnesium and fluorine substitution on electrochemical performance of LMR-NMC is studied by electrochemical impedance spectroscopy and galvanostatic charge-discharge cycling. Mg-F doped LMR-NMC (Mg-0.02 mole) composite cathodes show excellent discharge capacity of $\sim 300 \text{ mAh g}^{-1}$ at C/20 rate whereas pristine LMR-NMC shows the initial capacity around 250 mAh g^{-1} in the voltage range between 2.5 and 4.7 V. The Mg-F doped LMR-NMC shows lesser Ohmic and charge transfer resistance, cycles well and delivers a stable high capacity of $\sim 280 \text{ mAh g}^{-1}$ at C/10 rate. The voltage decay which is the major issue of LMR-NMC is minimized in Mg-F doped LMR-NMC compared to pristine and F-LMR-NMC.

4.2. Background and Motivation

The current research efforts in LIBs are directed to achieve high energy density, reducing the cost and improved safely [1]. As discussed in Chapter 3, layered LMR-NMC cathodes are the possible substitutes to current transition metal oxide, phosphate cathodes [1-5] which can deliver high stable reversible capacity of $>250 \text{ mAh g}^{-1}$ when it is cycled in the voltage window of 2.5 - 4.8 V [6-12]. Layered LMR-NMC cathodes are attractive cathodes for powering electric vehicle (EV) because of their high energy density ($>1000 \text{ Wh kg}^{-1}$). But still the application of LMR-NMC in EVs and HEV's is limited because of serious materials issues associated with it. As discussed in Chapter 1 and 3, the energy loss is due to suppression of voltage profiles during cycling which is related with the phase transformation from a layered structure to spinel structure, need to be addressed before it is considered as a potential candidate for next generation cathode material for lithium-ion batteries [6-13]. The transition metal ions such as Ni, Mn, Co (mostly Ni) migrate in the lattice from transitional metal layer to Li-layer. This leads to the formation of spinel domain during high voltage cycling $>4.4 \text{ V}$ [7-11]. The structural transformation from layered to spinel causes significant voltage drop from 3.8 V region to $< 3 \text{ V}$ region thereby reducing energy density from 1000 Wh kg^{-1} to 750 Wh kg^{-1} which makes LMR-NMC practically not suitable for EVs or related applications [7, 9-10]. Besides, LMR-NMC electrodes have the limited capacity retention upon prolonged high voltage ($>4.4 \text{ V}$) cycling, due to formation of insulating surface films, formed on the electrode surface because of electrolyte decomposition and reaction products [10].

The improved electrochemical performance of LMR-NMC can be obtained by a nanometer layer of surface coatings such as of lithium conducting solid electrolyte: lithium phosphorus oxynitride (LiPON) [9], Al_2O_3 , RuO_2 , TiO_2 , AlPO_4 , CoPO_4 , AlF_3 , LiFePO_4 , LiV_3O_8 , $\text{Li}_4\text{Mn}_5\text{O}_{12}$, VO_2 , Mgo , $\text{AlF}_3 \text{ ZrF}_4$ etc. surface coatings or blendings in order to improve the interfacial stability and cyclability [14-24]. Although the surface coatings improves the rate performance and cycle life to some extent but does not help to mitigate the voltage fade associated with structural transition of LMR-NMC during cycling.

In continuation to Chapter 3, in this Chapter we describe another attempt to improve interfacial stability and reduce voltage decay through both cation and anion dopings. By cation doping or substituting Mn or Ni or Co with other cations (like Ru, Mg, Ti, Al etc.) [14, 22-24] voltage fade has been significantly improved due to structural stabilization. Park et al. revealed that the substitution of 6 mole % of Al³⁺ ions with Mn and Ni in LMR-NMC [Li_{1.15}(Ni_{0.275-x/2}Mn_{0.575-x/2}Al_x)O₂] could avoid the structural deterioration of electrode material allowing greater discharge capacities of 210 mAh g⁻¹ at a cut off voltage of 2.5-4.6 V while the undoped cathode delivers 150 mAh g⁻¹ [24]. 5 wt. % Na doping significantly improves conductivity and mitigate layer to spinel structure conversion because Na⁺ ion exchange occurs upon contact of the cathode material with the electrolyte produces a volume expansion of the crystal lattice which accelerates Ni migration to Li depleted regions during oxidation of Li₂MnO₃ component in the first cycle [25]. Besides, Na doped NMC has better Ni reduction efficiency to provide higher rate capability and Na doped NMC was oxidized to a higher Mn valence state compared to its undoped NMC. In an another approach, Aurbach and coworkers demonstrated 5% Al doping onto Mn site of LMR-NMC exhibits 96% capacity retention as compared to 68% capacity retention for LMR-NMC after 100 cycles. Al doping reduces voltage decay and improve thermal stability of LMR-NMC [26]. Wang et al. stabilized the crystal structure by partial substituting 4% of Mg with lithium in transitional metal layer of Li(Li_{0.2-2x}Mg_xCo_{0.13}Ni_{0.13}Mn_{0.54})O₂ and delivers an initial capacity of 272 mAh g⁻¹ (between 2.0 V and 4.8 V) and retains 93 % of capacity after 300 charge-discharge cycles [27]. The superior electrochemical performances of the Mg-doped material is due to the enhancement of the structural stability by substitution of Li by Mg in the TM layer, which effectively suppresses the cation mixing arrangement, leading to the alleviation of the phase change during lithium-ion insertion and extraction.

Chapter 3 briefly explained about the anion doping/ LiF coating onto LMR-NMC, improves interfacial stability thereby improves capacity retention, irreversible capacity and reduces voltage decay. Partial substitution oxygen with fluorine stabilizes the crystal lattice structure [27-35] due to smaller c-axis variation and fluorine coatings.

There are reports of both cation and anion dopings such as magnesium and fluorine substitution in NMC [$\text{Li}(\text{Ni}_{1/3}\text{Co}_{1/3}\text{Mn}_{1/3-x}\text{Mg}_x)\text{O}_{2-y}\text{F}_y$] reduces cation mixing during cycling, improves crystallinity and tap density which in turn influence the improvement in capacity retention and thermal stability[33-34, 36-38].

It is preferable to replace Ni site with Mg because of same charge [8, 36-38]. Besides, Mg^{2+} ions do not participate in redox process, making it possible to maintain the inter layer space during repetitive Li^+ de/intercalation [34].

In this work, we studied partial substitution of Mg^{2+} with Ni^{2+} and oxygen with fluorine onto LMR-NMC. Mg^{2+} is substituted in Ni^{2+} site because both the elements have same charge and Ni^{2+} and Mg^{2+} have approximately same ionic radii (0.69 Å for Ni^{2+} and 0.72 Å for Mg^{2+}). Moreover, majority of reports indicate Ni migration is more from transition metal layer to the lithium layer. Substitution of oxygen with fluorine partially replaces M-O bonds with M-F bonds, helps in protecting surface from degradation due to decomposition of electrolyte at higher voltages and stabilizing the structure as M-F bond is stronger than M-O bond (Discussed in Chapter 3). Besides, F-substitution helps to reduce charging voltage which is beneficial for LMR-NMC to obtain high capacity at low voltages without electrolyte additives. And further substituting Ni^{2+} with Mg^{2+} helps in minimizing the cation migration as it blocks the tetrahedral void through which movement of cations takes place from transition metal layer to Li-layer [37-44]. Moreover, presence of high ionic radii metal ion increases the bond strength thus stabilizing the crystal system.

4.3. Experimental

4.3.1. Synthesis of LMR-NMC and Mg-F doped -LMR-NMC

Mg-doped LMR-NMC is synthesized by combustion method by taking stoichiometric amounts of $\text{Li}(\text{NO}_3)$ (1.2 mole), $\text{Mn}(\text{NO}_3)_2 \cdot 4\text{H}_2\text{O}$ (0.55 mole), $\text{Ni}(\text{NO}_3)_2 \cdot 6\text{H}_2\text{O}$ (0.13 mole), $\text{Co}(\text{NO}_3)_2 \cdot 6\text{H}_2\text{O}$ (0.1 mole), $\text{Mg}(\text{NO}_3)_2 \cdot 6\text{H}_2\text{O}$ (0.02 mole) as oxidants and glycine (all chemicals from Alfa Aesar) as fuel in a beaker and dissolved in minimum amount of water, stirred and heated at 100 °C till thick gel is obtained followed by placing it in a furnace which is preheated to 400 °C. At this temperature auto ignition takes place and finally gives the product. The as prepared sample was kept at 400 °C

for about 30 min for complete removal of organics. The obtained product is mixed with LiF (in the wt. ratio of 1:50 = LiF: LMR-NMC) and ground in a mortar pestle for half an hour followed by annealing at 800 °C for 20 hrs in air. As discussed in Chapter 3, 1: 50 weight % LiF: LMR-NMC gives optimum electrochemical performance. So this composition was chosen for the current study.

4.3.2. Structural, physical and electrochemical characterization of LMR-NMC and F-LMR NMC

Structural, physical and compositional analyses were conducted by using powder XRD, SEM and EDAX, respectively as explained in experimental part of Chapter 3. The electrochemical performance of the samples comprising pristine LMR-NMC and different ratios of Mg and F-doped LMR-NMC [$\text{Li}_{1.2}\text{Ni}_{0.15-x}\text{Mg}_x\text{Mn}_{0.55}\text{Co}_{0.1}\text{O}_{2-y}\text{F}_y$] ($x=0.02, 0.05, 0.08$ mole and 1:50 -LiF: LMR-NMC; $y= 0.02$) as active masses were measured by using Solartron cell test system and Arbin battery cyler similar to the electrochemical experiments explained in Chapter 3. The impedance measurements were carried out in a frequency range between 1 MHz and 10 mHz in fully discharged condition (State-of-Charge, SoC 0) after 50 cycles at 3.1 V (2hrs rest after discharging to 2.5V). Charge-discharge cycling were carried out in the potential range between 2.5 V and 4.7 V using CC-CV protocol.

The electrodes were prepared by making the composite of 80% active material, 10% PVdF (Kynar) and 10% carbon black (C65, Timcal) in N-methyl pyrrolidone (Sigma Aldrich) and coated on to the Aluminum foil (>99.9%, Strem chemicals, Inc., USA) current collector by using doctor blade technique. The composite electrodes were dried under vacuum at 90 °C followed by punching them into 1 cm² area circular discs. The electrodes were calendared at 1 Ton/cm². The cells were assembled in an Argon filled glove box similar to the cell assembly explained in experimental part of Chapter 3.

4.4. Results and Discussion

4.4.1. Structure and morphology

The XRD pattern of the pristine and Mg-F doped LMR-NMC samples are presented in Fig. 4.1, is indexed based on α -NaFeO₂ structure. It shows a small peak in the range

of 21° to 25° indicating the formation of monoclinic Li_2MnO_3 phase having C2/m space group and rest of the peaks belong to rhombohedral LiMO_2 (M=Ni, Mn, Co) with $R\bar{3}m$ space group. No extra peaks are observed indicating that there is no formation of impure phase in the LMR-NMC crystal system by doping with Mg^{2+} and F.

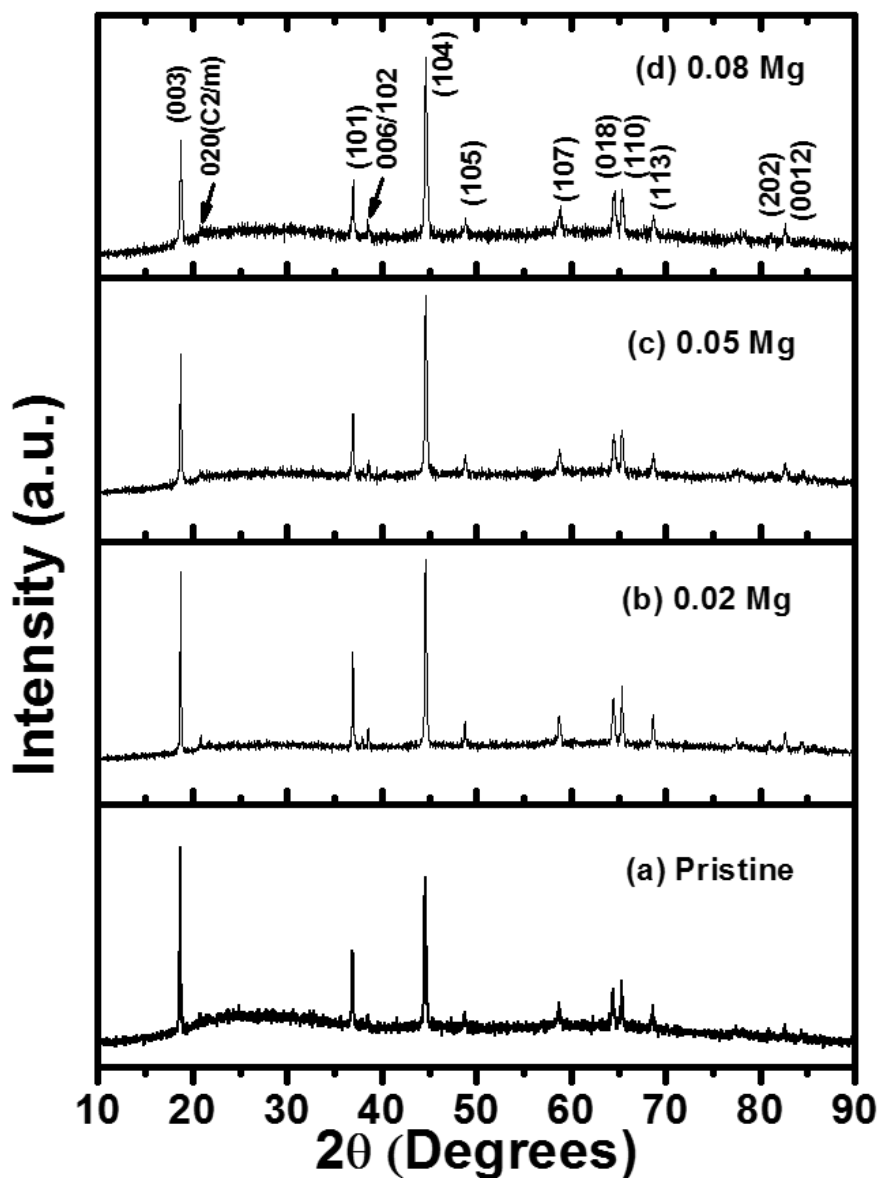


Fig. 4.1: XRD patterns of: (a) pristine LMR-NMC, (b) Mg(0.02)-F-LMR-NMC (c) Mg (0.05)-F-LMR-NMC, and (d) Mg (0.08)-F-LMR-NMC synthesized by solution combustion method followed by LiF coating on to LMR-NMC by solid state synthesis at 800°C for 20 hrs

From the data in Fig. 4.1, the calculated ratio of relative intensity of I_{003}/I_{104} is 1.28, 0.94, 0.72, 0.62 for pristine, 0.02, 0.05, 0.08 Mg-F doped LMR-NMC, respectively indicating degree of cation ordering decreases for the 0.02 Mg-F-LMR-NMC to 0.08 Mg-F-LMR-NMC. Thereby the electrochemical activity of pristine and 0.02 Mg-F-doped LMR-NMC cathode materials in terms of capacity and rates of Li de-insertion/insertion are supposed to be very good. So the results and discussion for electrochemical performance here is limited to pristine and 0.02 Mg-F-doped LMR-NMC ($\text{Li}_{1.2}\text{Ni}_{0.13}\text{Mg}_{0.02}\text{Mn}_{0.55}\text{Co}_{0.1}\text{O}_{2-x}\text{F}_x$) cathodes only [33-34]. There is a clear splitting of (006)/(102) peaks and (018)/(110) peaks in all the XRD plots suggest the formation of a well ordered layered structure. The XRD patterns of pristine LMR-NMC and different ratios of magnesium with F-doped LMR-NMC samples are refined by Reitveld refinement using Full Prof Suite Program to find the lattice parameters. The lattice parameter of pristine LMR-NMC is $a = 2.8539 \text{ \AA}$ and $c = 14.2519 \text{ \AA}$ and for $\text{Li}_{1.2}\text{Ni}_{0.13}\text{Mg}_{0.02}\text{Mn}_{0.55}\text{Co}_{0.1}\text{O}_{2-x}\text{F}_x$ is $a = 2.85728 \text{ \AA}$ and $c = 14.2437 \text{ \AA}$. The increase in a-lattice parameter is due to relatively higher ionic radii of Mg^{2+} compared to Ni^{2+} and partial reduction of metal ions due to partial substitution of oxygen with fluorine.

The morphology of the LMR-NMC and Mg-F doped sample are shown in Fig. 4.2(a) and (b-c), respectively. The SEM images in both pristine and doped material have multifaceted morphology. The pristine LMR-NMC has particle sizes in the range of 25-100 nm uniformly distributed whereas Mg-F doped LMR-NMC have agglomeration of particles leading to nearly pomegranate like morphology having secondary particles in the range of 1.5-2 μm and primary particles in the range of 75-150 nm. This clearly indicates Mg-F doping increases the tap density of the material.

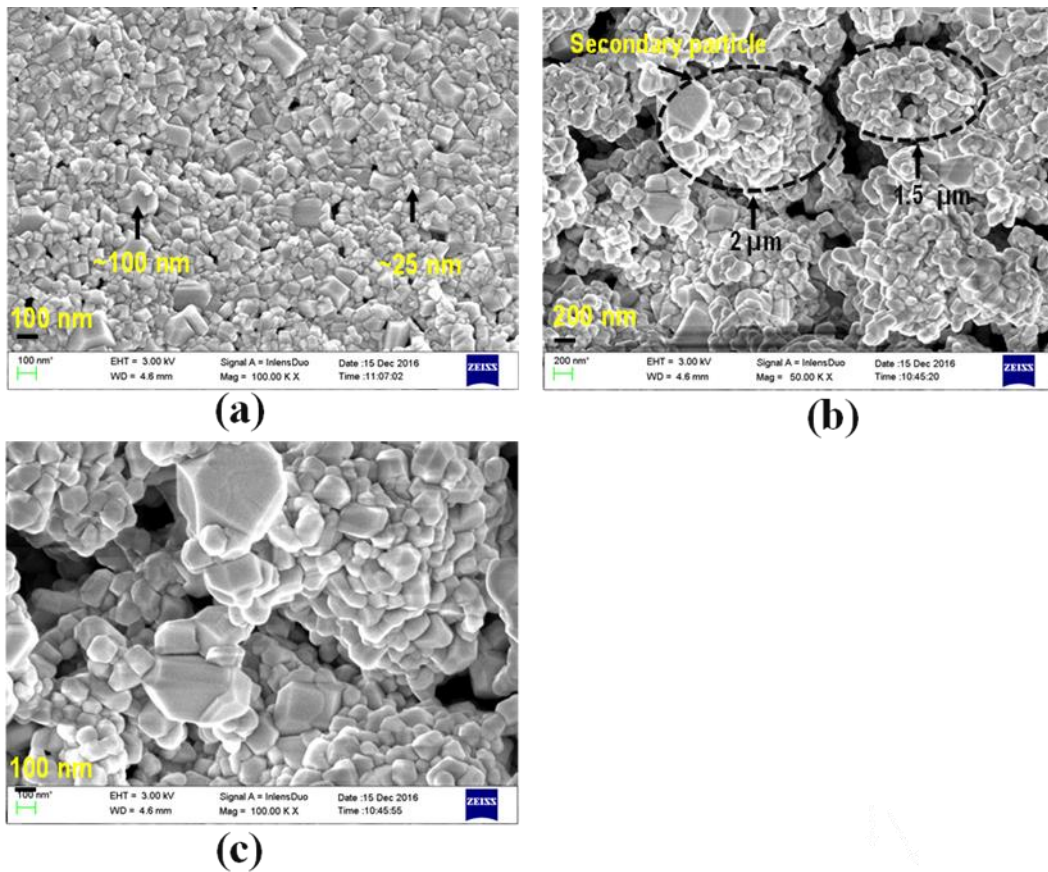


Fig. 4.2: FESEM image of: (a) pristine LMR-NMC, and (b-c) $\text{Li}_{1.2}\text{Ni}_{0.13}\text{Mg}_{0.02}\text{Mn}_{0.55}\text{Co}_{0.1}\text{O}_{2-x}\text{F}_x$ at 50 K X and 100 K X magnifications, respectively

Mg and F dopings/coatings have been confirmed by EDAX. From the elemental mapping presented in Fig. 4.3, it is clear that the LMR-NMC material has Mg and F dopings and show the uniform distribution of Mg and F throughout the material. ICP analysis shows the composition of $\text{Li}_{1.2}\text{Ni}_{0.13}\text{Mg}_{0.02}\text{Mn}_{0.55}\text{Co}_{0.1}\text{O}_{2-x}\text{F}_x$ and ion chromatography confirms the 0.02 mole of F doping onto Mg-doped LMR-NMC.

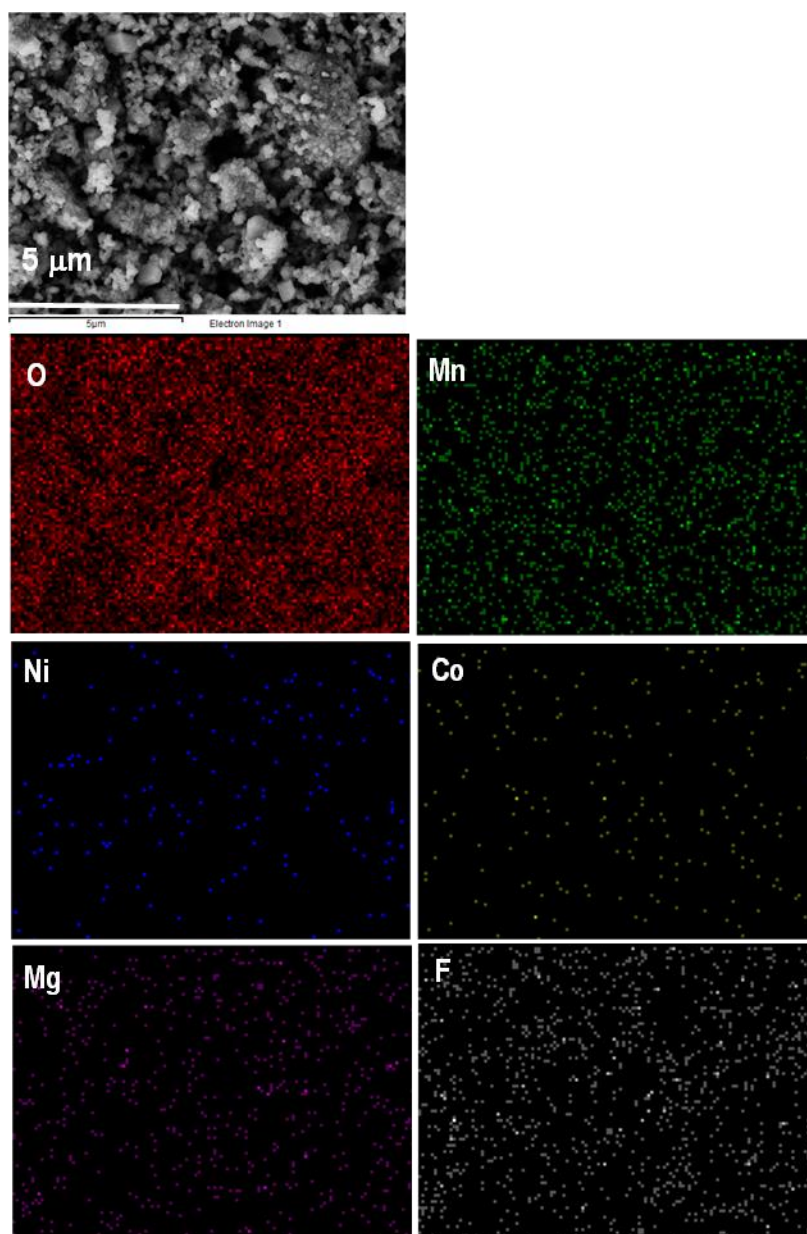


Fig.4.3: O, Mn, Ni, Co, Mg, F mapping of $\text{Li}_{1.2}\text{Ni}_{0.13}\text{Mg}_{0.02}\text{Mn}_{0.55}\text{Co}_{0.1}\text{O}_{2-x}\text{F}_x$. The 1st image is corresponding SEM image of elemental mapping

4.4.2. Electrochemical performance

Mg-F doped LMR-NMC has improved electrochemical performance compared to pristine LMR-NMC. The Mg-F doped LMR-NMC composite cathodes show high initial discharge capacity of 300 mAh g^{-1} at C/20 rate and $\sim 280 \text{ mAh g}^{-1}$ at C/10 rate (Fig. 4.4(a) and (b)) whereas first discharge capacity of pristine LMR-NMC is around 250 mAh g^{-1} at C/10 rate (Fig. 4.4(a-b)). Mg-F doped LMR-NMC composite cathodes

cycles very well over 70 cycles whereas pristine LMR-NMC cathodes shows significant loss in capacity, over 15%, in 50 cycles (Fig. 4.4(a)). Besides, Mg-F doped LMR-NMC composite cathodes delivers high capacity of 10-15% at low and high C rates (1C and 3C) compared to pristine LMR-NMC (Fig. 4.4(b)). The coulombic efficiency of doped composite cathodes are over 99% compared to 98% for pristine LMR-NMC cathodes. The coulombic efficiency of pristine LMR-NMC at higher C rates (1C and 3C) are comparatively lower than low C rates. This could be due to high interfacial instability (high IR drops) at high currents. Moreover, the voltage fade is observed in pristine LMR-NMC (discussed in Chapter 3) which could contribute considerably to loss of energy. Mg-F doped LMR-NMC composite cathodes have improved capacity and capacity retention because of improved conductivity and electrochemical stability due to Mg and F doping.

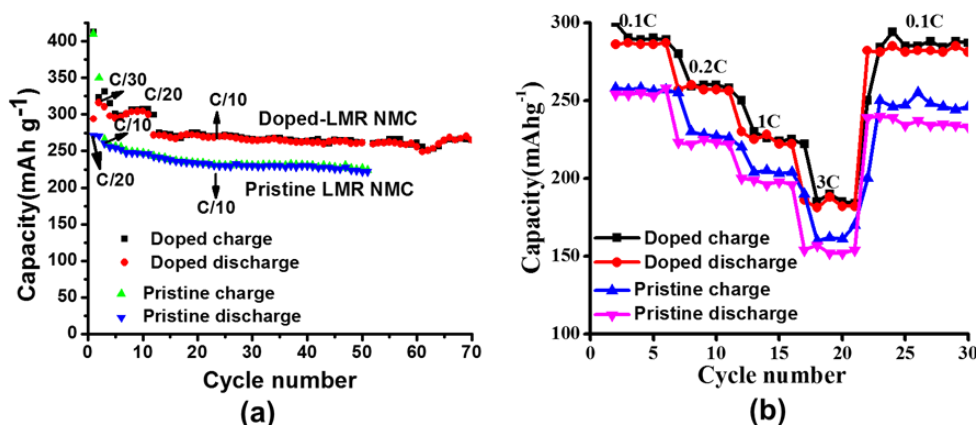


Fig 4.4: (a) Capacity vs. cycle number at C/10 rate (initial cycles at C/30-20 rate as marked), and (b) C rate performance of pristine and Mg-F doped LMR NMC (1st cycle in Fig. 4.4(b) is removed for better clarity between the charge-discharge capacities)

The differential capacity curves (dQ/dV vs. V plots) of both pristine and doped LMR-NMC composite cathodes are compared in Fig. 4.5(a), and (b), respectively. The 1st charge and discharge plots for both pristine and doped LMR-NMC composite cathodes are compared in Fig. 4.6(a) indicating low charge and high-discharge plateau

voltage for the doped composite cathodes. This is due to improved conductivity and interfacial stability (Low IR drops) due to Mg and F dopings. More than 200 mAh g^{-1} is obtained for doped cathodes compared to $\sim 100 \text{ mAh g}^{-1}$ for the pristine LMR-NMC composite cathode below 4.5 V. This helps to get high capacity of doped cathodes below 4.7 V without electrolyte additives. Comparison of discharge capacities between Fig. 4.6(b) and (c) (even Fig. 4.4(a)) shows LMR-NMC composite cathodes have $>15\%$ loss in capacity in 50 cycles whereas doped samples have any loss in capacity after 70 cycles (Fig. 4. 4(a)) at C/10 rate. LMR-NMC composite cathodes shows significant voltage drop compared to doped LMR-NMC sample (Fig 4.5(a) and (b), Fig. 4.6(b-d)). This indicates loss of energy density of Mg-F doped LMR- NMC is minimized compared to F- LMR-NMC and pristine LMR-NMC in which capacity and voltage fade are very high (Fig. 4.6(d)).

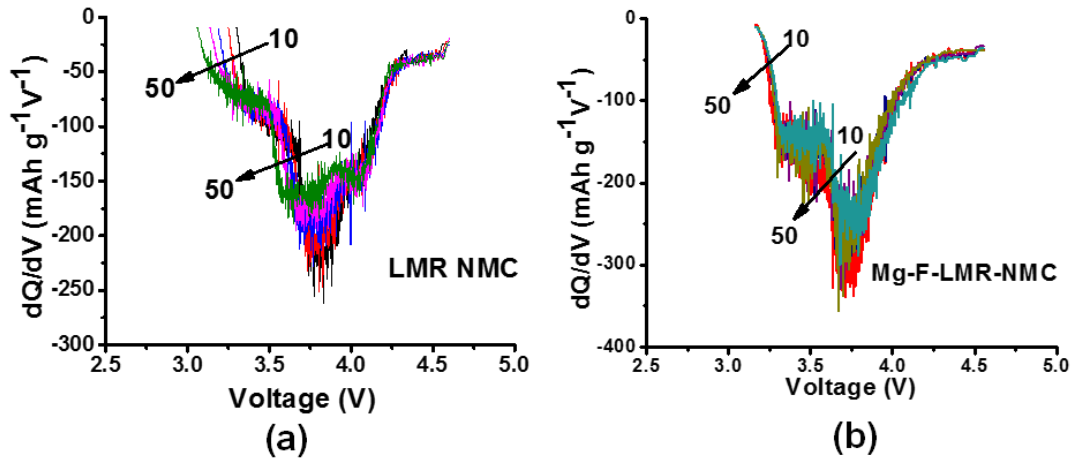


Fig. 4.5: Comparison of dQ/dV vs. V plots for (a) Pristine, and (b) doped LMR-NMC plots during 10^{th} , 30^{th} , 40^{th} , and 50^{th} discharge cycles

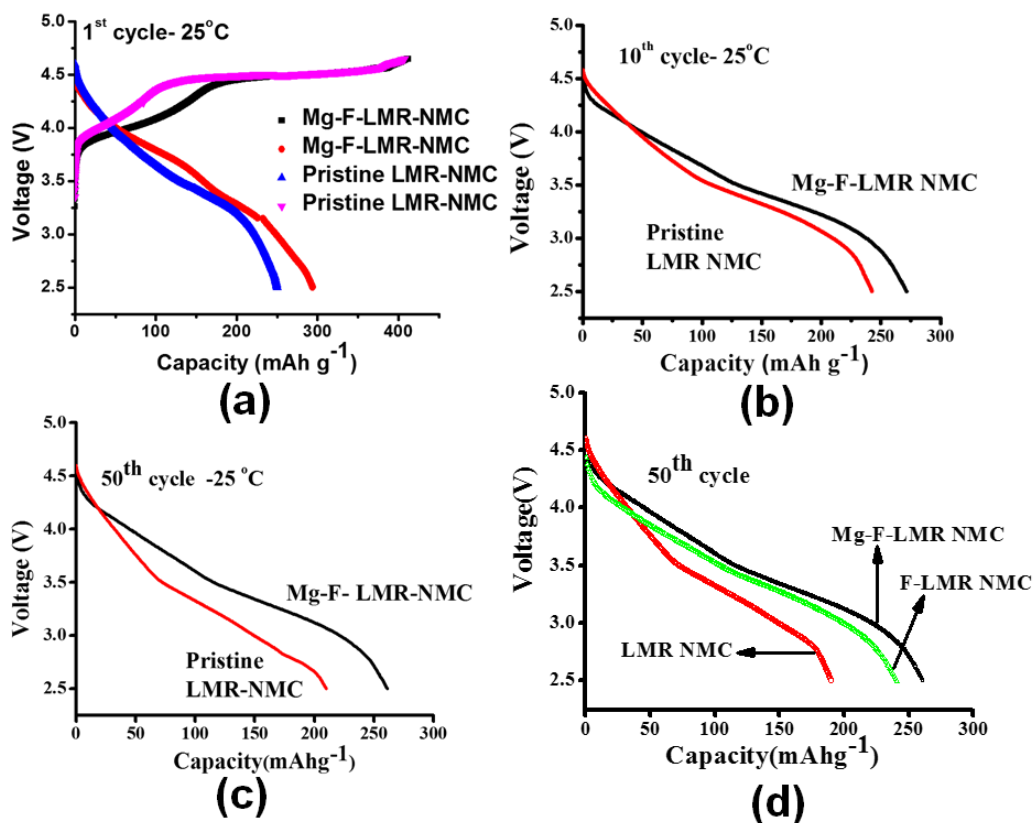


Fig. 4.6: Comparison of voltage profiles for the Pristine and doped LMR-NMC during: (a) 1st cycle at C/20 rate, (b-c) 10th and 50th cycle at C/10 rate, respectively, and (d) Comparison of voltage profiles for the Pristine, Mg-F-LMR-NMC and F-LMR-NMC during 50th cycle at C/10 rate

In pristine LMR-NMC, there is shift of discharge profile from higher voltage (3.8 V) to lower voltage (3.4 V) whereas no such voltage shift is observed in Mg-F doped LMR-NMC during cycling. The high discharge capacities and minimized voltage decay of Mg-F doped LMR-NMC is attributed to attainment of stability of crystal structure of LMR-NMC during cycling by Mg and F dopings [33-34]. Magnesium is stabilizing the crystal structure from bulk whereas fluorine is stabilizing the structure from surface and synergistic effect of Mg and F dopings help in minimizing layered to spinel transformation which is evident from improved electrochemical performance of Mg-F doped LMR-NMC compared to pristine LMR-NMC. High ratio of magnesium substitution leading to low capacity because magnesium is electrochemically inactive whereas high ratio of fluorine substitution leading to formation of impure phases. As discussed in Chapter 3, 1:50 wt. % of LiF:

LMR-NMC is the optimized ratio for fluorine and delivers the best electrochemical performance.

In this work, Mg^{2+} is substituted in Ni^{2+} site because both the elements have same charge and Ni^{2+} has ionic radii is 0.69\AA which is approximately equivalent to ionic radii of Li^+ (0.73\AA), which may be the reason for cation mixing [33-34]. So by decreasing the Ni^{2+} content partially by substituting by Mg^{2+} helps to minimize the cation mixing. Moreover, magnesium blocks the tetrahedral void which is the path of migration for transition metal ions (typically nickel) from transition metal layer to lithium layer [8, 38-44]. Partial substitution of oxygen (O^{2-}) by fluorine (F^-) leads to M-F bond formation which is stronger than M-O bond. This may leads partial reduction of transitional metal ions which causes the partial increase of ionic radii, is evident from increase of 'a' lattice parameter (in XRD Fig. 4.1) which is basis of M-M bond. Formation of M-F bond stabilizes the structure during cycling. Besides, LiF coating helps to increase interfacial stability at high voltage cycling without any electrolyte additives to the current carbonate based electrolytes. As size increases, movement of ions decreases, so the movement of transitional metal ions decreases which minimizes the cation mixing and reduces the layered to spinel transformation and thus suppresses the voltage decay. So synergistic effect of Mg and F co-dopings are helping in improvement of electrochemical performance of LMR-NMC in terms of minimized voltage decay, high initial capacity and cycling stability. High energy density close to 1000 Wh kg^{-1} could be obtained for doped samples (for the initial cycles and even after 50 cycles) compared to the pristine samples where significant energy loss occurs.

The impedance analysis provide very useful information about resistive components associated with the cell. In order to get further understanding of enhanced capacity and good capacity retention, we compare Nyquist plots of both pristine and doped-LMR-NMC during 50th cycles in discharged condition (SoC 0) at equilibrium potential of 3.1 V as presented in Fig. 4.7. The data shows LMR-NMC composite cathodes have Ohmic resistance of about 10 Ohm cm^2 whereas Mg-F doped LMR-NMC have 5.25 Ohm cm^2 . The charge transfer resistances for Mg-F- doped LMR-NMC is much lower (400 Ohm cm^2) in relation to LMR-NMC (830 Ohm cm^2). From

this it can be explained that both LiF coating, F-doping and Mg doping (increases overall conductivity) are synergistically helping in decreasing the impedance thus improving the rate capability, cycling performance and storage capacity of the electrode.

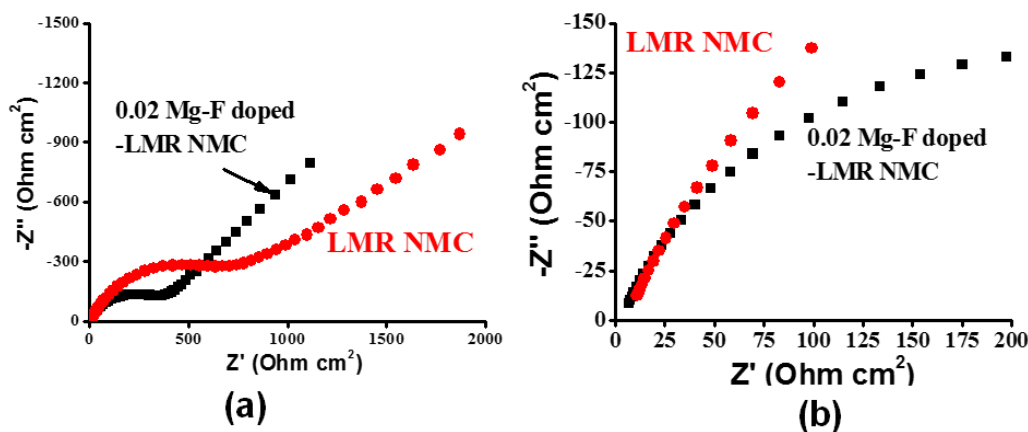


Fig. 4.7: Impedance spectra of LMR- NMC and Mg-F doped LMR-NMC: a) after 50 cycles in discharged condition (SoC 0) at equilibrium potential of 3.1V, and b) the zoomed image of the impedance response in the high frequency region

4.5. Conclusions

Mg and F doping does not change the crystal system of LMR-NMC which is evident from XRD plot where no impure phase peaks are observed. Doped sample especially 0.02 mole % of Mg and (1:50 wt. %- LiF: LMR-NMC) F doped LMR-NMC show excellent electrochemical performance, delivers capacity $\sim 300 \text{ mAh g}^{-1}$ at C/20 rate, 10-15 % excess capacity than pristine LMR-NMC. Doped sample shows improved capacity retention, minimized voltage decay and high C rate performances compared to Pristine LMR-NMC. The improved electrochemical performance is attributed to the minimized cation mixing and stabilization of crystal structure during cycling. Magnesium doping blocks the tetrahedral void which is the path of migration of transition metal ions (typically nickel) from transition metal layer to lithium layer. Partial substitution of oxygen (O^{2-}) by fluorine (F) leads to partial M-F bond formation, which stabilizes the structure during cycling. Besides, LiF coatings (or additives during synthesis) help to increase interfacial stability at high voltage cycling without any electrolyte additives. It is believed that the study will open a new possibility for LMR-NMC cathode development which has almost double the capacity

of currently available cathodes, and could be a possible choice for LIBs used in electric vehicles.

References

- [1] M. Armand, J.-M. Tarascon, Building better batteries, *Nature*. 451 (2008) 652–657.
- [2] B. Scrosati, J. Garche, Lithium batteries: Status, prospects and future, *J. Power Sources*. 195 (2010) 2419–2430.
- [3] C. Wang, A.J. Appleby, F.E. Little, Charge–discharge stability of graphite anodes for lithium-ion batteries, *J. Electroanal. Chem.* 497 (2001) 33–46.
- [4] L. Zhao, Y.-S. Hu, H. Li, Z. Wang, L. Chen, Porous $\text{Li}_4\text{Ti}_5\text{O}_{12}$ Coated with N-Doped Carbon from Ionic Liquids for Li-Ion Batteries, *Adv. Mater.* 23 (2011) 1385–1388.
- [5] N. Yabuuchi, T. Ohzuku, Novel lithium insertion material of $\text{LiCo}_{1/3}\text{Ni}_{1/3}\text{Mn}_{1/3}\text{O}_2$ for advanced lithium-ion batteries, *J. Power Sources*. 119 (2003) 171–174.
- [6] M.M. Thackeray, S.-H. Kang, C.S. Johnson, J.T. Vaughey, R. Benedek, S. Hackney, Li_2MnO_3 -stabilized LiMO_2 (M= Mn, Ni, Co) electrodes for lithium-ion batteries, *J. Mater. Chem.* 17 (2007) 3112–3125.
- [7] S.K. Martha, J. Nanda, G.M. Veith, N.J. Dudney, Electrochemical and rate performance study of high-voltage lithium-rich composition: $\text{Li}_{1.2}\text{Mn}_{0.525}\text{Ni}_{0.175}\text{Co}_{0.1}\text{O}_2$, *J. Power Sources*. 199 (2012) 220–226.
- [8] D. Mohanty, A.S. Sefat, S. Kalnaus, J. Li, R.A. Meisner, E.A. Payzant, D.P. Abraham, D.L. Wood, C. Daniel, Investigating phase transformation in the $\text{Li}_{1.2}\text{Co}_{0.1}\text{Mn}_{0.55}\text{Ni}_{0.15}\text{O}_2$ lithium-ion battery cathode during high-voltage hold (4.5 V) via magnetic, X-ray diffraction and electron microscopy studies, *J. Mater. Chem. A*. 1 (2013) 6249–6261.
- [9] S.K. Martha, J. Nanda, Y. Kim, R.R. Unocic, S. Pannala, N.J. Dudney, Solid electrolyte coated high voltage layered–layered lithium-rich composite cathode: $\text{Li}_{1.2}\text{Mn}_{0.525}\text{Ni}_{0.175}\text{Co}_{0.1}\text{O}_2$, *J. Mater. Chem. A*. 1 (2013) 5587–5595.
- [10] S.K. Martha, J. Nanda, G.M. Veith, N.J. Dudney, Surface studies of high voltage lithium rich composition: $\text{Li}_{1.2}\text{Mn}_{0.525}\text{Ni}_{0.175}\text{Co}_{0.1}\text{O}_2$, *J. Power Sources*. 216 (2012) 179–186.
- [11] M. Bettge, Y. Li, K. Gallagher, Y. Zhu, Q. Wu, W. Lu, I. Bloom, D.P. Abraham, Voltage fade of layered oxides: Its measurement and impact on energy density, *J. Electrochem. Soc.* 160 (2013) A2046–A2055.
- [12] P. K. Nayak, J. Grinblat, E. Levi, T.R. Penki, M. Levi, Y.-K. Sun, B. Markovsky, D. Aurbach, Remarkably Improved Electrochemical Performance of Li-and Mn-Rich

- Cathodes upon Substitution of Mn with Ni, *ACS Appl. Mater. Interfaces*. 9 (2016) 4309–4319.
- [13] A.R. Armstrong, M. Holzapfel, P. Novák, C.S. Johnson, S.-H. Kang, M.M. Thackeray, P.G. Bruce, Demonstrating oxygen loss and associated structural reorganization in the lithium battery cathode $\text{Li}[\text{Ni}_{0.2}\text{Li}_{0.2}\text{Mn}_{0.6}]\text{O}_2$, *J. Am. Chem. Soc.* 128 (2006) 8694–8698.
- [14] J. Liu, A. Manthiram, Functional surface modifications of a high capacity layered $\text{Li}[\text{Li}_{0.2}\text{Mn}_{0.54}\text{Ni}_{0.13}\text{Co}_{0.13}]\text{O}_2$ cathode, *J. Mater. Chem.* 20 (2010) 3961–3967.
- [15] S.B. Chikkannanavar, D.M. Bernardi, L. Liu, A review of blended cathode materials for use in Li-ion batteries, *J. Power Sources*. 248 (2014) 91–100.
- [16] L. Fu, H. Liu, C. Li, Y.P. Wu, E. Rahm, R. Holze, H. Wu, Surface modifications of electrode materials for lithium ion batteries, *Solid State Sci.* 8 (2006) 113–128.
- [17] C. Li, H. Zhang, L. Fu, H. Liu, Y. Wu, E. Rahm, R. Holze, H. Wu, Cathode materials modified by surface coating for lithium ion batteries, *Electrochim. Acta.* 51 (2006) 3872–3883.
- [18] K.G. Gallagher, S.-H. Kang, S.U. Park, S.Y. Han, $x\text{Li}_2\text{MnO}_3 \cdot (1-x)\text{LiMO}_2$ blended with LiFePO_4 to achieve high energy density and pulse power capability, *J. Power Sources*. 196 (2011) 9702–9707.
- [19] Y. Zuo, B. Huang, C. Jiao, R. Lv, G. Liang, Enhanced electrochemical properties of $\text{Li}[\text{Li}_{0.2}\text{Mn}_{0.54}\text{Ni}_{0.13}\text{Co}_{0.13}]\text{O}_2$ with ZrF_4 surface modification as cathode for Li-ion batteries, *J. Mater. Sci. - Mater. Electron.* (2017) 1–11.
- [20] Q. Wang, J. Liu, A.V. Murugan, A. Manthiram, High capacity double-layer surface modified $\text{Li}[\text{Li}_{0.2}\text{Mn}_{0.54}\text{Ni}_{0.13}\text{Co}_{0.13}]\text{O}_2$ cathode with improved rate capability, *J. Mater. Chem.* 19 (2009) 4965–4972.
- [21] Y.-K. Sun, M.-J. Lee, C.S. Yoon, J. Hassoun, K. Amine, B. Scrosati, The Role of AlF_3 Coatings in Improving Electrochemical Cycling of Li-Enriched Nickel-Manganese Oxide Electrodes for Li-Ion Batteries, *Adv. Mater.* 24 (2012) 1192–1196.
- [22] S. Shi, J. Tu, Y. Tang, X. Liu, Y. Zhang, X. Wang, C. Gu, Enhanced cycling stability of $\text{Li}[\text{Li}_{0.2}\text{Mn}_{0.54}\text{Ni}_{0.13}\text{Co}_{0.13}]\text{O}_2$ by surface modification of MgO with melting impregnation method, *Electrochim. Acta.* 88 (2013) 671–679.
- [23] J. Zheng, J. Li, Z. Zhang, X. Guo, Y. Yang, The effects of TiO_2 coating on the electrochemical performance of $\text{Li}[\text{Li}_{0.2}\text{Mn}_{0.54}\text{Ni}_{0.13}\text{Co}_{0.13}]\text{O}_2$ cathode material for lithium-ion battery, *Solid State Ionics*. 179 (2008) 1794–1799.
- [24] S.H. Park, Y.-K. Sun, Synthesis and electrochemical properties of layered $\text{Li}[\text{Li}_{0.15}\text{Ni}_{(0.275-x/2)}\text{Al}_x\text{Mn}_{(0.575-x/2)}]\text{O}_2$ materials prepared by sol-gel method, *J. Power Sources*. 119 (2003) 161–165.

- [25] M.N. Ates, Q. Jia, A. Shah, A. Busnaina, S. Mukerjee, K. Abraham, Mitigation of layered to spinel conversion of a Li-rich layered metal oxide cathode material for Li-Ion batteries, *J. Electrochem. Soc.* 161 (2014) A290–A301.
- [26] P. K. Nayak, J. Grinblat, E. Levi, T.R. Penki, M. Levi, Y.-K. Sun, B. Markovsky, D. Aurbach, Remarkably Improved Electrochemical Performance of Li-and Mn-Rich Cathodes upon Substitution of Mn with Ni, *ACS Appl. Mater. Interfaces.* 9 (2016) 4309–4319.
- [27] Y.X. Wang, K.H. Shang, W. He, X.P. Ai, Y.L. Cao, H.X. Yang, Magnesium-doped $\text{Li}_{1.2}[\text{Co}_{0.13}\text{Ni}_{0.13}\text{Mn}_{0.54}]\text{O}_2$ for lithium-ion battery cathode with enhanced cycling stability and rate capability, *ACS Appl. Mater. Interfaces.* 7 (2015) 13014–13021.
- [28] Y.-K. Sun, Y.-S. Jeon, H.J. Lee, Overcoming Jahn-Teller Distortion for Spinel Mn Phase, *Electrochem. Solid-State Lett.* 3 (2000) 7–9.
- [29] R. Robert, C. Villevieille, P. Novák, Enhancement of the high potential specific charge in layered electrode materials for lithium-ion batteries, *J. Mater. Chem. A.* 2 (2014) 8589–8598.
- [30] G.-H. Kim, J.-H. Kim, S.-T. Myung, C. Yoon, Y.-K. Sun, Improvement of High-Voltage Cycling Behavior of Surface-Modified $\text{Li}[\text{Ni}_{1/3}\text{Co}_{1/3}\text{Mn}_{1/3}]\text{O}_2$ Cathodes by Fluorine Substitution for Li-Ion Batteries, *J. Electrochem. Soc.* 152 (2005) A1707–A1713.
- [31] H.-S. Shin, S.-H. Park, C.S. Yoon, Y.-K. Sun, Effect of fluorine on the electrochemical properties of layered $\text{Li}[\text{Ni}_{0.43}\text{Co}_{0.22}\text{Mn}_{0.35}]\text{O}_2$ cathode materials via a carbonate process, *Electrochem. Solid-State Lett.* 8 (2005) A559–A563.
- [32] S.-U. Woo, B.-C. Park, C. Yoon, S.-T. Myung, J. Prakash, Y.-K. Sun, Improvement of electrochemical performances of $\text{Li}[\text{Ni}_{0.8}\text{Co}_{0.1}\text{Mn}_{0.1}]\text{O}_2$ cathode materials by fluorine substitution, *J. Electrochem. Soc.* 154 (2007) A649–A655.
- [33] H.-S. Shin, D. Shin, Y.-K. Sun, Improvement of electrochemical properties of $\text{Li}[\text{Ni}_{0.4}\text{Co}_{0.2}\text{Mn}_{(0.4-x)}\text{Mg}_x]\text{O}_{2-y}\text{F}_y$ cathode materials at high voltage region, *Electrochim. Acta.* 52 (2006) 1477–1482.
- [34] G.-H. Kim, S.-T. Myung, H. Bang, J. Prakash, Y.-K. Sun, Synthesis and Electrochemical Properties of $\text{Li}[\text{Ni}_{1/3}\text{Co}_{1/3}\text{Mn}_{(1/3-x)}\text{Mg}_x]\text{O}_{2-y}\text{F}_y$ via Coprecipitation, *Electrochem. Solid-State Lett.* 7 (2004) A477–A480.
- [35] S.K. Kumar, S. Ghosh, P. Ghosal, S.K. Martha, Synergistic effect of 3D electrode architecture and fluorine doping of $\text{Li}_{1.2}\text{Ni}_{0.15}\text{Mn}_{0.55}\text{Co}_{0.1}\text{O}_2$ for high energy density lithium-ion batteries, *J. Power Sources.* 356 (2017) 115–123.
- [36] R.L. Axelbaum, M. Lengyel, Doped lithium-rich layered composite cathode materials, United States Patent, US2015/0270545A1.

- [37] W. Luo, F. Zhou, X. Zhao, Z. Lu, X. Li, J. Dahn, Synthesis, Characterization, and Thermal Stability of $\text{LiNi}_{1/3}\text{Mn}_{1/3}\text{Co}_{1/3-z}\text{Mg}_z\text{O}_2$, $\text{LiNi}_{1/3-z}\text{Mn}_{1/3}\text{Co}_{1/3}\text{Mg}_z\text{O}_2$, and $\text{LiNi}_{1/3}\text{Mn}_{1/3-z}\text{Co}_{1/3}\text{Mg}_z\text{O}_2$, *Chem. Mater.* 22 (2009) 1164–1172.
- [38] D. Mohanty, K. Dahlberg, D.M. King, L.A. David, A.S. Sefat, D.L. Wood, C. Daniel, S. Dhar, V. Mahajan, M. Lee, others, Modification of Ni-rich FCG NMC and NCA cathodes by atomic layer deposition: preventing surface phase transitions for high-voltage lithium-ion batteries, *Nature Scientific Reports.* 6 (2016) 26532.
- [39] W. Liu, P. Oh, X. Liu, M.-J. Lee, W. Cho, S. Chae, Y. Kim, J. Cho, Nickel-Rich Layered Lithium Transition-Metal Oxide for High-Energy Lithium-Ion Batteries, *Angew. Chem. Int. Ed.* 54 (2015) 4440–4457.
- [40] J. Bareno, Y. Li, M. Bettge, R. Benedek, H. Iddir, Z. Chen, I. Bloom, D.P. Abraham, Voltage Fade in LMR-NMC Oxides Cycled below the Activation Plateau, in: *Meeting Abstracts, Electrochem. Soc.*, 2015: pp. 401–401.
- [41] A. Manthiram, J.C. Knight, S.-T. Myung, S.-M. Oh, Y.-K. Sun, Nickel-Rich and Lithium-Rich Layered Oxide Cathodes: Progress and Perspectives, *Adv. Energy Mater.* 6 (2016).
- [42] P. Rozier, J.M. Tarascon, Li-rich layered oxide cathodes for next-generation Li-ion batteries: chances and challenges, *J. Electrochem. Soc.* 162 (2015) A2490–A2499.
- [43] Y. Cho, P. Oh, J. Cho, A new type of protective surface layer for high-capacity Ni-based cathode materials: nanoscaled surface pillaring layer, *Nano Lett.* 13 (2013) 1145–1152.
- [44] F. Yang, Y. Liu, S.K. Martha, Z. Wu, J.C. Andrews, G.E. Ice, P. Pianetta, J. Nanda, Nanoscale morphological and chemical changes of high voltage lithium–manganese rich NMC composite cathodes with cycling, *Nano Lett.* 14 (2014) 4334–4341.

Chapter 5

LMR-NMC-Carbon Coated-LiMnPO₄ Blended Electrodes for High Performance Lithium-Ion Batteries

5.1. Abstract

This Chapter demonstrates another attempt in improvement in energy density, capacity retention and C rate performance of “layered-layered” lithium rich $\text{Li}_{1.2}\text{Mn}_{0.55}\text{Ni}_{0.15}\text{Co}_{0.1}\text{O}_2$ (LMR-NMC) material by blending with carbon coated LiMnPO_4 (C-LMP) using mechanical milling. The presence of the C-LMP provides interfacial stability under high current (rate) and voltage cycling conditions and thereby improves the energy loss over cycle life in relation to the pristine LMR-NMC. Blend composite electrodes shows stable reversible capacities of $>225 \text{ mAh g}^{-1}$ in the voltage window of 2.5 to 4.7 V for more than 200 cycles, and shows improvements in the rate performance, reduction in irreversible capacity loss and Mn dissolution than the pristine LMR-NMC composite electrode. We characterize details of electrochemical performance studies to understand the role of C-LMP in improving the interfacial stability at the interface.

5.2. Background and Motivation

As discussed in Chapter 3 and 4, Lithium and manganese rich Ni-Mn-Co layered oxides, such as LMR-NMC cathodes have attracted attention as high energy density ($>1000 \text{ Wh kg}^{-1}$) [1-12] cathode materials for rechargeable Lithium-ion batteries due to their high achievable reversible capacity $>250 \text{ mAh g}^{-1}$ in the voltage range between

2.5 and 4.8 V [1-5]. Besides, this material is thermally safer than $\text{Li}[\text{Ni}_{1/3}\text{Co}_{1/3}\text{Mn}_{1/3}]\text{O}_2$ (NMC) cathode material due to their lower cobalt content [1, 3]. The capacity of LMR-NMC closely matches with that of graphite anode [3]. But LMR-NMC has numerous disadvantages such as high irreversible capacity, low capacity retentions and energy loss in this material during cycling which limits its application in developing high energy density LIBs to power EVs [1-12]. The energy density reduces from 1000 Wh kg^{-1} to 700 Wh kg^{-1} during 1-200 cycles [4-5]. The energy loss occurred in LMR-NMC is due to the voltage decay because of transformation of layered to the spinel structure of LMR-NMC [4-10]. As discussed in Chapter 3 and 4, transition metal layer migration to the lithium layer leads to transformation of layered to spinel structure [5-9]. The structural transition causes voltage decay from 3.7 V to <3 V operating voltage during discharge which causes significant loss of energy density [4-5]. Moreover, during high voltage cycling, salt decomposition products from the electrolyte deposits on the surface of the cathode, increases the cell impedance and leads to capacity fade [12]. Besides, gradual capacity fade is due to the dissolution of transition metal ions such as Mn [13-14]. So there is intense need to stabilize the material and its interface to mitigate capacity and energy loss.

Many strategies have been followed for the mitigation of the voltage decay and improving capacity retention in LMR-NMC. In general, surface modifications (Chapter 3 and 4) [5, 15-34], cations doping such as chromium, nickel, ruthenium etc. [16-19] and anions such as fluorine [20-21] or both cation and anion such as Mg and F have been doped in LMR-NMC to improve the electrochemical performance [22]. As discussed in Chapter 3, LiF coating/ F-doping onto LMR-NMC cathodes deliver high capacity of $\sim 300 \text{ mAh g}^{-1}$ at C/10 rate (10-20% greater than the pristine LMR-NMC cathodes), have high discharge voltage plateau ($> 0.25 \text{ V}$) and low charge voltage plateau (0.2 to 0.4 V) compared to pristine LMR-NMC cathodes [21]. Beside, irreversible capacity, voltage fade, capacity loss are significantly reduced in-relation to the pristine LMR-NMC electrodes. F-doped LMR-NMC partially replaces M-O bonds of the material by M-F bonds thereby increasing interfacial stability and high voltage stability over 200 cycles [21]. Besides, both Mg and F (Chapter 4) doping helps to mitigate capacity loss, reduces irreversibly capacity from $>25 \%$ to $< 10 \%$,

increases C rate performance and cyclability compared to pristine LMR-NMC. Both Mg and F doping reduces charging voltage, i.e., increases surface stability and conductivity thereby delivers high capacity at low voltages. Both Mg and F doping reduces structural transition from layered to the spinel phase thereby reducing voltage drop and loss of energy during high voltage cycling [22].

In this Chapter, we made another attempt to overcome the issues of capacity loss, irreversible capacity and voltage decay of LMR-NMC through blending. Blending is one of the most classical and practical strategy to overcome the drawbacks associated with both the blended cathode materials and get most optimized electrochemical performance than that is possible with individual cathode materials [23-34]. Oxide cathode materials such as $x\text{Li}_2\text{MnO}_3 \cdot (1-x)\text{LiMO}_2$ [26], $\text{LiNi}_{1/3}\text{Mn}_{1/3}\text{Co}_{1/3}\text{O}_2$ (NMC) [27], $\text{LiNi}_{0.8}\text{Co}_{0.15}\text{Al}_{0.5}\text{O}_2$ (NCA) [28], LiMn_2O_4 (NMS) [29-31] etc. are blended each other or with olivine type LiFePO_4 [23-25] active materials to meet different design requirements such as improved interfacial stability, reduced irreversible capacity, increased cycle life, C-rate performance (pulse power operation), and safety as olivine compounds contain much stronger P-O bonds than other oxide materials [35-37]. In 2001, Numata et al. suggested an approach to improve the capacity retention, reduce Li loss, Mn dissolution of NMS based electrodes by simply mixing NMS and $\text{LiNi}_{0.8}\text{Co}_{0.2}\text{O}_2$ together [29]. In a similar report, blending of NMC with NMS helps to suppress Mn dissolution from NMS, which is a major factor of capacity loss and coulombic inefficiency of the NMS/Li cells [30]. Blending the olivine $\text{LiFe}_{0.3}\text{Mn}_{0.7}\text{PO}_4$ (LFMP) with spinel $\text{LiMn}_{1.9}\text{Al}_{0.1}\text{O}_4$ (LMO) shows high capacity of LFMP with the rate capability of the spinel [32]. In a recent report by Manthiram and coworkers shows blending of LMR-NMC with spinel $\text{Li}_4\text{Mn}_5\text{O}_{12}$ or LiV_3O_8 eliminates the irreversible capacity loss completely at 30 wt. % $\text{Li}_4\text{Mn}_5\text{O}_{12}$ and 18 wt. % LiV_3O_8 . The elimination is due to the ability of $\text{Li}_4\text{Mn}_5\text{O}_{12}$ and LiV_3O_8 to insert the extracted lithium that could not be inserted back into LMR-NMC [33]. Blending of 20 wt. % LiFePO_4 with LMR-NMC have achieved high energy density and pulse power capability [26].

In this Chapter, we present blending of LMR-NMC with carbon coated LiMnPO_4 to overcome the issues of irreversible capacity loss, low capacity retention

and improved interface instability of LMR-NMC thereby reducing voltage decay and dissolution. LiMnPO_4 is an attractive high voltage cathode with an operating voltage of 4.1 V vs. Li/Li^+ , offers more safety features compared to transition metal oxide cathode due to the strong P–O bond [35-37]. But it has low practical capacity (155 mAh g^{-1} at C/10 rate) and low ionic and electronic conductivity which could limit the battery performance. Poor ionic and electronic conductivity of LiMnPO_4 can be mitigated through synthesis of nanoparticles with in-situ/ex-situ carbon coatings. 20% of carbon coated LiMnPO_4 blending onto LMR-NMC could further improve rate performance; cycle life, thermal and interfacial stability. The structural, morphological, electrochemical performance of blended composite electrode have been investigated in this manuscript. The goal of this work is to demonstrate the probability of blending of two Manganese based positive electrode materials but not to present an optimization study.

5.3. Experimental

5.3.1. Synthesis of C-coated LiMnPO_4 nanoparticles

LMP nano-particles were synthesized by polyol method [35-36]. In brief, 0.06 mol of manganese acetate tetrahydrate (Aldrich, 99%) was dissolved with 30 mL of deionized water and poured into 200 mL of diethylene glycol (DEG, Aldrich, 99%). The DEG– H_2O mixture solution was vigorously stirred and heated at 100°C for 1 h. 30 mL of lithium dihydrogen phosphate (LiH_2PO_4 , 97%, Alfa Aesar) aqueous solution (2 mol L^{-1}) was added drop wise. The DEG suspension was kept for another 6 h at this temperature and cooled down to room temperature. The resulting LiMnPO_4 material was separated by centrifugation and washed several times with ethanol to remove residual DEG and organic fragments. Finally, the material was dried in an oven at 120 °C for 12 hrs. The produced LMP powder was ball-milled (Materials to ball (ZrO_2 cylindrical balls) ratio was 1:10) using planetary ball mill (Gelon, China) with 20 wt. % high surface area carbons (ACS 2200 from China Steel Chemical Corporation, Taiwan; BET surface area $>2000 \text{ m}^2 \text{ g}^{-1}$) to obtain carbon-coated LiMnPO_4 (C-LMP).

5.3.2. Synthesis of LMR-NMC and blended cathode materials

The LMR-NMC materials were prepared from solid-state reaction from lithium hydroxide and manganese-nickel-cobalt hydroxides as discussed elsewhere [10]. The manganese-nickel-cobalt hydroxide was prepared by coprecipitation method from a mixture of Mn, Ni, Co nitrates (in the molar ratio of Mn: Ni: Co = 0.55:0.15:0.10) (Alfa Aesar) in aqueous solution and 2.0 mol L⁻¹ of LiOH (Alfa Aesar) aqueous solution with the desired amount of NH₄OH (Across organics, India). During the reaction temperature was kept at 60 °C, with stirring speed controlled at 800 rpm, and the pH of the mixed solution was kept ~12 during the precipitation process. Finally, the precipitated (Co, Ni, Mn)(OH)₂ particles were filtered, washed, dried under vacuum at 100 °C. Thus obtained (Mn, Ni, Co)(OH)₂ and LiOH were mixed in the molar ratio of 1.0:1.2 by using a mortar and pestle, and pressed into pellets, in which 10% of excess lithium was added to compensate for the lithium evaporation during the calcinations at high temperature. The pellets were heated at 450 °C for 5 hrs followed by 900 °C for 15 hrs in air and then quenched to room temperature to obtain spherical LMR-NMC. Blended materials was obtained ball-milling 80 % LMR-NMC with 20 wt. % C-LMP.

5.3.3. Structural, physical and electrochemical characterization of LMR-NMC, LMP and blended materials

Structural, physical and compositional analyses were conducted by using powder XRD, SEM and EDAX, respectively as explained in the experimental part of Chapter 3. The electrochemical performance of comprising pristine LMR-NMC, C-LMP and blended as active masses were measured by using Solartron cell test system consists of 1470E multi-channel potentiostats and multiple 1455A series frequency response analyzers (FRAs) (driven by Corrware and ZPlot software from Scribner Associates) and Arbin battery cycler (Arbin BT2000 - Battery Test Equipment, USA). The impedance measurements were carried out in a frequency range between 1 MHz and 10 mHz in open circuit condition after 12 hrs assembly of cells.

C-LMP composite electrodes comprised of 90.0% C-LMP, 2.5% carbon black (Timcal) and 7.5% polyvinylidene fluoride (PVdF; Kynar). LMR-NMC and blended composite electrodes were prepared by making the composite of 85% active material,

7.5% PVdF (Kynar) and 6 % carbon black (Timcal) and 1.5 % graphitic carbon nano fibers (outer diameter of 100–200 nm) in N-methyl pyrrolidone (Sigma Aldrich) and coated on to the Aluminum foil (>99.9%, Strem chemicals, Inc., USA) current collector by using doctor blade technique. The composite electrodes were dried under vacuum at 90°C followed by punching them into 1 cm² area circular discs. All electrodes comprised 7-10 mg of active materials per cm² on Al current collector. The cells were fabricated in a glove box (M-Braun, Germany) filled with ultrahigh purity argon (99.999 %). The moisture and oxygen content of the glove box were less than 0.1 ppm. CR2032 coin type cells were assembled using lithium foil as a counter electrode, polyethylene-polypropylene trilayer (Celgard Inc.) as separator and LMR-NMC or C-LMP or blended LMR-NMC composite as cathodes, 1M LiPF₆ in 1:2 ratio of ethylene carbonate and dimethyl carbonate as electrolyte. Charge-discharge cycling were carried out in the potential range between 2.5 V and 4.7 V using CC-CV protocol.

5.3.4. Ageing test LMR-NMC, LMP and blended materials

The ageing of materials was carried out in an argon-filled glove box using magnetic stirrers at 50 °C in standard EC-DMC 1:2/LiPF₆ 1.0 M solutions for 2 weeks. The powdery materials were separated from solutions by a centrifuge, followed by washing several times before measuring with pure DMC solvent. The possible dissolution of Mn, from LMR-NMC, C-LMP and blended powder upon aging in solutions at 50 °C for 2 weeks was measured by inductively coupled plasma (Prodigy High Dispersion ICP, Teledyne Technologies, USA).

5.4. Results and Discussion

5.4.1. Structural, physical characterization of LMR-NMC, LMP and blended materials

XRD patterns (Fig. 5.1(a)) of LMR-NMC is indexed based on α -NaFeO₂ structure. It has composite of LiMO₂ (M is a mixture of Mn, Ni, Co) belong to rhombohedral crystal system having the space group of $R\bar{3}m$ and minor diffraction peak around 22° belongs to LiMn₂O₃ monoclinic phase having the C2/m space group which is formed due to ordering between Li⁺ in the transition metal layer [2-10]. The powder XRD

patterns of the C-LiMnPO₄ (Fig. 5.1(b)) belong to a well ordered olivine, indexed by orthorhombic structure, space group Pnma [35-37]. XRD pattern of blended electrodes are not presented here as it is difficult to analyze.

Pristine LMR-NMC has nearly spherical ball type morphology (Fig. 5.2(a)) having the size ranging from 5-12 μm . Secondary particles formed by agglomeration of multifaceted primary particles having the particle size ranging from 20 to 80 nm (Fig. 5.2(b)). Pristine LiMnPO₄ has needle like morphology having the diameter of 50 nm and length could be several micrometers (Fig. 5.2(c)). Upon ball milling and carbon coating the needle like morphology breaks forming spherical particles about 30 nm in size (Fig. 5.2(d)).

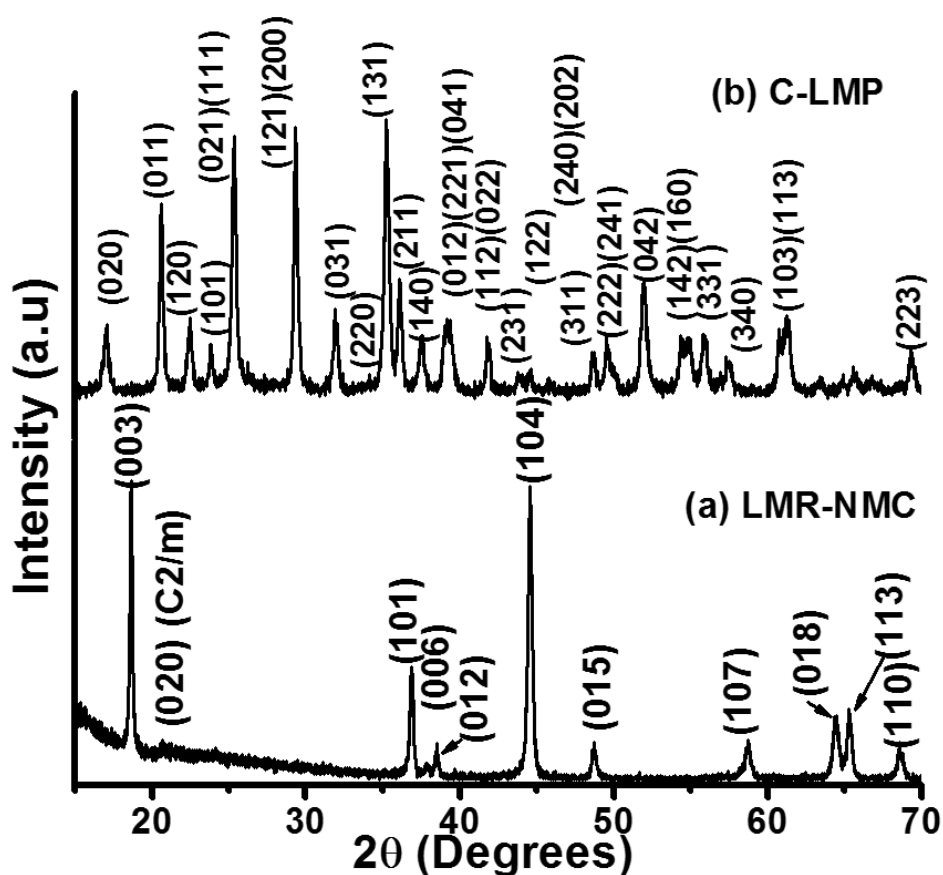


Fig. 5.1: XRD patterns for: (a) LMR-NMC and (b) C-LiMnPO₄

C coating onto C-LMP Powder has been confirmed by Raman spectroscopy as shown in Fig. 5.2(e). The broad peak at 1330 cm^{-1} corresponds to the D-line associated with disordered carbon vibrations of the C-LMP powder, and band at 1600

cm^{-1} corresponds to the G-line associated with the optically allowed E_{2g} vibration of the graphitic structure [38-39]. The D/G ratio is ~ 2 , indicates mostly sp^2 -type carbons, which helps to obtain good electronic conductivity of LMP. The spectrum also shows a weak peak at 950 cm^{-1} that can be assigned to the A_g mode of the symmetric stretching vibration of the PO_4^{3-} anions. The relatively weak intensity of PO_4^{3-} is due to masking effect of high amount of carbon coating [36].

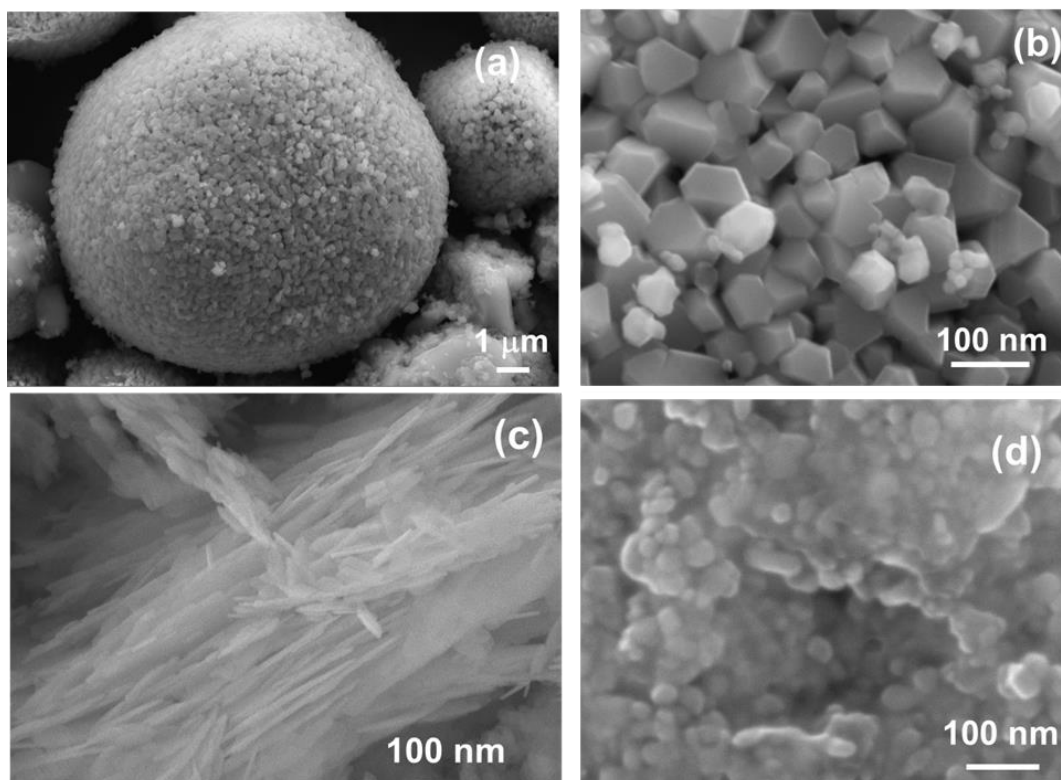


Fig.5. 2: SEM image of: (a) pristine LMR-NMC, (b) High resolution SEM image of pristine LMR-NMC showing primary particles, (c) pristine LiMnPO_4 synthesized by polyol method, and (d) C-coated LiMnPO_4 (C-LMP)

Figure 5.2(f) shows the SEM image of CNFs. They appear to be thread-like structures with an outer diameter of 100 to 200 nm. Fig. 5.2(g) presents the Raman spectrum of the CNFs, reflecting the strong graphitic nature of the material with a small peak D-band could be due to surface oxidation of CNFs during storage, associated with disordered carbon vibrations. The strong graphitic peak at 1590 cm^{-1} followed by a weak defect (D) band at $\sim 1350 \text{ cm}^{-1}$ suggest that the fibers are highly conducting with carbon atoms mainly having sp^2 type bond geometry [39]. The second order peaks at 2700 and 2450 cm^{-1} are marked by an asterisk in the Fig. 5.2(g).

Figure 5.2(h-i) shows the blend of LMR-NMC and C-LMP which has uniform distribution of both the blended materials.

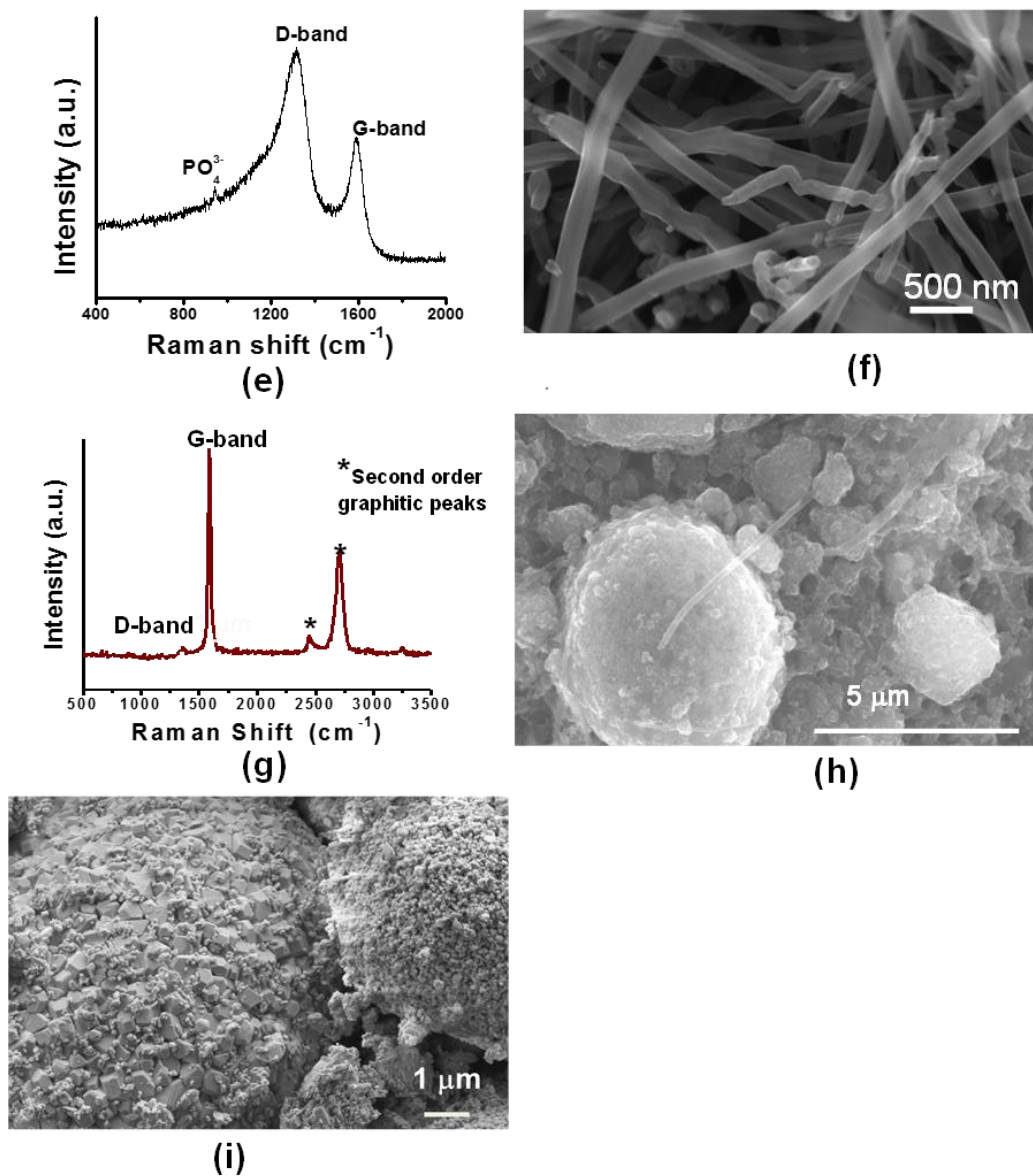


Fig. 5. 2: (e) Raman spectrum of C-LMP, (f) High resolution SEM image of pristine CNFs, (g) Raman spectrum of CNFs, (h) blend of LMR-NMC and LiMnPO_4 spot 1, and (i) blend of LMR-NMC and C-LMP spot 2

5.4.2. Electrochemical performance studies of LMR-NMC, LMP and blended materials

The charge and discharge voltage profiles (Fig. 5.3(a) and (b)) shows different voltages and capacities which is very obvious due to their inherent electronic and

crystal environment. C-LMP shows the voltage plateau at 4.2 V during charging and 4.0 V during discharging. LMR-NMC shows the activation of LiMn_2O_3 component above 4.4 V where oxygen is released as Li_2O and forms the MnO_2 [11]. LMR-NMC has an operating voltage of about 3.75 V. As the operating voltage of C-LMP matches with that of LMR-NMC, C-LMP is an ideal to blend with LMR-NMC. In the discharge voltage profile of blended material, the flat plateau corresponds to C-LMP and the later the sloppy curve is attributed to LMR-NMC. 20 wt. % of C-LMP blended electrode material delivers good electrochemical performance (C rate performance data shown in Fig. 5.5(b-c)). More than 20 wt. % of C-LMP was not chosen for blending as the capacity of blend LMR-NMC may drastically reduce.

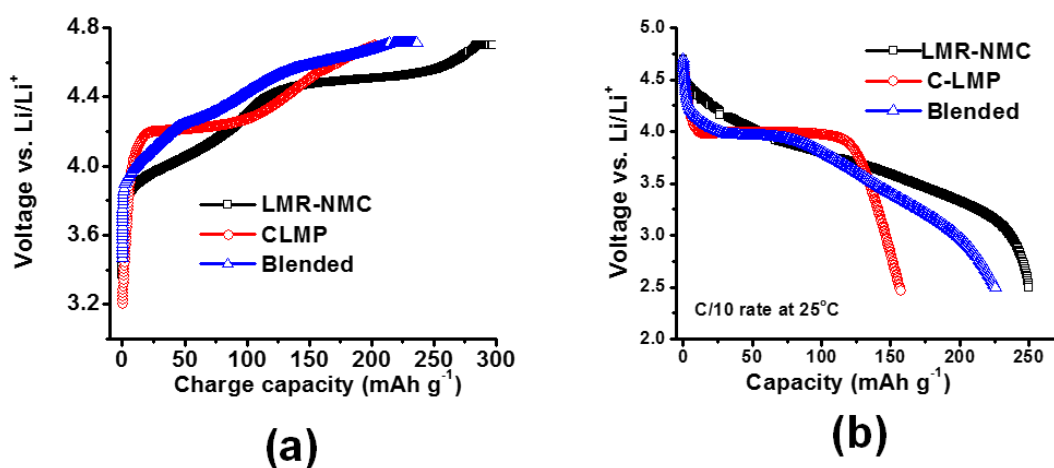


Fig. 5.3: (a) 1st charge voltage profiles, (b) 5th discharge voltage profiles (maximum capacity obtained) pristine LMR-NMC, pristine C-LMP and blend of LMR-NMC and C-LMP as indicated in the figure

The 20 wt. % C-LMP blending gives a reasonable flat plateau at 4 V. Also literature reports 15-30 wt. % blended materials give best electrochemical performance [23-26]. One of the drawback of LMR-NMC is the high irreversible capacity in first cycle which is alleviated by the blend which shows very less irreversible capacity (9%) compared to pristine LMR-NMC (17%). This reduced irreversible capacity may be attributed to approximate 100% electrochemical efficiency of C-LMP and stabilization of interface of LMR-NMC by the C-LMP coating. This coating protects the interface from degradation due to deposition of electrolyte at higher voltages. Another possible reason for reduced irreversible

capacity is due to the retention of oxide ion vacancies during de-lithiation which is due to surface coating of C-LMP to LMR-NMC [33]. The other major disadvantage of LMR-NMC is the rapid loss of energy density during progress of cycling due to decay of voltage which is limiting its application in powering the hybrid EVs and EVs. The blend of LMR-NMC and C-LMP shows improved electrochemical performance in terms of energy density compared to pristine LMR-NMC which is evident from Fig. 5.4(a) and (b) where the energy density of pristine LMR-NMC is declined from 870 Wh kg⁻¹ (5th cycle) to 681 Wh kg⁻¹(200th cycle). The blended material shows the energy density of 880 Wh kg⁻¹ (5th cycle) to 750 Wh kg⁻¹ (200th cycle).

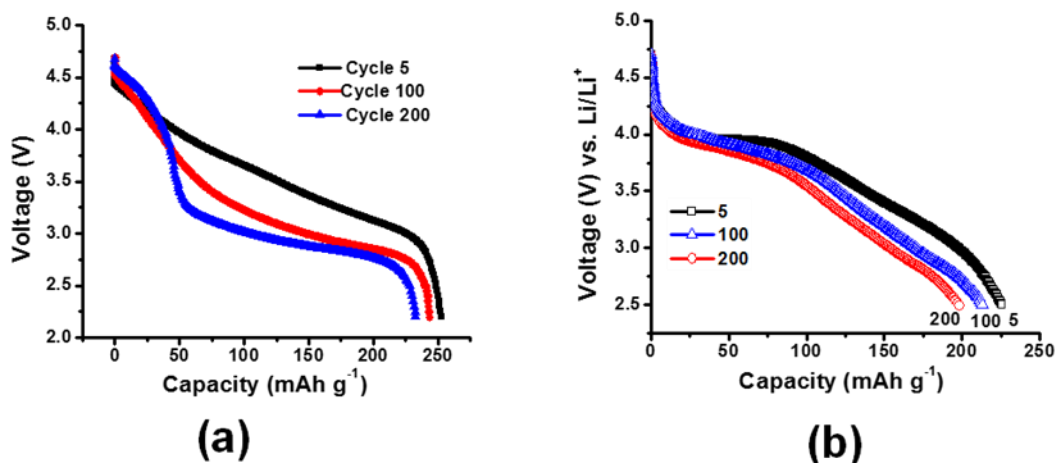


Fig. 5.4: Discharge voltage profiles at 5th, 100th and 200th cycles of (a) LMR-NMC, and (b) blend of LMR-NMC-C-LMP

The improvement in energy density of the blend is accredited to symbiotic effect of high voltage, stable capacity and stable crystal system of C-LMP [36-37], and high capacity of LMR-NMC [4-5]. Partly, the surface protection of LMR-NMC by C-LMP also helps in the improvement of energy density of LMR-NMC. It should be noted that, blended electrode has almost no voltage decay, it has about 10 % of loss of capacity after 200 cycles. If the capacity loss is further improved, blended electrode material may have still higher in energy.

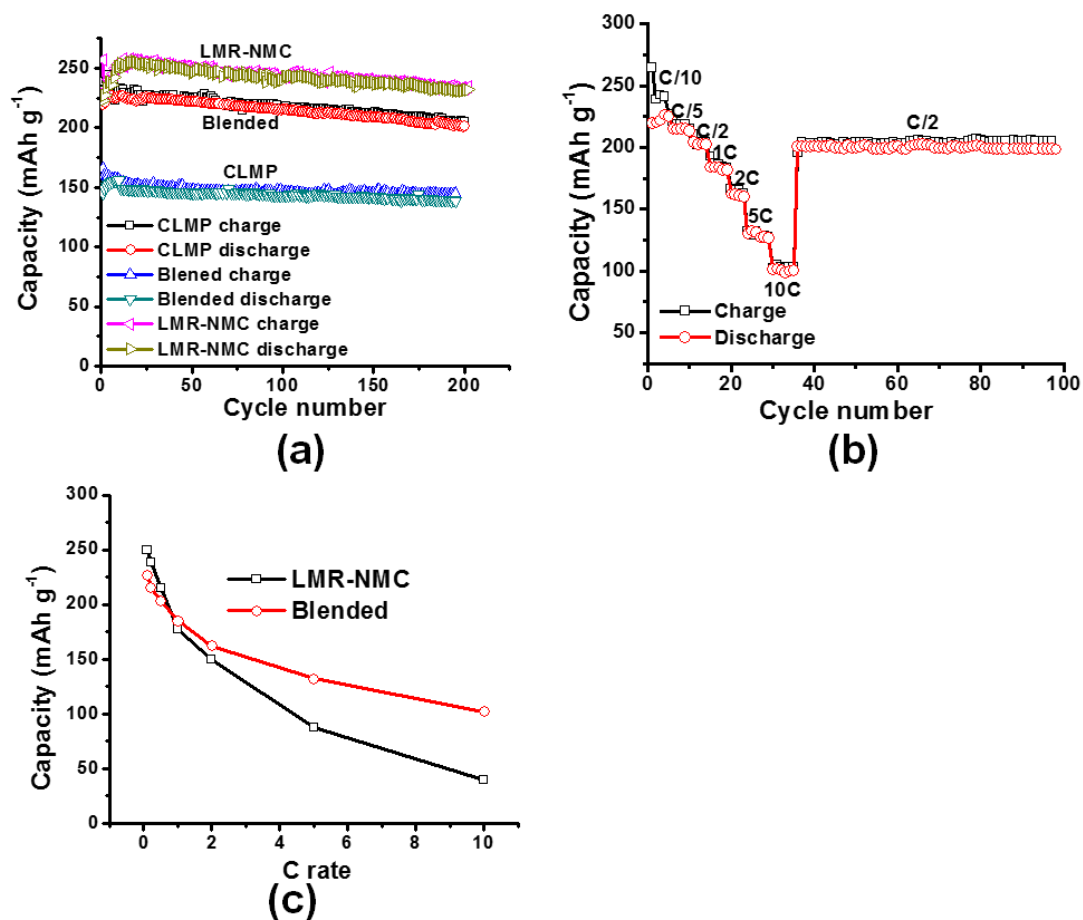


Fig.5.5: Cycle life of: (a) LMR-NMC, blended LMR-NMC and C-LMP, (b) C-Rate performance of blended electrode, (c) Comparison of rate capability of LMR-NMC and blended electrode

Cycle life of blended material, LMR-NMC and C-LMP composite materials are shown in Fig. 5.5(a). All the electrodes shows stable cycling behavior. At the end of 200 cycles, the blended and LMR-NMC composite electrodes have 10 % loss in capacity. The carbon nano fiber (CNFs) additives (1.5 wt. %) used here to keep the conductivity of the sample, thereby the cells improve cyclability along the cycles. It has been reported that when CNF additives are not used the cells have rapid capacity fade after 100 cycles [4, 12]. The CNFs make a good electronic contact along the particle thereby reduce electrode impedance even though the electrodes have salt decomposition products on the surface upon cycling to 4.7 V. There is an enhancement in the rate capability (at 1C and higher, of the blended electrode compared to pristine LMR-NMC (Fig. 5.5(b-c)) which is attributed to the superficial intercalation of lithium ions in the C-LMP and carbon coating on to C-LMP also

improves the overall conductivity of the blend. Moreover, the C-LMP on the surface of LMR-NMC also acts as excellent lithium ion conductor at high potentials (4.1 V vs. Li/Li⁺) which is also responsible for high rate capability of the blended material.

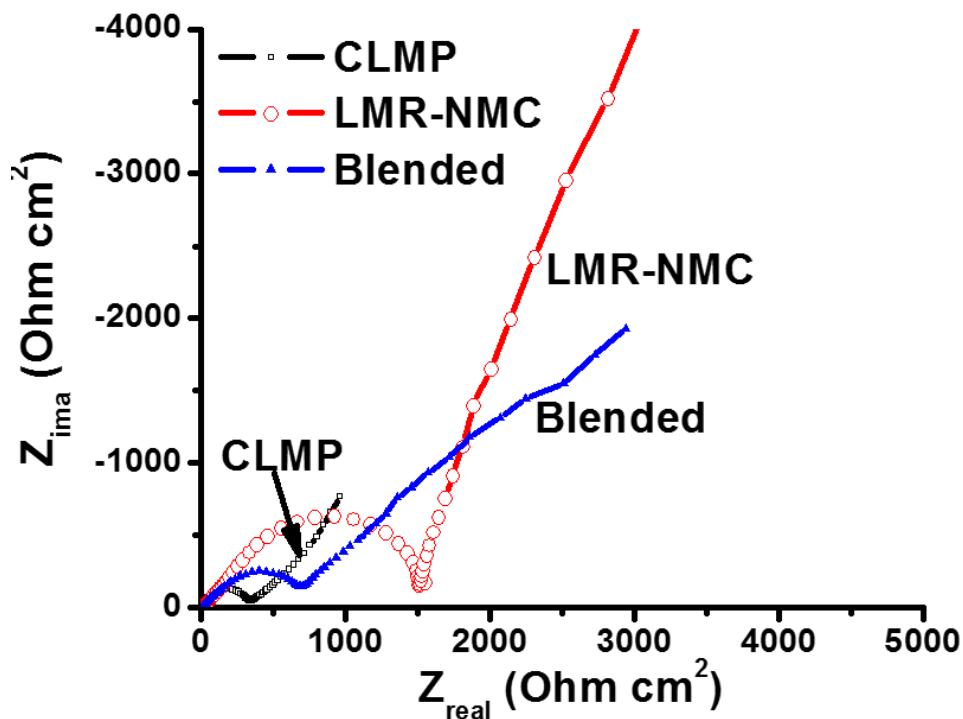


Fig. 5.6: Impedance spectra, represented as Nyquist plots for the LMR-NMC, C-LMP and blended composite electrodes measured under open circuit condition after 12 h assembly of cells in the frequency range 1 MHz and 10 mHz

Impedance spectra provide very useful information about various resistances associated with the cell. EIS data of LMR-NMC, C-LMP and blended composite electrodes are measured under similar conditions in open circuit condition are presented in Fig. 5.6. The result indicates that all the three composite electrodes show a small Ohmic resistances of 4.5, 7.63 and 14.7 Ohm cm² for the C-LMP and blended and LMR- NMC composite electrodes, respectively. Similarly, the charge transfer resistances for the C-LMP, blended and LMR-NMC composite electrodes were 348, 722 and 1585 Ohm cm², respectively. C-LMP blending with LMR-NMC reduces Ohmic resistance and charge transfer resistances by 50% thereby improves the rate capability, cycling performance.

5.4.3. Mn dissolution studies of LMR-NMC, LMP and blended materials

Dissolution of Mn is the major cause of capacity fade and structural transformation for the Mn rich layered and spinel oxides [5, 35]. Mn dissolution has been explained by the disproportionation of Mn^{3+} to Mn^{4+} and the soluble Mn^{2+} [40]. Besides, Mn dissolution depends on the temperature, state of charge, and the spinel composition, and presence of surface coating. Dissolution of Mn in cells can cause Mn^{2+} cations migration to the anode side, where they are reduced. The metallic clusters thus formed destroy the passivation of Li and Li-graphite electrodes. Hence, we measure the dissolution of Mn from LMR-NMC, C-LMP and blended LMR-NMC-C-LMP powder during aging in EC-DMC 1:2/ LiPF_6 1.0 M solutions under a pure argon atmosphere during 2 weeks at 50 °C. In general, Mn dissolves freely, >10 times at higher temperatures. Typical results of Mn dissolutions are presented in Fig. 5.7 and indicate that the amounts of dissolved Mn is drastically reduced in blended LMR-NMC compared to pristine LMR-NMC due to C-LMP coating.

5.4.4. Discussions

Similar to LiFePO_4 , the olivine type C-LMP material shown to have excellent capacity retention and rate capability because of small nanoparticles, coated with carbon, and free from blockage of 1D lithium-ion transport channels [36-37]. Furthermore, the olivine compound contains much stronger P-O bonds than other oxide materials resulting a very safe and stable cathode [36-37, 41]. However, C-LMP has reversible practical capacity of 160 mAh g^{-1} (Theoretical capacity = 170 mAh g^{-1}) at an operative voltage of 4.1 V, 0.7 V higher than that of LiFePO_4 and is very stable. The operating voltage of C-LMP matches with that of LMR-NMC. Besides, C-LMP has excellent structural stability makes C-LMP an ideal candidate to blend with the LMR-NMC materials to improve the positive electrode impedance. C-LMP blending drastically improves the electrode impedance, thereby improves C rate performance and capacity retention. Improvement in energy density of the blended material is due to high flat plateau voltage, stable capacity and stable crystal system of C-LMP and high capacity of LMR-NMC.

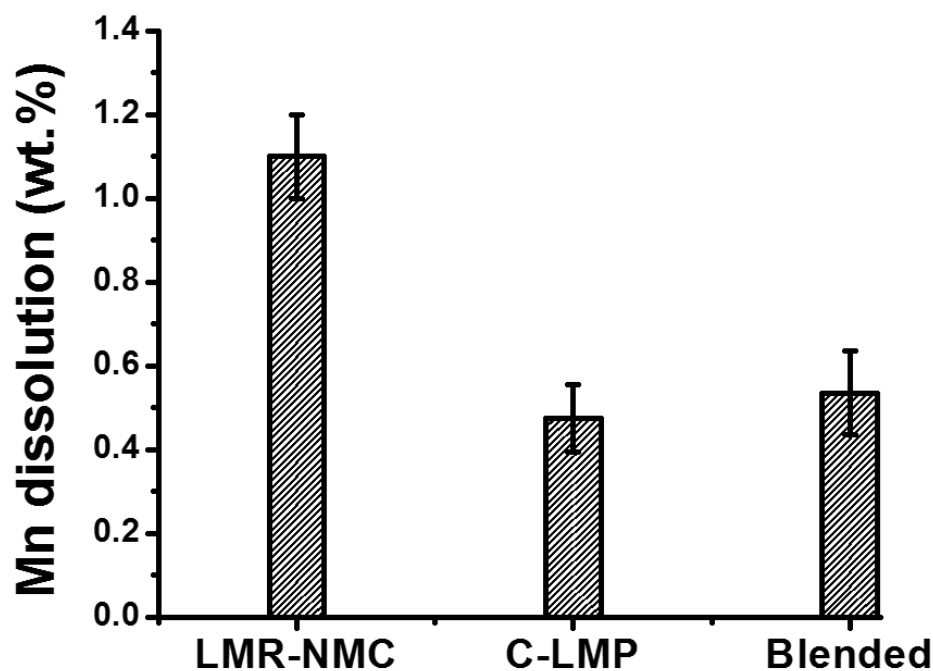


Fig. 5.7: Mn dissolution of LMR-NMC, C-LMP and blended LMR-NMC-C-LMP powders during aging in EC-DMC 1:2/LiPF₆ 1.0 M powders stirred at 50 °C for 2 weeks. The dissolved Mn content was normalized to the Mn content of the pristine untreated powders

5.5. Conclusions

Physical blending of LMR-NMC with C-LMP is demonstrated as a path to lower the interfacial instability, and impedance of LMR-NMC thereby improves the C rate performance of blended LMR-NMC. The carbon coated LMP acts as an internal low impedance pathway over Mn²⁺/Mn³⁺ active potential window, carrying the current for the more resistive LMR-NMC material. The high flat plateau voltage of C-LMP provides improvement in energy density of the blended electrode material. C-LMP provides high interfacial stability thereby reduces irreversible capacity loss and Mn dissolution, improves electrochemical performance. Optimization of the blending electrode approach and further improvement in capacity are underway.

References

- [1] J. W. Choi, D. Aurbach, Promise and reality of post-lithium-ion batteries with high energy densities, *Nat. Rev. Mater.*, 1 (2016) 1-16.
- [2] M. M. Thackeray, S.-H. Kang, C. S. Johnson, J. T. Vaughey, R. Benedek, S. A. Hackney, Li_2MnO_3 -stabilized LiMO_2 (M = Mn, Ni, Co) electrodes for lithium-ion batteries, *J. Mater. Chem.*, 17 (2007) 3112–3125.
- [3] Y. Li, M. Bettge, B. Polzin, Y. Zhu, M. Balasubramanian D. P. Abraham, Understanding long-term cycling performance of $\text{Li}_{1.2}\text{Ni}_{0.15}\text{Mn}_{0.55}\text{Co}_{0.1}\text{O}_2$ -graphite lithium-ion cells, *J. Electrochem. Soc.* 160 (5) (2013) A3006-A3019.
- [4] S. K. Martha, J. Nanda, G. M. Veith, N. J. Dudney, Electrochemical and rate performance study of high-voltage lithium-rich composition: $\text{Li}_{1.2}\text{Mn}_{0.525}\text{Ni}_{0.175}\text{Co}_{0.1}\text{O}_2$, *J. Power Sources* 199 (2012) 220– 226.
- [5] S. K. Martha, J. Nanda, Y. Kim, R. R. Unocic, S. Pannala, N. J. Dudney, Solid electrolyte coated high voltage layered-layered lithium-rich composite cathode: $\text{Li}_{1.2}\text{Mn}_{0.525}\text{Ni}_{0.175}\text{Co}_{0.1}\text{O}_2$, *J. Mater. Chem. A*, 1 (2013) 5587–5595.
- [6] D. Mohanty, J. Li, D. P. Abraham, A. Huq, E. A. Payzant, D. L. Wood, III, C. Daniel, Unraveling the voltage-fade mechanism in high-energy-density lithium-ion batteries: Origin of the tetrahedral cations for spinel conversion, *Chem. Mater.* 26 (2014) 6272–6280.
- [7] M. Bettge, Y. Li, K. Gallagher, Y. Zhu, Q. Wu, W. Lu, I. Bloom, D. P. Abraham, Voltage fade of layered oxides: Its measurement and impact on energy density, *J. Electrochem. Soc.* 160 (11) (2013) A2046-A2055.
- [8] F. Yang, Y. Liu, S. K. Martha, Z. Wu, J. C. Andrews, G. E. Ice, P. Pianetta, J. Nanda, Nanoscale Morphological and Chemical Changes of High Voltage Lithium–Manganese Rich NMC Composite Cathodes with Cycling, *Nano Lett.*, 14 (2014) 4334.
- [9] D. Mohanty, S. Kalnaus, R. A. Meisner, K. J. Rhodes, J. Li, E. A. Payzant, D. L. Wood III, C. Daniel, Structural transformation of a lithium-rich $\text{Li}_{1.2}\text{Co}_{0.1}\text{Mn}_{0.55}\text{Ni}_{0.15}\text{O}_2$ cathode during high voltage cycling resolved by in situ X-ray diffraction, *J. Power Sources* 229 (2013) 239-248.
- [10] N. Yabuuchi, K. Yoshii, S.-T. Myung, I. Nakai, S. Komaba, Detailed studies of a high-capacity electrode material for rechargeable batteries, Li_2MnO_3 - $\text{LiCo}_{1/3}\text{Ni}_{1/3}\text{Mn}_{1/3}\text{O}_2$, *J. Am. Chem. Soc.*, 133 (2011) 4404–4419.

- [11] A.R. Armstrong, M. Holzapfel, P. Novák, C.S. Johnson, S.-H. Kang, M.M. Thackeray, P.G. Bruce, Demonstrating oxygen loss and associated structural reorganization in the Lithium battery cathode $\text{Li}[\text{Ni}_{0.2}\text{Li}_{0.2}\text{Mn}_{0.6}]\text{O}_2$, *J. Am. Chem. Soc.* 128 (2006) 8694–8698.
- [12] S. K. Martha, J. Nanda, G. M. Veith, N. J. Dudney, Surface studies of high voltage lithium rich composition: $\text{Li}_{1.2}\text{Mn}_{0.525}\text{Ni}_{0.175}\text{Co}_{0.1}\text{O}_2$, *J. Power Sources* 216 (2012) 179–186.
- [13] J. Wandt, A. Freiberg, R. Thomas, Y. Gorlin, A. Siebel, R. Jung, H. A. Gasteiger, M. Tromp, Transition metal dissolution and deposition in Li-ion batteries investigated by operando X-ray absorption spectroscopy, *J. Mater. Chem. A* 4 (2016) 18300–18305.
- [14] J. A. Gilbert, I. A. Shkrob, D. P. Abraham, Transition metal dissolution, ion migration, electrocatalytic reduction and capacity loss in lithium-ion full cells, *J. Electrochem. Soc.* 164 (2) (2017) A389–A399.
- [15] K. R. Prakash, M. Sathish, P. Bera, A. S. Prakash, Mitigating the surface degradation and voltage decay of $\text{Li}_{1.2}\text{Ni}_{0.13}\text{Mn}_{0.54}\text{Co}_{0.13}\text{O}_2$ cathode material through surface modification using Li_2ZrO_3 , *ACS Omega* 2 (2017) 2308–2316.
- [16] L. F. Jiao, M. Zhang, H. T. Yuan, M. Zhao, J. Guo, W. Wang, X. D. Zhou, Y. M. Wang, Effect of Cr doping on the structural, electrochemical properties of $\text{Li}[\text{Li}_{0.2}\text{Ni}_{0.2-x/2}\text{Mn}_{0.6-x/2}\text{Cr}_x]\text{O}_2$ ($x = 0, 0.02, 0.04, 0.06, 0.08$) as cathode materials for lithium secondary batteries, *J. Power Sources* 167 (2007) 178–184.
- [17] P. K. Nayak, J. Grinblat, E. Levi, T. R. Penki, M. Levi, Y.-K. Sun, B. Markovsky and D. Aurbach, *ACS Appl. Mater. Interfaces*, **9** (5), 4309 (2017).
- [18] B. Song, M. O. Lai and L. Lu, Influence of Ru substitution on Li-rich $0.55\text{Li}_2\text{MnO}_3 \cdot 0.45\text{LiNi}_{1/3}\text{Co}_{1/3}\text{Mn}_{1/3}\text{O}_2$ cathode for Li-ion batteries, *Electrochim. Acta* 80 (2012) 187–195.
- [19] O. Sha, Z. Tang, S. Wang, W. Yuan, Z. Qiao, Q. Xu, L. Ma, The multi-substituted $\text{LiNi}_{0.475}\text{Al}_{0.01}\text{Cr}_{0.04}\text{Mn}_{1.475}\text{O}_{3.95}\text{F}_{0.05}$ cathode material with excellent rate capability and cycle life, *Electrochim. Acta* 77 (2012) 250–255.
- [20] L. Li, B.H. Song, Y.L. Chang, H. Xia, J.R. Yang, K.S. Lee, L. Lu, Retarded phase transition by fluorine doping in Li-rich layered $\text{Li}_{1.2}\text{Mn}_{0.54}\text{Ni}_{0.13}\text{Co}_{0.13}\text{O}_2$ cathode material, *J. Power Sources* 283 (2015) 162–170.
- [21] S. K. Kumar, S. Ghosh, P. Ghosal, S. K. Martha, Synergistic effect of 3D electrode architecture and fluorine doping of $\text{Li}_{1.2}\text{Ni}_{0.15}\text{Mn}_{0.55}\text{Co}_{0.1}\text{O}_2$ for high energy density lithium-ion batteries, *J. Power Sources* 356 (2017) 115–123.

- [22] S. K. Kumar, S. Ghosh, S. K. Martha, Synergistic effect of magnesium and fluorine doping on the electrochemical performance of lithium-manganese rich (LMR)-based Ni-Mn-Co-oxide (NMC) cathodes for lithium-ion batteries, *Ionics* 23 (2017) 1655–1662.
- [23] S. B. Chikkannanavar, D. M. Bernardi, L. Liu, A review of blended cathode materials for use in Li-ion batteries. *J. Power Sources* 248 (2014) 91–100.
- [24] K. Zaghib, M. Trudeau, A. Guerfi, J. Trottier, A. Mauger, C. M. Julien, New advanced cathode material: LiMnPO_4 encapsulated with LiFePO_4 . *J. Power Sources*, 204 (2012) 177–181.
- [25] C. M. Julien, A. Mauger, J. Trottier, K. Zaghib, P. Hovington, H. Groult, Olivine-based blended compounds as positive electrodes for lithium batteries, *Inorganics*, 4 (2016) 17.
- [26] K. G. Gallagher, S.-H. Kang, S. U. Park, S. Y. Han, $x\text{Li}_2\text{MnO}_3 \cdot (1-x)\text{LiMO}_2$ blended with LiFePO_4 to achieve high energy density and pulse power capability, *J. Power Sources* 196 (2011) 9702–9707.
- [27] H.-S. Kim, S.-Il Kim, W.-S. Kim, A study on electrochemical characteristics of $\text{LiCoO}_2/\text{LiNi}_{1/3}\text{Mn}_{1/3}\text{Co}_{1/3}\text{O}_2$ mixed cathode for Li secondary battery, *Electrochim. Acta* 52 (2006) 1457–1461.
- [28] H. Y. Tran, C. Taubert, M. Fleischhammer, P. Axmann, L. Küppers, M. W.-Mehrens, LiMn_2O_4 Spinel/ $\text{LiNi}_{0.8}\text{Co}_{0.15}\text{Al}_{0.05}\text{O}_2$ Blends as Cathode Materials for Lithium-Ion Batteries, *J. Electrochem. Soc.* 158 (5) (2011) A556-A561.
- [29] T. Numata, C. Amemiya, T. Kumeuchi, M. Shirakata, M. Yonezawa, Advantages of blending $\text{LiNi}_{0.8}\text{Co}_{0.2}\text{O}_2$ into $\text{Li}_{1+x}\text{Mn}_{2-x}\text{O}_4$ cathodes, *J. Power Sources* 97-98 (2001) 358-360.
- [30] A. J. Smith, S. R. Smith, T. Byrne, J. C. Burns and J. R. Dahn, Synergies in blended LiMn_2O_4 and $\text{Li}[\text{Ni}_{1/3}\text{Mn}_{1/3}\text{Co}_{1/3}]\text{O}_2$ positive electrodes, *J. Electrochem. Soc.*, 159 (2012) A1696-A1701.
- [31] K.-W. Nam, W.-S. Yoon, H. Shin, K. Y. Chung, S. Choi, X.-Q. Yang, In situ X-ray diffraction studies of mixed LiMn_2O_4 – $\text{LiNi}_{1/3}\text{Co}_{1/3}\text{Mn}_{1/3}\text{O}_2$ composite cathode in Li-ion cells during charge–discharge cycling, *J. Power Sources* 192 (2009) 652–659.
- [32] A. Klein, P. Axmann, M. W.-Mehrens, Synergetic effects of $\text{LiFe}_{0.3}\text{Mn}_{0.7}\text{PO}_4$ - $\text{LiMn}_{1.9}\text{Al}_{0.1}\text{O}_4$ blend electrodes, *J. Power Sources* 309 (2016) 169-177.
- [33] J. Gao, A. Manthiram, Eliminating the irreversible capacity loss of high capacity layered $\text{Li}[\text{Li}_{0.2}\text{Mn}_{0.54}\text{Ni}_{0.13}\text{Co}_{0.13}]\text{O}_2$ cathode by blending with other lithium insertion hosts, *J. Power Sources* 191 (2009) 644–647.

- [34] P. Rozier, J. M. Tarascon, Li-rich layered oxide cathodes for next-generation Li-ion batteries: chances and challenges, *J. Electrochem. Soc.*, 162 (2015) A2490-A2499.
- [35] D. Wang, H. Buqa, M. Crouzet, G. Deghenghi, T. Drezen, I. Exnar, M. Grätzel, High-performance, nano-structured LiMnPO_4 synthesized via a polyol method, *J. Power Sources*, 189 (2009) 624-628.
- [36] S. K. Martha, B. Markovsky, J. Grinblat, Y. Gofer, O. Haik, E. Zinigrad, D. Aurbach, T. Drezen, D. Wang, G. Deghenghi, I. Exnar, LiMnPO_4 as an advanced cathode material for rechargeable lithium batteries, *J. Electrochem. Soc.* 156 (7) (2009) A541-A552.
- [37] V. Aravindan, J. Gnanaraj, Y.-S. Lee, S. Madhavi, LiMnPO_4 – A next generation cathode material for lithium-ion batteries, *J. Mater. Chem. A*, 1 (2013) 3518-3539.
- [38] A. C. Ferrari, J. Robertson, Interpretation of Raman spectra of disordered and amorphous carbon, *Phys. Rev. B*, 61(20) (2000) 14095.
- [39] E. F. Antunes, A. O. Lobo, E. J. Corat, V. J. Trava-Airoldi, A. A. Martin, C. Veríssimo, Comparative study of first-and second-order Raman spectra of MWCNT at visible and infrared laser excitation, *Carbon*, 44(11) (2006) 2202-2211.
- [40] R. J. Gummow, A. d. Kock, and M. M. Thackeray, Improved capacity retention in rechargeable 4 V lithium/lithium-manganese oxide (spinel) cells, *Solid State Ionics*, 69, 59 (1994).
- [41] S. K. Martha, J. Grinbat, O. Haik, E. Zinigrad, T. Drezen, J. H. Miners, I. Exnar, A. Kay, B. Markovsky, D. Aurbach, $\text{LiMn}_{0.8}\text{Fe}_{0.2}\text{PO}_4$: an advanced cathode material for rechargeable lithium batteries, *Angew. Chem. Int. Ed.*, 48 (2009) 8559–8563.

Chapter 6

Binder and Conductive Additive Free Silicon Electrode Architectures for Advanced Lithium-Ion Batteries

6.1. Abstract

Silicon is of great interest as anode material for LIBs since it has ten times higher specific capacity than traditional graphite anodes. The large volume change (~400%) during lithiation and de-lithiation induces large stresses, leading to pulverization of Si which in turn causes loss of electrical contact and eventually leads to capacity fade. To overcome the issues due to pulverization, this Chapter describes an attempt of binder and conducting additive free Silicon nanoparticles (Si-NPs) as anodes for LIBs. The Si-NPs are pressure embed onto copper foil current collector without using any organic binder or conductive carbon additive. The physical and structural studies are carried out by XRD, SEM, Raman, TEM, and electrochemical performance of Si-NPs by electrochemical impedance spectroscopy and galvanostatic charge-discharge cycling. Binder-free Si-NP electrodes exhibit an initial reversible capacity of 950 mAh g⁻¹ at C/10 rate and more than 650 mAh g⁻¹ during 500 cycles at 1C rate. The electrodes shows excellent rate capability (800 mAh g⁻¹ at 5C rate) and cycling stability, because of available free space for volume change during cycling of silicon NPs without pulverization. The binder-free anode fabrication enables Si-NPs to obtain the real capacity of silicon without any interference of capacity contribution from composite materials.

6.2. Background and Motivation

Silicon is considered as one of the most attractive anode materials for advanced LIBs. While the commonly used graphite anodes have a specific capacity of only 372 mAh g⁻¹, silicon can alloy up to 4.4 Li atoms at room temperature, delivering capacity close to 4200 mAh g⁻¹ [1-4] which is the highest theoretical capacity of all known anode material available today. In addition to the capacity, it has a lithiation potential close to that of graphite (i.e., 0.4 V vs. Li/Li⁺) [1-4] and is non-toxic, and high abundance in the earth's crust. In spite of these advantages, there are certain fundamental challenges to the use of silicon as a viable anode material for LIBs. These include (i) large volume expansion/contraction (~400%) during lithium insertion/extraction induces large stresses, leading to pulverization of Si which in turn causes loss of electrical contact and eventually leads to capacity fade [2-5], (ii) the lack of a mechanistic understanding of the nature of SEI formation on the silicon surface and its stability during the repeated expansion and contraction during cycling [2-4, 6].

It has been shown that nanostructured silicon anodes circumvent volume modification as they can accommodate large strain without pulverization, provide good electronic contact and conduction, and display short lithium insertion distances [3-5, 7-25]. A variety of silicon nanostructures [3-4, 7-25] and silicon/carbon composites [12-22], 3D electrode architectures [3, 9, 14, 24], and core shell structures [9,14, 17-18] have been investigated to overcome the problems associated with volume expansion, capacity fade and low cycling stability. There are many reports to overcome the issues of pulverization due to volume change. Si nanowires deposited onto SS foil current collector showed a reversible capacity of approximately 2900 mAh g⁻¹ at a C/20 rate, but capacity retention was less than 50% at 2C rate [9]. The nest-like Si nanospheres showed a reversible lithium storage of 3952 mAh g⁻¹ at 100 mA g⁻¹) but retained only 36% of capacity after 50 cycles [10]. Amorphous silicon coated onto carbon nanofibers to form a core-shell structure and the resulted core-shell nanowires showed great, stable charge capacity over 2000 mAh g⁻¹ by introducing the carbon-silicon core-shell nanowires for high power and long cycle life LIBs [11]. Carbon core experiences less stress during lithium insertion and de-insertion and can act as a mechanical support for an efficient electron conducting

pathway. 2D amorphous silicon nanowalls which retains the advantages of 1D silicon nanotubes shown to have improved initial coulombic efficiency and stable capacity of 2100 mAh g⁻¹ at C/5 rate due to effective release of mechanical stress to avoid structure pulverization [18]. 3D porous bulk Si particles by the thermal annealing and etching showed a reversible capacity of ~2800 mAh g⁻¹ for 100 cycles [14]. Si@C@Void@C nanohybrids shows an enhanced reversible capacity of 1366 mAh g⁻¹ after 50 cycles at 500 mA g⁻¹ by developing core-shell yolk-shell structure [19]. Hollow core-shell structured silicon@carbon nanoparticles embedded in carbon nanofibers attained high reversible capacity of 1020.7 mAh g⁻¹ after 100 cycles at a current density of 0.2 A g⁻¹ [20]. Pomegranate-inspired Si-C nanoscale designs of Si nanoparticles showed an initial reversible capacity of 2350 mAh g⁻¹ at C/20 rate and 97% capacity retention after 1,000 cycles have been achieved for these electrodes [21].

However, the nano-size interface between the nanostructured active material and the current collector results in a high electrical contact resistance, which also impairs the efficiency of electron transport. In addition, the small contact area undergoes a high shear stress when silicon swells during lithiation, potentially causing separation of active material from the substrate [5]. Like this there are many ways of making silicon with different shape and sizes or morphologies which involves many complex steps to circumvent the volume change during cycling. Moreover, there is also a challenge of fabricating the silicon anode with free expansion of space for silicon, i.e., proper attaching of the different silicon morphologies with the copper current collector for stable electrochemical cycling.

In this work, we present a simple method of electrode fabrication where we use spherical Si-NPs synthesized by magnesiothermic reduction [15] from fumed silica. The as-synthesized Si-NPs were manually pressed onto copper foil as the current collector, without the addition of any conductive carbon or organic binder. The goal is to ensure proper attachment of the active material onto the current collector by pressure-embedding the Si-NPs, in order to eliminate the interface between the two as far as possible. This in turn will minimize the contact resistance, facilitating electron transport and thus improving cycling capability. In addition, less particle

loading, uniform distribution of Si-NPs will ensure that all the active material which has been pressed onto the current collector takes part in the electrochemical reaction, further enhancing electrochemical performance. This is the simplest and most cost effective method of electrode fabrication compared to other methods.

6.3. Experimental

6.3.1. Synthesis of Si-NPs by magnesiothermic reduction

Si-NPs are synthesized by magnesiothermic reduction [15] where the stoichiometric amounts of fumed silica and magnesium powder (1:2 mole ratio) are mixed well in a mortar pestle for 1 hr followed by annealing at 700 °C for 2 hrs under argon gas. The Si-NPs are obtained by removing the MgO and Mg₂Si by treating the obtained product with 1N HCl solution.

6.3.2. Structural, physical and characterization of Si-NPs

Structural, physical, compositional analyses were conducted by using powder XRD, SEM, EDAX, Raman, TEM similar to the experiments explained in experimental part of Chapter 3.

6.3.3. Electrode preparation

Electrodes were prepared by embedding the as-synthesized Si-NPs by pressure (25 psi) onto copper foil current collector, without using any additional conductive carbon or organic binder. The electrodes were then punched into circular discs (1 cm² area). For comparison, composite electrodes were prepared using 50 wt. % active material (Si-NPs), high surface area carbon, ACS 2500 (40 wt. %) (China Steel Chemical Corporation, Taiwan) and binder 10 wt. % polyvinylidene fluoride binder (Kynar, Japan), dissolved in N-methyl-2-pyrrolidone (Sigma Aldrich) were mixed in a planetary ball mill mixture (Gelon, China) for 1h to form slurry. This slurry was then coated onto copper foil using the doctor-blade technique. The as-prepared conventional Si composite electrode was then dried at 90 °C under vacuum for overnight, punched, weighed and used as anodes.

6.3.4. Cell assembly and electrochemical characterization

The electrochemical performance of the as-prepared Si on Cu and composite electrodes was evaluated in two-electrode Swagelok type cells with pure lithium foil (Alfa Aesar) as the counter electrode, Si electrode sandwiched between 2 polyethylene-polypropylene- polyethylene membrane separators (Celgard Inc.). The electrolyte comprised 1 M LiPF₆ dissolved in a mixture of ethylene carbonate (EC) and dimethyl carbonate (DMC) (1:1 by volume) (Merck, India). The cells were assembled in a glove box filled with pure argon gas (MBraun, Germany). Galvanostatic charge–discharge cycling was carried out using a multichannel battery tester (Arbin BT2000 - Battery Test Equipment, USA) within the operating voltage range of 1.2 to 0.05 V. The impedance measurements of these composite electrodes were measured by using Solartron cell test system consists of 1470E multi-channel potentiostats and multiple 1455A series frequency response analyzers (FRAs) (driven by Corrware and Z-Plot software from Scribner Associates). The impedance measurements were carried out in a frequency range between 1 MHz and 10 mHz before and after 1st cycle and 500 cycles at 1.2 V.

6.3.5. Post-mortem TEM analyses

Post-mortem TEM analyses were conducted on cycled Si anodes. The powdery Si-NPs were separated from Cu current collector by sonication, followed by washing several times with pure DMC solvent, dried under vacuum and used for analysis.

6.4. Results and Discussion

6.4.1. Structural, physical characterization of Si-NPs

Powder XRD pattern of the as-prepared Si-NPs is presented in Fig. 6.1(a). The characteristic peaks are for a crystalline silicon having a face-centred cubic lattice. No impurity phases were detected. Raman spectra of Si-NPs presented in Fig. 6.1(b) have sharp, intense peak at 510 cm⁻¹ due to crystalline Si-Si stretching [26]. The weak band at 928 cm⁻¹ corresponds to the second order Raman signal for silicon [26].

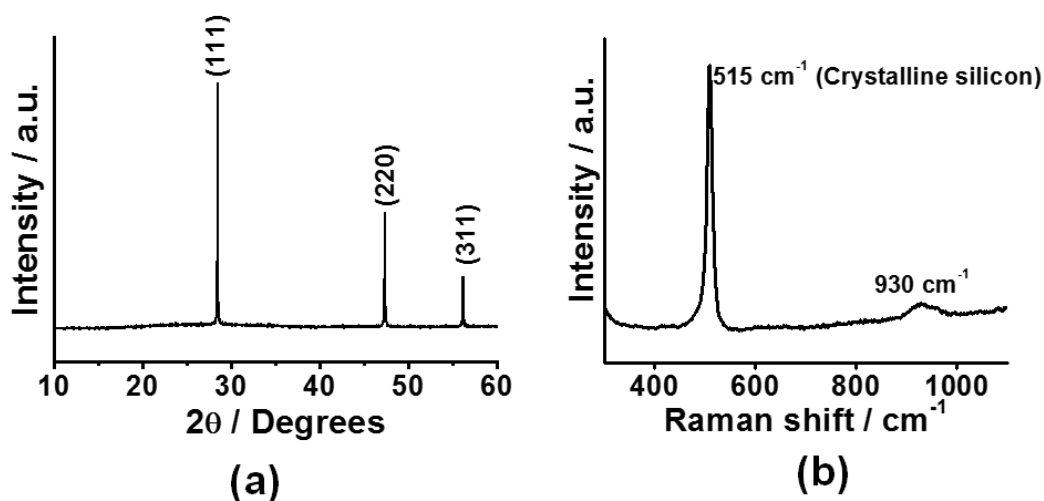


Fig. 6.1: (a) X-ray diffraction pattern of as-synthesized Si-NPs by magnesiothermic reduction from fumed silica; (b) Raman spectra of the as-synthesized Si-NPs

Figure 6.2(a) and (b) shows the FESEM images of the as-prepared Si-NP powders and Si-NPs on electrode, respectively. Si-NPs have typical spherical morphology having particle sizes in the range of 50-100 nm as shown in Fig. 6.2 (a). The pure Si-NP active material on the copper (Fig. 6.2 (b)) foil are uniformly distributed having enough vacant space for silicon volume change during electrochemical cycling.

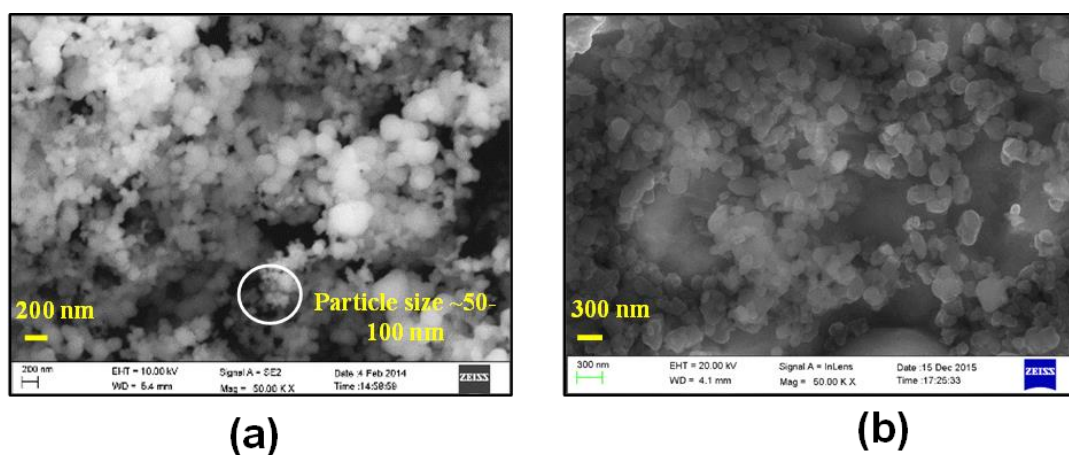


Fig. 6.2: (a) SEM image of the as-synthesized Si-NPs indicating few particle sizes; (b) SEM image of the as-prepared Si- NPs on copper current collector

Figure 6.3 shows EDAX analysis of as-prepared electrode. It shows that Si and Cu are the major components of the electrode. The presence of oxygen indicates Si NPs and Cu foil may be slightly oxidized.

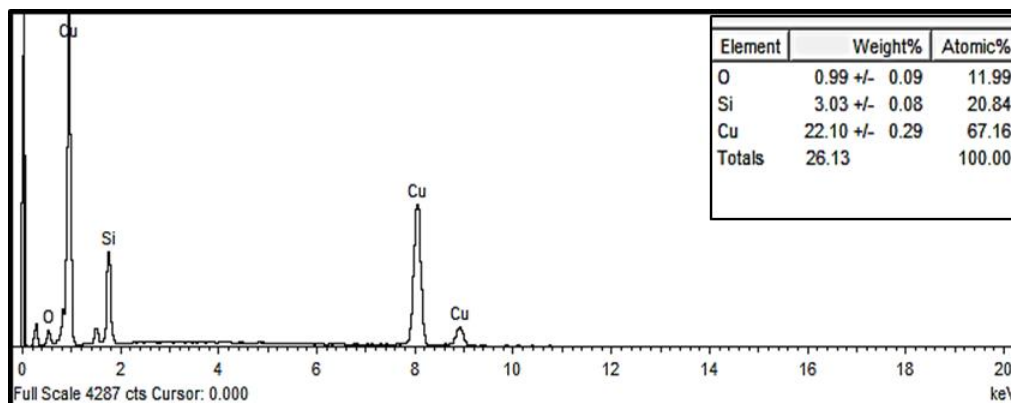


Fig. 6. 3: EDAX image of the as-prepared Si-NPs on Cu electrode

6.4.2. Electrochemical performance studies of Si- electrodes

Cycling, silicon anodes at different cut-off potentials provide different capacity and stability. It has been reported in the literature that cycling above 50 mV of silicon anodes reduces the formation of crystallized phases completely and results in better cycling performance [6, 27]. As our Si-NPs are crystalline, galvanostatic charge-discharge cycling was conducted in the operating voltage range between 1.2 V to 0.05 V. Figure 6.4 shows the cyclability of pure Si-NPs on copper foil for 500 cycles and composite electrode on copper foil for 60 cycles. The electrodes show very high initial lithiation capacity, close to 2800 and 1256 mAh g⁻¹ for the composite and pure Si-NPs, respectively. Reversible capacity of 1500 mAh g⁻¹ is obtained for the composite Si-NPs. However, composite Si-NP electrodes loses their capacity in 20 cycles, could be attributed to their pulverization, loss of contact of active Si-NPs with the current collector.

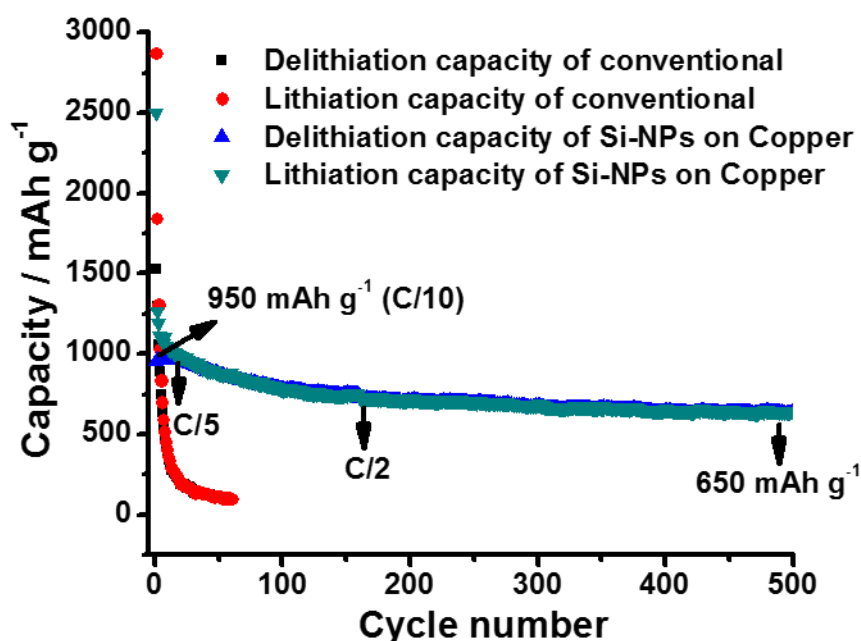


Fig. 6.4: Capacity vs. cycle number for the Si-NPs on composite electrode for 60 cycles and pressure embodied on copper foil current collector during 500 cycles at 25°C. For the composite electrodes charge-discharges were carried out at C/10 rate. For pressure embodied Si-NPs on copper foil electrode was cycled at C/10 rate (1-20 cycles), C/5 rate for cycle # 21-150 and at C/2 rate during 151-500 cycles

Pure Si-NPs on copper foil delivers an initial reversible capacity of 950 mAh g⁻¹ (at C/10 rate), ~900 mAh g⁻¹ (at C/5 rate). These Si-NPs cycles well over 500 cycles due to good electrical contact of Si-NPs with current collector. These Si-NPs retain 650 mAh g⁻¹ (at C/2 rate) at the end of 500 cycles. Coulombic efficiency of > 99 % (after 20 cycles) observed for the Si-NPs due to absence of SiO_x leads to improved coulombic efficiency. Significant improvement in capacity retention of the pressure embodied Si-NPs compared to composite anodes indicates that pressure embodied Si-NPs are uniformly dispersed on current collector and have good electrical contact compared to the composite anodes where Si-NPs are not uniformly dispersed between carbon black and not adhered well with the current collector. Besides, it is likely that the conventional composite electrode fabrication approach may involve a certain degree of agglomeration of particles and absence of sufficient spaces between these particles causes them to fracture and detach from the current collector. Moreover, it is possible that in presence of the organic binder, a resistive layer tends to exist

between the current collector and the silicon active material, preventing the proper adhesion of the latter and consequently interfering in electron transport. In overall, Si-NPs in composite electrode losses contact with current collector due to pulverization which causes capacity fade.

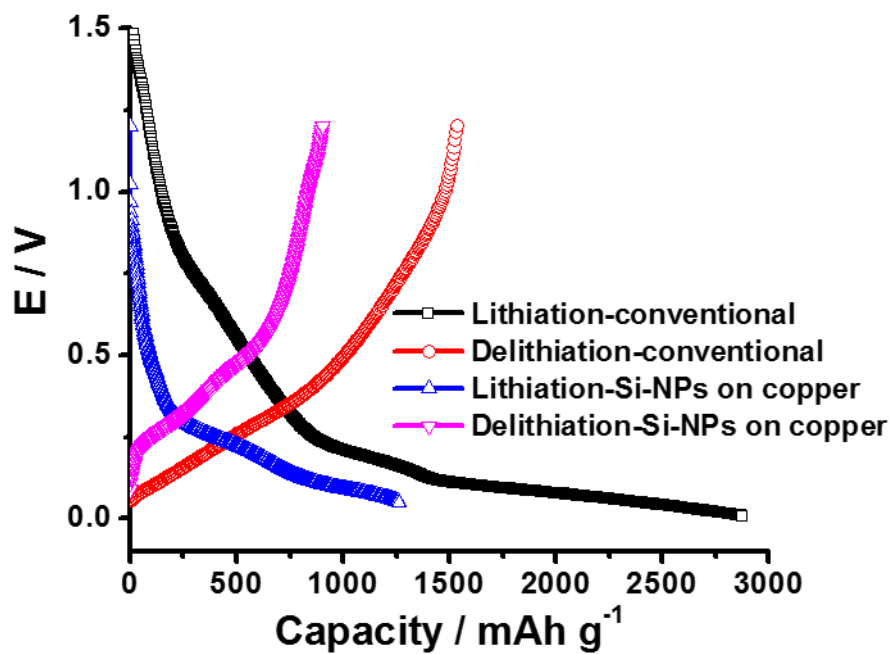


Fig. 6.5: Galvanostatic charge-discharge voltage profile for the composite and pressure embodied Si-NPs on copper foil current collector electrode during first cycle at C/10 rate

The charge-discharge voltage profiles during the first cycle for the composite and Pristine Si-NPs are presented in Fig. 6.5. The first lithiation voltage profile of Si-NPs have capacity contribution at voltages between 0.2 V and 0.8 V, which could be attributed to the SEI on the surface of Si-NPs [24]. As expected at potentials of ≤ 0.2 V the capacity contribution is derived from the alloying reaction between Li and Si [6, 24, 28-30]. The amount of lithium that is irreversibly (irreversible capacity) consumed during the formation of SEI formation for the composite electrode is about 50% compared to that of pressure embodied Si-NPs of 25%. High irreversibility of Lithium in composite anodes contribute to the rapid capacity fade. On other hand, reduced SEI formation of pressure embodied Si-NPs can lead to higher coulombic efficiency of 99%.

The various C-rate charge-discharge experiments were performed to explore how a charge-discharge processes degrade the cell performances. The rate capability

studies performed at C/20, C/10, C/5, 1 C, 5C rates and back to C/10 rate for about 80 cycles are shown in Fig. 6.6. The Si-NPs on Cu electrode shows excellent rate capability. Si-NPs on Cu electrode delivers $> 875 \text{ mAh g}^{-1}$ capacity at 1C and about 800 mAh g^{-1} capacity at 5C rates. After cycling of cells at high C rates, followed by cycling at slow rates of C/10, the cells retain almost 100 % capacity indicating that the electrode fabrication approach mitigate pulverization leading to improved capacity retention at the high C rates. Besides, as Si-NPs are in direct electrical contact with copper current collector, the active material utilization is much higher leading to excellent electrochemical performance at low to high C rates.

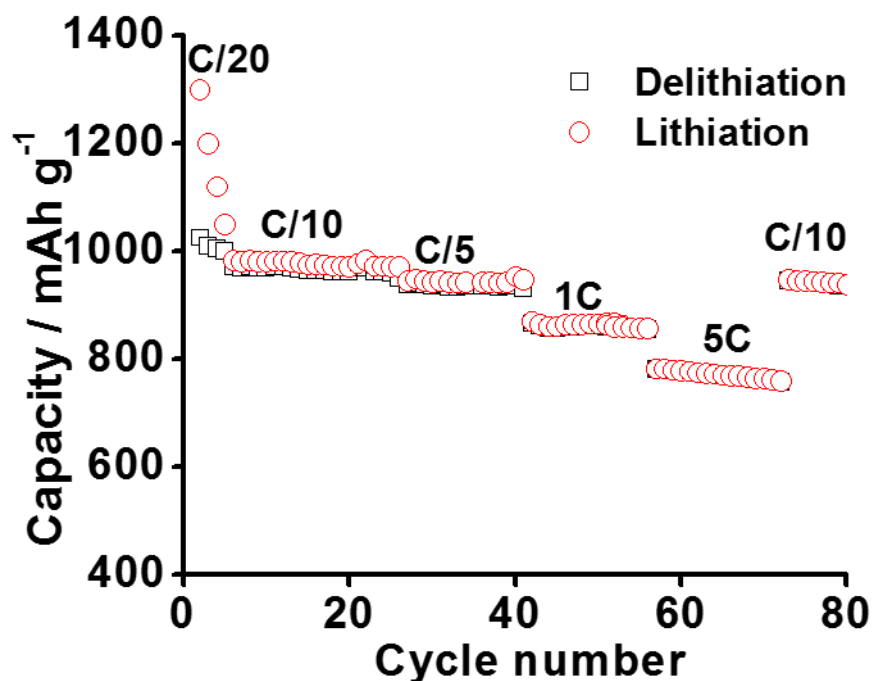


Fig. 6.6: The C rate performance of Si-NPs pressure embodied on copper foil current collector during 80 cycles at C/20, C/10, C/5, 1C and 5C rates

In order to evaluate excellent electrochemical performance of Si-NPs on copper electrode at high C rates and during long cycling, EIS were carried out before and after cycling, as presented in Fig. 6.7. The Ohmic resistance (R_{Ω}) is seen to be $2.6 \Omega \text{ cm}^2$ before cycling and after 1st cycle. R_{Ω} in the de-lithiated state (1.2 V) after 500 cycles shows very little change (3.8 Ohm cm^2) in relation to the Si-NPs on copper electrode before cycling. Moreover, little change in charge transfer resistance of the cell is observed after 500 cycles ($480 \Omega \text{ cm}^2$) compared to $290 \Omega \text{ cm}^2$ of Si-NPs

embodied onto copper anode before cycling. This signifies its excellent electrochemical performance during long cycling.

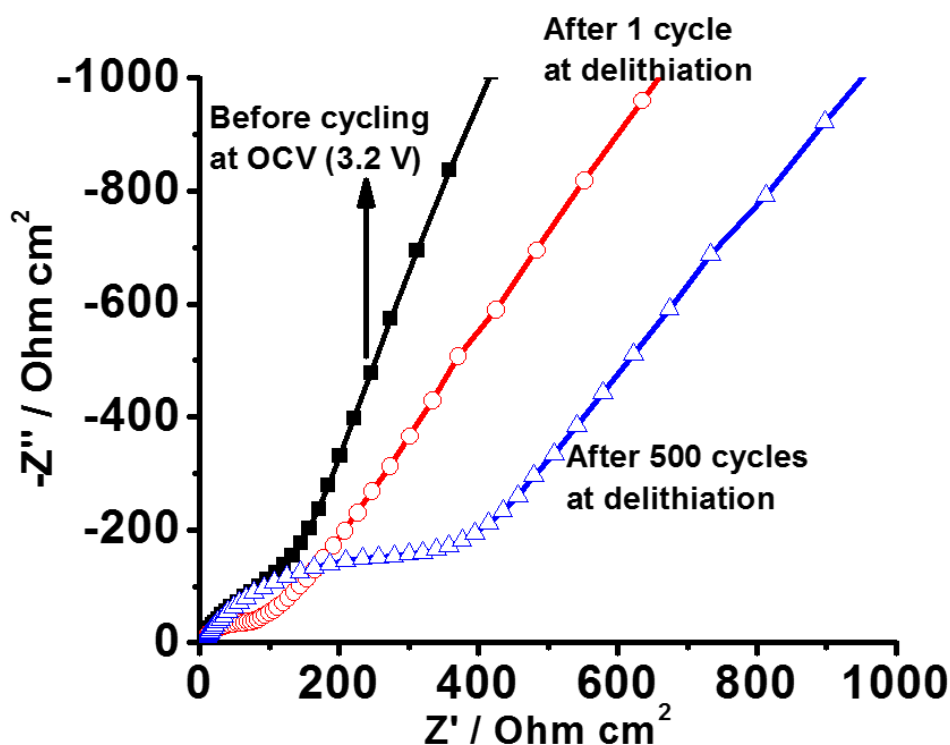


Fig. 6.7: Nyquist plots for the Si-NPs on Cu electrode in the frequency range between 1 MHz and 10 mHz during before cycling at OCV, after first cycle de-lithiation and after 500 cycles de-lithiation

6.4.3. Post-mortem analysis of Si-electrodes

In order to understand the importance of the pressure embed electrode architecture of Si-NPs which delivers excellent electrochemical performance due to minimized pulverization, particle size and morphologies before and after cycling were studied by HR-TEM (Fig. 6.8(a-c)). The HR-TEM of pristine Si-NPs presented in Fig. 6.8(a) and (b) shows spherical morphology with particle sizes ranging from 50-100 nm. TEM image in Fig. 6.8(b) shows lattice fringes corresponding to (111) plane of pristine Si-NPs which suggest the crystalline nature of silicon. There is not much difference in particle size and morphology of pristine and cycled Si-NPs (Fig. 6.8(a) and (c)) which strongly supports that Si-NPs embodied onto copper foil current collector, and is one of the best approach of electrode fabrication where all problems associated with silicon as anode are alleviated and excellent electrochemical performance is achieved.

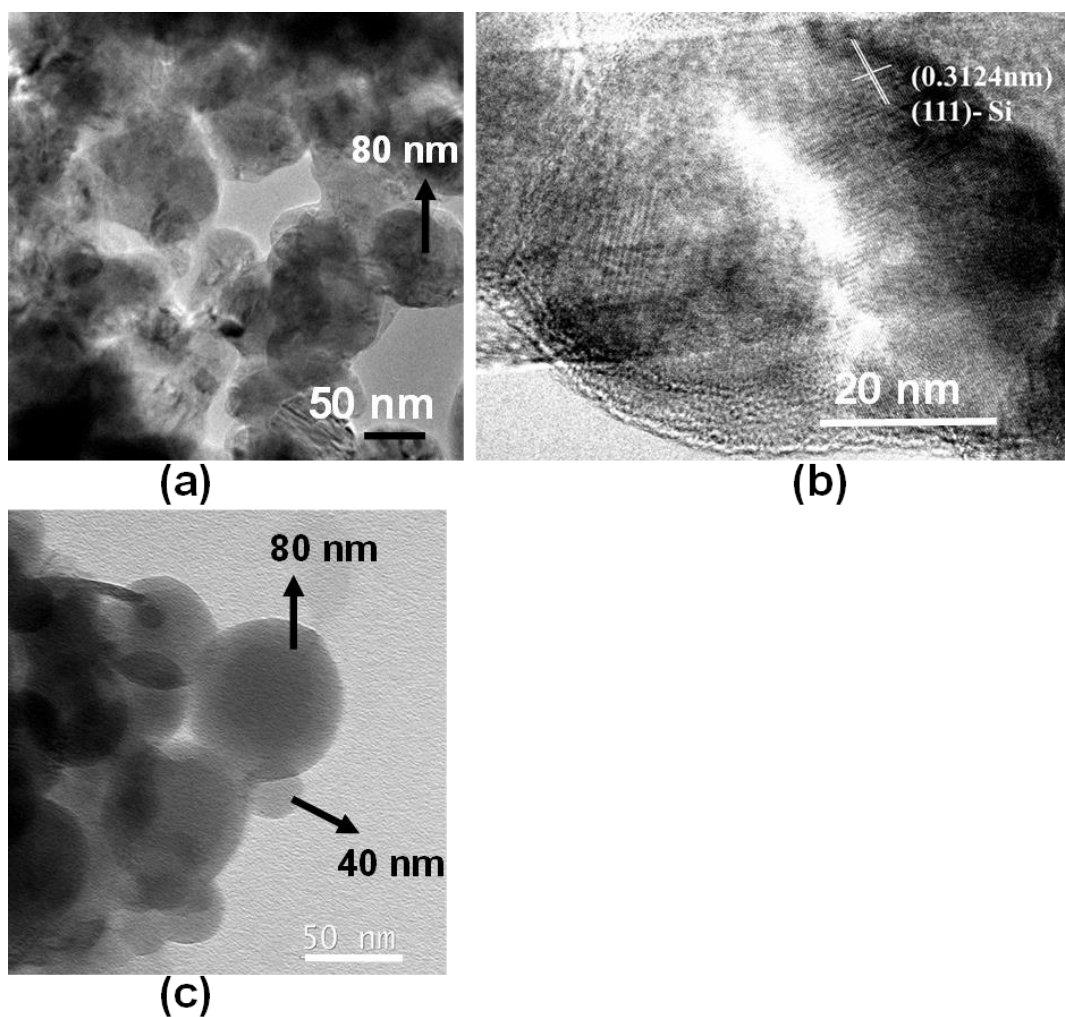


Fig. 6.8: (a) and (b) are TEM images of pristine silicon NPs, and (c) silicon- NPs cycled for 500 cycles

6.4.4. Discussions

The primary issues associated with silicon anodes is the pulverization that occurs as a result of volume expansion and contraction during lithiation and de-lithiation, respectively. This pulverization includes fracturing of individual particles and also the detachment of the material from the current collector due to stress induced by the alloying-dealloying process at the level of the entire electrode. The goal is therefore to design an electrode that will improve capacity retention and cycling stability by accommodating the issue of volume modification. In composite electrode, the cohesive forces between the binder and active materials play a vital role for the electrochemical performance. While some binders may be better suited to a specific

active material than others. The electrochemically inactive binder itself may contribute to the impedance of the cell. Further, resistive layer of micro or nano dimensions exist between the active material and the current collector tends to interfere with the electron transport, resulting poor electrochemical performance.

The as-prepared Si-NPs pressure embodied on copper foil current collector overcome the issues of silicon anodes in multifaceted ways. The current electrode fabrication approach is free from conductive diluents and polymeric binders. Consequently, the entire electrode material is electrochemically active and contributes to the capacity of the cell. Besides, the electrode fabrication ensures excellent adhesion of the active material to the current collector, without leaving any space for a resistive layer that would else have interfered with the electron transport. Moreover, electrodes with less silicon content have been shown to cycle at larger capacities. In our electrode fabrication approach the silicon particles are dispersed uniformly on the copper foil with sufficient gaps between them (Fig. 6.2), thus providing enough space to accommodate the volume expansion and compression of the Si-NPs. This accounts for the reasonably high capacity and remarkably stable cycling of the electrode.

6.5. Conclusions

We have successfully demonstrated a binder-free, additive free Si anodes by pressure-embedding Si-NPs onto copper foil. The low silicon content and the even distribution of particles on the copper foil with sufficient gaps in between provide vacant spaces to accommodate the volume expansion and contraction of silicon, thereby effectively alleviating the problem of pulverization. The application of pressure ensures excellent adhesion of the active material to the current collector, thus minimizing the contact resistance at the interface and thereby improving electron transport. The as-prepared electrode shows high initial discharge capacity $\sim 1050 \text{ mAh g}^{-1}$ (C/20), 950 mAh g^{-1} at C/10 and good cycling stability and retains more than 650 mAh g^{-1} (C/2) capacity even after 500 cycles.

References

- [1] G.-A. Nazri, G. Pistoia, eds. *Lithium Batteries - Science and Technology*, Kluwer Academic Publishers (2004) 259.
- [2] S. Bourderau, T. Brousse, D. M. Schleich, Amorphous silicon as a possible anode material for Li-ion batteries, *J. Power Sources* 81–82 (1999) 233–236.
- [3] C. K. Chan, H. Peng, G. Liu, K. McIlwrath, X. F. Zhang, R. A. Huggins, Y. Cui, High-performance lithium battery anodes using silicon nanowires, *Nat. Nanotech.*, 3 (2008) 31–35.
- [4] M. Gu, Y. He, J. Zheng, C. Wang, Nanoscale silicon as anode for Li-ion batteries: The fundamentals, promises, and challenges, *Nano Energy*, 17 (2015) 366–383.
- [5] A. Mukhopadhyay, B. W. Sheldon, Deformation and stress in electrode materials for Li-ion batteries, *Progress Mater. Sc.*, 63 (2014) 58–116.
- [6] L. A. Berla, S. W. Lee, I. Ryu, Y. Cui, W. D. Nix, Robustness of amorphous silicon during the initial lithiation/delithiation cycle, *J. Power Sources* 258 (2014) 253–259.
- [7] C. Erk, T. Brezesinski, H. Sommer, R. Schneider, J. Janek, Towards silicon anodes for next-generation lithium ion batteries: a comparative performance study of various polymer binders and silicon nanopowders, *ACS Appl. Mater. Interfaces* 5 (2013) 7299–7307.
- [8] H. Zhou, J. Nanda, S. K. Martha, R. R. Unocic, H. M. Meyer III, Y. Sahoo, P. Miskiewicz, T. F. Albrecht, Role of surface functionality in the Electrochemical performance of silicon nanowire anodes for rechargeable lithium batteries, *ACS Appl. Mater. Interfaces* 6 (2014) 7607–7614.
- [9] L.F. Cui, R. Ruffo, C. K. Chan, H. Peng, Y. Cui, Crystalline-amorphous core-shell silicon nanowires for high capacity and high current battery electrodes, *Nano Lett.*, 9 (1) (2009) 491–495.
- [10] H. Kim, J. Cho, Superior Lithium Electroactive Mesoporous Si@Carbon Core–Shell Nanowires for Lithium Battery Anode Material, *Nano Lett.*, 8 (2008) 3688–3691.
- [11] H. Ma, F. Cheng, J. Chen, J. Zhao, C. Li, Z. Tao, J. Liang, Nest-like Silicon Nanospheres for High-Capacity Lithium Storage, *Adv. Mater.* 19 (2007) 4067–4070.
- [12] J. P. Maranchi, A. F. Hepp, P. N. Kumta, High capacity, Reversible silicon thin-film anodes for lithium-ion batteries, *Electrochem. Solid State Lett.*, 6 (9) (2003) A198–A201.

- [13] J. Liang, X. Li, Q. Cheng, Z. Hou, L. Fan, Y. Zhu, Y. Qian., High yield fabrication of hollow vesica-like silicon based on the Kirkendall effect and its application to energy storage, *Nanoscale* 7 (2015) 3440-3444.
- [14] H. Kim, B. Han, J. Choo, J. Cho, Three-dimensional porous silicon particles for use in high-performance lithium secondary batteries, *Angew. Chem. Int. Ed.*, 47 (2008) 10151–10154.
- [15] P. Gao, H. Tang, A. Xing, Z. Bao, Porous silicon from the magnesiothermic reaction as a high-performance anode material for lithium ion battery applications, *Electrochim. Acta*, 228 (2017) 545-552.
- [16] C. Zhu, K. Han, D. Geng, H. Ye, X. Meng, Achieving High-Performance Silicon Anodes of Lithium-Ion Batteries via Atomic and Molecular Layer Deposited Surface Coatings: an Overview, *Electrochim. Acta* 251(2017) 710-728.
- [17] J. Tang, A. D. Dysart, D. H. Kim, R. Saraswat, G. M. Shaver, V. G. Pol, Fabrication of Carbon/Silicon Composite as Lithium-ion Anode with Enhanced Cycling Stability, *Electrochim. Acta*, 247 (2017) 626-633.
- [18] J. Wan, A. F. Kaplan, J. Zheng, X. Han, Y. Chen, N. J. Weadock, N. Faenza, S. Lacey, T. Li, J. Guo, L. Hu, Two dimensional silicon nanowalls for lithium ion batteries, *J. Mater. Chem. A*, 2 (2014) 6051-6057.
- [19] J. Xie, L. Tong, L. Su, Y. Xu, L. Wang, Y. Wang, Core-shell yolk-shell Si@C@Void@C nanohybrids as advanced lithium ion battery anodes with good electronic conductivity and corrosion resistance, *J. Power Sources* 342 (2017) 529-536.
- [20] N. Liu, Z. Lu, J. Zhao, M. T. McDowell, H.W. Lee, W. Zhao, W., Y. Cui, A pomegranate-inspired nanoscale design for large-volume-change lithium battery anodes. *Nat. Nanotech.*, 9(3), (2014) 187-192.
- [21] Y. Chen, Y. Hu, Z. Shen, R. Chen, X. He, X. Zhang, Y. Li, K. Wu, Hollow core shell structured silicon@carbon nanoparticles embed in carbon nanofibers as binder-free anodes for lithium-ion batteries, *J. Power Sources* 342 (2017) 467-475.
- [22] J. Qin, M. Wu, T. Feng, C. Chen, C. Tu, X. Li, C. Duan, D. Xia, D. Wang, High rate capability and long cycling life of graphene-coated silicon composite anodes for lithium ion batteries, *Electrochim. Acta* 256 (2017) 259-266.
- [23] W. Wang, P. N. Kumta, Nanostructured hybrid silicon/carbon nanotube heterostructures: reversible high-capacity lithium-ion anodes, *ACS Nano* 4 (2010) 2233–2241.

- [24] C. K. Chan, R. Ruffo, S. S. Hong, Y. Cui, Surface chemistry and morphology of the solid electrolyte interphase on silicon nanowire lithium-ion battery anodes, *J. Power Sources* 189 (2009) 1132–1140.
- [25] J. Qu, H. Li, J. J. Henry Jr., S. K. Martha, N. J. Dudney, H. Xua, M. Chi, M. J. Lance, S. M. Mahurin, T. M. Besmann, S. Dai, Self-aligned Cu–Si core–shell nanowire array as a high-performance anode for Li-ion batteries, *J. Power Sources* 198 (2012) 312–317.
- [26] J. Liu, J. Niu, D. Yang, M. Yan, J. Sha, Raman spectrum of array-ordered crystalline silicon nanowires, *Physica E: Low-dimensional Systems and Nanostructures* 23 (2004) 221-225.
- [27] M. N. Obrovac, L. Christensen, Structural changes in silicon anodes during lithium insertion/ extraction, *Electrochem. Solid-State Lett.*, 7 (2004) A93-A96.
- [28] V. Etacheri, O. Haik, Y. Goffer, G. A. Roberts, I. C. Stefan, R. Fasching, and D. Aurbach, Effect of fluoroethylene carbonate (FEC) on the performance and surface chemistry of Si-nanowire Li-ion battery anodes, *Langmuir* 28 (2012)965–976.
- [29] C. C. Nguyen, B. L. Lucht, Comparative Study of fluoroethylene carbonate and vinylene carbonate for Silicon anodes in Lithium ion batteries, *J. Electrochem. Soc.*, 161 (2014) A1933-A1938.
- [30] H. Gao, L. Xiao, I. Plüme, G.-L. Xu, Y. Ren, X. Zuo, Y. Liu, C. Schulz, H. Wiggers, K. Amine, Z. Chen, Parasitic reactions in nanosized silicon anodes for Lithium-ion batteries, *Nano Lett.*, 17 (2017) 1512–1519.

Chapter 7

In-situ 3D Electrode Fabrication of High Capacity Silicon-Carbon Anodes for Lithium-Ion Batteries

7.1. Abstract

In this Chapter we make another attempt to solve the issues of pulverization, significantly improve irreversible capacity, capacity fade and C rate performances through organic binder and conducting diluent free Silicon-Carbon (Si-C) 3D electrodes architectures. Si-NPs are synthesized by magnesiothermic reduction in Chapter 6 are used as active mass along with carbons derived from petroleum pitch (P-pitch) onto 3D carbon fiber (CF) current collector. Highly conductive CFs of 5-10 μm in diameter have been used to replace a conventional copper foil current collector. We demonstrate here P-pitch which adequately coat between the CFs and Si-NPs above 700 $^{\circ}\text{C}$ under Argon atmosphere. P-pitch makes uniform continuous layer of 10-15 nm thick coating along the exterior surfaces of Si-NPs. Capacities in excess of 2200-2050 mAh g^{-1} (at C/10) for 100s cycles at 900 and 1000 $^{\circ}\text{C}$, respectively have been achieved in half-cell configuration. Synergistic effect of carbon coating and 3D carbon fiber electrode architecture improves the efficiency of the Si-C composite during long cycling at 1000 $^{\circ}\text{C}$. The usual organic binder and copper current collector can be replaced by a high temperature binder of carbonized P-pitch and CFs, respectively. Together these replacements increase the specific energy density and energy per unit area of the electrode.

7.2. Background and Motivation

US Department of Energy (DOE) year 2022 goals to develop next generation lithium ion batteries that have high energy density (300-400 Wh kg⁻¹) which enable a large market penetration of HEV's and EV's [1]. Besides, the LIBs should have reduced cost, improved safety and cycle life. So current research emphasis is given to develop high energy density cathodes, high voltage electrolytes coupled with high capacity silicon anodes for increasing energy density in LIBs [2-8]. As discussed in Chapter 3 and 4 Li and Mn rich TM oxide (LMR-NMC) composite cathodes which has almost double the capacity (372 mAh g⁻¹ for 1.2 Li transfer) of currently available cathodes have been investigated as a promising cathode material for LIBs [4, 9-13]. To enhance the performance of anodes which meet the requirement of the automotive industry, researchers have been investigating materials which form alloys with lithium to generate anodes that have specific capacities an order of magnitude higher than graphite [2-3, 6]. Silicon is an attractive anode material for LIBs mainly because of its very high theoretical charge capacity of 4200 mAh g⁻¹ (Li_{4.4}Si). But silicon has various issues of low electronic and ionic conductivity and most important one is high volume change of ~400% during lithiation and de-lithiation leading to structural degradation (pulverization) followed by capacity fade and reduced cycle life [6,14-21] need to be addressed before it is considered a potential candidate as anodes for lithium-ion batteries.

As discussed in Chapter 6, there has been an intense research to mitigate volume change during cycling, such as producing Si-NPs [15-21], aligned Si-nanowires/nanotubes [14, 22-24], dispersing silicon into an active (such as carbon) /inactive (eg. SiO₂) matrix [25-33], silicon based thin films [34-38], free standing Si-C electrodes and different morphologies of silicon [39-49]. Taking benefit of high conductivity of carbon and high capacity silicon, recent reports demonstrate carbon-silicon nanocomposites can circumvent the issues associated with silicon and improve the overall electrochemical performance of Si-anode for LIBs [25-33]. This is because Si-C nanocomposites can accommodate huge strain with reduced pulverization, provide good electronic contact, and exhibit short diffusion path for lithium ion insertion.

Another interesting approach of Si-C composite free standing electrodes (binder less and current collector less) which are flexible and are used to create thin and flexible LIBs. Flexible free standing graphene-silicon composite film prepared by in-situ filtration method shows discharge capacity of 708 mAh g⁻¹ beyond 100 cycles [39]. Composites of Si-NPs and graphene accommodated on 3D network of graphite exhibited high Li ion storage capacities of >2200 mAh g⁻¹ after 50 cycles and >1500 mAh g⁻¹ after 200 cycles [40]. Freestanding macroporous silicon film in combination with pyrolyzed polyacrylonitrile composite anode shows discharge capacity of 1260 mAh g⁻¹ for 20 cycles [41]. Light-weight free-standing carbon nanotube-silicon films prepared by sputtering method shows specific charge storage capacity (~2000 mAh g⁻¹) for 50 cycles [42]. Binder and additive free 3D porous nickel based current collector coated conformally with layers of silicon delivers high capacity of 1650 mAh g⁻¹ after 120 cycles of charge/discharge [42]. There are also several reports such as carbon-coated Silicon nanowires on carbon fabric [43], 3D free-standing carbon nanotubes [44], flexible nanoporous Si-carbon nanotube paper [45-48], hierarchical nano-branched C-Si/SnO₂ nanowire free standing electrodes [49] as tested as anodes which delivers reasonable good capacity ~1000 mAh g⁻¹ for 100s of charge-discharge cycles. In overall, Si-C composite free standing electrodes prepared by various synthesis approaches shows capacity between 700-2000 mAh g⁻¹ for about 100 cycles.

Here, we present a unique organic binder less, additive free 3D electrode architecture of Si-C NPs on CF current collector which replaces usual copper foil current collector [50-51]. P-pitch is used as carbon source which makes a good electrical contact between the CF current collector and Si- active particles at high temperatures >500 °C. CF mat has numerous advantages over copper current collector such as incorporation of large amount of active material into the 3D CF network, provides high interfacial contact of active material to the conductive network. Besides the carbon fibers are more flexible and can accommodate the volume change of silicon. But the silicon nanoparticles will lose the contact from CF due to absence of binder. So there is need of a material which supports the volume change, improves conductivity and binds silicon onto CF. P-pitch which is complex mixture of

polynuclear aromatic hydrocarbons, derived from heat treatment of coal and petroleum tars can be used as a high temperature binder to bind Si-NPs on to CF. Pitch undergoes carbonization above 500 °C to form conducting carbon through mesophase (liquid crystalline state) [50-52]. So annealing mixture of P-pitch and Si-NPs coated on to CF current collector at high temperatures ≥ 500 °C, melts the P-Pitch and allows the conformal coating throughout the silicon and carbon fiber which enables to have a conductive network and enough space for the volume expansion and contraction without undergoing pulverization. In addition, the binding strength of carbonized pitch with silicon and carbon fiber is influenced by temperature. In this work, we have studied effect of different annealing temperatures (700, 900, and 1000 °C) on the electrochemical performance of Si-C 3D electrodes. Electrodes developed by this method provide enough space for silicon surrounded by carbonized pitch on carbon fiber which support the volume expansion and contraction during cycling thus reducing the pulverization of the silicon. In this type of electrode, all the active material is exposed to electrolyte which implies the entire silicon is electrochemically active whereas in conventional composite electrode in which copper foil is used as current collector, interior part of the electrode is electrochemically inactive due to lack of access to electrolyte. Moreover, polyvinylidene fluoride (PVdF) binder in the composite electrode causes impedance rise leading to detrimental in the electrochemical performance. In addition, copper foil adds extra weight to the electrode. But 3D Si-C freestanding CF electrodes does not contain any organic binder, and less weight. This would further enhance energy density.

7.3. Experimental

7.3.1. Synthesis of Si-NPs and structural-physical characterizations

Si-NPs are synthesized by magnesiothermic reduction [20] of fumed silica discussed in Chapter 6. Powder XRD patterns of Si-NPs, carbon fibers etc. were performed by using a Panalytical X'Pert Pro diffractometer (The Netherlands), surface morphologies of the composite powders were measured by scanning electron microscope (Carle Zeiss SUPRA™ 40, Field Emission Scanning Electron Microscope) coupled with Thermo Noran EDS system for surface element analysis, transmission electron microscopy (JEOL-JSM-700F), and the physical properties by

Raman spectroscopy using a micro Raman spectrometer HR800 (Jobin Yovn Horiba, France), similar to the experiment discussed in Chapter 3. The surface area of the Si-C composites annealed at 700 °C, 900 °C and 1000 °C are measured by Brunauer–Emmett–Teller (BET) experiment (Quantachrome instruments, USA).

7.3.2. Structural-physical characterizations carbon fibers, carbonized pitch and electrodes

CF mats having diameter in the range between 5-10 μm as shown in Chapter 3, Fig. 3.8(c) are obtained from Advanced Fiber Nonwovens (AFN) (Hollingsworth & Vose Company, MA, USA) are mostly non-graphitic in nature (Only disordered carbons) as discussed in Chapter 3, Section 3.4.2.1. Structural, physical, electrochemical assessment of CFs (Fig. 3.8(e) and (f)). Graphitic carbon fibers are not used as they are very brittle. The current carbon fibers have good mechanical strength, flexible and have electrical conductivity of order of 10^4 S cm^{-1} . 1: 1 wt. ratio of Si-NPs and P. pitch are thoroughly mixed with required amount of N-vinyl pyrrolidone (NVP) to make slurry followed by coating on CF mats. The coated mats are dried at 90 °C under vacuum for overnight followed by punching, calendaring and carbonized the electrodes at 700-900-1000 °C for 5 hrs under argon atmosphere (Hereafter the electrodes are call Si-C composite electrodes on 3D CF). At temperature of $\geq 700 \text{ }^\circ\text{C}$, P-pitch forms foam like structure (Fig. 7.1(a)) and coats on to Si-NPs and along CFs (Fig.7.1(b)). Thereby P-pitch makes a good electronic contact between Si-NPs and CFs. The electrode structure of 700 °C annealed sample is shown in Fig. 7.1(b).

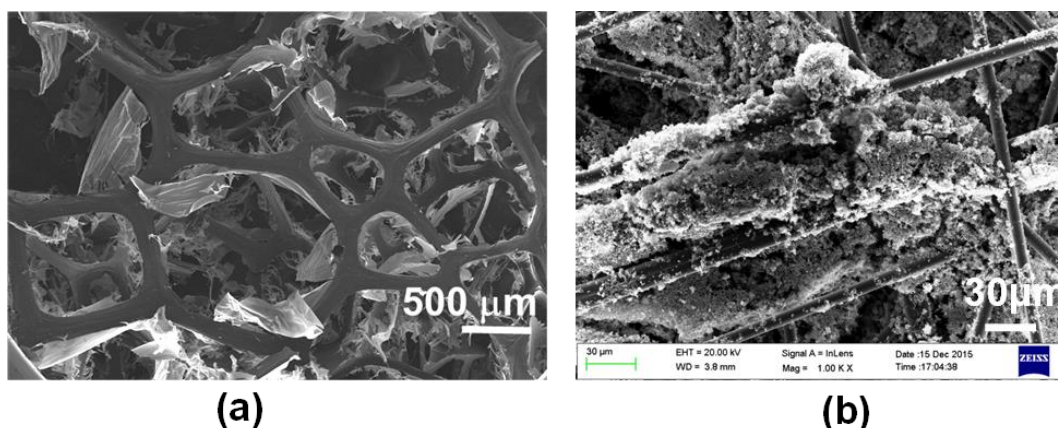
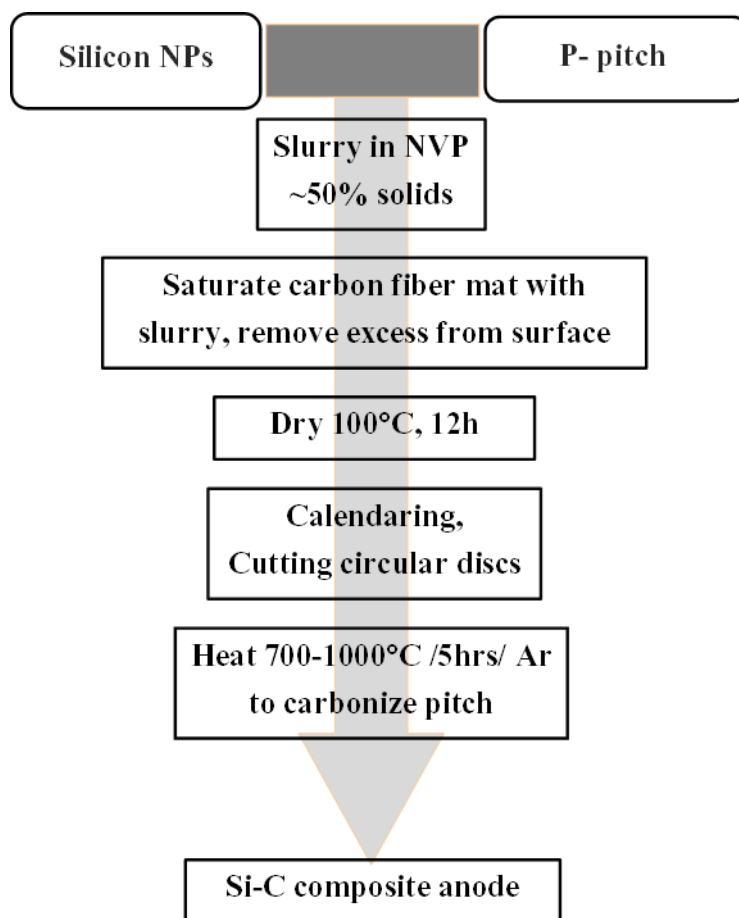


Fig. 7.1: (a) Foam like structure of P-pitch at temperature of $\geq 700 \text{ }^\circ\text{C}$, and b) Electrode structure of Si-NPs with P-pitch on CF current collector at $700 \text{ }^\circ\text{C}$

The complete scheme of electrode fabrication is presented in Scheme 7.1. The loading of Si-C composite on CF was between 6-10 mg cm⁻².



Scheme 7.1: Electrode fabrication approach of Si-NPs-C composite electrode on 3D carbon fiber

7.3.3. Electrode preparation and cell assembly

The conventional electrodes were prepared by making the composite of 60% active material, 10% PVdF (Kynar) and 30% carbon black (Super C65, Timcal), in N-methyl pyrrolidone (Sigma Aldrich) coated on to the copper foil (>99.9%, Strem chemicals, Inc., USA) current collector by using doctor blade technique. All the composite electrodes were dried under vacuum at 90 °C followed by punching them into 1 cm² area circular discs. The cells were fabricated in a glove box (M-Braun, Germany) filled with ultrahigh purity argon (99.999 %). The moisture and oxygen content of the glove box were less than 0.1 ppm. CR2032 coin type cells (MTI, China) were assembled using lithium foil as a counter electrode, polyethylene-polypropylene trilayer (Celgard Inc.) as separator and conventional silicon electrode or Si-C

composite on CF or only CF as working electrodes, 1M LiPF₆ in 1:2 ratio of ethylene carbonate and dimethyl carbonate as electrolyte. Full cells are assembled using Mg-F doped LMR-NMC composite cathodes as developed in Chapter 4 and with current Si-C composite anodes.

7.3.4. Electrochemical performance studies

The electrochemical performance of the samples comprising pristine Si-NPs, on copper foil (conventional electrode) and only pitch coated carbon fiber and finally silicon-carbon composite on carbon fiber as active masses were measured by using Solartran Cell Test system and Arbin battery cyler as explained in Chapter 6. The impedance measurements were carried out in a frequency range between 1 MHz and 10 mHz before cycling on open circuit condition (OCV) and in full charged condition after 100 cycles. Charge-discharge cycling were carried out in the potential range between 1.2 V and 50 mV using constant current. LMR-NMC cathode and Si anode full cells were cycled in the potential range between 2.0 V and 4.6V.

7.4. Results and Discussion

7.4.1. Structural-physical properties of Si-NPs, Si-C composite electrodes

The diffraction patterns of Si-NPs are shown in Fig.7.2. As discussed in Chapter 6, the diffraction planes (111), (220) and (311) at Bragg positions of 28.66°, 47.57° and 56.39° correspond to pure silicon (Face centered cubic lattice, space group: Fd3m, JCPDS No.895012). XRD of Si-C freestanding electrodes fabricated at different temperatures shows the corresponding peaks of carbon and silicon suggesting the successful blend of Si-C composite. The weak and broad peak between 20°-30° of (002) plane indicates the formation of amorphous carbon. As annealing temperature increases there is an increase in intensity of carbon peak, which indicates the increase in crystallinity. The d-spacing value of broad peak in Si-C composite formed by annealing at 700 °C, 900 °C and 1000 °C are 3.65 Å, 3.57 Å and 3.52 Å, respectively. The decrease in d-spacing 700 °C, 900 °C and 1000 °C are 3.65 Å, 3.57 Å and 3.52 Å, respectively. The decrease in d-spacing value with increase in temperature clearly indicates the increase of ordering of carbon [53].

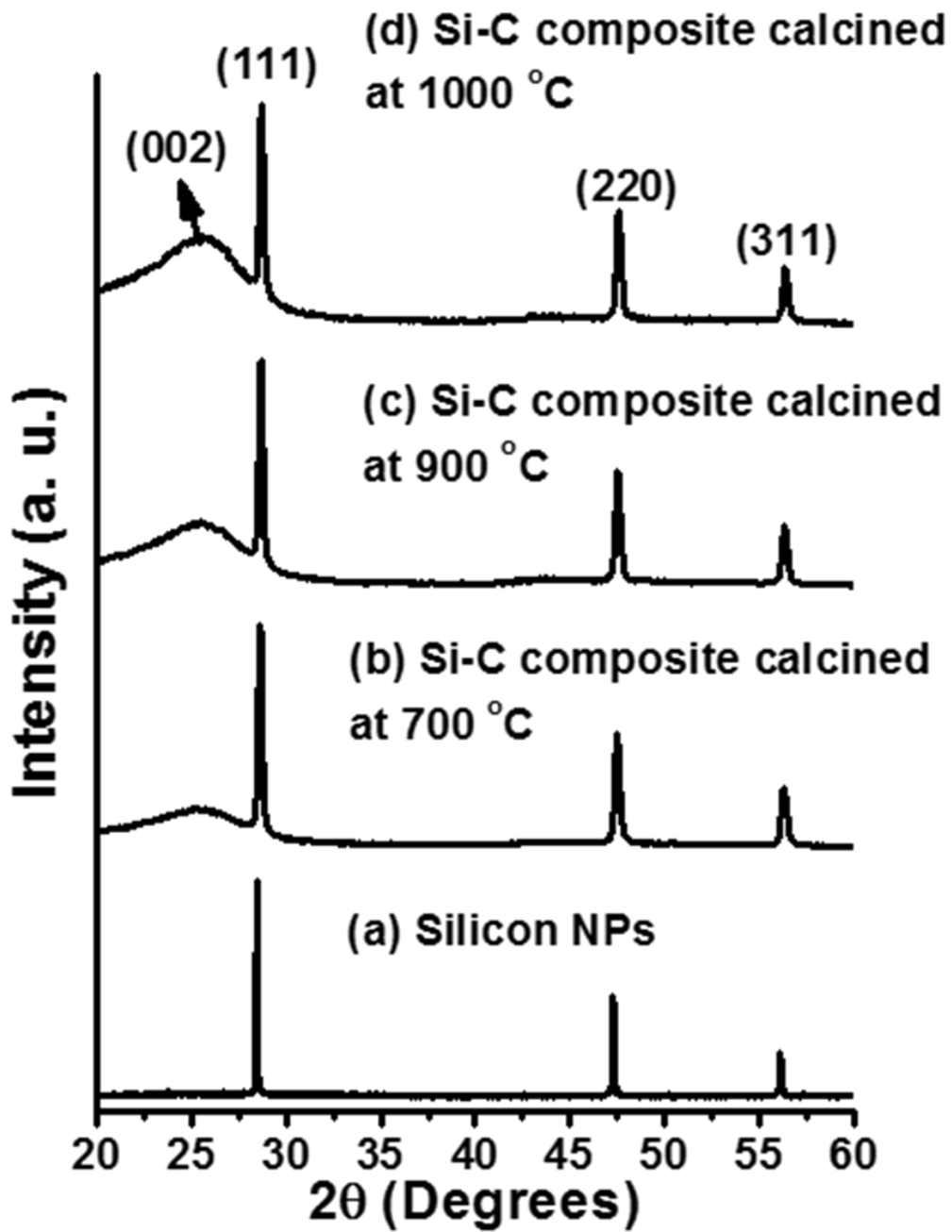


Fig. 7.2: X-ray diffraction patterns of: (a) as synthesized Si-NPs and 3D Si-C free-standing electrodes annealed at (b) 700 °C, (c) 900 °C, and (d) 1000 °C

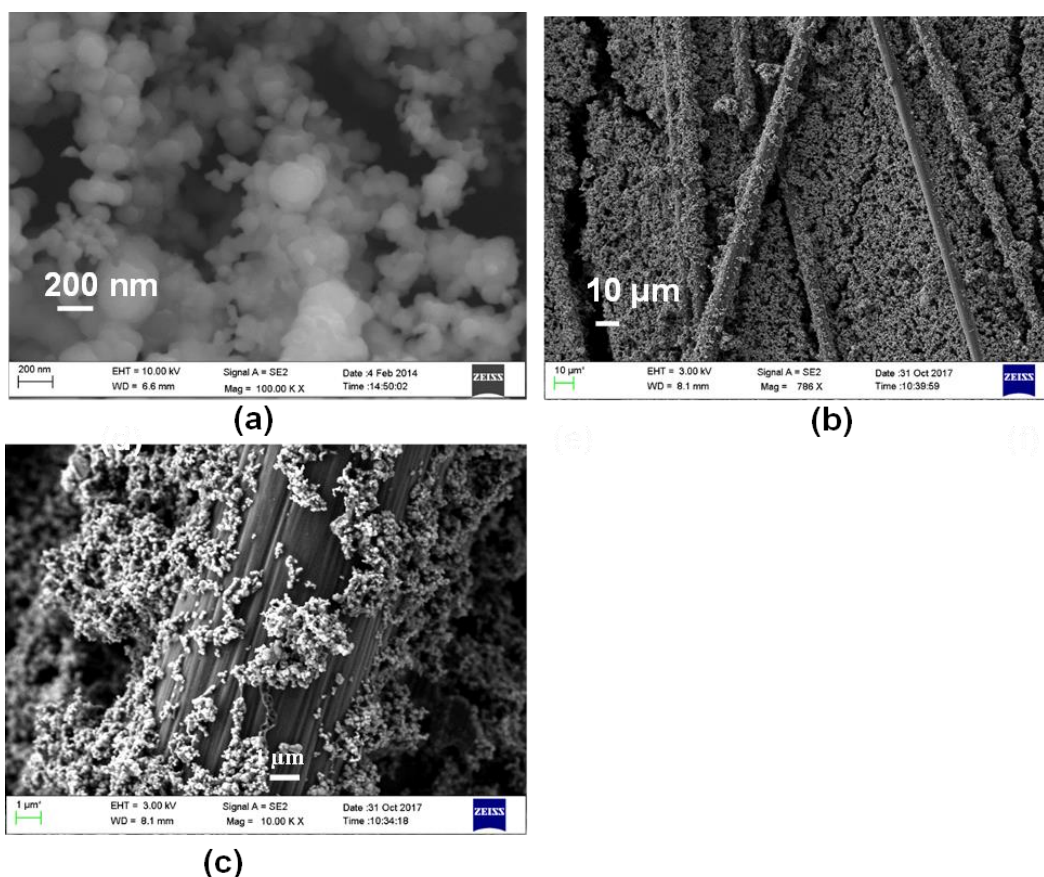


Fig.7.3: FESEM images of: (a) Si-NPs synthesized by magnesiothermic reduction, (b) 3D Si-C freestanding electrode, and (c) High resolution image 3D Si-C free-standing electrode

Si-NPs synthesized by magnesiothermic reduction are of typical spherical morphology having particle sizes in the range of 50-100 nm (Fig. 7.3 (a)). 3D Si-C composite free standing electrodes fabricated at temperatures of 700 °C, 900 °C and 1000 °C are shown in Fig. 7.3(b-c). At high temperatures >700 °C, P-pitch coats onto the fiber and Si-NPs, makes a good electronic contact along and between the fibers and on to the particle. Typically, pitch forms about 6-14 nm of C-coating onto Si-NPs when annealed at the temperatures between 700-1000 °C (discussed later in Fig.7.4). The 3D electrode architecture of Si-NPs on CF electrode shows uniform distribution of silicon and carbon throughout the CF (Fig. 7.3(b)). The high resolution image (Fig. 7.3(c)) indicates the good binding of Si-C composite on carbon fiber with enough space for free expansion and contraction of silicon during alloying and dealloying with lithium. Si-C composite annealed between 700 °C -1000 °C (Fig.7.4(a-c)) shows partial increase in particle size of Si-NPs due to agglomeration compared to pristine

silicon (Fig. 7.3(a)). The BET surface area of Si-C composites were found to be 105, 46 and 15.8 m² g⁻¹ annealed at 700, 900 and 1000 °C.

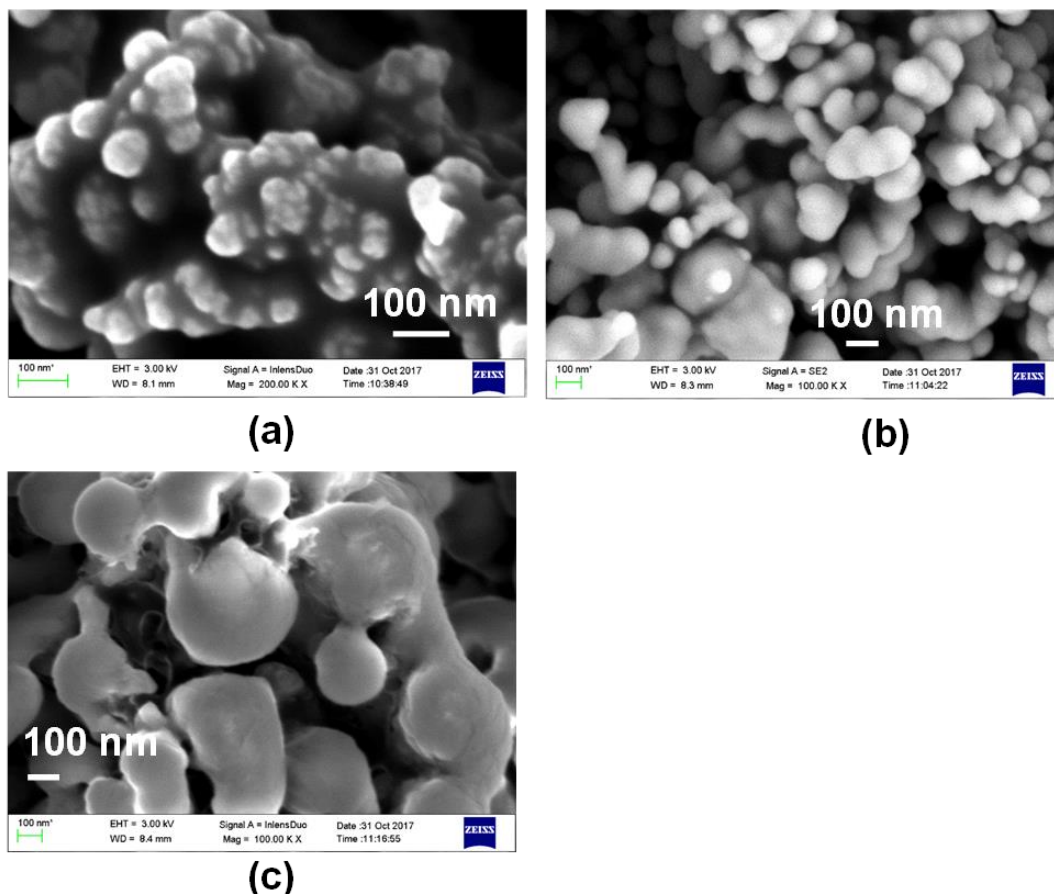


Fig.7.4: FESEM images of Si-C composites annealed at: (a) 700 °C, (b) 900 °C, and 1000 °C

As expected SEM and TEM images of pure Si-NPs converge. Si-NPs have 50-100 nm in size (Fig. 7.5(a)). Si-C composite electrodes annealed between 700-1000 °C shows Si-NPs particles covered by a thick carbon film of 6-14 nm. The crystallites have a typical, well-defined face centered cubic symmetry, and the atomic layers are also clearly observed. The d-spacing values of about 0.315 correspond to 111 reflections in the XRD pattern of Si. Si-C composite electrodes annealed between 900 and 1000 °C shows about 8 nm and 6 nm of thick carbon coatings respectively onto Si-NPs. The thickness of carbon coating decreases with increase of temperature which implies with increasing temperature the carbon coatings sinters, allowing to gain more mechanical strength. This increase in mechanical strength helps in increasing the

physical binding of carbon, silicon and CFs. The carbon coatings are stronger and malleable on increasing the temperature, allowing the silicon volume change during cycling without undergoing pulverization.

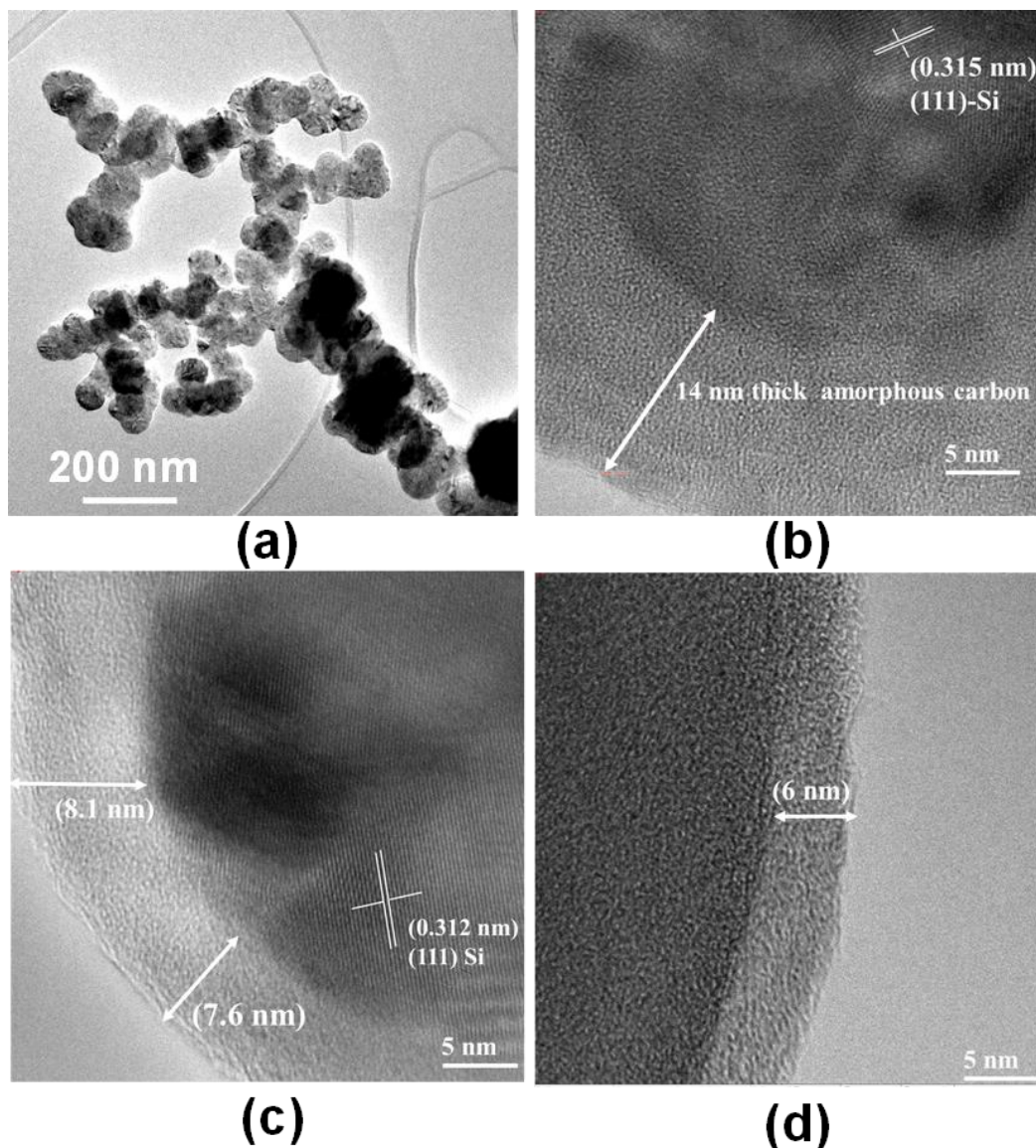


Fig. 7.5: TEM images of (a) Si-NPs synthesized by magnesiothermic reduction; Si-C composite annealed at (b) 700°C, (b) 900 °C and (c) 1000 °C indicating carbon coating, lattice fringes, and atomic layers (scale bar: 5 nm)

Raman spectra (Fig.7.6) of Si-C composite fabricated at different temperatures corresponds to Si-Si stretching (peak at 512 cm^{-1}) and D-band (disorder band) and G-band (graphitic band) at 1355 cm^{-1} and 1597 cm^{-1} , respectively. The presence of silicon and hard carbon peaks indicates the successful formation of Si-C composite.

The integral intensity ratio of D to G bands for the Si-C composite samples annealed at 700 °C - 1000 °C was estimated to be 1.4 and 0.785, which indicated the formation of a disordered carbons. The decrease of D/G ratio with increase of temperature in Fig. 7.6 suggest, the increase in graphitic nature with increase of temperature. This in turn increases the conductivity of the electrode material.

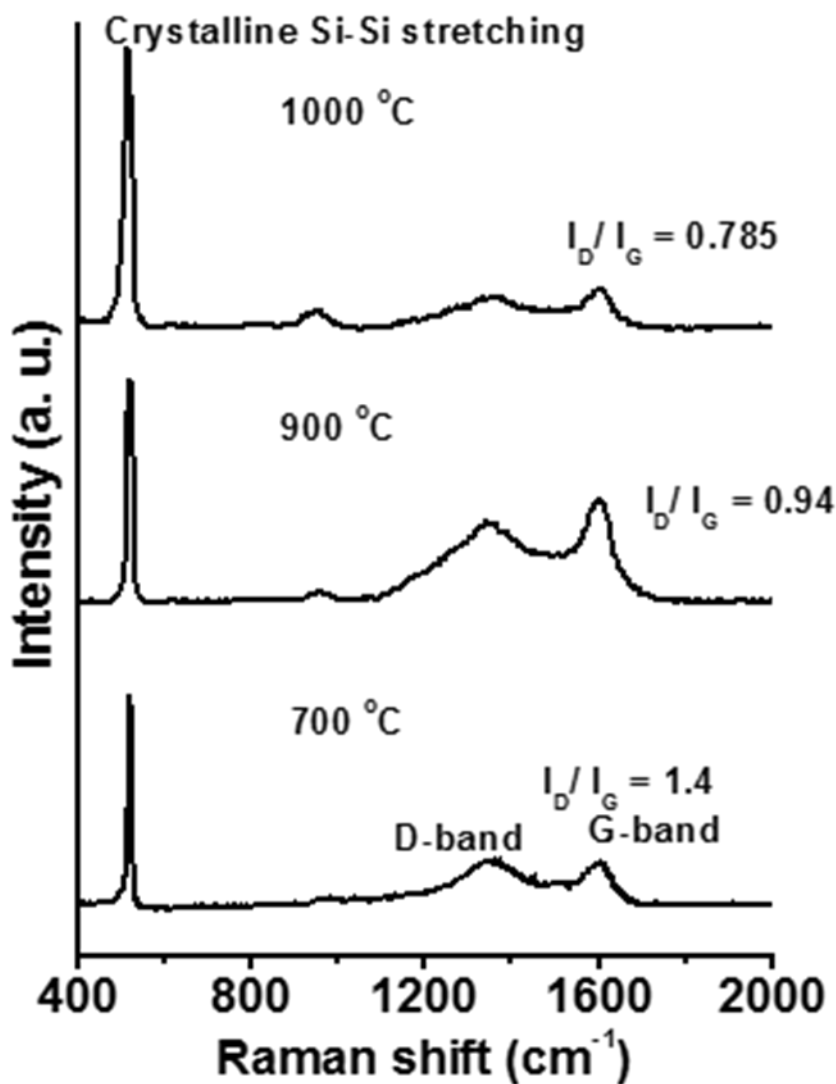


Fig.7.6: Raman spectrum of: (a) Si-C composite formed by calcination at different temperatures 700 °C, 900 °C and 1000 °C for 5 hrs under argon atmosphere

7.4.2. Electrochemical performance studies

Reversible capacity and cycle stability of silicon anodes significantly reduces upon cycling at deep cut-off potentials. Cycling silicon anodes above 50 mV reduces the formation of crystalline phases and results good electrochemical performance [14, 54-

56]. Thus galvanostatic charge-discharge cycling of our Si-NPs were carried out in the potential range between 1.2 V to 0.05 V. 3D Si-C composite electrodes annealed at different temperatures shows higher reversible capacity (Fig. 7.7) compared to conventional silicon composite electrode which suggest 3D electrode architecture enables the complete utilization of active material coated onto the CF compared to conventional silicon electrode. The conventional silicon composite electrodes show high irreversible capacity 48% with initial lithiation capacity of 3201 mAh g^{-1} . High irreversible capacity is attributed to the high intake of Li during the formation of SEI in the conventional Si composite electrode. The low conductivity of the composite electrode and pulverization lead to rapid capacity fade of Si-NPs in conventional composite electrode.

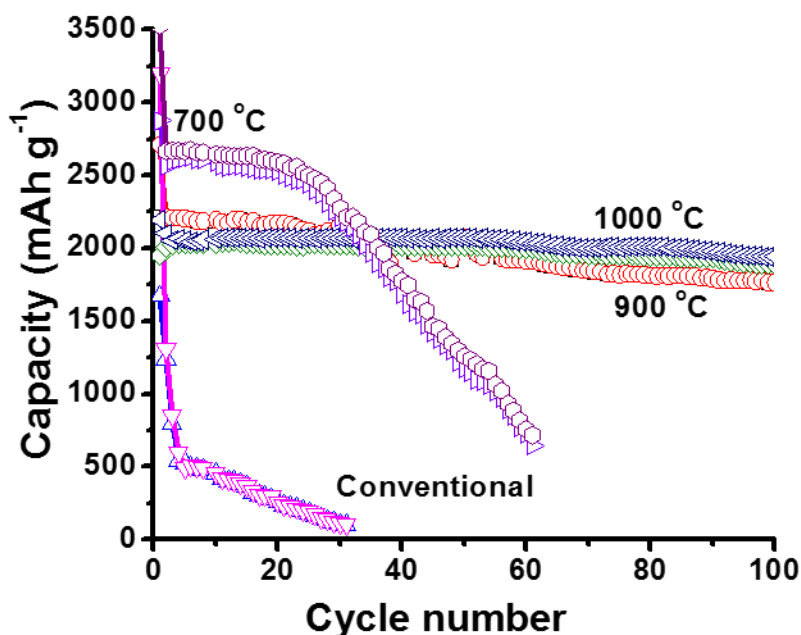


Fig.7.7: Comparison of cycle life of 3D Si-C freestanding electrodes prepared at 700 °C, 900 °C, 1000 °C and conventional electrode (as indicated)

The initial lithiation capacity of 3D Si-C free standing composite electrodes annealed at 1000, 900, 700 °C were 2193 mAh g^{-1} , 2712 mAh g^{-1} , 3201 mAh g^{-1} and 3533 mAh g^{-1} and that for conventional electrode was 3201 mAh g^{-1} at 0.1C rate and corresponding irreversible capacities were 11%, 16%, 18%, and 48% during 1st cycle (Figs. 7.7 and 7.8). The improvement in irreversible capacity of 3D Si-C freestanding electrodes during first cycle is due to coating of carbon onto Si-NPs which reduces

the side reactions of silicon with electrolyte, this in turn reduces with increase in annealing temperature (Fig. 7.8(a-d)).

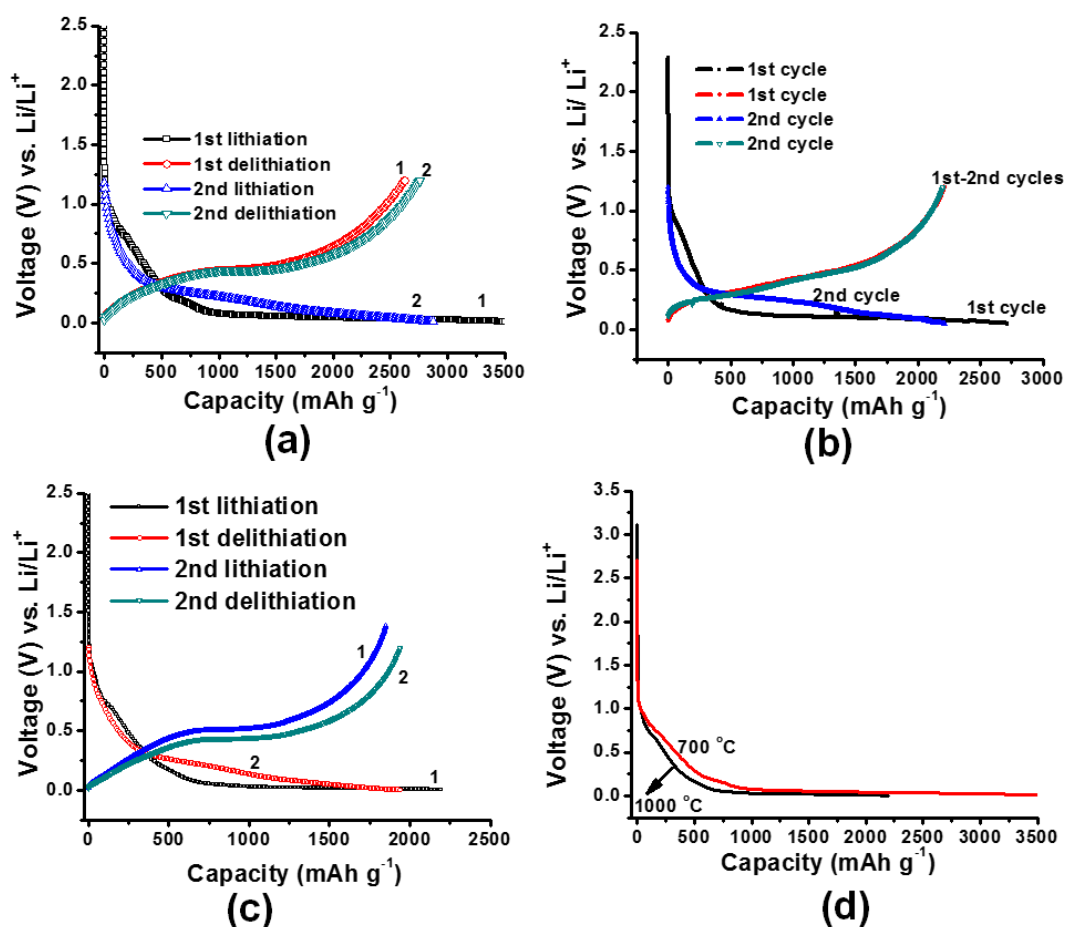


Fig. 7.8: Voltage profiles during lithiation and de-lithiation process for the free-standing electrode annealed at: (a) 700 °C, (b) 900 °C and (c) 1000 °C, and (d) comparison of voltage profiles during lithiation process for the freestanding electrode annealed at 700 °C and 1000 °C

Si-C composite annealed at 700 °C shows initial high discharge capacity than the Si-C composite electrodes annealed at 900 °C and 1000 °C due to high surface area of Si-C composite annealed at 700 °C than 900 and 1000 °C. In discharge voltage profile, there is a plateau below 1 V (7.8(a) and (d)) is due to the alloying of Li⁺ with silicon and the plateau from 0.25-0.5 V during charging is due to dealloying of Li⁺ with silicon. All the 3D Si-C freestanding electrodes annealed between 700-1000 °C

shows similar voltage profiles (Fig. 7.8(a-d)). 3D Si-C freestanding electrode shows enhanced electrochemical performance than conventional silicon electrode. In this architecture, coating of carbonized pitch onto Si-NPs efficiently prevents the direct exposure of Si-NPs to electrolyte which helps in maintaining the interfacial and structural stability. In addition to this, the 3D CF and carbonized pitch effectively accommodates the volume expansion and contraction thus enabling the electrical and structural integrity of the electrode. Figure 7.8(a) 3D Si-C electrodes at 700 °C shows high initial stable discharge capacity ($\sim 2600 \text{ mAh g}^{-1}$) than that of 900 °C (2220 mAh g^{-1}) and 1000 °C (2060 mAh g^{-1}) due to high surface area ($105 \text{ m}^2 \text{ g}^{-1}$) of Si-C composite. But, Si-C composite annealed at 700 °C shows rapid capacity fade with progress of cycling (after 25 cycles), whereas Si-C composite electrodes annealed at 900 °C and 1000 °C shows enhanced electrochemical performance in terms of capacity retention and cyclability (Fig. 7.7). The 3D Si-C free-standing electrodes annealed at 1000 °C shows very stable capacity of about 2000 mAh g^{-1} for over 200 cycles with little loss in capacity ($\sim 5\%$), whereas about 20% capacity loss was observed for the electrodes annealed at 900 °C. High capacity retention is due to the high conductivity of 3D Si-C free standing electrodes annealed at 1000 °C compare to 900 °C.

The C rate performance of Si-C free standing electrodes annealed at 1000 °C shows $\sim 1000 \text{ mAh g}^{-1}$ capacity at 5C rate could be achieved and these cells cycles very well for over 250 cycles with little loss in capacity (Fig. 7.9). We have further evaluated the capacity contribution from the carbon derived from pitch and CFs used in this study. The pitch coated carbons on CF annealed at 900 °C and 1000 °C shows very stable capacities between $250\text{-}280 \text{ mAh g}^{-1}$ (Fig. 7.10). The pitch coated carbons on CF annealed at 700 °C high initial capacity of $>300 \text{ mAh g}^{-1}$ and capacity reduces to 225 mAh g^{-1} in 60 cycles.

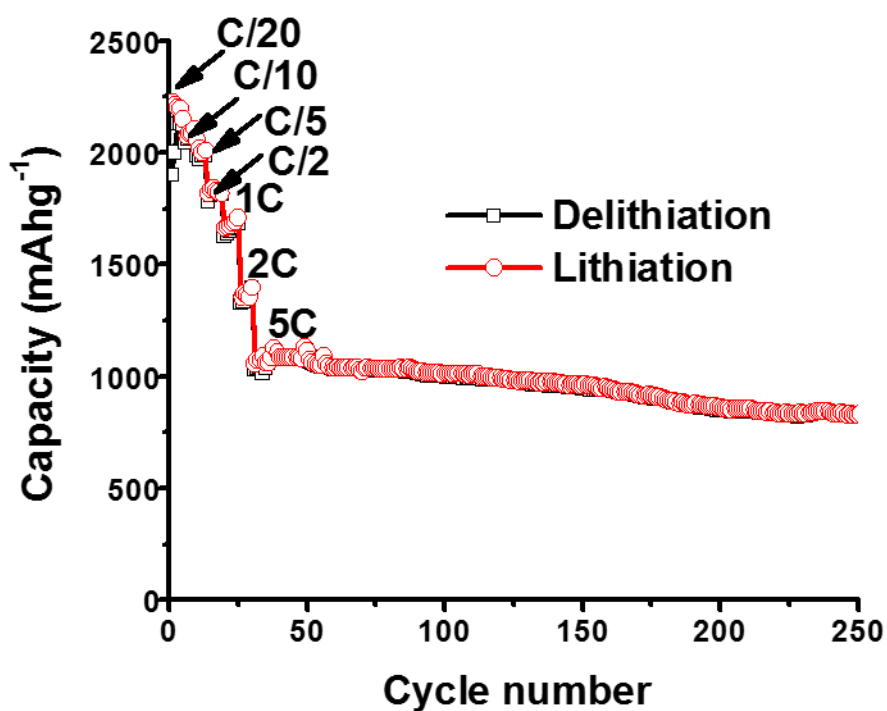


Fig. 7.9: C rate performance for the Si-C composite free standing electrode annealed at 1000 °C

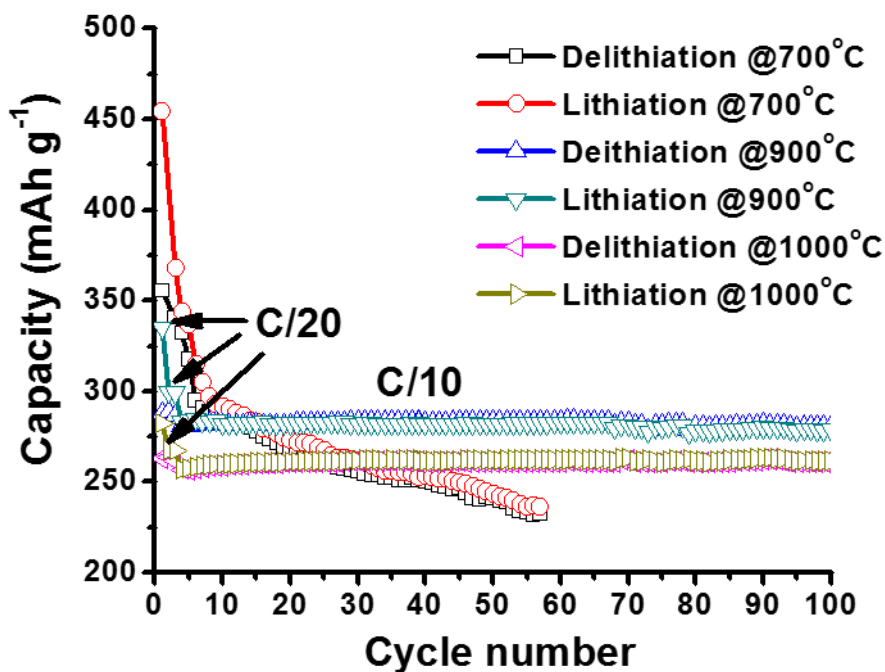


Fig. 7.10: The capacity vs. cycle number for the pitch coated CFs annealed at 700, 900 and 1000 °C (as indicated) (Capacity was calculated w.r.t total weight of the electrode)

The EIS behavior of Si-C composite 3D electrode architectures annealed between 700-1000 °C before and after cycling (Fig. 7.11(a-b)) have been investigated

in order further understand the kinetics of electrochemical processes which influence the electrochemical performance. The impedance spectra of Si-C composite 3D electrodes were measured in equilibrium conditions using lithium reference electrode. The impedance of 3D Si-C composite electrode (Fig.7.11a) annealed at 1000 °C have low Ohmic (2.07 Ohm cm²) and charge transfer resistances (151.45 Ohm cm²) before cycling and that of the electrode fabricated at 700 °C shows 10.14 Ohm cm² and 183.46 Ohm cm². The electrode fabricated at 900 °C shows intermediate resistances (6.50 Ohm cm² and 156.67 Ohm cm²) (Fig.7.11a). The Ohmic resistance of electrode fabricated at 900 °C increases to 17.14 Ohm cm² and charge transfer resistance increases to 158.57 Ohm cm² after 100 cycles whereas the electrode fabricated at 700 °C shows high ohmic resistance of 39.96 Ohm cm² and charge transfer resistance of 366.18 Ohm cm² after 60 cycles (Fig.7.11(b)). The impedance analysis shows the contribution of both surface resistance and solid state diffusion through the bulk of the Si-NPs. The surface process is dominated by a SEI layer consisting of an inner, inorganic insoluble part and several organic compounds at the outer interface. The surface resistivity, which seems to be correlated with the coulombic efficiency of the electrode, grows at very high lithium contents due to an increase in the inorganic SEI thickness. EIS illustrates that on increasing annealing temperature there is an improvement in conductivity which in turn helps in improving electrochemical performance.

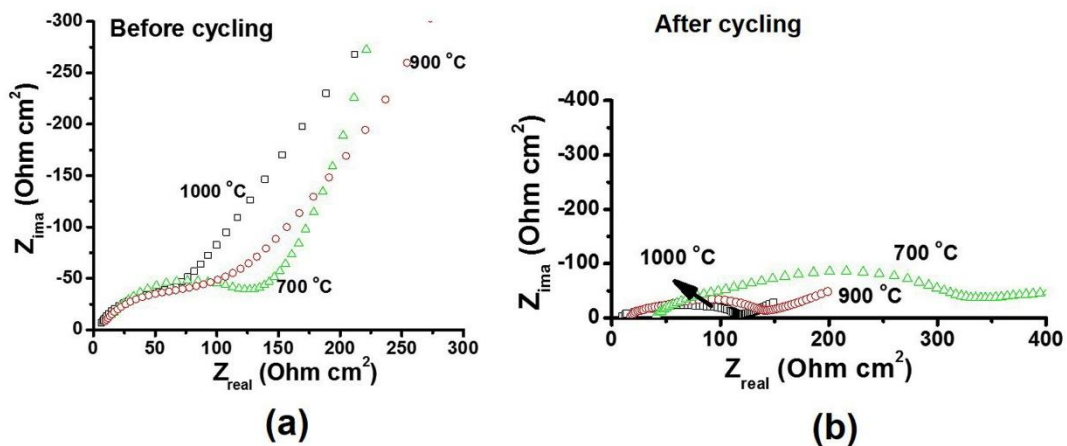


Fig. 7.11: Nyquist plots for the Si-NPs for the 3D CF electrodes annealed at 700-1000 °C (as indicated) in the frequency range between 1 MHz and 10 mHz during (a) before cycling at OCV, (b) after 60 cycles delithiation for 700 °C and after 100 cycles for the 900 and 1000 °C

In order to characterize the performance Si-C composite 3D electrode as an anode, electrochemical performance Si-C composite anode and LMR-NMC composite cathodes tested in a full cell configuration. As discussed in Chapter 4, Mg-F doped LMR-NMC cathodes deliver as high as 300 mAh g⁻¹ capacity with an operating voltage of >3.7 V and cycles very well [57]. Coin cells fabricated using Si-C composite 3D electrodes and Mg-F-LMR-NMC cathode shows high open circuit voltage of >4 V, (Fig. 7.12(a)) high energy density of > 500 Wh kg⁻¹ (Calculated from the integration of discharge capacity) in the voltage range between 4.6 to 2.0 V as shown in Fig. 7.12(a). The irreversible capacity for these cells were less than 10%. These coin cells show stable cycling for 50 cycles with little loss in capacity (Fig. 7.12(b)). Further improvement in electrochemical performance in full cells in pouch type configuration are underway.

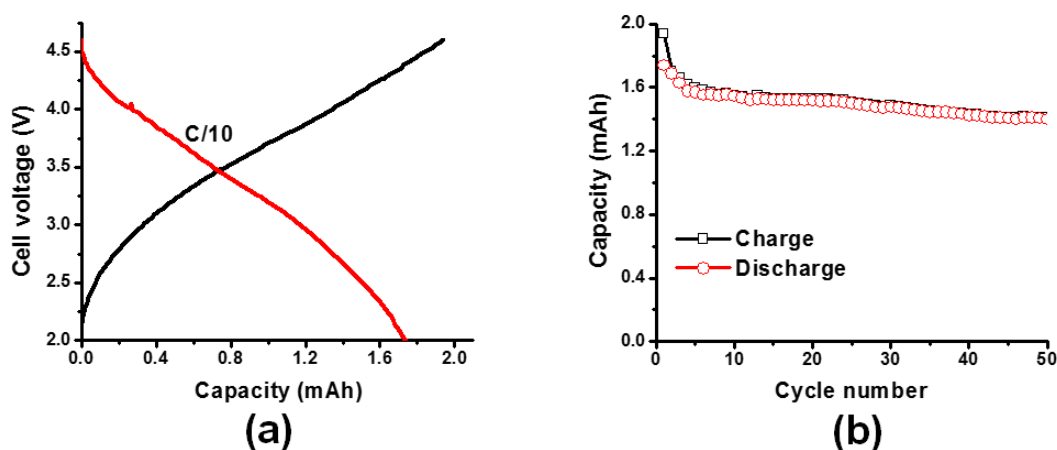


Fig. 7.12: (a) Charge-discharge voltage profile, (b) cycle life data of full cell consisting of Si-C 3D composite electrode as an anode with LMR-NMC cathode at C/10 rate

7.4.3. Discussions

3D electrode architecture of Si-NPs on CF allows the continuous conducting framework having excellent electronic properties, adaptable and flexible medium (carbon formed from the pitch and CF) which accommodates the volume change of silicon during lithiation and de-lithiation. Further, increasing temperature 700 to 1000 °C, increases the structural ordering of carbon and silicon which allows coating of carbon layers throughout Si-NPs. The carbon coating increases the contact strength of carbon with silicon and CF, thereby increases in mechanical strength of 3D Si-C composite electrode. The integrity of the Si-C composite material is well-maintained largely

due to the mechanical strength of the CF and pitch. When the electrodes are fabricated with CFs coated with pitch and Si-NPs, the pitch improves the connectivity between fiber-fiber and fiber-Si active material contacts, thereby reducing total internal impedance of the cell. During lithiation and de-lithiation carbon strongly holds silicon and allows expansion and contraction without undergoing pulverization. In addition, the improvement in conductivity with increase of temperature also enhances the electrochemical performance. The 3D electrode CF architecture with pitch controls the degradation of Si anode. All these features offer ample opportunities for modifying towards better Si-anode materials for optimal cell performance.

7.5. Conclusions

Organic binder and conducting diluent free 3D Si-C free-standing electrodes prepared at 1000 °C shows excellent electrochemical performance. Reversible capacities over 2000 mAh g⁻¹ at C/10 rate and ~1000 mAh g⁻¹ at 5C rate could be obtained for these electrodes for 100s of charge-discharge cycles. Pitch provides a very thin layer of coating between 6-14 nm (annealed at temperature between 700 to 1000 °C) onto Si-NPs, improves the connectivity between fiber-fiber and fiber-Si active material contacts, thereby reducing total internal impedance of the cell. During insertion and extraction of Li, carbon strongly holds Si-NPs, allows expansion and contraction without undergoing pulverization. The 3D electrode CF architecture with pitch controls the degradation of Si anode and improves the overall electrochemical performance during cycling. Besides, usual copper foil current collector is replaced by CFs which in fact contribute about 10 % capacity of Si-C composite electrodes. The Si-C composite electrodes do not contain any organic binder and extra conductive diluents. All these factors contribute towards improved energy density of Si-C composite electrodes. Full cells fabricated using Si-C composite 3D electrodes and Mg-F-LMR-NMC cathode shows high open circuit voltage of >4 V, and almost the double the energy density (530 Wh kg⁻¹) of the currently available lithium-ion cells. The study described here opens a new realm of possibility for the development of next generation cathodes and anodes for LIBs.

References

- [1] Year 2022 Major Goals for Batteries, Office of EERE, Department of Energy, (USA) <https://energy.gov/eere/vehicles/batteries>.
- [2] J.W. Choi, D. Aurbach, Promise and reality of post-lithium-ion batteries with high energy densities, *Nature Rev. Mater.*, 1 (2016) 16013.
- [3] S. Zhang, K. Zhao, T. Zhu, J. Li, Electrochemomechanical Degradation of High-Capacity Battery Electrode Materials, *Progress in Mater. Sci.*, 89 (2017) 479-521.
- [4] P.K. Nayak, E.M. Erickson, F. Schipper, T.R. Penki, N. Munichandraiah, P. Adelhelm, H. Sclar, F. Amalraj, B. Markovsky, D. Aurbach, Review on Challenges and Recent Advances in the Electrochemical Performance of High Capacity Li-and Mn-Rich Cathode Materials for Li-Ion Batteries, *Adv. Energy Mater.* (2017), DOI: 10.1002/aenm.201702397.
- [5] J. Jaguemont, L. Boulon, Y. Dubé, A comprehensive review of lithium-ion batteries used in hybrid and electric vehicles at cold temperatures, *Appl. Energy*. 164 (2016) 99–114.
- [6] X. Su, Q. Wu, J. Li, X. Xiao, A. Lott, W. Lu, B.W. Sheldon, J. Wu, Silicon-based nanomaterials for lithium-ion batteries: a review, *Adv. Energy Mater.*, 4 (2014) 1300882.
- [7] H. Lee, M. Yanilmaz, O. Toprakci, K. Fu, X. Zhang, A review of recent developments in membrane separators for rechargeable lithium-ion batteries, *Energy Environ. Sci.* 7 (2014) 3857–3886.
- [8] X.-B. Cheng, R. Zhang, C.-Z. Zhao, F. Wei, J.-G. Zhang, Q. Zhang, A review of solid electrolyte interphases on lithium metal anode, *Adv. Sci.* 3 (2016)3.
- [9] M.M. Thackeray, S.-H. Kang, C.S. Johnson, J.T. Vaughey, R. Benedek, S.A. Hackney, Li_2MnO_3 -stabilized LiMO_2 (M= Mn, Ni, Co) electrodes for lithium-ion batteries, *J. Mater. Chem.*, 17 (2007) 3112–3125.
- [10] S.K. Martha, J. Nanda, G.M. Veith, N.J. Dudney, Electrochemical and rate performance study of high-voltage lithium-rich composition: $\text{Li}_{1.2}\text{Mn}_{0.525}\text{Ni}_{0.175}\text{Co}_{0.1}\text{O}_2$, *J. Power Sources*, 199 (2012) 220–226.
- [11] P. Rozier, J.M. Tarascon, Li-rich layered oxide cathodes for next-generation Li-ion batteries: chances and challenges, *J. Electrochem. Soc.*, 162 (2015) A2490–A2499.
- [12] J. Yan, X. Liu, B. Li, Recent progress in Li-rich layered oxides as cathode materials for Li-ion batteries, *RSC Adv.*, 4 (2014) 63268–63284.

- [13] J. Zheng, S. Myeong, W. Cho, P. Yan, J. Xiao, C. Wang, J. Cho, J.-G. Zhang, Li-and Mn-Rich Cathode Materials: Challenges to Commercialization, *Adv. Energy Mater.*, 7 (2017) 1601284.
- [14] C. K. Chan, H. Peng, G. Liu, K. McIlwrath, X. F. Zhang, R. A. Huggins, Y. Cui, High-performance lithium battery anodes using silicon nanowires, *Nat. Nanotech.*, 3 (2008) 31–35.
- [15] M. Gu, Y. He, J. Zheng, C. Wang, Nanoscale silicon as anode for Li-ion batteries: The fundamentals, promises, and challenges, *Nano Energy*, 17 (2015) 366–383.
- [16] H. Kim, B. Han, J. Choo, J. Cho, Three-dimensional porous silicon particles for use in high-performance lithium secondary batteries, *Angew. Chem. Int. Edn.*, 120 (2008) 10305–10308.
- [17] L.-F. Cui, R. Ruffo, C.K. Chan, H. Peng, Y. Cui, Crystalline-amorphous core-shell silicon nanowires for high capacity and high current battery electrodes, *Nano Lett.*, 9 (2008) 491–495.
- [18] C. Erk, T. Brezesinski, H. Sommer, R. Schneider, J. Janek, Toward silicon anodes for next-generation lithium ion batteries: a comparative performance study of various polymer binders and silicon nanopowders, *ACS Appl. Mater. Interfaces*. 5 (2013) 7299–7307.
- [19] J.P. Maranchi, A.F. Hepp, P.N. Kumta, High capacity, reversible silicon thin-film anodes for lithium-ion batteries, *Electrochemical and Solid-State Lett.*, 6 (2003) A198–A201.
- [20] P. Gao, H. Tang, A. Xing, Z. Bao, Porous silicon from the magnesiothermic reaction as a high-performance anode material for lithium ion battery applications, *Electrochim. Acta*, 228 (2017) 545–552.
- [21] C. Zhu, K. Han, D. Geng, H. Ye, X. Meng, Achieving High-Performance Silicon Anodes of Lithium-Ion Batteries via Atomic and Molecular Layer Deposited Surface Coatings: an Overview, *Electrochim. Acta* 251(2017) 710-728.
- [22] W. Wang, P.N. Kumta, Nanostructured hybrid silicon/carbon nanotube heterostructures: reversible high-capacity lithium-ion anodes, *ACS Nano*. 4 (2010) 2233–2241.
- [23] H. Song, H.X. Wang, Z. Lin, X. Jiang, L. Yu, J. Xu, Z. Yu, X. Zhang, Y. Liu, P. He, Highly Connected Silicon–Copper Alloy Mixture Nanotubes as High-Rate and Durable Anode Materials for Lithium-Ion Batteries, *Adv. Funct. Mater.* 26 (2016) 524–531.
- [24] E. Moyen, M.R. Zamfir, J. Joe, Y.W. Kim, D. Pribat, Si nanowires grown by Al-catalyzed plasma-enhanced chemical vapor deposition: synthesis conditions, electrical properties and application to lithium battery anodes, *Mater. Res. Express*, 3 (2016) 015003.

- [25] Y. Chen, Y. Hu, Z. Shen, R. Chen, X. He, X. Zhang, Y. Li, K. Wu, Hollow core-shell structured silicon@ carbon nanoparticles embed in carbon nanofibers as binder-free anodes for lithium-ion batteries, *J. Power Sources*, 342 (2017) 467–475.
- [26] J. Qin, M. Wu, T. Feng, C. Chen, C. Tu, X. Li, C. Duan, D. Xia, D. Wang, High rate capability and long cycling life of graphene-coated silicon composite anodes for lithium ion batteries, *Electrochim. Acta.* 256 (2017) 259–266.
- [27] J. Tang, A.D. Dysart, D.H. Kim, R. Saraswat, G.M. Shaver, V.G. Pol, Fabrication of Carbon/Silicon Composite as Lithium-ion Anode with Enhanced Cycling Stability, *Electrochim. Acta*, 247 (2017) 626–633.
- [28] H. Kim, J. Cho, Superior lithium electroactive mesoporous Si@ Carbon core-shell nanowires for lithium battery anode material, *Nano Lett*, 8 (2008) 3688–3691.
- [29] X. Bai, Y. Yu, H.H. Kung, B. Wang, J. Jiang, Si@ SiO_x/graphene hydrogel composite anode for lithium-ion battery, *J. Power Sources*, 306 (2016) 42–48.
- [30] X. Hu, S. Huang, X. Hou, H. Chen, H. Qin, Q. Ru, B. Chu, A Double Core-shell Structure Silicon Carbon Composite Anode Material for a Lithium Ion Battery, *Silicon*, (2017) 1–8.
- [31] X. Wang, G. Li, M.H. Seo, G. Lui, F.M. Hassan, K. Feng, X. Xiao, Z. Chen, Carbon-Coated Silicon Nanowires on Carbon Fabric as Self-Supported Electrodes for Flexible Lithium-Ion Batteries, *ACS Appl. Mater. Interfaces.* 9 (2017) 9551–9558.
- [32] L. Fei, B.P. Williams, S.H. Yoo, J. Kim, G. Shoorideh, Y.L. Joo, Graphene folding in Si rich carbon nanofibers for highly stable, high capacity Li-ion battery anodes, *ACS Appl. Mater. Interfaces*, 8 (2016) 5243–5250.
- [33] J. Xie, L. Tong, L. Su, Y. Xu, L. Wang, Y. Wang, Core-shell yolk-shell Si@ C@ Void@ C nanohybrids as advanced lithium ion battery anodes with good electronic conductivity and corrosion resistance, *J. Power Sources*, 342 (2017) 529–536.
- [34] S. Suresh, Z.P. Wu, S.F. Bartolucci, S. Basu, R. Mukherjee, T. Gupta, P. Hundekar, Y. Shi, T.-M. Lu, N. Koratkar, Protecting Silicon Film Anodes in Lithium-Ion Batteries Using an Atomically Thin Graphene Drape, *ACS Nano*, 11 (2017) 5051–5061.
- [35] A. Ulvestad, H.F. ten Andersen, J.P. M\aelen, Ø. Prytz, M. Kirkengen, Long-term Cyclability of Substoichiometric Silicon Nitride Thin Film Anodes for Li-ion Batteries, *Sci. Reports*, 7 (2017) 13315.
- [36] D.B. Polat, O. Keles, K. Amine, Compositionally-graded silicon-copper helical arrays as anodes for lithium-ion batteries, *J. Power Sources*, 304 (2016) 273–281.

- [37] T. Meng, K. Young, D. Beglau, S. Yan, P. Zeng, M.M.-C. Cheng, Hydrogenated amorphous silicon thin film anode for proton conducting batteries, *J. Power Sources*, 302 (2016) 31–38.
- [38] J.P. Maranchi, A.F. Hepp, P.N. Kumta, High capacity, reversible silicon thin-film anodes for lithium-ion batteries, *Electrochemical and Solid-State Lett*, 6 (2003) A198–A201.
- [39] L. David, R. Bhandavat, U. Barrera, G. Singh, Silicon oxycarbide glass-graphene composite paper electrode for long-cycle lithium-ion batteries, *Nature Commun.*, 7 (2016) 10998.
- [40] J.K. Lee, K.B. Smith, C.M. Hayner, H.H. Kung, Silicon nanoparticles–graphene paper composites for Li ion battery anodes, *Chem. Commun.*, 46 (2010) 2025–2027.
- [41] M. Thakur, R.B. Pernites, N. Nitta, M. Isaacson, S.L. Sinsabaugh, M.S. Wong, S.L. Biswal, Freestanding macroporous silicon and pyrolyzed polyacrylonitrile as a composite anode for lithium ion batteries, *Chem. Mater.*, 24 (2012) 2998–3003.
- [42] S.R. Gowda, V. Pushparaj, S. Herle, G. Girishkumar, J.G. Gordon, H. Gullapalli, X. Zhan, P.M. Ajayan, A.L.M. Reddy, Three-dimensionally engineered porous silicon electrodes for Li ion batteries, *Nano Lett.*, 12 (2012) 6060–6065.
- [43] X. Wang, G. Li, M.H. Seo, G. Lui, F.M. Hassan, K. Feng, X. Xiao, Z. Chen, Carbon-Coated Silicon Nanowires on Carbon Fabric as Self-Supported Electrodes for Flexible Lithium-Ion Batteries, *ACS Appl. Mater. Interfaces*, 9 (2017) 9551–9558.
- [44] C. Kang, E. Cha, R. Baskaran, W. Choi, Three-dimensional free-standing carbon nanotubes for a flexible lithium-ion battery anode, *Nanotechnol.*, 27 (2016) 105402.
- [45] A. Abnavi, F.M. Sadati, A. Abdollahi, R. Ramzani, S. Ghasemi, Z. Sanaee, SnO₂ @ a-Si core–shell nanowires on free-standing CNT paper as a thin and flexible Li-ion battery anode with high areal capacity, *Nanotechnol.*, 28 (2017) 255404.
- [46] S. Yehezkel, M. Auinat, N. Sezin, D. Starosvetsky, Y. Ein-Eli, Bundled and densified carbon nanotubes (CNT) fabrics as flexible ultra-light weight Li-ion battery anode current collectors, *J. Power Sources*, 312 (2016) 109–115.
- [47] K. Yao, J.P. Zheng, R. Liang, Binder-Free Freestanding Flexible Si Nanoparticles-Multi-Walled Carbon Nanotubes Composite Anodes for Li-Ion Batteries, *ECS Trans.*, 72 (2016) 67–86.
- [48] E. Biserni, A. Scarpellini, A.L. Bassi, P. Bruno, Y. Zhou, M. Xie, High-performance flexible nanoporous Si-carbon nanotube paper anodes for micro-battery applications, *Nanotechnol.*, 27 (2016) 245401.

- [49] H. Song, H.X. Wang, Z. Lin, Y.U. Linwei, X. Jiang, Z. Yu, X.U. Jun, L. Pan, M. Zheng, Y. Shi, Hierarchical nano-branched c-Si/SnO₂ nanowires for high areal capacity and stable lithium-ion battery, *Nano Energy*, 19 (2016) 511–521.
- [50] S.K. Martha, J. Nanda, H. Zhou, J.C. Idrobo, N.J. Dudney, S. Pannala, S. Dai, J. Wang, P. V. Braun, Electrode architectures for high capacity multivalent conversion compounds: iron (II and III) fluoride, *RSC Adv.*, 4 (2014) 6730–6737.
- [51] S.K. Martha, J.O. Kiggans, J. Nanda, N.J. Dudney, Advanced lithium battery cathodes using dispersed carbon fibers as the current collector, *J. Electrochem. Soc.*, 158 (2011) A1060–A1066.
- [52] J. Klett, R. Hardy, E. Romine, C. Walls, T. Burchell, High-thermal-conductivity, mesophase-pitch-derived carbon foams: effect of precursor on structure and properties, *Carbon*, 38 (2000) 953–973.
- [53] R. Andrews, D. Jacques, D. Qian, E.C. Dickey, Purification and structural annealing of multiwalled carbon nanotubes at graphitization temperatures, *Carbon*, 39 (2001) 1681–1687.
- [54] M.N. Obrovac, L. Christensen, Structural changes in silicon anodes during lithium insertion/extraction, *Electrochem. Solid-State Lett.*, 7 (2004) A93–A96.
- [55] J.H. Ryu, J.W. Kim, Y.-E. Sung, S.M. Oh, Failure modes of silicon powder negative electrode in lithium secondary batteries, *Electrochem. Solid-State Lett.*, 7 (2004) A306–A309.
- [56] S.D. Beattie, M.J. Loveridge, M.J. Lain, S. Ferrari, B.J. Polzin, R. Bhagat, R. Dashwood, Understanding capacity fade in silicon based electrodes for lithium-ion batteries using three electrode cells and upper cut-off voltage studies, *J. Power Sources*, 302 (2016) 426–430.
- [57] S.K. Kumar, S. Ghosh, S.K. Martha, Synergistic effect of magnesium and fluorine doping on the electrochemical performance of lithium-manganese rich (LMR)-based Ni-Mn-Co-oxide (NMC) cathodes for lithium-ion batteries, *Ionics*, 23 (2017) 1655–1662.

Appendix-1

Techniques Employed During the Study

The various electrochemical and physical characterization techniques employed in this thesis include Electrochemical Impedance Spectroscopy (EIS), Chronopotentiometry, Chronoamperometry, Powder X-ray Diffraction (XRD) analysis, Electron Microscopy, X-ray photoelectron spectroscopy (XPS) and Raman Spectroscopy. These techniques are briefly described below.

A.1.1. Electrochemical impedance spectroscopy

The EIS technique involves excitation of an electrochemical cell by a small amplitude alternating current (AC) signal and measuring the response over a wide frequency range. When an electrochemical cell is excited by a low amplitude AC signal, the output is generally out of phase owing to the presence of capacitive and inductive components of the cell. The measured total impedance of the cell could be represented by an equivalent circuit comprising resistors (R) and capacitors (C) in series and/or parallel.

On applying AC voltage (e) across the cell, the corresponding current (i) passing through it, can be expressed as,

$$i = i_0 \sin \omega t \quad (\text{A.1.1})$$

Where, ω is the angular frequency ($\omega = 2\pi f$, and f being the frequency) and i_0 is the value of i at $t=0$.

For a capacitor, capacitance (C) is the product of voltage (e) across the plates and the charge (q) residing on them. Accordingly,

$$q = Ce \tag{A.1.2}$$

On differentiating Eq. (A.1.2), the current (i) is expressed as,

$$i = dq / dt = i_o \text{Sin } 2\pi f t \tag{A.1.3}$$

Integrating Eq. (A.1.3) yields,

$$q = (-1/2\pi f) i_o \text{Cos } 2\pi f t \tag{A.1.4}$$

Where, the constant of integration, representing a constant charge on the capacitor, has been set equal to zero.

From Eq. (A.1.2),

$$e = q/C = (-1/2\pi f C) i_o \text{Cos } 2\pi f t \tag{A.1.5}$$

Since the current and voltage lag each other by a phase angle (ϕ) equal to 90° . The root mean square voltage E, i.e. the effective value of voltage, is obtained from Eq. (A.1.5) by squaring the voltage and taking its average. Accordingly,

$$E = (1/2\pi f C) I \tag{A.1.6}$$

where I is the root mean square value of the current, i.

This can be placed in a form corresponding to Ohm's law by writing,

$$E = X_c I \tag{A.1.7}$$

where the quantity $X_c = (1/2\pi f C)$ and is called capacitive reactance, and is a measure of the impeding effect of capacitor on current.

In complex notation, the magnitudes of the ordinate are multiplied by $j = (-1)^{1/2}$. Thus,

$$E = -jX_c I \tag{A.1.8}$$

In mathematical terms, the component E and I can be represented in an Argand diagram with the real component on the abscissa and the imaginary component on the ordinate. In a circuit containing resistance and capacitance in series (Fig. A.1.1), the total voltage drop across the circuit, E, is given by,

$$E = E_1 + E_2 \tag{A.1.9}$$

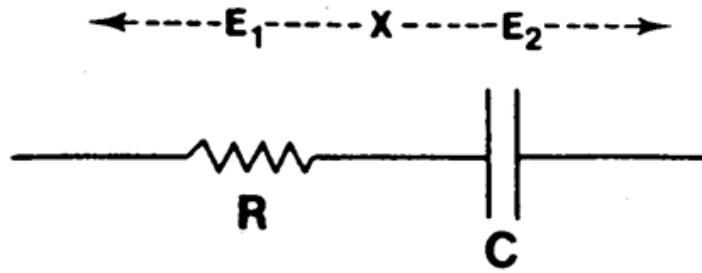


Fig. A.1.1: Series combination of resistance and capacitance with respective voltage drops E_1 and E_2 , across them

The impedance (Z) of the circuit is expressed as,

$$Z = E/I \quad (\text{A.1.10})$$

The total impedance of the circuit given by,

$$Z = R + (1/j\omega C) = R - (j/\omega C) \quad (\text{A.1.11})$$

It contains real and imaginary terms, namely R and $(-1/\omega C)$, respectively, and is called the complex impedance, Z^* , given by,

$$Z^* = Z' - jZ'' \quad (\text{A.1.12})$$

where $Z' = R$ and $Z'' = 1/\omega C$.

Impedance data is represented graphically in Cartesian coordinates or in complex coordinates as shown in Fig. A.1.2(a). It may be noted that the parameters – impedance (Z), modulus of impedance $|Z|$, real part (Z'), imaginary part (Z''), phase angle (ϕ) are interrelated and are functions of frequency (f). The plot of $\log |Z|$ and ϕ versus $\log f$ is known as Bode diagram. In the Bode $\log |Z|$ diagram, if resistance and capacitance are connected in series, the impedance is contributed by both the elements and the magnitude of this contribution varies with the ac frequency as shown in Fig. A.1.2(b). If resistance and capacitance are connected in parallel (Fig. A.1.2(c)), $\log |Z|$ decreases linearly with $\log f$ with a slope value equal to -1 .

From Eqns. (A.1.11 and A.1.12),

$$Z^* = R / (1 + j\omega CR) \quad (\text{A.1.13})$$

If R and C are in parallel as shown in Fig. A.1.2(c), the impedance of the equivalent circuit is given by,

$$1/Z^* = (1/R) + j\omega C \quad (\text{A.1.14})$$

$1/Z^*$ can be termed as complex admittance (A^*).

$$\text{So, } A^* = 1/Z^* = (1/R) + j\omega C = (1 + j\omega CR)/R \quad (\text{A.1.15})$$

The complex impedance can be evaluated as follows.

$$Z^* = A^{*-1} = R / (1 + j\omega CR) \quad (\text{A.1.16})$$

$$Z^* = \frac{R(1 - j\omega CR)}{1 + \omega^2 C^2 R^2} \quad (\text{A.1.17})$$

$$Z^* = \frac{R}{1 + \omega^2 C^2 R^2} - \frac{j\omega CR^2}{1 + \omega^2 C^2 R^2} \quad (\text{A.1.18})$$

As, $Z^* = Z' - jZ''$ (From Eq. A.1.13)

$$\text{Where, } Z' = \frac{R}{1 + \omega^2 C^2 R^2} \quad (\text{A.1.19})$$

$$\text{and } Z'' = \frac{\omega CR^2}{1 + \omega^2 C^2 R^2} \quad (\text{A.1.20})$$

Dividing Eq. (A.1.19) by Eq. (A.1.20), we get,

$$\frac{Z'}{Z''} = \frac{1}{\omega CR}$$

(A.1.21)

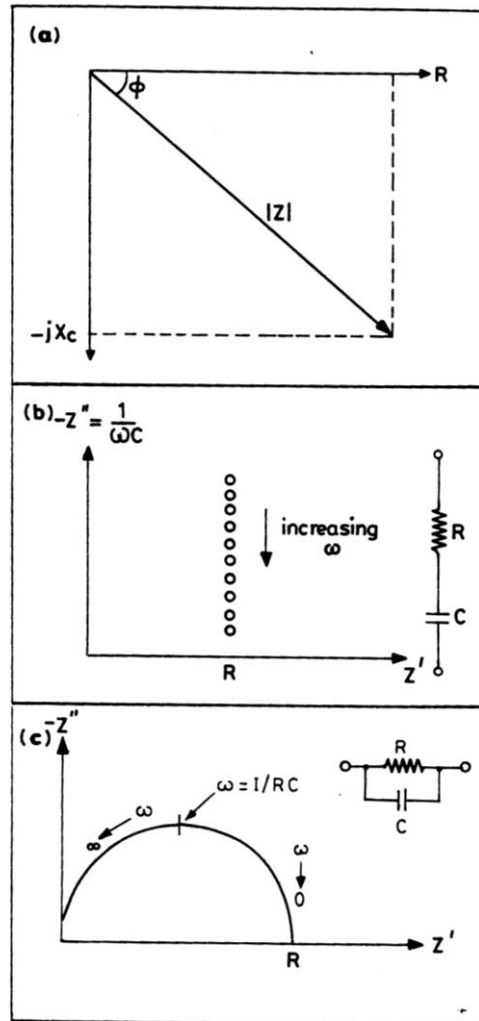


Fig. A.1.2: (a) Argand diagram showing relationship among resistance (R), capacitive reactance (X_c), modulus of impedance $|Z|$ and phase angle (ϕ), (b) Complex plane (Argand) diagram for a series RC circuit and (c) Complex plane diagram for a parallel RC circuit

or,

$$\omega = \frac{Z''}{Z'CR} \quad (\text{A.1.22})$$

Substituting ω from Eq. (A.1.22) in Eq. (A.1.19), we get,

$$Z' = \frac{R}{1 + (Z''^2 / Z'^2)} \quad (\text{A.1.23})$$

$$\text{or } Z' \{1/R [1 + (Z''^2 / Z'^2)]\} = 1 \quad (\text{A.1.24})$$

Eq. (A.1.24) can be rearranged as,

$$Z'^2 + Z''^2 - Z'R = 0 \quad (\text{A.1.25})$$

By adding $(R/2)^2$ to both sides of Eq. (A.1.25), we get,

$$(Z' - R/2)^2 + Z''^2 = (R/2)^2 \quad (\text{A.1.26})$$

Eq. (A.1.26) represents a semicircle with $R/2$ as radius. Thus, a plot of Z'' vs. Z' (Nyquist) of the impedance data measured over a wide frequency range takes the shape of a semicircle as shown in Fig. A.1.2(c). The diameter of the semicircle provides the value of the resistor, R . The value of C is calculated from,

$$C = 1 / (2\pi f^* R) \quad (\text{A.1.27})$$

Where, f^* is the frequency corresponding to the maximum value of Z'' on the semicircle.

The electrical equivalent circuit of a battery comprises electrochemical processes occurring at the anode, the cathode, and in the electrolyte as shown in Fig. A.1.3(a). The significance of various circuit elements may be explained as follows. L_a and L_c refer to inductance values associated with the anode and cathode, respectively. R_Ω refers to ohmic resistance of the cell, which includes the resistances of the electrolyte, electrode base metal, electrode leads, terminals, etc. The charge-transfer

resistances (R_a and R_c), the double-layer capacitances (C_a and C_c) and the Warburg impedances (W_a and W_c) of the respective anode and the cathode are included in the circuit following Randles equivalent circuit model.

The charge-transfer resistance (R_a or R_c) of an electrochemical process is related to exchange current ($I_{0,a}$ or $I_{0,c}$) by,

$$R_a = RT / n_a F I_{0,a} \quad (\text{A.1.28})$$

And Warburg impedance (W_a or W_c) is defined as,

$$W_a = \sigma_a \omega^{-1/2} - j \sigma_a \omega^{-1/2} \quad (\text{A.1.29})$$

Where, n is the number of electrons and σ is Warburg coefficient, which is related to diffusion coefficient and concentrations of the species involved in the reaction. Subscripts a and c refer to anode and cathode, respectively. As R_a (or R_c) and σ_a (or σ_c) are related to concentrations, it follows that these parameters and hence the total impedance of the battery would vary with its SoC.

A semicircle on a complex-plane diagram, i.e., imaginary part (Z'') vs. real part (Z'), indicates the presence of a parallel combination of a resistor and a capacitor if Z'' is negative, or a parallel combination of a resistor and an inductor if Z'' is positive. For an equivalent circuit of a two-terminal storage battery (Fig. A.1.3(a)), inductive, capacitive and linear distribution of the spectrum characterizing separately the anode and cathode of the battery are expected. One may observe this as an experimental spectrum, provided the magnitude of the parameters and time constants (RC) corresponding to the anode and the cathode differ appreciably. In general, the total resistance of a storage cell is less than an ohm, and the parameters of the anode and the cathode are comparable in magnitude. As a result, the impedance spectrum may not clearly resolve corresponding to the individual electrode parameters, but it may represent the cell as a whole. The equivalent circuit may, therefore, be reduced as shown in Fig. A.1.3(b) [1]. As the inductance offers reactance at high AC frequencies, and if the experiments are carried out at low frequencies, the contribution of the

impedance by the inductance becomes negligibly small. Under these conditions, the inductance (L) may be omitted from Fig. A.1.3(b) and the equivalent circuit further reduce to the one shown in Fig. A.1.3(c). The complex-plane diagram of the impedance spectrum corresponding to the simplified equivalent circuit contains a semicircle and a linear spike as shown in Fig. A.1.3(d).

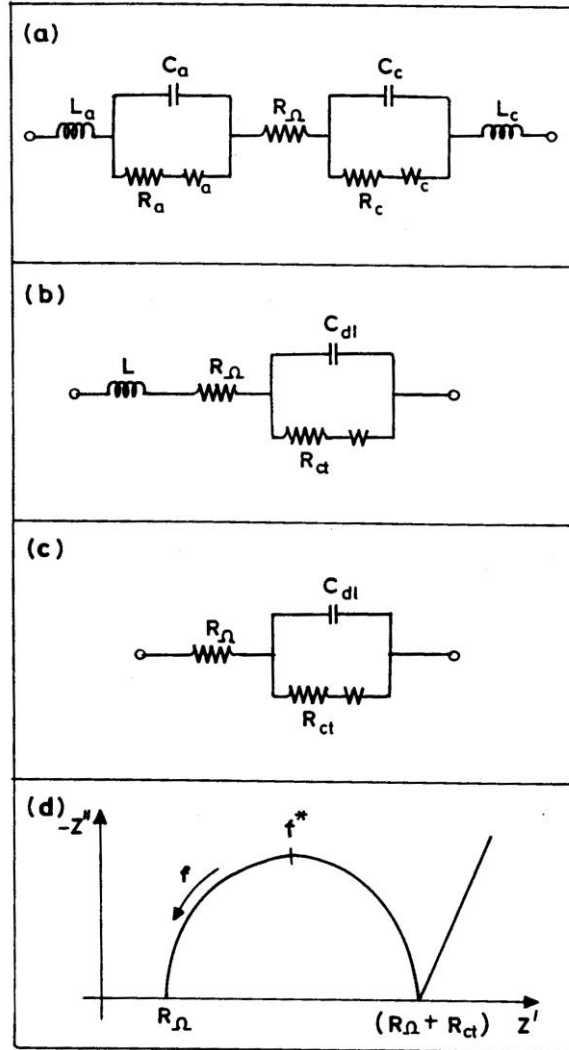


Fig. A.1.3: (a) Equivalent circuit of a two terminal energy storage cell with individual electrode parameters. L , C , R and W refer to inductance, double-layer capacitance, charge-transfer resistance and Warburg impedance, respectively. Subscripts a and c refer to the anode and the cathode. R_Ω is the ohmic resistance. (b) Equivalent circuit with lumped parameters of the cell. R_{ct} ,

C_{dl} and W refer to charge-transfer resistance, double-layer capacitance and Warburg impedance of the battery, respectively. (c) Equivalent circuit same as in (b) but without inductance, and (d) a schematic complex plane impedance spectrum corresponding to the equivalent circuit shown in (c)

The semicircle provides the value of R_{Ω} and the low-frequency intercept gives the value of charge-transfer resistance, R_{ct} . The double-layer capacitance (C_{dl}) can be obtained from the ac frequency corresponding to the maximum on the semicircle (f^*) from Eq. (A.1.27).

In recent years, the non-destructive evaluation of the available capacity of primary and secondary cells or batteries has been the subject of much interest. The ratio of available capacity of a cell to its maximum attainable capacity is usually referred to as its state-of-charge (SoC). An estimation of SoC facilitates optimum utilization of a battery for a given application as well as evaluation of its state-of-health (SoH). Among the techniques which have been employed, ac impedance measurements provide knowledge of several parameters, the magnitudes of which may depend on the SoC of the cell. The first impedance measurements of batteries appear to have been made by Willihnganz in 1941[2]. These involved excitation of the electrochemical cell by an ac voltage of small amplitude (about 5 mV) and evaluation of the resistive and capacitive components, or other related parameters. As the measurements encompass a wide range of AC signal frequencies, various characteristic parameters of the electrochemical cell and kinetics of the associated reactions can be evaluated.

During the impedance experiment, when a low-frequency ac signal is impressed, a time-dependent diffusion layer is created. As no net current flows, a steady state is set up after a few cycles. The overall impedance (Z) comprising combinations from diffusion and charge-transfer resistance can be expressed as [3],

$$Z = R_{ct} + \sigma / \omega^{1/2} + \sigma / j \omega^{1/2} \quad (A.1.30)$$

Where, σ is the Warburg coefficient. In the case of planar diffusion, σ , is defined as,

$$\sigma = (RT / 2^{1/2} n^{1/2} F^2 A D^{1/2})(1/C_O^0 + 1/C_R^0) \quad (A.1.31)$$

Where, A is the electrode area, D is the diffusion coefficient, C_O^0 and C_R^0 are the bulk concentrations of O and R, respectively. The frequency dependent reactance due to diffusion, which includes the last two terms in Eq. (A.1.30), is known as Warburg impedance (W).

Various processes occurring in an electrochemical cell may be represented by an electrical equivalent circuit. The equivalent circuit comprises electrical elements such as resistors and capacitors. Each element represents an electrochemical process involving the transport of mass and charge.

In such a case, an analytical procedure is required for evaluation of the impedance parameters. Using the non-linear-least-square (NLLS) fit technique due to Boukamp [4], all parameters in the equivalent circuit model are adjusted simultaneously, thus obtaining the optimum fit to the measured dispersion data. The ‘Data Cruncher’ section of the analysis program assists in the decomposition of the impedance dispersion into simple sub-circuits. This decomposition leads to an understanding of the possible equivalent circuits and provides a reasonable set of starting values for the adjustable circuit parameters by the general NLLS-fit procedure. The program involves assignment of an appropriate equivalent circuit in the form of a circuit description code (CDC). In a simple case of a circuit consisting of a resistance and a capacitance in series, for example, the CDC is RC, i.e. the elements are written without parentheses. If a resistance is present in series with a parallel combination of another resistance and a capacitance the CDC becomes R (RC). Subsequent to assigning the CDC for the purpose of NLLS-fit of impedance dispersion, has to enter an approximate initial value of the circuit parameters and start the program. The iterations continue till the best fit of the parameters with the experimental impedance data is obtained. In the output, the value of χ^2 of the NLLS-fit [5] and a chart of the correlation coefficients [6] are displayed together with the impedance parameters. A low value of χ^2 and a value of at least ± 0.1 for correlation coefficient of the impedance parameters [5] ensure confidence in the values of the impedance parameters. Additionally, the theoretical impedance dispersion simulated using the impedance parameters can be

compared with the experimental dispersion. An overlap of the dispersion further provides confidence in the NLLS-fit procedure.

A.1.2. Chronopotentiometry

Chronopotentiometry is an electrochemical technique which measures the potential response of a working electrode under an applied current pulse as a function of time. The potential response vary abruptly at the moment when the current is first applied due to iR loss and later changes gradually due to the development of concentration overpotential as the concentration of the reactant is exhausted at the electrode surface [7, 8]. If the current is larger than the limiting current, the required flux for the current cannot be provided by the diffusion process and, therefore, the electrode potential rapidly rises until it reaches the electrode potential of the next available reaction, and so on [7-9]. The chronopotentiometry techniques are of different types depending on the current patterns used for the analysis as shown in Fig. A.1.4.

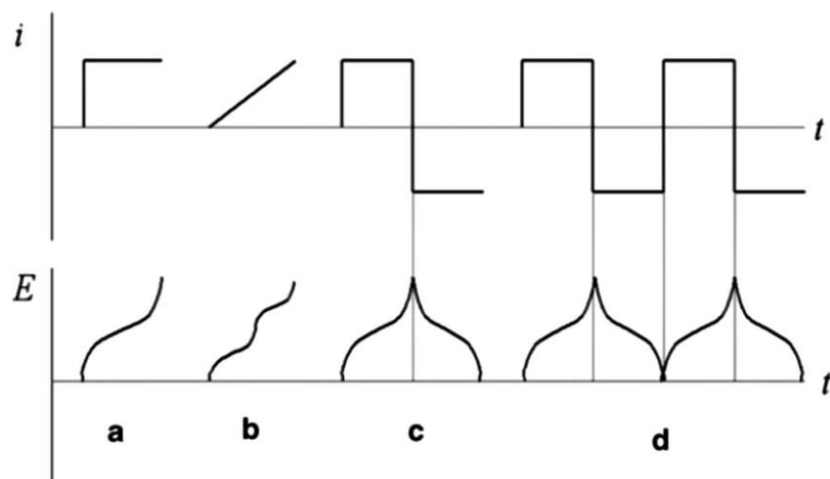


Fig. A.1.4: Different types of chronopotentiometric experiments: (a) Constant current chronopotentiometry, (b) Chronopotentiometry with linearly rising current, (c) Current reversal chronopotentiometry, and (d) Cyclic chronopotentiometry (Adopted from Ref. [9])

A constant anodic/cathodic current is applied in constant current chronopotentiometry (Fig. A.1.4(a)), however the applied current is linearly increased (or decreased) with time, rather than keeping constant, in chronopotentiometry with linearly varying current (Fig. A.1.4(b)). On the other hand, the current is reversed after

some time from anodic to cathodic in current reversal chronopotentiometry (Fig. A.1.4(c)) and the current is repeatedly reversed in cyclic chronopotentiometry (Fig. A.1.4(d)). When the applied current is changed suddenly from anodic to cathodic (current reversal), anodic reaction (i.e., anodic product) starts to be reduced. Then, the potential moves in the cathodic direction as the concentration of the cathodic product increases. Hence, the typical chronopotentiometric techniques can be readily extended to characterize the electrochemical properties of insertion materials. In particular, current reversal and cyclic chronopotentiometries are frequently used to estimate the specific capacity and to evaluate the cycling stability of the battery, respectively. The multi-step redox reactions during insertion process (in LIB/NIB) can be effectively characterized using the voltage profile from the current reversal or cyclic chronopotentiometry [9]. Moreover, the chemical diffusion coefficient of the species in the insertion materials can also be estimated using another most useful chronopotentiometry technique called galvanostatic intermittent titration technique (GITT) [10-12].

A.1.3. Chronoamperometry

Chronoamperometry is also known as the current transient technique. In this technique, the electrode potential is abruptly changed from E_1 (the electrode is usually in the equilibrium state) to E_2 and the resulting current variation is recorded as a function of time. The interpretation of the results is typically based on a planar electrode in a stagnant solution and an extremely fast interfacial redox reaction as compared to mass transfer. The schematic of potential stepping in chronoamperometry, the resulting current variation with time and the expected content profile of the active species O (with bulk concentration C_o^* , and it is electrochemically inactive at E_1 , but is reduced at E_2) in the electrolyte are shown in Fig. A.1.5.

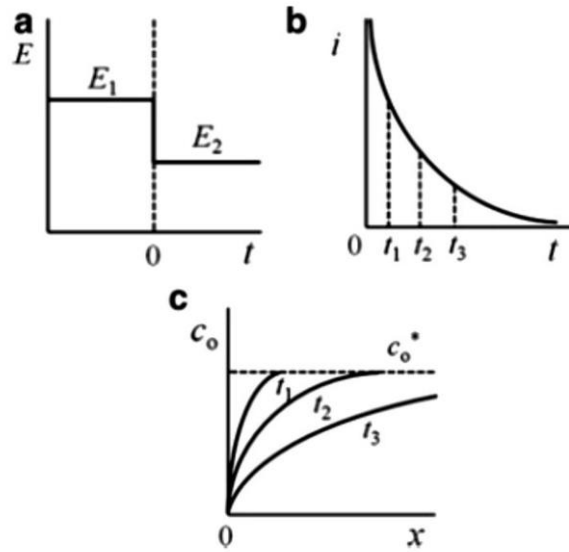


Fig. A.1.5: The schematic of: (a) the potential stepping in chronoamperometry, (b) the resulting current variation with time, and (c) the expected content profile of the active species O in the electrolyte (Adopted from Ref. [9])

The kinetic behavior of the insertion materials can be characterized using chronoamperometry technique based on the typical assumption that the diffusion of the active species governs the rate of the whole insertion process (that means by considering the assumption on potentiostatic and impermeable constraints) [9, 13, 14]. In order to determine the exact form of current-time dependence for a planar electrode, the current density Cottrell equation (Eq. A.1.32) is used. Which describes the observed current (planar electrode) at any time following a large forward potential step in a reversible redox reaction (or to large overpotential) as a function of $t^{-1/2}$.

$$i_t = \frac{nFAC_0D_0^{1/2}}{\pi^{1/2}t^{1/2}} \quad (\text{A.1.32})$$

Where, n is the stoichiometric number of electrons involved in the reaction; F is Faraday's constant (96,485 C/equivalent), A is electrode area (cm^2), C_0 is the concentration of electroactive species (mol/cm^3), and D_0 is the diffusion constant for electroactive species (cm^2/s). For diffusion controlled process, it can be noticed that the current falls as $t^{-1/2}$. This feature is frequently used as a test for this type of process and

from the slope of i_t vs. $t^{-1/2}$ the diffusion coefficient D_o can be calculated. However, it has been reported that the chemical diffusion coefficient determined from the current transient technique on the basis of the diffusion control process show a large discrepancy from those values determined by other electrochemical techniques such as the GITT and EIS [15, 16].

A.1.4. X-ray diffraction (XRD) analysis

X-ray diffraction provides both qualitative and quantitative information regarding various phases present in a material. For a crystal with interplanar spacing (d_{hkl}), Bragg's Law,

$$2d_{hkl} \sin \theta = n\lambda \quad (\text{A.1.33})$$

Eq. A133 gives the relationship between the X-ray wavelength (λ) and the angle (θ) at which constructive interference occurs. In Eq. (A.1.33), n is an integer indicating the order of the plane.

X-ray diffraction for a crystalline material produces well-defined peaks. The key to interpret powder X-ray diffraction pattern is that each phase produces its own pattern not withstanding the presence or absence of any other phases. The identification of the phases present in an unknown sample using the powder diffraction technique is based on comparison of the diffraction pattern of the material with its powder diffraction file collected and maintained at the Joint Committee on Powder Diffraction Standards (JCPDS).

The most popular method used for identifying the structure of an unknown sample is indexing which provides a cell that can be matched against the available Crystal Diffraction File (CDF) database. Computer analysis of diffraction data and the various software available for this purpose are well documented by Edmonds [17] and Smith [18]. Several methods are available for determining the composition of solid solutions and the relative amount of phases present in multi-component phase mixtures by X-ray diffractometer [19-21]. The XRD quantitative analysis is based on the premise

that each crystalline phase in a mixture has a unique diffraction pattern and the intensity is maintained at a constant level. The composition of a solid solution can be determined from the XRD pattern if the variation of lattice parameters with composition is calibrated independently. Quantitative and qualitative aspects of X-ray diffraction analysis are well documented by Synder [19] and Synder and Bish [20].

The factors affecting the accuracy of the experimental diffraction patterns can be broadly classified into those affecting the d-spacing and the intensity. In spite of several sources of error in the measurement of 2θ values and the subsequent conversion to d-spacing, the derived d-values are generally sufficient for qualitative phase identification. The major factors influencing the d-spacing accuracy are specimen displacement, diffractometer misalignment, problems of finding the true peak position and errors in conversion of 2θ to d.

The magnitude of the systematic error in 2θ maxima ($\Delta 2\theta$) because of the displacement of the sample surface downward on a vertical goniometer from the center of the goniometer focusing circle is equal to $-2s \cos\theta / r$, where s is the sample displacement and r is the radius of the goniometer circle. At low angles, where $\cos\theta$ is closer to unity, the magnitude of error in 2θ is roughly equal to $-2s/r$.

Instrument misalignment due to the wrong setting of the mechanical zero and the 2:1 rotation axis of the goniometer can introduce systematic errors into the observed 2θ values. The mechanical zero of the goniometer is the angle at which a single line bisects the center of the receiving slit, the center of the goniometer rotation axis, and the center of the projected source from the X-ray tube. An error in mechanical setting will produce an equivalent error in all observed 2θ values. Any error in the 2:1 angular speed relationship will introduce a cyclic error into the observed 2θ values.

The shape of the diffracted line profile is determined by various factors like axial divergence of the X-ray beam, particle size, microstrain of specimen and monochromaticity of the source. The distortion of the peak shape from these effects leads to problems in finding the peak maxima. In such cases, the peak maxima is

obtained by differentiating the peak and taking the point corresponding to $dI/d\theta = 0$, or by taking the average of inflection points. The parameters measured in diffraction experiments are the line intensities and the angles at which these lines occur. The effect of an error in 2θ on the d-spacing can be expressed as: $\Delta d/d = \theta \cot\theta$. Thus, fixed error in 2θ has greater impact on d-spacing accuracy at low angles.

Major factors affecting the accuracy of the measured intensity in a powder pattern can be classified as instrument sensitive and sample sensitive factors. Instrument sensitive factors include effect of variable divergence slit on relative intensities, and non-linearity of the detector (the measured count rate from the detector is not directly proportional to the photon rate entering the detector). Various sample sensitive issues and the methods adopted in addressing them are: (a) crystal particle statistics can be a major source of error. Favorable statistics requires about 10^8 crystallites [22]. A particle size of about $5 \mu\text{m}$ is generally recommended for a diffractometer sample. Rotating the sample in the diffractometer will expose more crystallites to the X-rays and hence provide improved intensities. (b) The preferred orientation is caused by the morphology of the particles constituting the sample. The X-ray intensities are known to depend strongly on the shape and orientation texture of phases present in the sample. Therefore, preferred orientation in the sample may invalidate the determination of relative amount of phases present in a polyphasic mixture when X-ray intensities are used for quantitative phase analysis. If only one peak from each phase is being used for the analysis, preferred orientation can give widely different results. (c) Peak broadening can occur if sample has particles of very small crystallite size. Micro stress, disorder and inhomogeneity of solid solutions can also cause broadening, resulting in errors in the measurement of intensity. The problem can be partially resolved by measuring the integrated intensity rather than that the peak height. (d) Sample preparation may affect the intensities of the peaks in XRD. The sample preparation technique must be the same for all the samples. For example, the density of the packed powder in the sample holder, size and shape of the sample holder and the thickness of the sample must be maintained uniformly.

A.1.5. Electron microscopy

One of the important tools for the characterization of materials is the electron microscope in which a beam of electron functions in the same way as the light beam does in a conventional optical microscope. Moving electrons exhibit wave characteristics with a de-Broglie wavelength ($\lambda = h/p = h/mv$) which is $\sim 1 \text{ \AA}$ for values of frequencies (ν) corresponding to acceleration voltage of 50-100 keV. As the resolving power of an optical microscope depends on the wavelength of the light beam used ($\sim 500 \text{ \AA}$), the potential increase in resolving power is obvious. As a result of the development in electron optics, this limit is almost realized. The difference between an optical microscope and an electron microscope is schematically depicted in the Fig. A.1.6. Electron microscope has as electron gun as source of electrons that uses thermionic emission from a filament or field emission from a tip and from which a beam of electrons of energy 50-100 keV emerges. A series of lenses converge the beam into a small spot on the specimen. The transmitted beam of electron passes through the optical and projection lenses and forms an image on a fluorescent screen or photoplate. The electron lenses consist of coils with suitably shaped soft iron pole pieces. Focusing is accomplished by precise control of current in the magnetizing coils thus varying the effective focal length of the lenses. Electron microscopes have the provision for observation of electron diffraction pattern via suitable alterations in the electron lens system.

Electron microscopy is an extremely versatile technique capable of providing structural information over a wide range of magnification. At one extreme, scanning electron microscopy (SEM) complements optical microscopy for studying the texture, topography and surface features of powders or solid pieces; features up to tens of micrometers in size can be seen and, because of the depth of focus of SEM instruments, the resulting pictures have a definite three-dimensional quality. At the other extreme, high-resolution electron microscopy (HREM) is capable, under favorable circumstances, of giving information on an atomic scale, by direct lattice imaging.

Resolution of $\sim 2\text{\AA}$ has been achieved, which means that it is now becoming increasingly possible to see individual atoms.

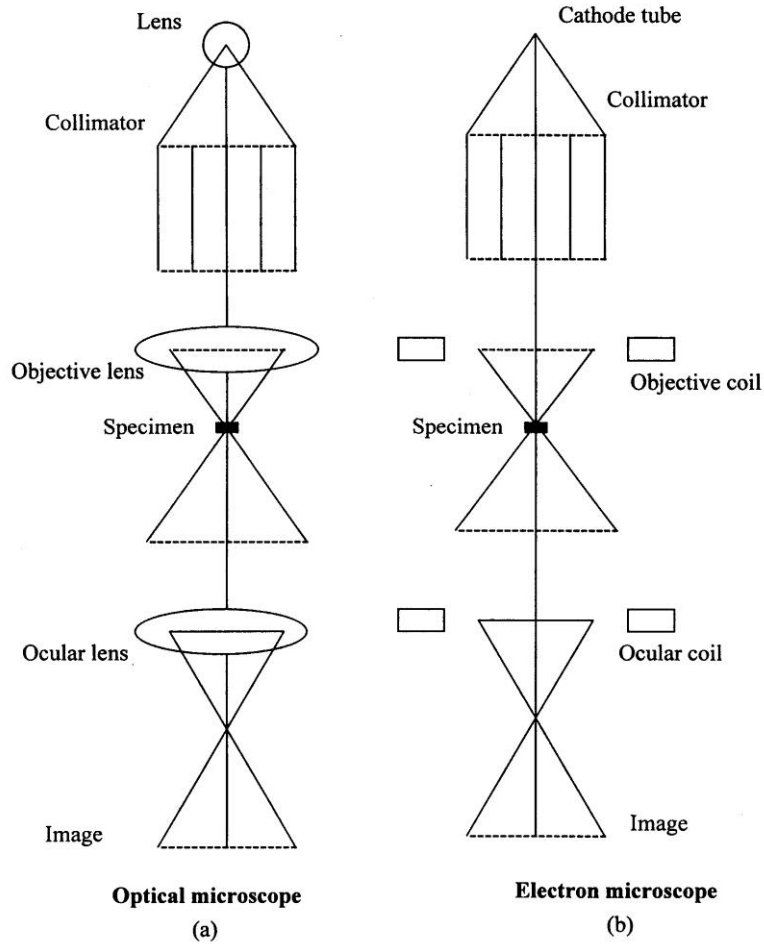


Fig. A.1.6: Schematic diagrams of (a) an optical, and (b) an electron microscope

In the scanning electron microscope, electrons from the electron gun are focused to a small spot, $50\text{-}100\text{\AA}$ in diameter, on the surface of the sample. The electron beam is scanned systematically over the sample, rather like a spot on a television screen. Both X-rays and secondary electrons are emitted by the sample; the former are used for chemical analysis and the latter are used to build up an image of the sample surface,

which is displayed on a screen. A limitation with SEM instruments is that the lower limit of resolution is $\sim 100 \text{ \AA}$. A recent advance is the development of the scanning transmission electron microscope (STEM). This combines the scanning feature of the SEM with the intrinsically higher resolution obtainable with transmission electron microscope (TEM).

The basic components of a TEM instrument are listed in Fig. A.1.7. Electrons emitted from a tungsten filament (electron gun) are accelerated through a high voltage (50-100 kV). Their wavelength (λ) is related to accelerating voltage, V , by

$$\lambda = h (2meV)^{-1/2} \quad (\text{A.1.34})$$

Where, m and e are the mass and charge of the electron, respectively. At high voltage, as the velocity of the electron approaches the velocity of light, m is increased by relativistic effects. The electron wavelengths are much smaller than the X-ray wavelengths used in diffraction experiments, e.g. λ is $\sim 0.04 \text{ \AA}$ at 90 kV accelerating voltage. Consequently, the Bragg angles for diffraction are small and the diffracted beams are concentrated into a narrow cone centered on the undiffracted beam [23].

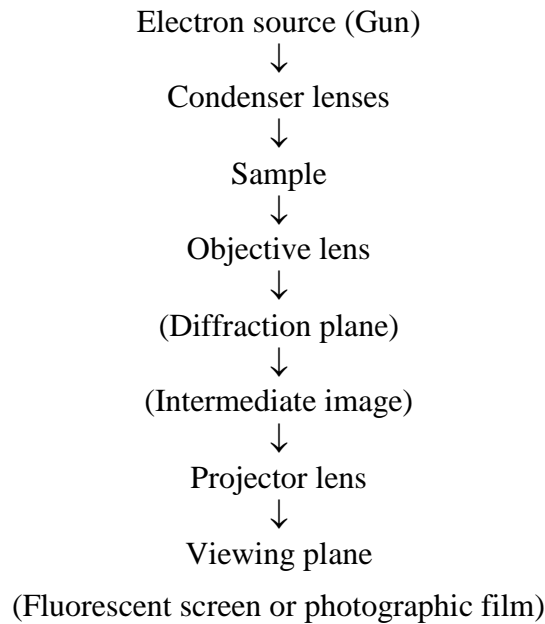


Fig. A.1.7: Basic components of a transmission electron microscope

Some SEM and TEM instruments have the very valuable additional feature of providing an elemental analysis of sample composition. There are various names for the technique including electron probe microanalysis (EPMA), electron microscopy with microanalysis (EMMA) and analytical electron microscopy (AEM). The main mode of operation makes use of the fact that when a sample is placed in the microscope and bombarded with high-energy electrons, many things can happen, including the generation of X-rays. These X-rays are characteristic emission spectra of the elements present in the sample. By scanning either the wavelength (wavelength dispersive analysis of X-rays (WDAX)) or the energy (energy dispersive analysis of X-rays (EDAX)) of the emitted X-rays, it is possible to identify the elements present. If a suitable calibration procedure has been adopted, a quantitative elemental analysis may be made. The basic operation, energy resolution, detector electronics and multichannel analysis regarding EDAX are well documented in the literature [24, 25]. At present, only elements heavier than and including sodium can be determined; lighter elements do not give suitable X-ray spectra. For lighter elements, however, there are alternative techniques such as Auger spectroscopy and electron energy loss spectroscopy (EELS).

A.1.6. X-ray photoelectron spectroscopy

XPS is a dedicated technique used for determining the chemical composition of materials based on photoelectric effect. It is also known as electron spectroscopy for chemical analysis (ESCA). XPS is a highly surface sensitive technique which can analyze a sample to a depth of 2 to 5 nanometers (nm). It can reveal the major chemical elements present on the surface and the nature of chemical bond existing between the elements. Except hydrogen and helium all other elements can be detected using XPS. The binding energy of an electron in a molecular orbital can be significantly influenced by the nature of its chemical environment. The kinetic energy distribution of emitted photoelectrons provides information regarding composition and electronic state of the sample surface [26-28]. In XPS, soft X-rays (with a photon energy of 200-2000 eV) is used to examine core-levels of the sample surface. XPS is usually carried out under

high vacuum for reducing the sample degradation. The photoemission principle forms the basic principle of XPS. When the material is irradiated with a beam of X-ray, the photon is absorbed by an atom in a molecule or solid, leading to ionization and the emission of a core (inner shell) electron. Thus sufficient energy is provided to break the photoelectron away from the nuclear attraction force of an element. A beta-ray spectrometer is used to determine the energy spectra of the ejected electron. A schematic of the photoelectron excitation process and the basic components of an XPS instrument along with the data formats are given in Fig. A.1.8.

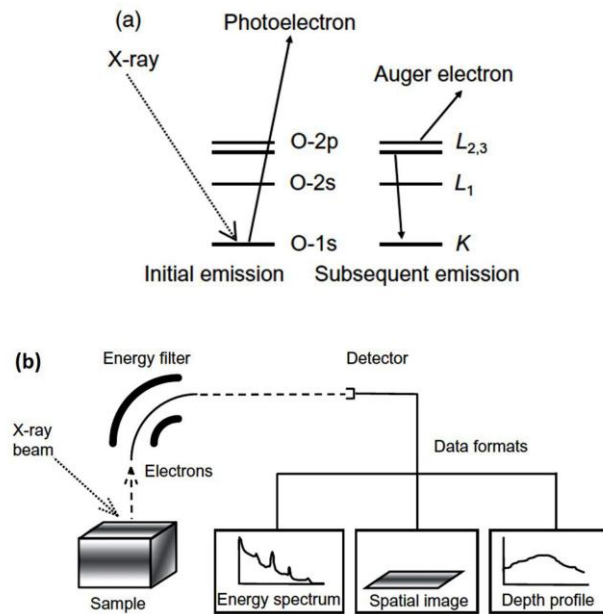


Fig. A.1.8: Schematic of: (a) the photoelectron excitation process, and (b) the basic components of an XPS instrument along with the data formats (Adopted from Ref. [28])

The kinetic energy of the photoelectrons are given by the Eq. A.1.35.

$$K.E. = h\nu - B.E. - \phi \quad (\text{A.1.35})$$

Where, $K.E.$ is the kinetic energy of the photoelectrons, $h\nu$ is the energy of the incident photon, $B.E.$ is the binding energy of electron and ϕ is the work function of material. The time required for photon absorption is less and takes place within 10^{-16} s. For the photoemission, $h\nu$ should be higher than $B.E. + \phi$. $K.E.$, and it increases with

decrease in the B.E. The photoemission intensity is proportional to the intensity of the photon. Since, the specific energy of an elemental core level transition occurs at a specific B.E., the element can be characterized accurately. The ejected photoelectron will be collected by the electron analyzer and its kinetic energy is measured. The presence of peaks at particular energies therefore indicates the presence of a specific element in the sample under study - furthermore, the intensity of the peaks is related to the concentration of the element within the sampled region. B.E. is a direct measure of strength of interaction between electrons and the nuclear charge. Hence it can provide information on the initial and final state of atom. The chemical state information can be obtained from the initial states as it accounts for the core level binding energy shifts. The ejected photoelectron from core level can undergo slight shift depending on the outer valence configuration of the sample tested [27]. Thus according to change in chemical surrounding, the effective charge is altered resulting in a change in B.E. value. Therefore, as the oxidation state of an atom changes, a chemical shift or surface core level shift could be observed. The increase in B.E. value shows that the electron is tightly held by nucleus and thus for element with high atomic number possess higher B.E. values. Coupling of magnetic fields of spin (s) and angular momentum (l) occurs if the electron in the orbital possesses orbital angular momentum. If ' j ' is the total momentum, the level of degeneracy for spin-orbital splitting will be $(2j+1)$. Thus s orbital will not undergo splitting whereas a doublet with intensity ratio at 1:2 for $p_{1/2}$ and $p_{3/2}$ could be observed for p orbital [26-28]. The most commonly employed X-ray sources are those giving rise to Mg $K\alpha$ radiation: $h\nu = 1253.6$ eV and Al $K\alpha$ radiation: $h\nu = 1486.6$ eV.

For the present study, the XPS measurements were carried out ESCA+, (Omicron nanotechnology, Oxford Instruments plc, Germany) equipped with monochromic Al $K\alpha$ (1486.6 eV) X-ray beam radiation operated at 15 kV and 20 mA, B.E. was calibrated vs. carbon (C1s = 284.6 eV). For these measurements, the powder samples were transferred to the XPS device using a hermetically sealed unit, which contains a sample holder attached to a magnetic manipulator, and a gate valve. A survey

spectrum was taken first followed by XPS of required elements, and the obtained spectra were deconvoluted using Gaussian functions based on Origin 8.0 software.

A.1.7. Raman spectroscopy

Raman scattering is one of a family of scattering processes involving interaction of a primary light quantum with atoms, molecules, or crystals by which a secondary light quantum is produced. Raman involves inelastic scattering, producing secondary light quanta of different energy from the primary light quanta. The energy difference is equal to the vibrational energy of a molecule or crystal and/or the rotational energy of a molecule, and thereby Raman scattering provides a means of measuring vibrational spectra, alternatively to infrared (IR) absorption spectroscopy. These two types of spectroscopy are illustrated schematically in Fig. A.1.9. If monochromatic radiation is used for the primary light quanta, recording the secondary quanta produces a Raman spectrum. Scattering from molecules or crystals in their ground rotational and/or vibrational states produces a Stokes, or red-shifted, Raman spectrum. Scattering from excited vibrational and/or rotational states produces an anti-Stokes, or blue-shifted, Raman spectrum [29].

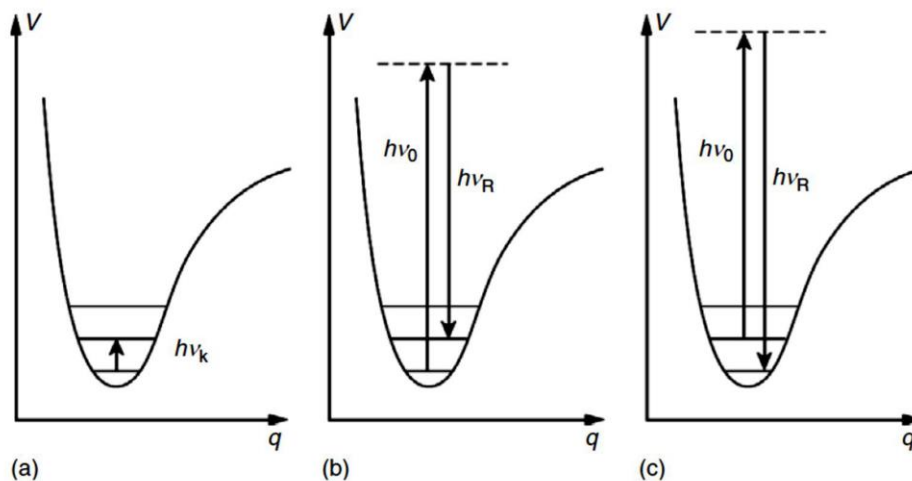


Fig. A.1.9: Energy level diagram for: (a) Infrared absorption, (b) Stokes Raman scattering, and (c) anti-Stokes Raman scattering (Adopted from Ref. [29])

The instrumentation of a typical Raman system consists of four major components: a) excitation source (Laser), b) sample illumination source and light collection optics, c) wavelength selector (filter) and d) a detector. A sample is normally illuminated with a laser beam in the ultraviolet (UV), visible or near infrared (NIR) range. The scattered light is collected with a lens and it is sent through the interference filter to obtain the Raman spectrum of the sample. As an example, the Raman spectra of different forms carbon are shown in Fig. A.1.10.

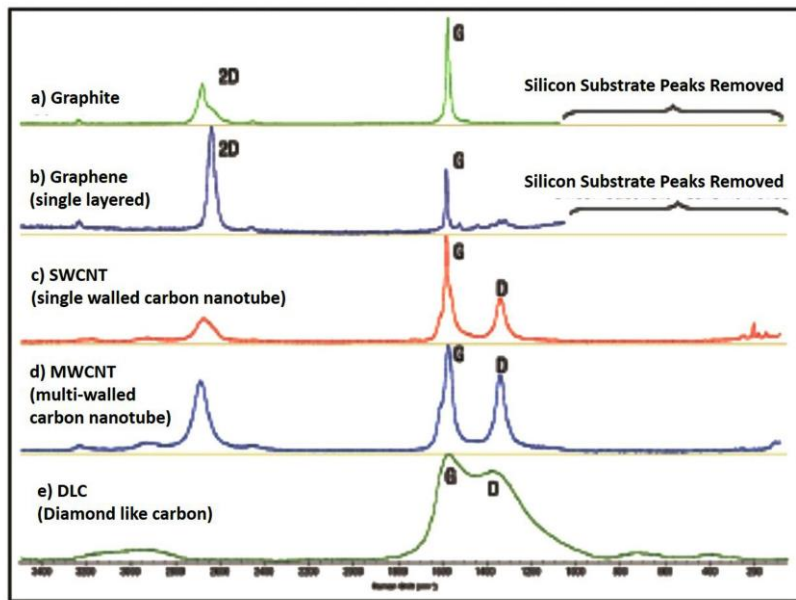


Fig. A.1.10: Raman spectra of different forms of carbon: (a) Graphite, (b) Single layer of graphene, (c) Single walled carbon nanotube (SWCNT), (d) Multi-walled carbon nanotube (MWCNT), and (e) Diamond like carbon (DLC) (Adopted from Ref. [30])

Raman spectroscopy technique has been emerged as a very important analytical tool for the characterization of battery materials. It can be used for the analysis of different types of battery components such as cathode materials, anode materials and electrolytes [31]. Among the various advantages of Raman spectroscopy, the most important one for battery application is the ability to detect the molecular structure or local chemical environments. Moreover, the Raman spectral results can be directly correlated with the electrochemical performance of the materials. In the present study, a

micro Raman spectrometer HR800 (Jobin Yovn Horiba, France), with He-Ne laser (excitation line 632.8 nm) and a microscope objective (50×, Olympus Mplan, 0.4 mm working, numerical aperture 0.75 in back scattering configuration) is used for the analysis.

References

- [1] S. Sathyanarayana, S. Venugopalan, M.L. Gopikanth, Impedance parameters and the state-of charge. I. Nickel-cadmium battery, *J. Appl. Electrochem.* 9 (1979) 125–139.
- [2] E. Willihnganz, A bridge for measuring storage battery resistance, *Trans. Electrochem. Soc.* 79 (1941) 253–258.
- [3] J. Robinson, R. Greef, R. Peat, L.M. Peter, D. Pletcher, *Instrumental Methods in Electrochemistry*, Ellis Horwood, Chichester, 1985.
- [4] B. A. Boukamp, *Equivalent Circuit, Users Manual*, University of Twente, The Netherlands, 1989.
- [5] R. R. Bevington, *Data reduction and Error Analysis for the Physical Sciences*, McGraw Hill, New York, 1969.
- [6] Mick Alt, *Exploring Hyperspace – A Non Mathematical Explanation of Multivariate Analysis*, McGraw-Hill, UK, 1990.
- [7] A.J. Bard, L.R. Faulkner, J. Leddy, C.G. Zoski, *Electrochemical methods: fundamentals and applications*, Wiley New York, 1980.
- [8] J. Wang, *Analytical electrochemistry*, John Wiley & Sons, 2006.
- [9] S.-I. Pyun, H.-C. Shin, J.-W. Lee, J.-Y. Go, *Electrochemistry of insertion materials for hydrogen and lithium*, Springer Science & Business Media, 2012.
- [10] W. Weppner, R.A. Huggins, Determination of the kinetic parameters of mixed-conducting electrodes and application to the system Li_3Sb , *J. Electrochem. Soc.* 124 (1977) 1569–1578.
- [11] Y.-M. Choi, S.-I. Pyun, J.-S. Bae, S.-I. Moon, Effects of lithium content on the electrochemical lithium intercalation reaction into LiNiO_2 and LiCoO_2 electrodes, *J. Power Sources.* 56 (1995) 25–30.
- [12] J.-S. Bae, S.-I. Pyun, Electrochemical lithium intercalation reaction of anodic vanadium oxide film, *J. Alloys Compd.* 217 (1995) 52–58.

- [13] J. Crank, *The mathematics of diffusion*, Oxford university press, 1979.
- [14] C.J. Wen, B.A. Boukamp, R.A. Huggins, W. Weppner, Thermodynamic and mass transport properties of "LiAl," *J. Electrochem. Soc.* 126 (1979) 2258–2266.
- [15] T. Uchida, Y. Morikawa, H. Ikuta, M. Wakihara, K. Suzuki, Chemical diffusion coefficient of lithium in carbon fiber, *J. Electrochem. Soc.* 143 (1996) 2606–2610.
- [16] D. Zhang, B.N. Popov, R.E. White, Modeling lithium intercalation of a single spinel particle under potentiodynamic control, *J. Electrochem. Soc.* 147 (2000) 831–838.
- [17] J.W. Edmonds, Generalization of the ZRD–SEARCH–MATCH program for powder diffraction analysis, *J. Appl. Crystallogr.* 13 (1980) 191–192.
- [18] D.K. Smith, Particle statistics and whole-pattern methods in quantitative X-ray powder diffraction analysis a, *Powder Diffr.* 16 (2001) 186–191.
- [19] M.A. Baker, *Materials Science and Technology, Characterization of Materials*, Wiley-VCH, 1994.
- [20] D.L. Bish, J.E. Post, *Modern powder diffraction*, Mineralogical Society of America Washington, DC, 1989.
- [21] H. P. Klug and L. E. Alexander, *X-ray Diffraction Procedure for Polycrystalline and Amorphous Materials*, John Wiley & Sons, New York, 1974.
- [22] C.R. Hubbard, D.K. Smith, Experimental and calculated standards for quantitative analysis by powder diffraction, in: *Advances in X-Ray Analysis*, Springer, 1977: pp. 27–39.
- [23] A. R. West, *Solid State Chemistry and its Applications*, John Wiley & Sons, New York, 1987, p. 64.
- [24] K. F. J. Heinrich and D. E. Newbury, *Metals Handbook*, 9th Edition, ASM, 1986, p. 516.
- [25] B. L. Gabriel, *SEM: A Users Manual for Material Science*, Am. Soc. Of Metals, Metals Park, Ohio, 1985.
- [26] Taglauer, E.; Vickerman, J. C., *Surface Analysis-The Principle Techniques*, In Wiley, New York, 1997.
- [27] D. Briggs, M.P. Seah, *Practical surface analysis: by auger and x-ray photoelectron spectroscopy*, Wiley, 2003.
- [28] P. Van der Heide, *X-ray photoelectron spectroscopy: an introduction to principles and practices*, John Wiley & Sons, 2011.
- [29] G. Gauglitz, D.S. Moore, *Handbook of Spectroscopy*, 4 Volume Set, John Wiley & Sons, 2014.

- [30] J. Hodkiewicz, Characterizing carbon materials with Raman spectroscopy, Thermo Scientific Application Note. 51946, 2010.
- [31] T.N. Lambert, C.C. Luhrs, C.A. Chavez, S. Wakeland, M.T. Brumbach, T.M. Alam, Graphite oxide as a precursor for the synthesis of disordered graphenes using the aerosol-through-plasma method, *Carbon*. 48 (2010) 4081–4089.

List of Publications

Publications included in the thesis

1. **S. Krishnakumar**, S. Ghosh, P. Ghosal, S. K. Martha, Synergistic effect of 3D electrode architecture and fluorine doping of $\text{Li}_{1.2}\text{Ni}_{0.15}\text{Mn}_{0.55}\text{Co}_{0.1}\text{O}_2$ for high energy density lithium-ion batteries, *J. Power Sources* 356 (2017) 115-123
2. **S. Krishnakumar**, S. Ghosh, S.K. Martha, Synergistic effect of magnesium and fluorine doping on the electrochemical performance of lithium-manganese rich (LMR)-based Ni-Mn-Co-oxide (NMC) cathodes for lithium-ion batteries, *Ionics*, 23 (2017) 1655–1662.
3. **S. Krishna Kumar** et al., Temperature effect on "Ragone Plots" of Lithium- Ion Batteries, *J. Electrochem. Soc.* (Accepted).
4. **S. Krishna Kumar**, S. K. Martha, $\text{Li}_{1.2}\text{Mn}_{0.55}\text{Ni}_{0.15}\text{Co}_{0.1}\text{O}_2$ (LMR-NMC)-Carbon Coated-LiMnPO₄ Blended Electrodes for High Performance Lithium Ion Batteries, *J. Electrochem. Soc.* 165 (3) A463-A468 (2018).
5. **S. Krishna Kumar**, R. Choudhury, S. K. Martha, Binder and Conductive Additive Free Silicon Electrode Architectures for Advanced Lithium- Ion Batteries, *J. Energy Storage* (Under Review).
6. **S. Krishna Kumar**, S. K. Malladi, J. Nanda, S. K. Martha In-situ 3D Electrode Fabrication of High Capacity Silicon-Carbon Anodes for Lithium-Ion Batteries (Submitted).

Book Chapter/ Proceedings

1. **S. Krishna Kumar**, S. Ghosh, S. K. Martha, J. Nanda, Lithium-Manganese Rich $\text{Li}_{1.2}\text{Mn}_{0.55}\text{Ni}_{0.15}\text{Co}_{0.1}\text{O}_2$ (LMR NMC) Based Cathodes for High Energy Density Lithium-Ion Batteries (A review), *Solid State Ionics: From Concept to Application*, Narosa Publication, New Delhi, India (In Press), Expected Jan 2018.

Publications not included in thesis

1. P. Naresh Kumar, A. Kolay, **S. Krishna Kumar**, P. K. Patra, A. N Aphale, A. K. Srivastava, and M. Deepa, The Counter Electrode Impact on Quantum Dot Solar Cell Efficiencies, *ACS Appl. Mater. Interfaces*, 2016, 8 (41), 27688–27700.

2. A. Kolay, P. Naresh Kumar, **S. Krishna Kumar**, M. Deepa, Titanium Oxide Morphology Controls Charge Collection Efficiency in Quantum Dot Solar Cells, *Phy. Chem. Chem. Phys.*, 19 (2017) 4607-4617.
3. D. Damodar, **S. Krishna Kumar**, S. K. Martha and A. S. Deshpande, Nitrogen Doped Graphene-like Carbon Nanosheets from Commercial Glue: Unique Structural Evolution and Li-ion Battery Performance (Under review).

Contribution to academic conferences

1. **S. Krishna Kumar**, Sourav Ghosh, Surendra K. Martha, Metal Free, Binder Free Electrode Architectures for Advanced Lithium-Ion Batteries, 56th International Battery Symposium of Japan, Meieki, Nakamura-ku, Nagoya, Aichi Prefecture 450-0002, November 11-13, 2015.
2. **S. Krishna Kumar**, Sourav Ghosh, Surendra K. Martha, Lithium Manganese rich based NMC oxide cathodes for advanced lithium ion batteries, Indo-US science and technology forum, Recent advances in multiscale, multiphysics, analysis of energy conversion in lithium ion batteries, VMCC auditorium, IIT Bombay, 17-19 June 2016.
3. **S. Krishna Kumar et al.** Lithium –Manganese rich $\text{Li}_{1.2}\text{Mn}_{0.55}\text{Ni}_{0.15}\text{Co}_{0.1}\text{O}_2$ as an advanced cathode material for high energy density lithium-ion batteries, International Conference on Materials Science & Technology (ICMTech), 2016, New Delhi, India.
4. **S. Krishna Kumar et al.** Lithium –Manganese rich $\text{Li}_{1.2}\text{Mn}_{0.55}\text{Ni}_{0.15}\text{Co}_{0.1}\text{O}_2$ as an advanced cathode material for high energy density lithium-ion batteries, 15th Asian Conference on Solid State Ionics, November 27-30, 2016, Patna, India.
5. **S. Krishna Kumar et al.**, Effect of Fluorine Doping on the Electrochemical Performance of Lithium –Manganese Rich (LMR) Based Ni-Mn-Co- Oxide (NMC) Cathodes for Lithium-Ion Batteries, 1st World Conference on Solid Electrolytes for Advanced Applications, 6-9, Sep. 2017, Pondicherry University, India.
6. **S. Krishna Kumar et al.**, Synergistic Effect of Magnesium and Fluorine Doping on the Electro-chemical Performance of Lithium –Manganese Rich (LMR) Based Ni-Mn-Co-Oxide (NMC) Cathodes for Lithium-Ion Batteries, 9th International Conference on Materials for Advanced Technologies, (D-11: Cathode Materials II), ICMAT 2017, 18-23 June 2017, Suntec Singapore.